Air-filled substrate integrated waveguide components : Design techniques and integration technologies

Nhu Huan Nguyen

POLYTECHNIQUE MONTRÉAL
UNIVERSITÉ D'INGÉNIERIE

UGA Université Grenoble Alpes

THÈSE

Pour obtenir le grade de

DOCTEUR DE L'UNIVERSITE GRENOBLE ALPES

préparée dans le cadre d'une cotutelle entre l'*Université Grenoble Alpes* et *l'École Polytechnique de Montréal*

Spécialité : **OPTIQUE ET RADIOFREQUENCES**

Arrêté ministériel : le 6 janvier 2005 – 25 mai 2016

Présentée par

Nhu-Huan NGUYEN

Thèse dirigée par **Pr Tan-Phu VUONG** et **Pr Ke WU**
codirigée par **Pr Anne VILCOT** et **MCF Anthony GHIOTTO**

préparée au sein des **Laboratoire IMEP-LaHC, Centre de recherche Poly-Grames, et Centre de recherche IMS**

dans **l'Écoles Doctorale Electronique, Electrotechnique, Automatique, et Traitement du Signal** et **Polytechnique Montréal**

Composants guides d'ondes remplis d'air intégrés au substrat : techniques de conception et technologies d'intégration

Thèse soutenue publiquement le 06 décembre 2021,
devant le jury composé de :

Monsieur Jean-Jacques LAURIN,
Professeur à l'École Polytechnique de Montréal, Président
Monsieur Hervé AUBERT
Professeur à l'Institut National Polytechnique de Toulouse, Rapporteur
Madame Elodie RICHALOT
Professeure à l'Université Gustave Eiffel, Rapportrice
Monsieur Ke WU
Professeur à l'École Polytechnique de Montréal, Membre
Monsieur Tan-Phu VUONG
Professeur à l'Institut Polytechnique de Grenoble, Membre
Madame Anne VILCOT
Professeure à l'Institut Polytechnique de Grenoble, Membre
Monsieur Anthony GHIOTTO
Maître de conférences à l'Institut Polytechnique de Bordeaux, Membre
Monsieur Mohammad S. SHARAWI,
Professeur à l'École Polytechnique de Montréal, Membre

DEDICATION

"A journey of a thousand miles begins with a single step"

- Lao Tzu -

ACKNOWLEDGEMENTS

To begin, I would like to express my deep gratitude to my supervisors and co-supervisors: Pr. Ke WU from the Poly-Grames research center, École Polytechnique de Montréal; Pr. Tan-Phu VUONG and Pr. Anne VILCOT from the IMEP-LaHC research center, University of Grenoble Alpes; and MCF. Anthony GHIOTTO from the IMS research center, University of Bordeaux for their unconditional guidance and supports, not only in my Ph.D., but also in my life. In particularly, Anthony, you have guided and trained me patiently from the very beginning. I am very grateful to you for your helps.

I would like also to thank my thesis committee: Pr. Jean-Jacques LAURIN and Pr. Mohammad S. SHARAWI from the École Polytechnique de Montréal; Pr. Hervé AUBERT from the Institut National Polytechnique de Toulouse; and Pr. Elodie RICHALOT from the University Gustave Eiffel for their participation and review.

I would like to thank the technical staffs for their supports and fruitful discussions: Mr. Nicolas CORRAO, Mr. Xavier MESCOT, and Ms. Martine GRI from the IMEP-LaHC research center; Mr. Traian ANTONESCU, Mr. Jean-Sébastien DÉCARIE, Mr. Steve DUBE, Mr. Maxime THIBAULT, Mr. Louis-Philippe CARIGNAN, and Mr. Jules GAUTHIER from the Poly-Grames research center; and Ms. Magali DE MATOS from the IMS research center. In particularly, I would like to thank Mr. Traian for his technical support in the fabrication and assembling.

I would like also to thank the administrative staffs: Ms. Isabelle MICHELIN, Ms. Dalhila ALOUANI, Ms. Anaïs DESCHAUX-BEAUME, Ms. Fabienne COURTIN, and Ms. Valérie MISCIOSCIA from the IMEP-LaHC research center; and Ms. Rachel LORTIE, Ms. Brigitte GAL, Ms. Nathalie LÉVESQUE, and Ms. Monique MALOUIN from École Polytechnique Montréal for their supports, especially for the double-diploma procedure.

I would like to thank all my colleagues and friends, especially Tifenn, Qingtao, Wentao, Desong, Xiaoqiang, Ngoc-Huy, Minh-Cong, Minh-Vuong, and Phan Anh for their technical and living supports.

Finally, I am truly grateful to my family: my father Nhu-Chan, my mother Thi-Loan, my sister Thi-Hoan, my brother-in-law Tri-Giap, my nephew Tri-Anh, my dear fiancée Anh-Thuong, my father-in-law Huu-Cuong, and my mother-in-law Thi-Anh for their unconditional supports and encouragement. You have been with me through my peaks and my valleys. I could not have completed my thesis without your support.

RÉSUMÉ

Depuis une vingtaine d'années, le guide d'ondes intégré au substrat (SIW en anglais) a démontré ses nombreux avantages pour le développement de circuits et systèmes intégrés à hautes performances dans les bandes RF, micro-ondes, et millimétriques. Le SIW hérite des caractéristiques du guide d'ondes métallique et de la ligne micro-ruban telles qu'un faible coût, une taille compacte, un blindage intrinsèque, une facilité d'intégration, et une bonne dissipation thermique. Afin d'améliorer les performances du SIW, le SIW creux (AFSIW en anglais) a été introduit en 2014. En utilisant de l'air pour transmettre le signal électromagnétique, l'AFSIW réduit significativement les pertes diélectriques. Grâce à cela, la capacité de tenue en puissance ainsi que le facteur de qualité d'une structure AFSIW sont augmentés. Depuis son introduction, de nombreux travaux ont été investis pour développer cette nouvelle technologie. Cependant, la plupart des recherches se sont concentrées uniquement sur la couche centrale pour réaliser la conception des fonctions hyperfréquences, les couches du dessus et du dessous n'étant utilisées que pour fermer la structure. Hors, l'AFSIW étant une structure multicouche, il reste plusieurs degrés de liberté à exploiter pour accroître la densité d'intégration et pour mettre à profit les couches du dessus et du dessous. Dans le cadre de cette thèse, la couche centrale ainsi que les couches du dessus et du dessous sont exploitées et utilisées afin de développer de nouvelles fonctions hyperfréquences.

Concernant le degré de liberté offert par la couche creuse au centre, une structure alternative que nous avons nommée AFSIW à barreau diélectrique (SAFISW en anglais) a été introduite dans le cadre de cette thèse. Elle offre un bon compromis entre le SIW traditionnel et l'AFSIW en termes de pertes et d'empreinte, mais avec une bande passante monomode plus large. Basés sur le SAFSIW, de nombreux composants ont été développés et prototypés comme le SAFSIW à demi-mode, des déphaseurs compensés à large bande, et des antennes. Ce type de déphaseurs et d'antennes ont été ensuite conjointement intégrés ensemble pour concevoir un réseau d'antennes mono-pulse.

Concernant le degré de liberté offert par la structure multicouche, une nouvelle structure multiport appelée jonction T magique aux ports delta équilibrés (balanced-delta-port magic-tee en anglais) a été introduite avec des analyses théoriques. Cette structure donne une capacité de tenue en puissance plus haute que celle de la jonction T magique traditionnelle. Utilisant cette topologie, de nombreux diviseurs/combineurs de puissance avec les sorties/entrées isolées ont été étudiés et démontrés, comprenant des solutions résistives et absorbantes. Les diviseurs/combineurs de puissance utilisant l'absorbant donnent un niveau d'isolation sur une

large bande et une tolérance aux erreurs de fabrication, qui sont deux facteurs importants dans un processus de production en série.

En plus, un réseau d’antennes mono-pulse multicouche et une matrice de Butler multicouche ont été développés, illustrant la mise à profit de la structure AFSIW multicouche.

Cette thèse vise à élargir et enrichir la bibliothèque de composants de la plateforme technologique AFSIW, en exploitant de nouveaux degrés de liberté, pour le futur développement de circuits et systèmes à haute performance dans les bandes millimétriques.

ABSTRACT

Over the past twenty years, the substrate integrated waveguide (SIW) has shown its irreplaceable position in the development of high-performance RF, microwave, and millimeter-wave integrated circuits and systems. Inheriting the good characteristics of the metallic waveguide and the microstrip line, the SIW features low-cost, compact, self-shielded, easy to integrate, and has good thermal dissipation. To improve further the performance of the conventional SIW, multilayer air-filled SIW (AFSIW) was introduced in 2014 at the expense of a larger footprint. By using channelized air region to transmit the electromagnetic power, the AFSIW structure reduces the dielectric loss significantly, especially at millimeter-wave frequencies, thus increasing the average power handling capability as well as the quality factor. Since then, many efforts have been invested to develop the high-performance AFSIW technological platform. However, most of the research works were focused on the middle layer to develop the functionalities. The top and bottom layers were mainly used to enclose the AFSIW structure. Nevertheless, the AFSIW is a multilayer structure and there are still many degrees of freedom to exploit so to further increase the integration density and to benefit from the multilayer PCB process. In this thesis, the degree of freedom in connection with the empty air-filled space as well as the multilayer aspect, is explored and used.

Regarding the freedom obtained from the empty space, an alternative guided-wave structure named slab AFISW (SAFSIW) is introduced and demonstrated as a compromise between the conventional SIW and the upgraded AFSIW structures in terms of loss and footprint, but with a larger mono-mode bandwidth. Then, numerous components and structures are developed and prototyped based on the SAFSIW such as half-mode SAFSIW, broadband compensating phase shifter, and antenna. The compensating phase shifter and the antenna are then integrated into a mono-pulse antenna array.

Regarding the freedom obtained from the multilayer aspect of the technology, a new multiport structure called balanced-delta-port magic-tee is presented with theoretical analysis. This proposed structure enhances the power handling capability compared to the conventional magic-tee and is implementable in a multilayer AFSIW structure. Based on the balanced-delta-port magic-tee, several isolated power dividers/combiners have been investigated and demonstrated including the resistive-based and the absorptive-based solutions. The absorptive AFSIW power dividers/combiners exhibit broadband isolated responses and an error-tolerant characteristic, which are both important factors considering the mass-production process.

Furthermore, a multilayer mono-pulse antenna array and a multilayer Butler matrix are also developed to make use of the multilayer aspect of the technology.

This thesis aims to increase and enrich the AFSIW component library as well as to exploit new degrees of freedom for the development of millimeter-wave high-performance circuits and systems.

TABLE OF CONTENTS

LIST OF TABLES

LIST OF FIGURES

LIST OF SYMBOLS AND ABBREVIATIONS

AFSIW	Air-filled substrate integrated waveguide
AI	Amplitude imbalance
ALTSA	Antipodal linearly tapered slot antenna
APHC	Average power handling capability
BW_m	Mono-mode bandwidth
Co-pol	Co-polarisation
CW	Continuous wave
DFSIW	Dielectric-filled substrate integrated waveguide
$\vec{E}$	Electric field
E_{bd}	Breakdown voltage
EMC	Electromagnetic compatibility
EW-EL	Equal-width equal-length
EW-UEL	Equal-width unequal-length
f	Frequency
f_0	Center frequency
f_c	Cutoff frequency
GCPW	Grounded coplanar waveguide
$\vec{H}$	Magnetic field
HM-AFSIW	Half-mode air-filled substrate integrated waveguide
HM-DFSIW	Half-mode dielectric-filled substrate integrated waveguide
HM-SAFSIW	Half-mode slab air-filled substrate integrated waveguide
HM-SIW	Half-mode substrate integrated waveguide
HPBW	Half power beamwidth
IL	Insertion loss

$\vec{J}$	Current density
k_0	Wave number in free-space
k_a	Cutoff wave number in air
k_d	Cutoff wave number in dielectric
K_H	Hammerstad-Jensen surface roughness coefficient
LTSA	Linearly tapered slot antenna
ND	Null depth
P_c	Power loss per unit length caused by conductor
PCB	Printed circuit board
P_d	Power loss per unit length caused by dielectric
P-I	Power-current
PI	Phase imbalance
PPHC	Peak power handling capability
P-V	Power-voltage
P_{tot}	Total power
Q-factor	Quality factor
Q_c	Quality factor related to conductor loss
Q_d	Quality factor related to dielectric loss
RFI	Radio frequency interference
RWG	Rectangular waveguide
SAFSIW	Slab air-filled substrate integrated waveguide
SLL	Side lobe level
SIW	Substrate integrated waveguide
tanδ	Loss tangent
TE	Transverse electric
TEM	Transverse electric magnetic

t_g	Glass temperature
TRL	Thru-reflect-line
TSA	Tapered slot antenna
UW-EL	Unequal-width equal-length
UW-UL	Unequal-width unequal-length
V-I	Voltage-current
X-pol	Cross-polarisation
Z_0	Characteristic impedance
α	Attenuation constant
α_d	Conductor loss
α_d	Dielectric loss
β	Phase constant
Δ_{rms}	Root-mean-square of conductor surface roughness
ϵ_0	Vacuum permittivity
ε_r	Relative permittivity
ε_{ra}	Relative permittivity of air
ε_{rd}	Relative permittivity of dielectric
η	Free-space impedance
Γ	Reflection coefficient
λ_0	Free-space wavelength
λ_d	Dielectric Wavelength
λ_g	Guided wavelength
μ	Permeability
φ	Phase shift
ω	Angular frequency

CHAPTER 1 INTRODUCTION

With the increasing communication needs and online services, low-cost and high data rate communication systems are required to augment user experiences. One possible way to increase the data rate is to increase the channel bandwidth. Nevertheless, the low frequency electromagnetic spectrum becomes saturated by huge amounts of applications such as GSM, cellular, Wi-Fi,… To accommodate more free channels as well as more bandwidth, millimeter-wave frequencies have been exploited.

At these frequencies, losses become the most significant bottleneck. To over this issue, metallic rectangular waveguide (RWG) has been always preferred to a large extent. However, RWG is bulky, high cost, and complex to integrate with planar structures. Planar transmission lines, taking advantage of PCB technology and other processing techniques, are generally low cost, compact, and easy to integrate but have more losses and leakages at higher frequencies.

Then, the idea of the substrate integrated waveguide (SIW) came of age and was reported in 2001 [1] to satisfy a low-cost and high-performance system at millimeter-wave frequencies. The SIW is created by embedding a RWG into a PCB substrate by using metallic via rows as illustrated in Figure 1.1. In this way, the SIW preserves the self-shielded structure stemmed from RWG while maintaining the ease of integration from planar structures. Since then, the SIW has been extensively exploited and utilized to develop circuits and components, including passive and active [2], [3].

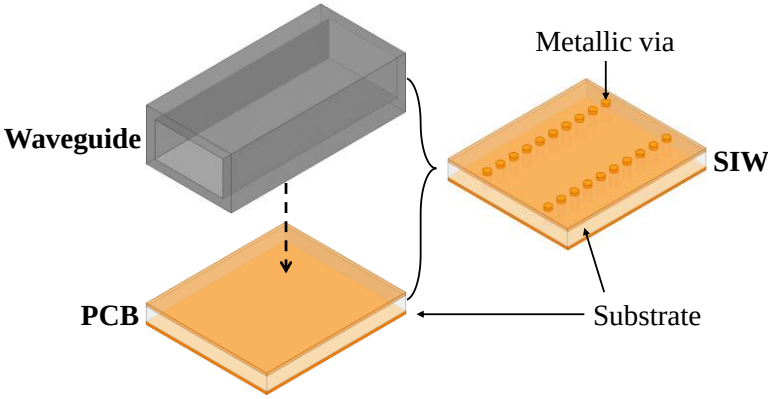

Figure 1.1 Realization of SIW

In 2014, an upgraded version of the SIW named air-filled SIW (AFSIW) [4] was introduced with the aim of reducing dielectric loss, which is an important contributing factor of losses at high frequencies. The AFSIW structure is illustrated in Figure 1.2, which is based on a multilayer PCB process. Since the guided-wave structure is filled with air instead of dielectric

in the conventional dielectric-filled SIW (DFSIW), the AFSIW presents a footprint of $\sqrt{\varepsilon_r}$ times larger than the DFSIW having the same cut-off frequency, where ε_r is the relative permittivity of the dielectric. Therefore, there is a need for alternative solutions, which can offer a compromise between DFSIW and AFSIW in terms of losses and footprint to provide design flexibility.

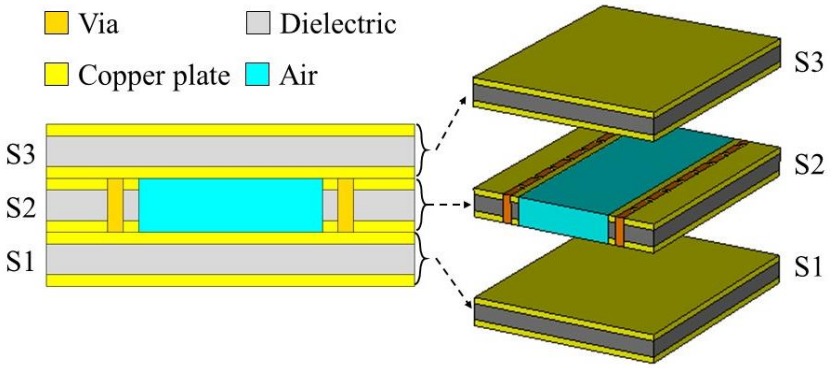

Figure 1.2 AFSIW structure

Since its first introduction, several components have been demonstrated using the AFSIW including power divider [5], coupler [5], [6], phase shifter [7], [8], filter [9]-[13], antenna [14], [15], and termination [16]. Most of them utilize the middle layer (S2) to develop circuit functions (Figure 1.3), the exploitation of multilayer aspects is still limited [6], [10], [13], [15] (Figure 1.4). Multilayer properties need to be further exploited to benefit from the fabrication process and to increase the integration density as well.

Also, since the AFSIW technological platform has been presented recently, there are a lack of AFSIW-based component library and a completed AFSIW-based system on substrate (SoS).

In this context, this double diploma Ph.D. thesis is realized in the framework of a multilateral collaboration among the IMEP-LaHC research center in France, the IMS research center in France, and the Poly-Grames research center in Canada. The journey and timeline of this Ph.D. thesis are presented in Figure 1.5.

The main objective of this Ph.D. thesis is to exploit the degrees of freedom in the AFSIW technological platform, including the hollowed space in layer S2 and multilayer aspect, to develop the circuits and components at millimeter-wave frequencies so to enrich the AFSIW component library. At the end, for the first time, an AFSIW-based SoS is demonstrated, for which the Ka-band is considered.

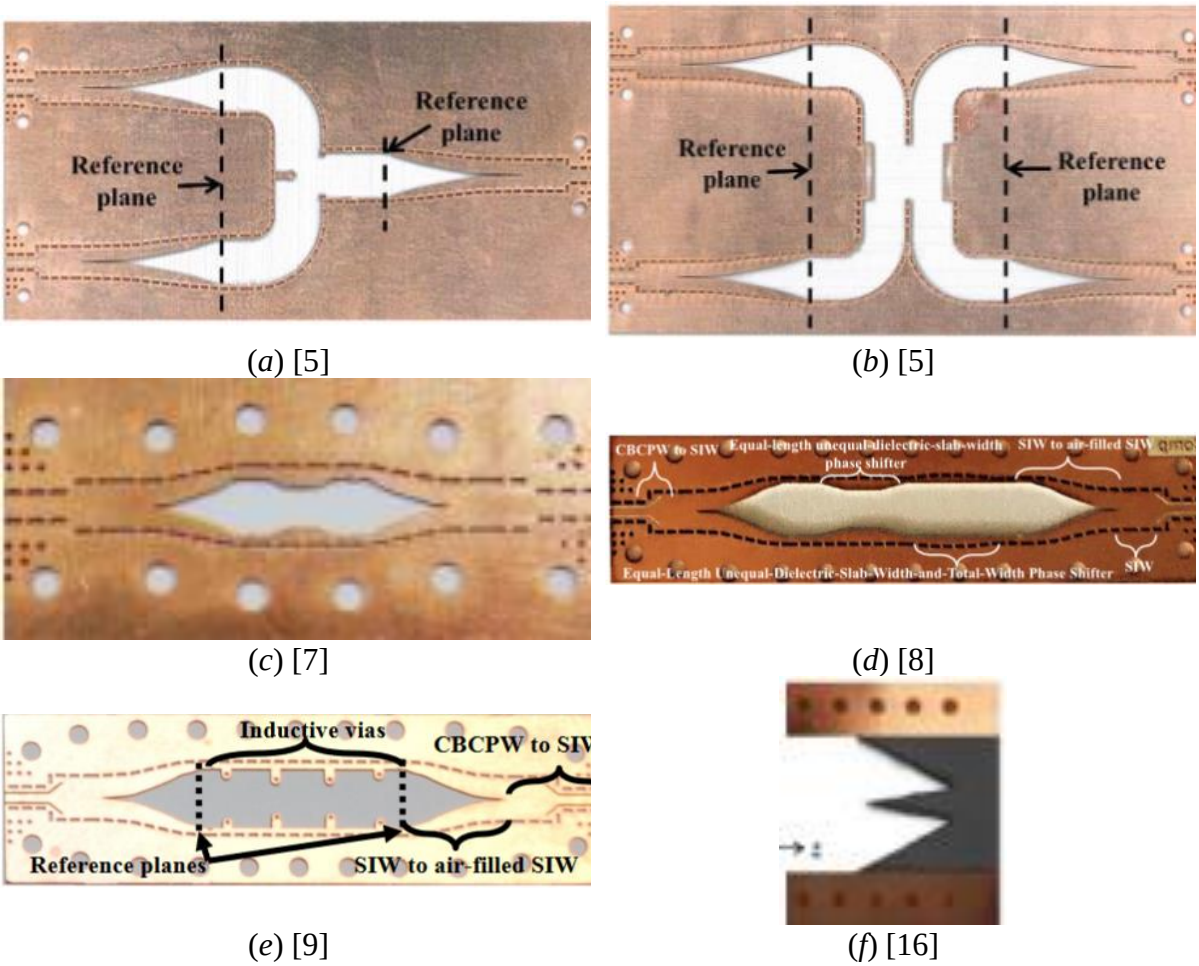

(*a*) [5] (*b*) [5]

(*c*) [7] (*d*) [8]

(*e*) [9] (*f*) [16]

Figure 1.3 Some AFSIW components developed in the middle layer: (*a*) power divider [5], (*b*) Riblet coupler [5], (*c*) U-band phase shifter [7], (*d*) Ka-band phase shifter [8], (*e*) iris filter [9], and (*f*) termination [16]

In order to fulfill this objective, Chapter 2 introduces an alternative guided-wave structure named slab AFSIW (SAFSIW) as a good compromise between the AFSIW and the DFSIW in terms of loss, footprint, power handling capability, and unloaded *Q*-factor. Furthermore, the SAFSIW offers a larger mono-mode bandwidth compared to the other two guided-wave structures as well as the capability of controlling the attenuation and phase constants. Theoretical analysis and experimental validation were carried out to demonstrate the flexibility of the SAFSIW. Based on that, half-mode SAFSIW is introduced to further reduce the component footprint and to bring more flexibility to the designer.

The SAFSIW concept is used to develop compensating phase shifters and cruciform coupler in Chapter 3. Thanks to the self-compensating effect, the proposed phase shifter presents an

equal-length topology with a more compact footprint. This self-compensating phase shifter is then used to develop monopulse antennas in Chapter 4.

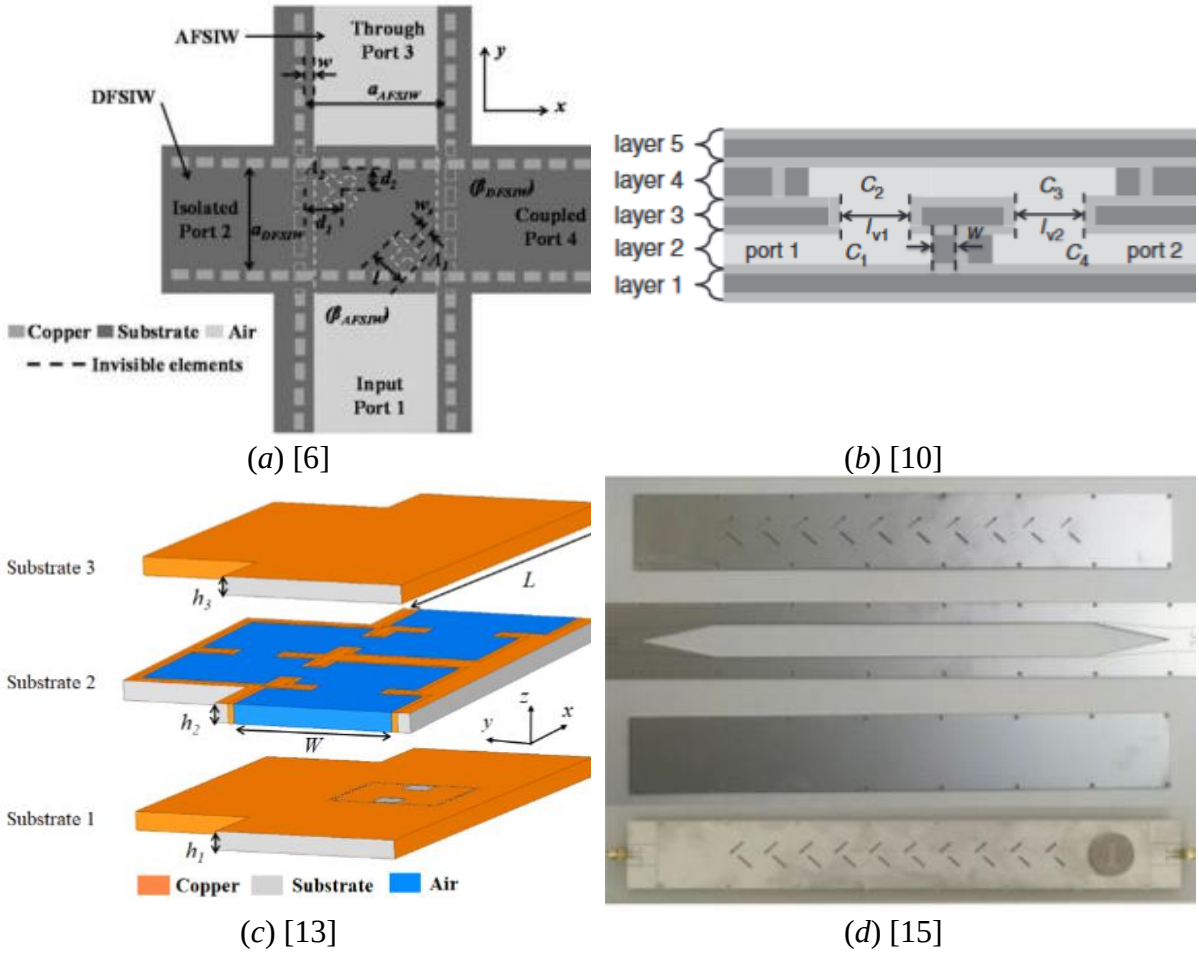

(*a*) [6] (*b*) [10]

(*c*) [13] (*d*) [15]

Figure 1.4 Some AFSIW components developed in multilayer: (*a*) Moreno coupler [6], (*b*) Ka-band filter [10], (*c*) K-band filter [13], and (*d*) leaky wave antenna [15]

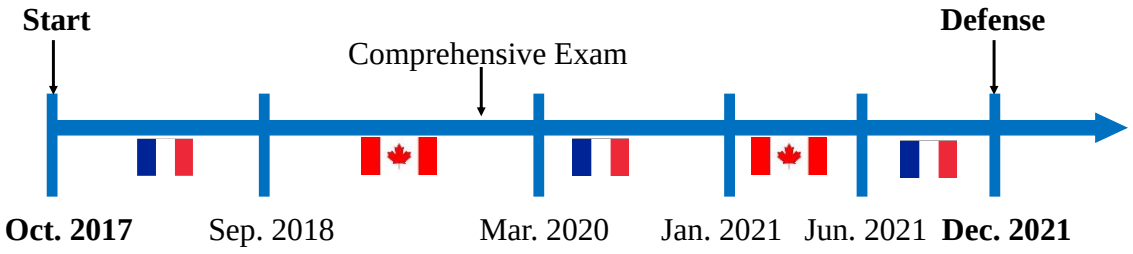

Figure 1.5 Timeline of the Ph.D. thesis

Moreover, the center dielectric slab in the SAFSIW structure can also be used to reduce cross-polarisation in an antipodal linearly tapered slot antenna (ALTSA). Chapter 4 validates this idea with a cross-polarisation reduction of 13.4 dB at 33 GHz. The proposed ALTSA is

then integrated into two monopulse antennas, one with 180° hybrid coupler feeding and the other with multilayer magic-tee feeding. The monopulse antenna implementing a magic-tee feeding was experimentally validated in measurement. It can be considered as the first AFSIW-based SoS.

The multilayer aspect is further exploited in Chapter 5 by introducing a new concept of multilayer five-port network named balanced-delta-port magic-tee with the ability to handle more power than the conventional magic-tee. This concept is used to developed isolated power dividers/combiners. Two isolated components are considered and demonstrated: resistor and absorbing material, which offer flexible solutions for designers. Furthermore, the absorptive-based solutions demonstrate their tolerance to misalignment and dimensional errors of absorbing material, which is an important factor for the mass-production process.

In each chapter, an overview is carried out to get a global view on literature and to highlight the needs. A brief conclusion is also included in each chapter to show the advantages of the proposed solutions.

Finally, Chapter 6 concludes the overall research activities with summarized scientific and technical contributions. For further exploitation, Chapter 6 also gives some perspectives for future works.

CHAPTER 2 FULL-MODE AND HALF-MODE SLAB AIR-FILLED SUBSTRATE INTEGRATED WAVEGUIDE

2.1 Overview

Future communication systems require higher frequency bands for high data rate transmission links. At these frequencies, losses become the most significant bottleneck, which generate lots of problems such as efficiency and overheat. Metallic rectangular waveguide (RWG) is preferred at millimeter-wave frequencies. However, RWG is bulky, high cost, and complex to integrate with planar structure. The planar transmission line, taking advantage of PCB technology, is low cost, compact, and easy to integrate but has more losses at higher frequencies.

The presence of the substrate integrated waveguide (SIW) technological platform in early 2001 [1] enables the high performance and high integration density in RF and millimeter-wave wireless systems [2], [3]. It inherits the advantages from both RWG and planar transmission lines such as compact, self-packaging, low cost, ease of integration, high performance, and good thermal dissipation. Since then, many research outcomes have been reported concerning SIW technology. An exponential increase in the number of publications on SIW, extracted from IEEE Xplorer, can be observed in Figure 2.1.

The conventional SIW uses a bounded dielectric channel to transmit electromagnetic waves, which suffers from a high dielectric loss at millimeter-wave frequencies. To increase further the transmission efficiency, the air-filled substrate integrated waveguide (AFSIW) has been developed since 2014 [4]-[18]. The idea of AFSIW is to remove the dielectric inside the SIW guided-wave structure, therefore, significantly reducing dielectric loss at the expense of a larger footprint.

In 2018, an alternative platform, named slab AFSIW (SAFSIW), was proposed as a flexible solution between dielectric-filled SIW (DFSIW) and AFSIW in terms of transmission efficiency and size [19]. Moreover, the SAFSIW gives a larger mono-mode bandwidth compared to the DFSIW and AFSIW [19]-[21]. The idea of SAFSIW has been implemented to develop several components including compensated phase shifters [19], [22], and leaky-wave antenna [23].

A qualitative comparison among different guided-wave technologies, including planar transmission line, RWG, DFSIW, AFSIW, and SAFISW is presented in Table 2.1.

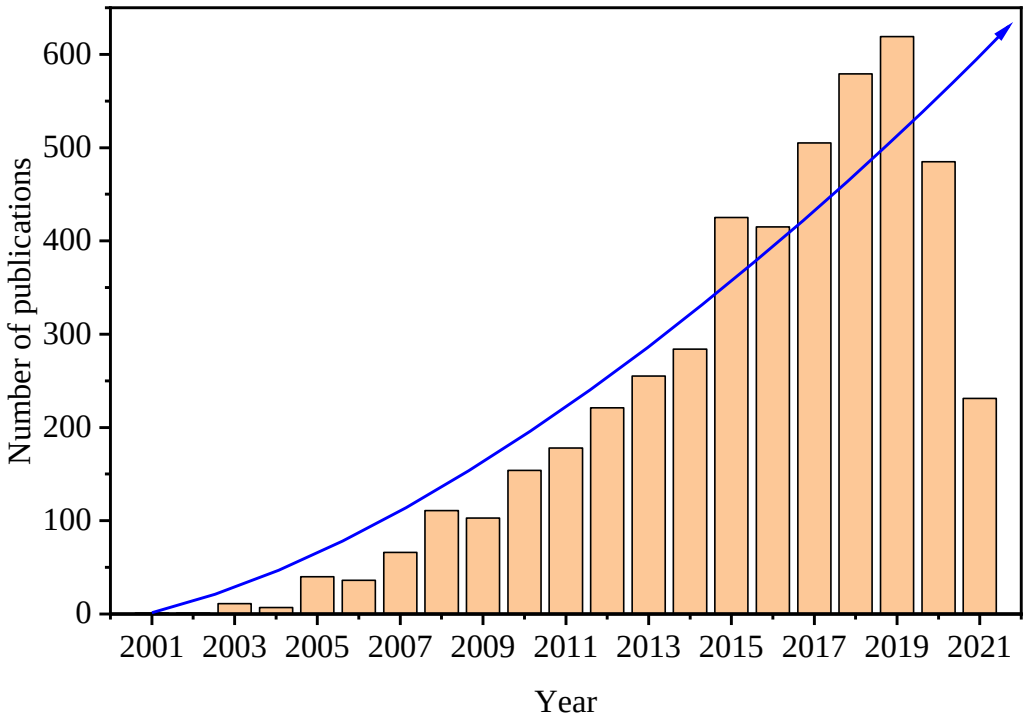

Figure 2.1 Number of publications on SIW from 2001 to September 2021, data extracted from IEEE Xplorer.

Table 2.1 Qualitative comparison among different guided-wave technologies

Technology	Loss	Q-factor	Power handling capability	Footprint	Cost
Planar transmission line	High	Low	Low	Compact	Low
RWG	Low	High	High	Bulky	High
DFSIW	Medium	Medium	Medium	Compact	Low
AFSIW	**Low**	**High**	**High**	**Large**	**Low**
SAFSIW	**Medium**	**Medium**	**Medium**	**Medium**	**Low**

In this Ph.D. thesis, the air-filled versions of the SIW platform are studied to develop and implement high-performance and low-cost components at millimeter-wave frequencies.

2.2 Slab air-filled substrate integrated waveguide

In this section, an analytical study will be introduced to provide a base for the analysis. Then, the characteristics of the SAFSIW will be presented. The characteristics are validated in

simulations and measurements. A comparison between the SAFSIW, AFSIW, and DFSIW has been made to highlight the flexibility of the proposed structure.

2.2.1 SAFSIW structure and analytical study

The general structure of SAFSIW is given in Figure 2.2. A dielectric slab of width w_s is integrated at the center of an AFSIW structure having a total width a and thickness h. Dielectric slabs of width w are maintained for metallization and mechanical purposes. The effect of these two-sided dielectric slabs is more significant with the decrease of waveguide width a.

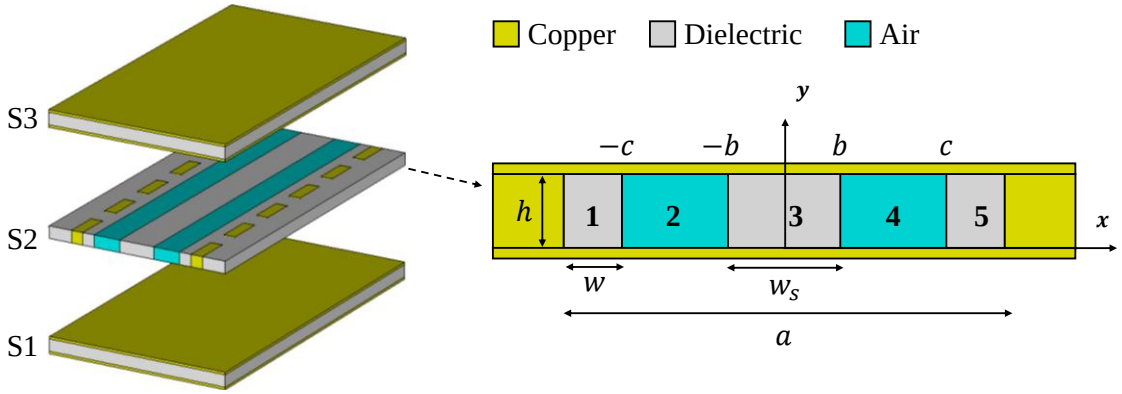

Figure 2.2 The SAFSIW structure.

The cutoff wave numbers in the dielectric- (k_d) and air-region (k_a) are defined as:

$$k_d^2 = \varepsilon_{rd} k_0^2 - \beta^2, \tag{1}$$

$$k_a^2 = \varepsilon_{ra} k_0^2 - \beta^2, \tag{2}$$

where β is the phase constant, k_0 is the wave number in free-space, ε_{rd} and ε_{ra} are the relative permittivity of dielectric and air, respectively.

The magnetic field H_z can be defined by (3) [24], where H_{zi} is the magnetic field in the i^{th}-region.

$$\frac{\partial^2 H_{zi}}{\partial x^2} + k_i^2 H_{zi} = 0, i = 1..5 \tag{3}$$

Applying Maxwell's equation, all the non-zero field components are given in the following [24]:

$$E_{yi} = \frac{j\omega\mu_i}{k_{ci}^2} \times \frac{\partial H_{zi}}{\partial x}, i = 1..5 \tag{4}$$

$$H_{xi} = -\frac{j\beta}{k_{ci}^2} \times \frac{\partial H_{zi}}{\partial x}, i = 1..5 \quad (5)$$

where E_{yi} and H_{xi} are the electric and magnetic fields, respectively, μ_i is the permeability, and k_{ci} is the cutoff wave number in the i^{th}-region.

The boundary condition sets the electric field E_{yi} to be zero at $x = \pm$ a. Combining with the continuity conditions at $x = \pm$ c, $x = \pm$ b, all the field components can be calculated.

The simulated magnitude electrical field distributions for the first and second mode are shown in Figure 2.3. The simulations are done using CST Microwave Studio.

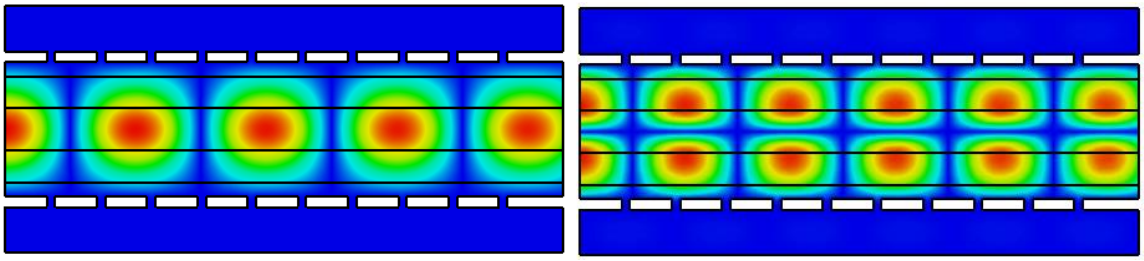

(*a*) (*b*)

Figure 2.3 The simulated magnitude E field distribution of (*a*) dominant mode at 30 GHz and (*b*) second mode at 60 GHz (a = 4.8 mm, w_s = 1.5 mm, w = 0.508 mm).

It can be observed from Figure 2.3 that the electrical field concentrates in the dielectric region for the dominant mode and more electrical field concentrates in the air region for the second mode. This field distribution explains the generation of a larger mono-mode bandwidth.

2.2.2 Phase constant and cutoff frequency

By solving the dispersion equations obtained from Maxwell's solutions, the phase constant of the TE_{10} mode can be calculated as follows [19]:

$$A_1 = \frac{1}{k_d k_a} cos\left(k_d\left(w + \frac{w_s}{2}\right)\right) cos\left(k_a\left(\frac{a}{2} - \frac{w_s}{2} - w\right)\right) \quad (6)$$

$$A_2 = \frac{1}{k_a^2} cos(k_d w)\, sin\left(k_a\left(\frac{a}{2} - \frac{w_s}{2} - w\right)\right) sin\left(\frac{k_d w_s}{2}\right) \quad (7)$$

$$A_3 = \frac{1}{k_d^2} sin(k_d w)\, sin\left(k_a\left(\frac{a}{2} - \frac{w_s}{2} - w\right)\right) cos\left(\frac{k_d w_s}{2}\right) \quad (8)$$

$$A_1 - A_2 - A_3 = 0 \quad (9)$$

The phase constant of the TE_{20} mode is calculated by equations (10) to (13) [19].

$$B_1 = \frac{1}{k_d k_a} sin\left(k_d\left(w + \frac{w_s}{2}\right)\right) cos\left(k_a\left(\frac{a}{2} - \frac{w_s}{2} - w\right)\right) \tag{10}$$

$$B_2 = \frac{1}{k_a^2}\cos(k_d w)\sin\left(k_a\left(\frac{a}{2} - \frac{w_s}{2} - w\right)\right)\cos\left(\frac{k_d w_s}{2}\right) \tag{11}$$

$$B_3 = \frac{1}{k_d^2}\sin(k_d w)\sin\left(k_a\left(\frac{a}{2} - \frac{w_s}{2} - w\right)\right)\sin\left(\frac{k_d w_s}{2}\right) \tag{12}$$

$$B_1 + B_2 - B_3 = 0 \tag{13}$$

The cutoff frequencies f_{c10} and f_{c20} of the first and second mode can be obtained by setting $\beta = 0$ into (6) to (9) and (10) to (13), respectively. Then, the mono-mode bandwidth BW_m is defined by the following equation [25]:

$$BW_m = \frac{f_{c20} - f_{c10}}{f_{c10}} \times 100\% \tag{14}$$

A comparison of phase constants among DFSIW, AFSIW, and SAFSIW is presented in Figure 2.4. The substrate is Rogers RT/Duroid 6002 (h = 0.508 mm, ε_r = 2.94, $tan\delta$ = 0.0012). The widths of AFSIW and DFSIW are 7.04 mm and 4.11 mm, respectively, to have the same cutoff frequency f_{c10} = 21.2 GHz (1.25 times below the Ka-band). The same AFSIW and DFSIW structures are used for the rest of this thesis, other than specified otherwise.

For SAFSIW, the slab w_s = 1.5 mm is chosen for two main reasons. Firstly, the BW_m of this guided-wave structure is about 142%, close to the optimum value of 146%. Secondly, the larger dielectric slab gives advantages from the fabrication point of view. The other dimensions are a = 4.8 mm and w = 0.508 mm.

It can be observed in Figure 2.4 that the SAFSIW presents a larger mono-mode bandwidth compared to conventional DFSIW and AFSIW. A very good agreement between theoretical equations and simulation is also obtained. In fact, the maximum electrical field of the first mode concentrates in the dielectric region while the maximum electrical field of the second mode concentrates in the air region. Therefore, the cutoff frequency of the first mode will be decreased while the cutoff frequency of the second mode will be increased. As a result, the mono-mode bandwidth is enlarged.

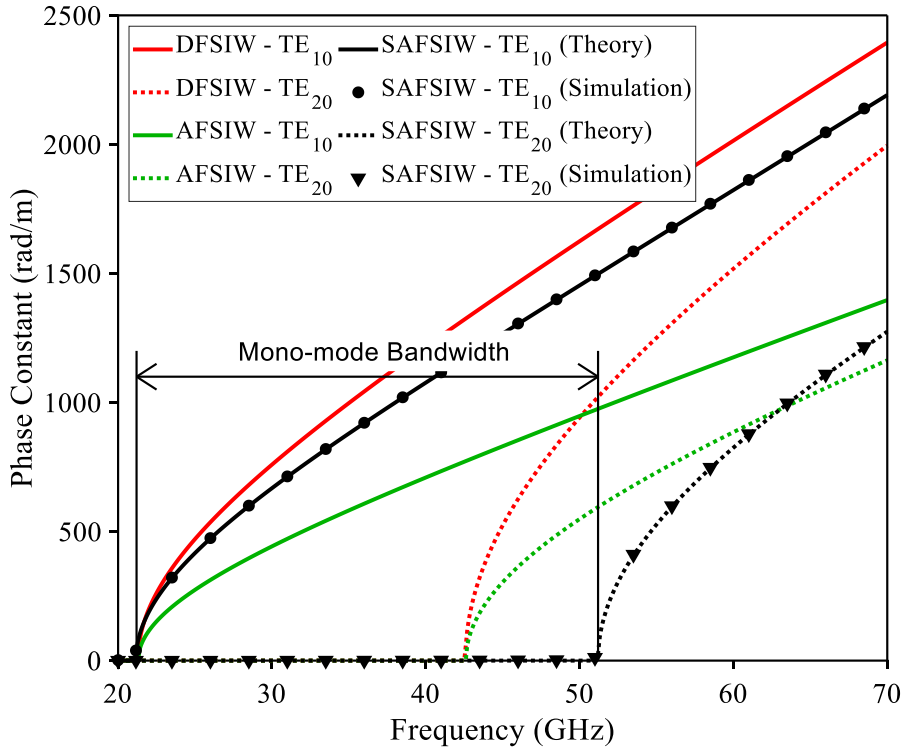

Figure 2.4 AFSIW, SAFSIW, and DFSIW TE_{10} and TE_{20} phase constant.

2.2.3 Attenuation constant

Since the SAFSIW is designed to cover the Ka-band with mono-mode bandwidth, only the attenuation of the first mode is considered for demonstration. The total attenuation α consists of dielectric α_d, ohmic α_c, and surface roughness losses determined with loss factor K_H [26] as given in (15). The factor K_H is mainly dependent on the rms surface roughness Δ_{rms} of the conductive material.

$$\alpha = \alpha_d + K_H \alpha_c \tag{15}$$

The dielectric and ohmic loss can be calculated by the perturbation method introduced in [24]. The total power flows through the waveguide can be determined by:

$$P_{tot} = Re\int_{-a/2}^{-c}\int_{0}^{h} E_{y1}H_{x1}^{*}dydx + Re\int_{-c}^{-b}\int_{0}^{h} E_{y2}H_{x2}^{*}dydx + \frac{1}{2}Re\int_{-b}^{b}\int_{0}^{h} E_{y3}H_{x3}^{*}dydx \tag{16}$$

The power loss per unit length caused by the dielectric is:

$$P_d = \frac{\omega \epsilon_0 \varepsilon_d tan\delta}{2}\left[2\int_{-a/2}^{-c}\int_0^h \left|E_{y1}\right|^2 dydx + \int_{-b}^{b}\int_0^h \left|E_{y3}\right|^2 dydx\right], \quad (17)$$

where ϵ_0 is the vacuum permittivity.

Then, the dielectric loss is given by [24]:

$$\alpha_d = \frac{P_d}{2P_{tot}} \quad (18)$$

The surface current on the left wall ($x = -a/2$) is:

$$J_{sy} = \hat{y}\left(\hat{x} \times \hat{z}H_{z1}|_{x=-\frac{a}{2}}\right) \quad (19)$$

The surface current on the bottom wall ($y = 0$) is:

$$J_{sbxi} = \hat{x}\left(\hat{y} \times \hat{z}H_{zi}|_{y=0}\right), i = 1..5 \quad (20)$$

$$J_{sbzi} = \hat{z}\left(\hat{y} \times \hat{x}H_{xi}|_{y=0}\right), i = 1..5 \quad (21)$$

The power loss per unit length caused by a finite conductor is:

$$P_c = R_s\int_0^h \left|J_{sy}\right|^2 dy + R_s\int_{xi}(|J_{sbxi}|^2 + |J_{sbzi}|^2)dx \quad (22)$$

Then, the conductor loss is [24]:

$$\alpha_c = \frac{P_c}{2P_{tot}} \quad (23)$$

The theoretical value of dielectric and ohmic losses are compared with the simulation using CST Studio in Figure 2.5. It can be observed in this figure that the analytical equations give a very good agreement with the 3D simulation.

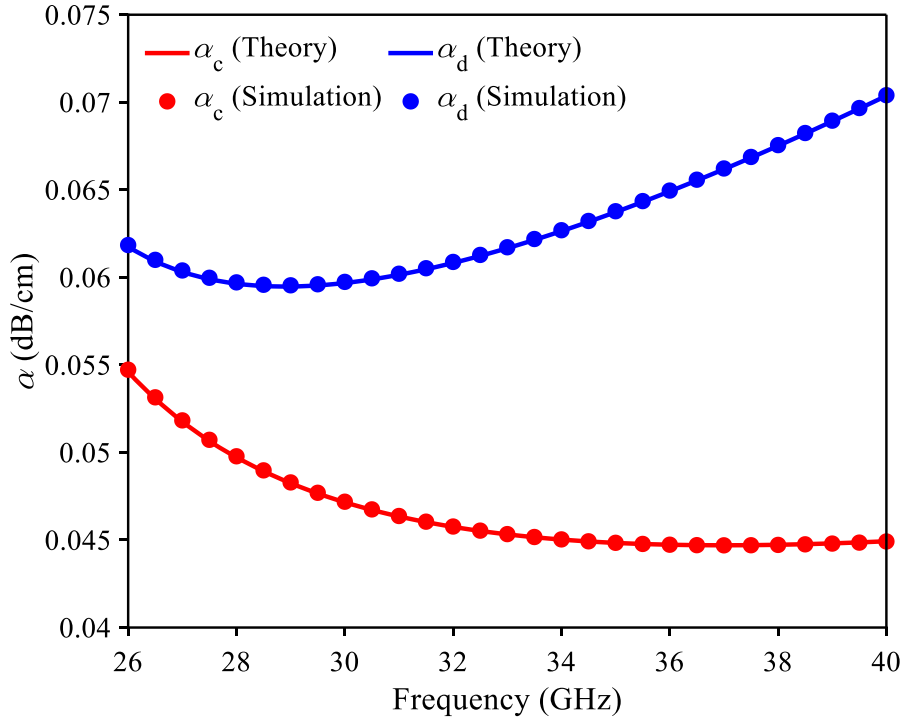

Figure 2.5 Simulated and theoretical attenuation constant of SAFIW (a = 4.8 mm and w_s = 1.5 mm).

2.2.4 Unloaded quality factor

The unloaded Q-factor is determined by the following equation [24]:

$$Q = \left(\frac{1}{Q_c} + \frac{1}{Q_d}\right)^{-1} \tag{24}$$

where Q_c and Q_d are the quality factors related to the conductor and dielectric losses, respectively.

From the electromagnetic fields obtained from Maxwell's solutions, the conductor loss and dielectric loss can be calculated, then the unloaded Q-factor is derived [24].

Excluding the surface roughness, the unloaded Q-factor of DFSIW, AFSIW, and SAFSIW can be calculated with different filling ratios (w_s/a). They are compared in Figure 2.6.

In Figure 2.6, the markers show the Q-factor of DFSIW (a = 4.11 mm), SAFSIW (a = 4.8 mm, w_s = 1.5 mm), and AFSIW (a = 7.04 mm). Sidewall dielectric slabs of w = 0.508 mm are maintained for AFSIW and SAFSIW. At 30 GHz, the Q-factor of those DFSIW, SAFSIW, and AFSIW are 1124, 527, and 468, respectively.

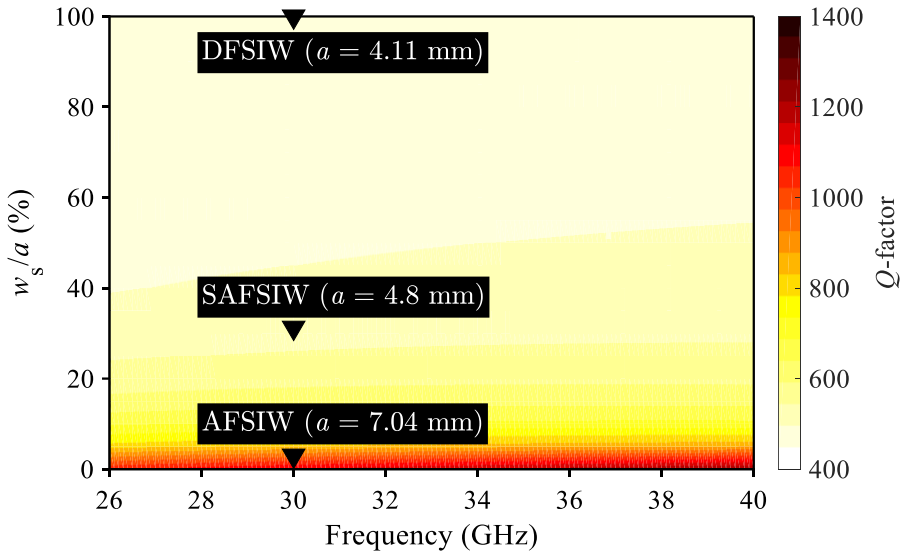

Figure 2.6 Calculated unloaded *Q*-factor of DFSIW, AFSIW, and SAFSIW.

It can be observed in Figure 2.6 that, the SAFSIW presents a higher unloaded *Q*-factor than the DFSIW at the expense of a larger footprint. Moreover, the SAFSIW gives a smaller unloaded *Q*-factor and size compared to the AFSIW. As a result, the SAFSIW is a good compromise between the conventional DFSIW and AFSIW, especially for filter design.

2.2.5 Power handling capability

Another important parameter that needs to be investigated, especially for high-power applications, is power handling capability.

2.2.5.1 Average power handling capability

For continuous wave (CW) applications, the losses inside the waveguide will turn into heat. At a high-power level (high temperature), the mechanical construction of the materials becomes unstable due to the glass temperature t_g. The average power handling capability (APHC) calculated based on losses and glass temperature is the most common metric to characterize this phenomenon [27], [28]. The glass temperature is considered t_g = 350°C for RT6002, and the losses can be calculated by the analytical equations introduced in 2.2.3 Based on that, the APHC can be obtained from the heat-transfer method presented in [28].

The APHC of DFSIW, AFSIW, and SAFSIW with different filling ratios (w_s/a) are compared in Figure 2.7.

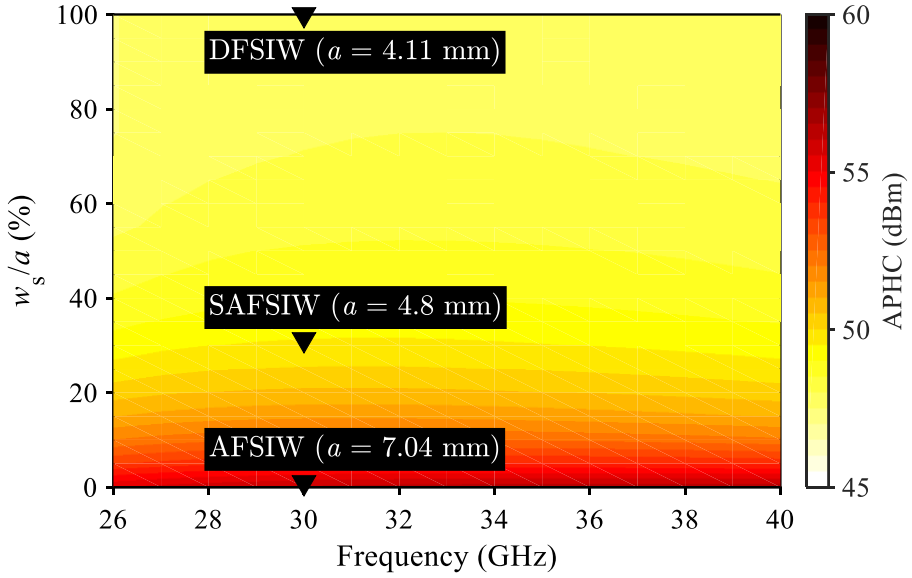

Figure 2.7 Theoretical APHC of AFSIW, DFSIW, and SAFSIW structures.

In Figure 2.7, the markers show the DFSIW (a = 4.11 mm), SAFSIW (a = 4.8 mm, w_s = 1.5 mm), and AFSIW (a = 7.04 mm). At 30 GHz, the APHC of those DFSIW, SAFSIW, and AFSIW structures are 47.9 dBm, 49.6 dBm, and 56.1 dBm, respectively.

It can be seen in Figure 2.7 that the SAFIW presents a good compromise between the conventional DFSIW and AFSIW for APHC level in transmitting a continuous signal.

2.2.5.2 Peak power handling capability

In transmission links where pulsed or modulated signals are used, a maximum peak power handling capability (PPHC) is defined to evaluate the maximum peak power that can be transmitted before breakdown. Only the ionization breakdown phenomenon and the dominant mode TE_{10} are interested to define the PPHC. The equations to determine the PPHC of DFSIW and AFSIW are given in [5].

Concerning the SAFSIW, since the breakdown voltage of air ($E_{bd,air}$ = 36 kV/cm) is much smaller than the breakdown voltage in RT6002 ($E_{bd,6002}$ = 239 kV/cm) and the maximum electrical field concentrates at the center of the waveguide, the PPHC is obtained by assuming that the guided-wave structure is broken down at the limit of air and center dielectric slab ($x = \pm b$ in Figure 2.2).

Considering the maximum electrical field in SAFSIW is $E_{bd,air}$ = 36 kV/cm, the PPHC can be calculated by the method presented in [28].

The theoretical PPHC of both DFSIW, AFSIW, and SAFSIW with different filling ratios (w_s/a) are compared in Figure 2.8. The markers show the DFSIW (a = 4.11 mm), SAFSIW (a = 4.8 mm, w_s = 1.5 mm), and AFSIW (a = 7.04 mm). At 30 GHz, the PPHC of those DFSIW, SAFSIW, and AFSIW structures are 29.8 dB, 14.5 dB, and 13.4 dB, respectively.

It can be observed in Figure 2.8 that the DFSIW and AFSIW can handle the highest and the lowest PPHC, respectively. Once more, the SAFSIW presents a compromise between dielectric-filled and air-filled versions of SIW.

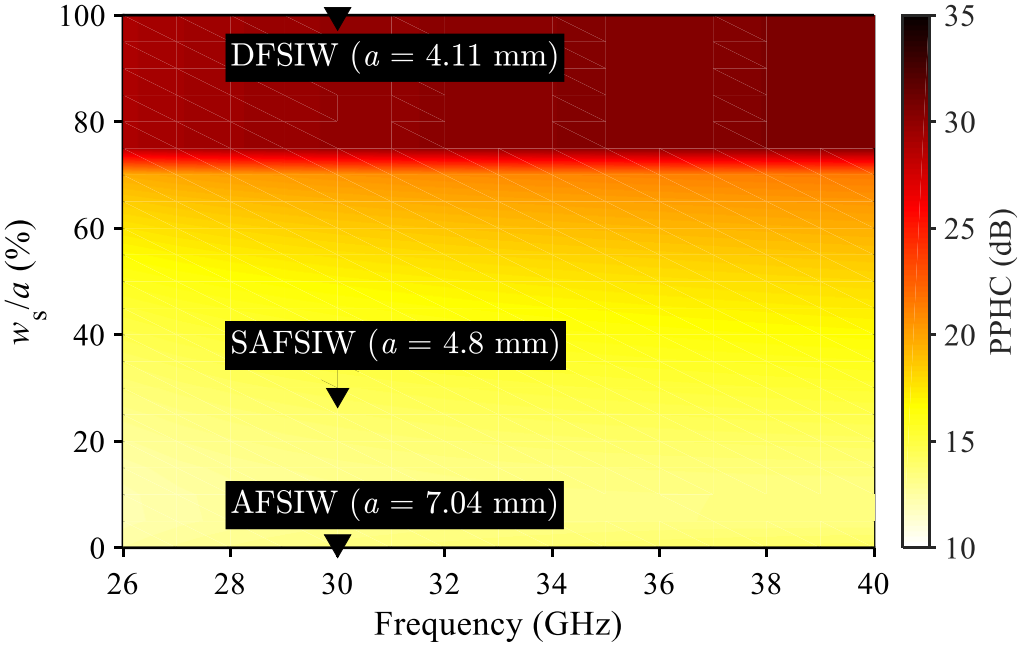

Figure 2.8 Theoretical PPHC of AFSIW, DFSIW, and SAFSIW structures.

2.2.6 Experimental demonstration

2.2.6.1 Broadband transition

A transition from grounded coplanar waveguide (GCPW) to SAFSIW was designed and prototyped (Figure 2.9). A DFSIW section is used to transmit the electromagnetic power from GCPW to the SAFSIW section. In this case, the mono-mode bandwidth is limited by the bandwidth of the DFSIW section. However, only the applications in Ka-band are considered in this thesis. Therefore, the mono-mode bandwidth of the DFSIW is sufficient, as can be seen in Figure 2.4. The DFSIW sections present the advantage in terms of space to accommodate the top and bottom layers.

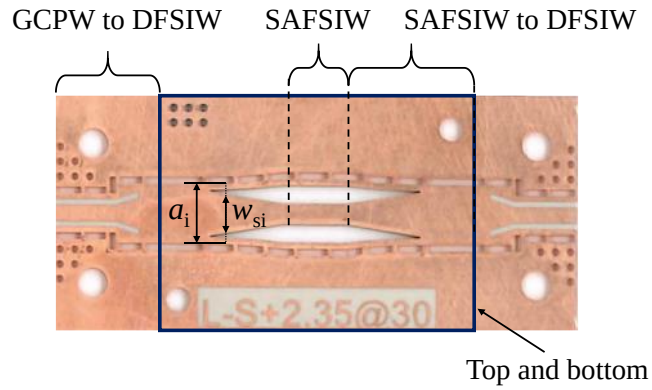

Figure 2.9 SAFSIW transmission line with transitions.

The taper transition from DFSIW to SAFSIW is designed by properly choosing a_i and w_{si} to maintain the cutoff frequency f_{c10} to avoid dispersion. With f_{c10} = 21.2 GHz, a design curve can be made as shown in Figure 2.10 for different values of a_i and w_{si}. Based on this design curve, a smooth transition from DFSIW to SAFSIW can be made.

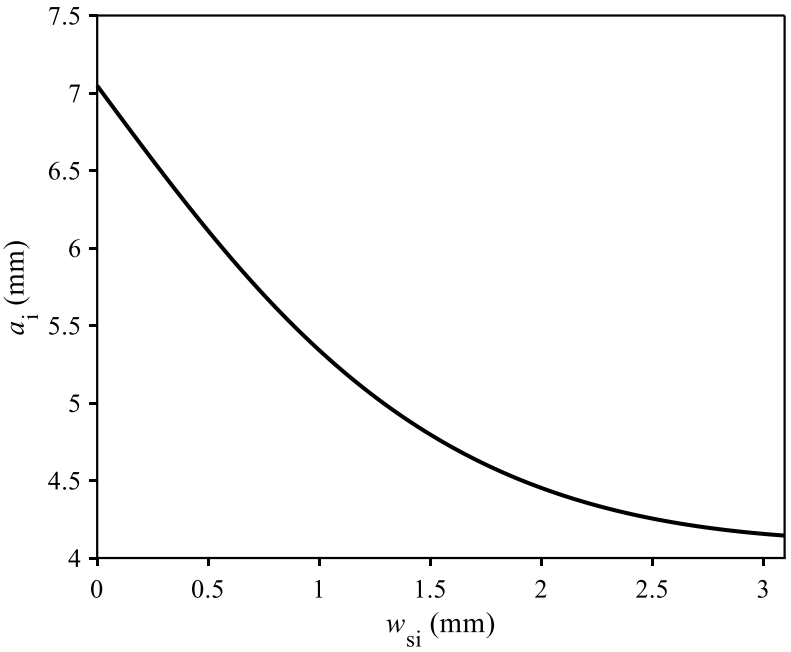

Figure 2.10 DFSIW to SAFSIW transition design curve.

For demonstration, an SAFSIW back-to-back transition was designed and fabricated with a = 4.8 mm and w_s = 1.5 mm. The prototype is shown in Figure 2.9. The simulation configuration is shown in Figure 2.11. In the simulation, the surface roughness of Δ_{rms} = 0.4 μm is considered for layer S2 and Δ_{rms} = 0.9 μm is considered for the FR-4 cover in layer S1 and S3 as suggested in [27] and [8]. The measured results are obtained by using an N4694A

electronic calibration module from Keysight and a 3680V test fixture from Anritsu. The simulated and measured reference plans are A-A' and D-D'.

The simulated and measured *S*-parameters of the SAFSIW back-to-back transition are compared in Figure 2.12. A good agreement between simulation and measurement can be seen from Figure 2.12. The obtained measured $|S_{11}|$ is lower than -14 dB over the Ka-band and the measured insertion loss is $|S_{21}| = -1.43 \pm 0.32$ dB compared to $|S_{21}| = -1.14 \pm 0.26$ dB in simulation. More losses are observed in measurement due to the assembly process and the variation of surface roughness [8].

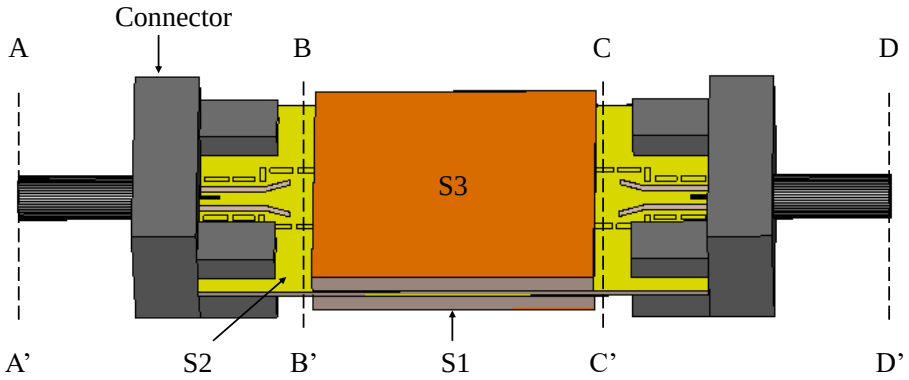

Figure 2.11 The simulation configuration for SAFSIW back-to-back transition.

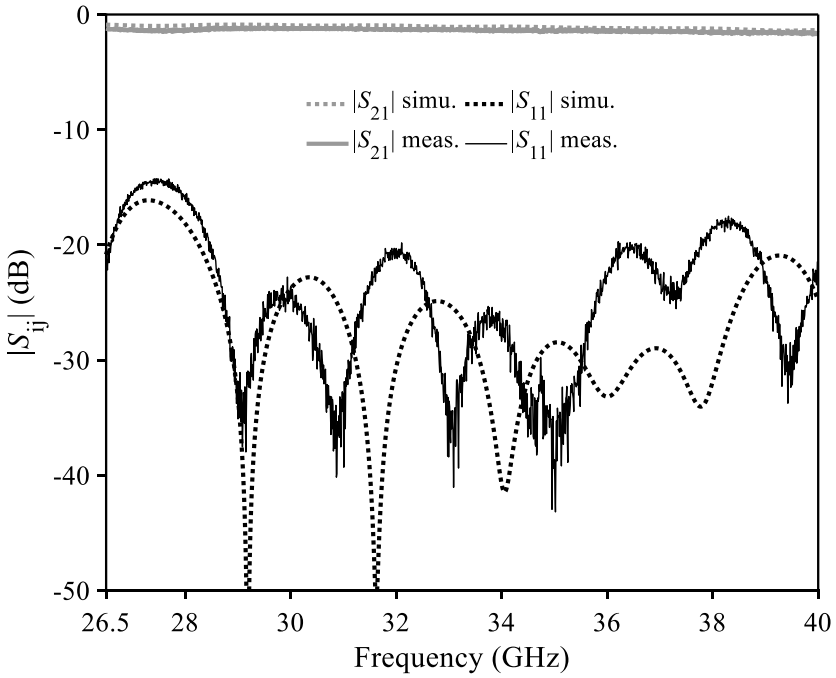

Figure 2.12 Simulated and measured *S*-parameters of SAFSIW back-to-back transition.

2.2.6.2 Characterization

Two back-to-back transitions of length L_1 and L_2 were fabricated to extract the attenuation constant by the different length method:

$$\alpha = \frac{S_{21}(L_1) - S_{21}(L_2)}{L_1 - L_2} \tag{25}$$

The measurement results are compared with the theoretical value obtained by equation (15) in Figure 2.13. In the theoretical analysis, the surface roughness is considered Δ_{rms} = 0.4 μm for DFSIW, Δ_{rms} = 0.3 μm for AFSIW, and Δ_{rms} = 0.9 μm for SAFSIW as suggested in [8].

It can be observed in Figure 2.13 that the SAFSIW presents a compromised loss between AFSIW and DFSIW structures. A maximum attenuation coefficient of 0.19 dB/cm is obtained for SAFSIW in measurement, compared to 0.17 dB/cm in simulation. The difference is due to the assembling process and the variation of Δ_{rms}. A peak value of 15.6 μm are observed for FR-4 in [8] instead of 0.9 μm in this investigation.

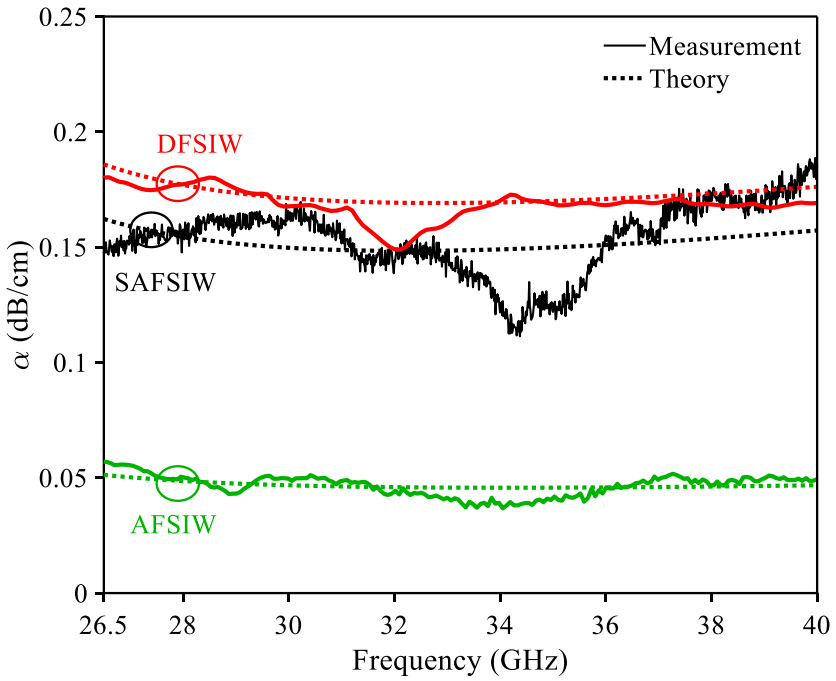

Figure 2.13 Attenuation constants of the dominant mode in AFSIW, SAFSIW, and DFSIW.

2.2.7 Conclusion on SAFSIW

The variations of attenuation constant (given at 30 GHz) versus center-dielectric-slab width w_s are shown in Figure 2.14. An increase of attenuation constant is observed in Figure 2.14 with the increase of center dielectric slab w_s. The mono-mode bandwidth increases from the

mono-mode bandwidth of AFSIW (w_s = 0 mm) to an optimum value, then decreases to the mono-mode bandwidth of DFSIW (w_s = 3.094 mm).

The variation of mono-mode bandwidth with various center dielectric slab width w_s is presented in Figure 2.14. The cutoff frequency f_{c10} is maintained at 21.2 GHz for this investigation. As it can be observed in this figure, there is a value of w_s giving the maximum mono-mode bandwidth. In this case, w_s = 1.2 mm gives an optimum mono-mode bandwidth of BW_m = 146%.

For comparison, Table 2.2 summarizes different performance properties of DFSIW, AFSIW, and SAFSIW at 30 GHz.

It can be noticed from Figure 2.14 and Table 2.2 that the SAFSIW topology offers a flexible solution for designers. If the mono-mode bandwidth is preferred, the optimum value for maximum mono-mode bandwidth should be chosen. If a low-loss component is preferred, the SAFSIW should be operated near the AFSIW region. Elsewhere, the operation of SAFSIW near the DFSIW region is preferred to reduce component footprint and for a stronger mechanism.

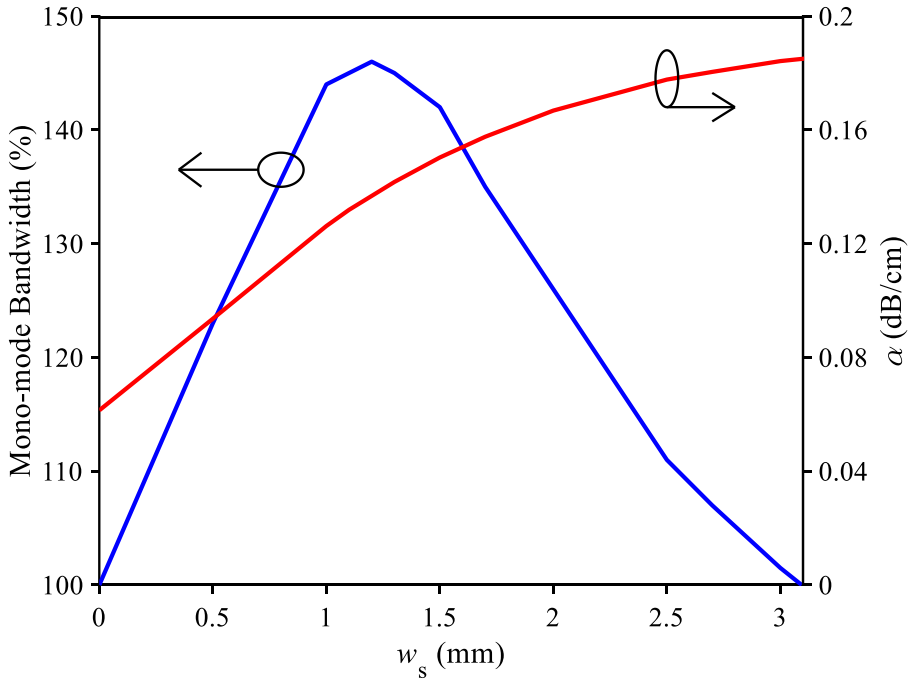

Figure 2.14 The variation of mono-mode bandwidth and attenuation versus various w_s.

With all the analyses above, the SAFSIW offers a good compromise between AFSIW and DFSIW structures for both losses, footprint, power handling capability, and unloaded Q-factor. By using a center dielectric slab, the mono-mode bandwidth is enhanced. Furthermore, by

changing the dimension of w_s, the mono-mode bandwidth and the impedance can be controlled and adjusted. The SAFSIW is a good candidate to implement high-performance components at millimeter-wave frequency.

Table 2.2 Comparison of theoretical properties of DFSIW, SAFSIW, and AFSIW at 30 GHz

Characteristics	DFSIW	**SAFSIW 1.5 mm**	**SAFSIW 1.5 mm**	AFSIW
Layer S2	RT6002	**RT6002**	**RT6002**	RT6002
Layer S1 and S3	/	**RT6002**	**FR-4**	RT6002
Dielectric loss (dB/cm)	0.080	**0.060**	**0.060**	0
Ohmic loss (dB/cm)	0.056	**0.047**	**0.047**	0.032
Surface roughness loss (dB/cm)	0.036	**0.021**	**0.043**	0.014
Total loss (dB/cm)	0.172	**0.128**	**0.150**	0.046
Mono-mode BW (%)	100	**142**	**142**	100
APHC (dBm)	46.93	**48.74**	**40.27**	54.52
PPHC (kW)	955.61	**28.82**	**28.82**	21.75
Width (mm)	4.11	**4.8**	**4.8**	7.04

2.3 Half-mode slab air-filled substrate integrated waveguide

The half-mode SAFSIW (HM-SAFSIW) is presented in this section as a good solution to reduce the footprint while maintaining the high-performance operation with air-filled technique.

Two configurations are proposed for the half-mode solution to increase further the flexibility in design.

2.3.1 Miniaturization techniques

To increase further the integration density, efforts have been made in the development of miniaturization techniques, which can be seen in Figure 2.15 including the ridged SIW, slow wave SIW, folded SIW, and half-mode SIW.

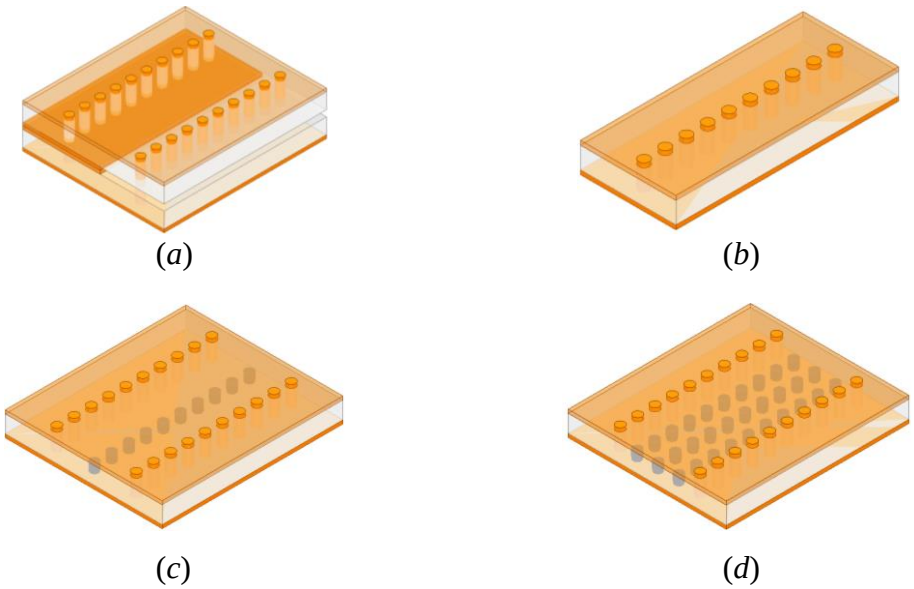

Figure 2.15 Some miniaturization techniques in SIW platform: (*a*) folded SIW, (*b*) half-mode SIW, (*c*) ridged SIW, and (*d*) slow-wave SIW.

In 2005, the folded SIW [29] was introduced as topology shown in Figure 2.15(*a*). The waveguide lateral width is "folded" resulting in a two-layer structure without significantly modifying the field pattern [30]. The mono-mode bandwidth of this structure is maintained. However, the total width is reduced by a factor of 2. The total width can be reduced by a factor of *N* by folding the original SIW structure *N* times [30] with the cost of fabrication complexity.

A 50% reduction of total width was also obtained in [31] using the single layer half-mode DFSIW (HM-DFSIW) as shown in Figure 2.15(*b*). Due to the symmetrical distribution of electrical fields for the dominant mode TE_{10} in conventional SIW, the symmetrical plan can be considered as a magnetic wall. Therefore, the conventional SIW can be cut at this symmetrical plan to generate a half-mode structure with the dominant mode is $TE_{0.5,0}$. By presenting a virtual magnetic wall at the cutting plane, the odd mode cannot exist in this structure. As a result, the next higher order mode is quasi $TE_{1.5,0}$ and the mono-mode bandwidth is enhanced by 1.5 times [30]. Moreover, the open-ended nature of this half-mode structure can be used to develop the circuits and components that require strong radiation such as leaky-wave antenna and coupler.

In 2008, the idea of the ridged SIW was successfully demonstrated in [32] with a 37% mono-mode bandwidth enhancement. In that paper, the central ridge was realized using blind via-holes (grey colour in Figure 2.15(c)). Similar to the ridged waveguide [24], the central septum helps increase the capacitance per unit length, therefore, lower the dominant mode cutoff frequency [30]. As a result, with the same cutoff frequency of the dominant mode, the width of ridged waveguide is reduced.

In 2014, a slow-wave SIW [33] was presented for the first time and its topology is shown in Figure 2.15(d). Blind via-holes (grey colour) are used to separate the electric and magnetic fields. By separating the fields, the propagation of the electromagnetic wave is slow-down. The term slow wave comes from this fact. Also, the effective relative permittivity is increased which leads to a reduction of footprint with the same cutoff frequency. A 43% reduction of total width is achieved in this paper.

Miniaturization techniques have been investigated in the AFSIW platform including the half-mode AFSIW (HM-AFSIW) [34] and the ridged AFSIW [35].

In this thesis, the idea of half-mode SIW is taken into consideration to realize the half-mode SAFSIW (HM-SAFSIW) due to the simplicity of design and analysis. Moreover, the HM-SAFSIW can be benefited to design high-performance leaky wave antennas.

2.3.2 Half-mode SAFSIW

As it can be seen in Figure 2.16 concerning the distribution of the electrical field of the dominant mode in SAFSIW, the distribution of the electrical fields is symmetrical about the plane A-A'. Moreover, the electrical field pattern is perpendicular to the broad wall. Therefore, the symmetrical plane A-A' can be considered as a magnetic wall. By cutting the SAFSIW at plane A-A', the HM-SAFSIW is obtained as shown in Figure 2.17 [36].

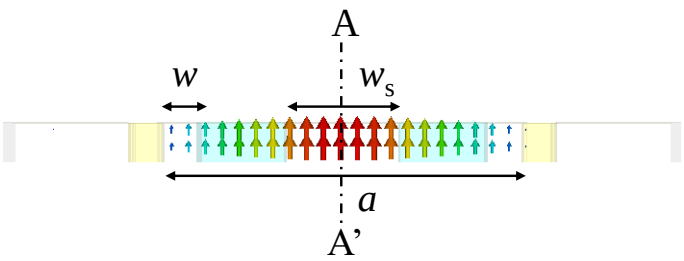

Figure 2.16 Simulated electric field distribution of the dominant mode in SAFSIW at 30 GHz (a = 4.8 mm, w_s = 1.5 mm, and w = 0.508 mm).

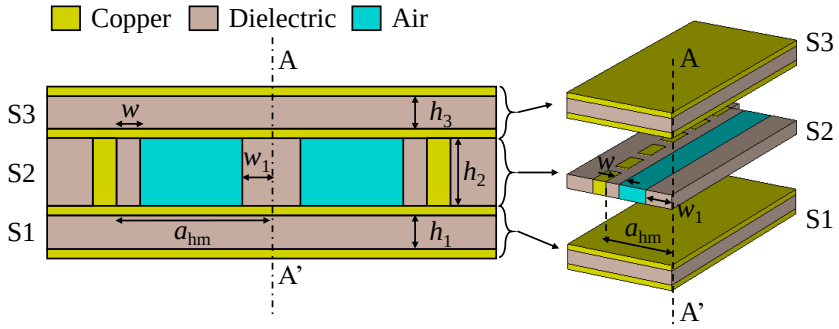

Figure 2.17 The realization of HM-SAFSIW from SAFSIW [36].

In that case, the analytical equations (6) to (9) can be used to approximate the cutoff frequency of the dominant mode in HM-SAFSIW (with $\beta = 0$):

$$A = \sqrt{\varepsilon_{rd}}\left[1 - \tan\left(\sqrt{\varepsilon_{rd}}k_0 w\right)\tan\left(\sqrt{\varepsilon_{rd}}k_0 w_1\right)\right] \quad (26)$$

$$B = \tan\left(\sqrt{\varepsilon_{rd}}k_0 w\right)\tan[k_0(a_{hm} - w_1 - w)] \quad (27)$$

$$C = \varepsilon_{rd}\tan[k_0(a_{hm} - w_1 - w)]\tan\left(\sqrt{\varepsilon_{rd}}k_0 w_1\right) \quad (28)$$

$$A - B - C = 0 \quad (29)$$

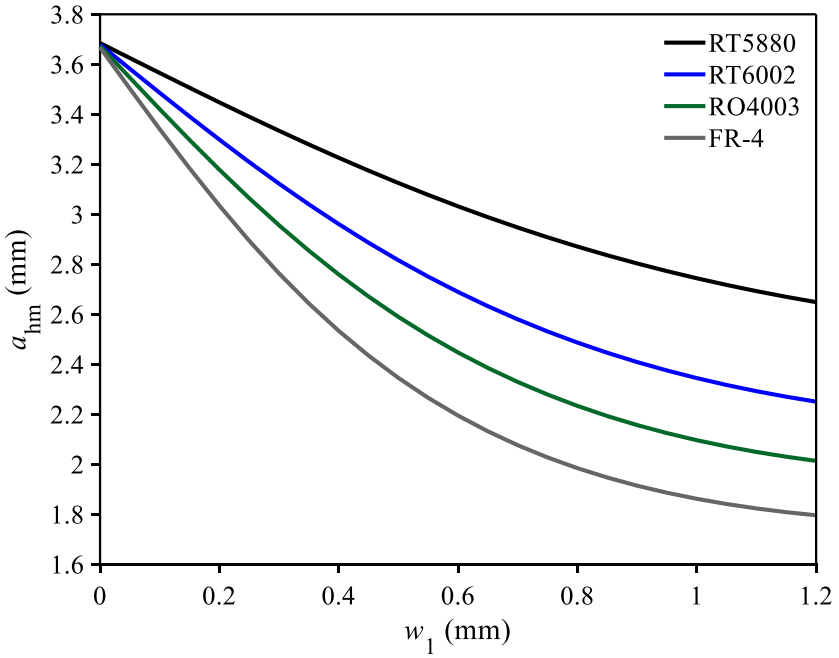

Figure 2.18 Calculated dimensions of HM-SAFSIW for various dielectric substrates [36].

Using the approximated equations (26) to (29), a design curve is generated as shown in Figure 2.18 for some common dielectric substrates including RT5880 ($\varepsilon_r = 2.2$), RT6002

(ε_r = 2.94), RO4003 (ε_r = 3.55), and FR-4 (ε_r = 4.3). The cutoff frequency of the dominant mode is set at $f_{c0.5,0}$ = 20.3 GHz for operation in Ka-band.

It can be observed from Figure 2.18 that the increase of w_1 leads to a reduction at the cutoff frequency of the dominant mode. Therefore, the total width a_{hm} is reduced to compensate for this effect and to maintain the cutoff frequency. This phenomenon is similar to the full-mode SAFSIW (see Figure 2.10).

On one hand, if w_1 = 0, i.e., there is no center dielectric slab, the HM-SAFSIW will become the conventional HM-AFSIW [34]. On the other hand, if w_1 = 0, the design is quite straightforward. Firstly, the dielectric width w_1 is chosen based on the fabrication capability. Then, the total width a_{hm} can be easily found depending on the available substrates.

2.3.3 Offset slab half-mode SAFSIW

2.3.3.1 Offset slab HM-SAFSIW

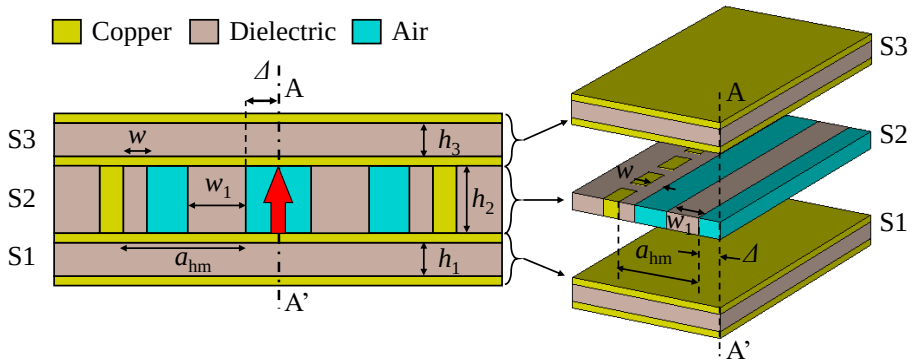

(*a*) [36] (*b*) [36]

Figure 2.19 The implementation of the offset slab HM-SAFSIW topology: (*a*) offset slab full-mode SAFSIW [36] and (*b*) offset slab HM-SAFSIW [36].

Taking benefits from the multilayer structure, an additional width Δ can be defined by top- and bottom-layers as shown in Figure 2.19(b). By inverse transform, the topology of the full-mode structure is realized as shown in Figure 2.19(a). In this case, the dielectric slab w_1 is offset with a value of Δ from the symmetrical plane A-A'. That is how the name offset slab HM-SAFSIW comes from.

In Figure 2.19(a), the red arrow represents the maximum electrical field pattern of the dominant mode. This maximum electrical field concentrates in an air region, instead of a dielectric region

as mentioned in the conventional SAFSIW structure. Therefore, the analytical equations from (6) to (9) cannot be used for this structure.

Using the same procedure described in section 2.2.1, the cutoff frequency of the dominant mode in an offset slab HM-SAFSIW can be approximated by the following equations [36]:

$$A_1 = \cos(k_0(a + \Delta - w_1))\cot(\sqrt{\varepsilon_r}k_0 w_1) \quad (30)$$

$$A_2 = \cos(k_0(a - w_1))\sin(k_0\Delta) \quad (31)$$

$$A_3 = \sin(k_0(a - w_1))\cos(k_0\Delta) \quad (32)$$

$$\sqrt{\varepsilon_r}A_1 - A_2 - \varepsilon_r A_3 = 0 \quad (33)$$

2.3.3.2 Effect of offset Δ

The effects of Δ on attenuation and phase constants are investigated by fixing the dielectric slab width w_1 and the waveguide width a_{hm}. For demonstration, the substrate RO4003 (h_2 = 0.6 mm, ε_r = 3.55) is used for implementation. Based on the design curve in Figure 2.18, the dielectric slab width is chosen as w_1 = 0.6 mm which gives a width of a_{hm} = 2.472 mm.

The effect of Δ on phase constant was examined in the simulation. The variation of normalized phase constant (β/k_0) with different values of Δ is shown in Figure 2.20 [36].

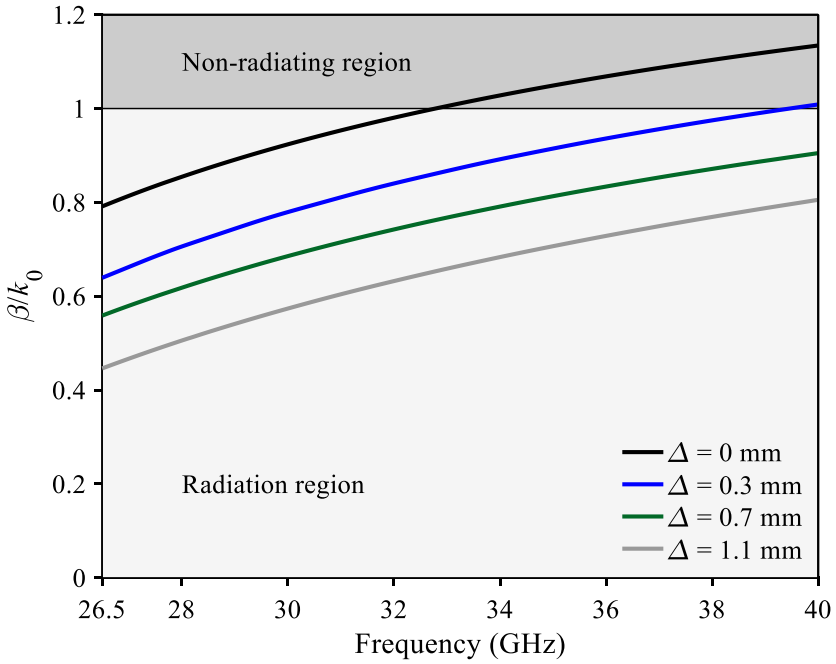

Figure 2.20 Calculated dimensions of HM-SAFSIW for various dielectric substrates [36].

It can be observed from Figure 2.20 is that the HM-SAFSIW tends to operate in the radiation region with an increase of Δ. It is due to the fact that, when Δ increases, more electric fields will concentrate in an air-region defined by Δ, less electric field confines in the dielectric. Therefore, more radiation happens. As a result, Δ can be modified to control the operation region of the HM-SAFSIW structure. For example, if the normalized phase constant $\beta/k_0 < 1$, the waveguide will operate in a fast-wave region that causes more radiation. For a better confinement, Δ should be chosen such that the normalized phase constant $\beta/k_0 > 1$.

Another interesting point observed from Figure 2.20 that, a non-uniform distribution of Δ could be implemented along the guided-wave structure to generate a non-uniform distribution of β, and therefore, the characteristic impedance. This property can be used to design a non-uniform leaky wave antenna to achieve low side lobe level [37].

Concerning the attenuation constant, the contributions on total losses are investigated at first to understand the nature of attenuation. For demonstration, Δ = 0.7 mm is chosen for simulation. For this study, surface roughness is not considered. The contributions on the total loss are presented in Figure 2.21.

It can be observed from Figure 2.21 that the radiation is the main contributor to the total losses over the lower frequency range (near cutoff frequency). As frequency increases, the dielectric loss becomes the dominant factor.

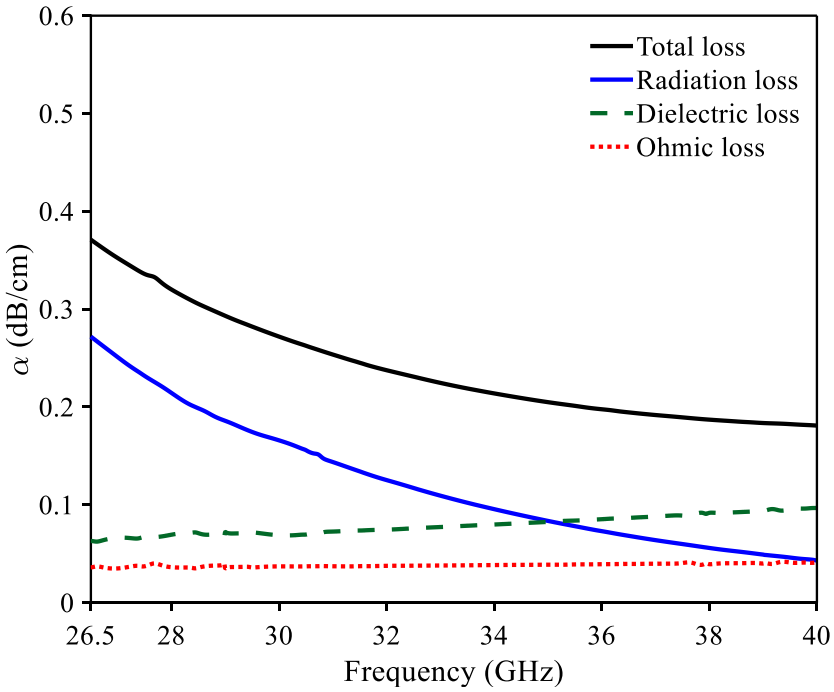

Figure 2.21 Contributions on total losses in offset slab HM-SAFSIW.

The effect of Δ on the total losses is analyzed by fixing the width $w_1 = 0.6$ mm and $a_{hm} = 2.472$ mm. This effect is shown in Figure 2.22.

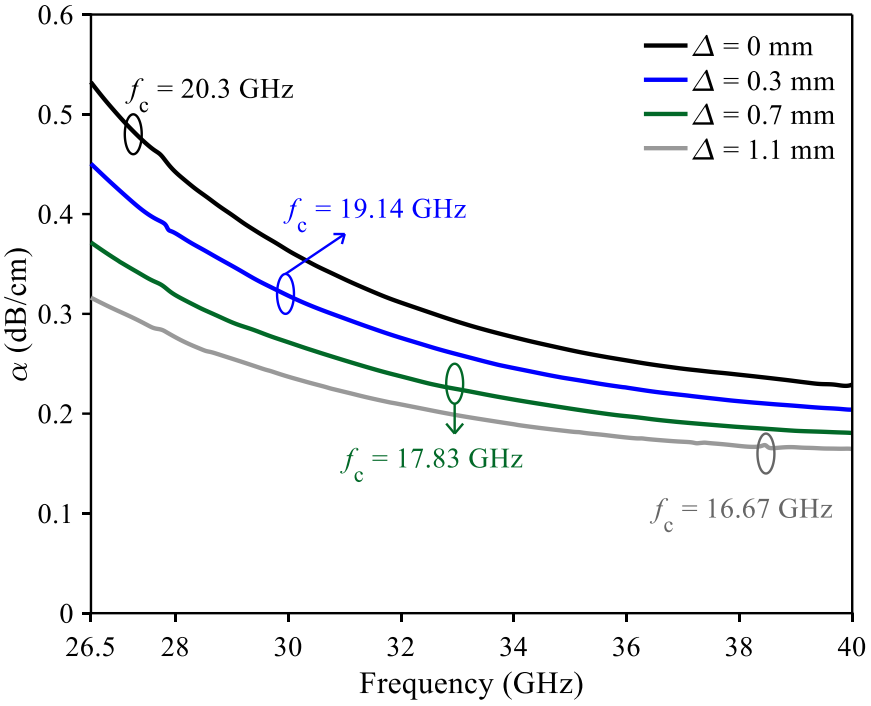

Figure 2.22 Contributions on total losses in offset slab HM-SAFSIW.

It can be noticed from Figure 2.22 that the total losses reduce with the increase of Δ. It is due to two main reasons. Firstly, the increase of Δ while the width a_{hm} is fixed causes an increase of total width ($a_{hm} + \Delta$). Therefore, the cutoff frequency of the dominant mode is reduced (from 20.3 GHz with $\Delta = 0$ mm to 16.67 GHz with $\Delta = 1.1$ mm). As was mentioned above, a strong radiation occurs near the cutoff frequency. By reducing the cutoff frequency, the radiation loss will be reduced. Secondly, more electric fields concentrate in the air-region defined by Δ that helps minimize the dielectric loss in a high frequency range. As a combination, radiation loss is reduced in a low frequency range and dielectric loss is reduced in the high frequency range. Finally, the total losses are reduced with the increase of Δ. So, the additional width Δ could also be controlled and carefully selected for proper applications.

At this stage, it should be noticed that the phase constant and attenuation constant can be controlled not only by Δ but also by the width a_{hm} and the dielectric slab w_1 as inherited characteristics from the SAFSIW structure. Therefore, this offset slab HM-SAFSIW gives lots of freedom in the control of phase and attenuation constants along with the structure.

2.3.4 Experimental demonstration

For demonstration, the offset slab HM-SAFSIW is considered for a back-to-back transition using RO4003 substrate. The dielectric slab w_1 = 0.6 mm together with a_{hm} = 2.472 mm is chosen for implementation. Concerning Δ, two factors need to be considered. Firstly, Δ should be large enough to reduce the transmission loss in a back-to-back transition. Secondly, the cutoff frequency should be about 1.25 to 1.5 times below the operating frequency band. For applications in Ka-band from 26.5 GHz to 40 GHz, Δ = 0.7 mm is chosen with f_c = 17.83 GHz (about 1.49 times below the Ka-band).

The back-to-back transition configuration and its fabricated prototype before assembling are shown in Figure 2.23(a) and Figure 2.23(b), respectively.

The detail dimensions in mm are shown in Figure 2.23(a). Two back-to-back transitions are fabricated with the length L = 10 mm and L = 20 mm to retrieve the attenuation constant by different lengths.

In measurement, a thru-reflect-line (TRL) calibration kit as shown in Figure 2.24 was used to remove the effect of GCPW to DFSIW transition. The measurement planes are A-A' and B-B'.

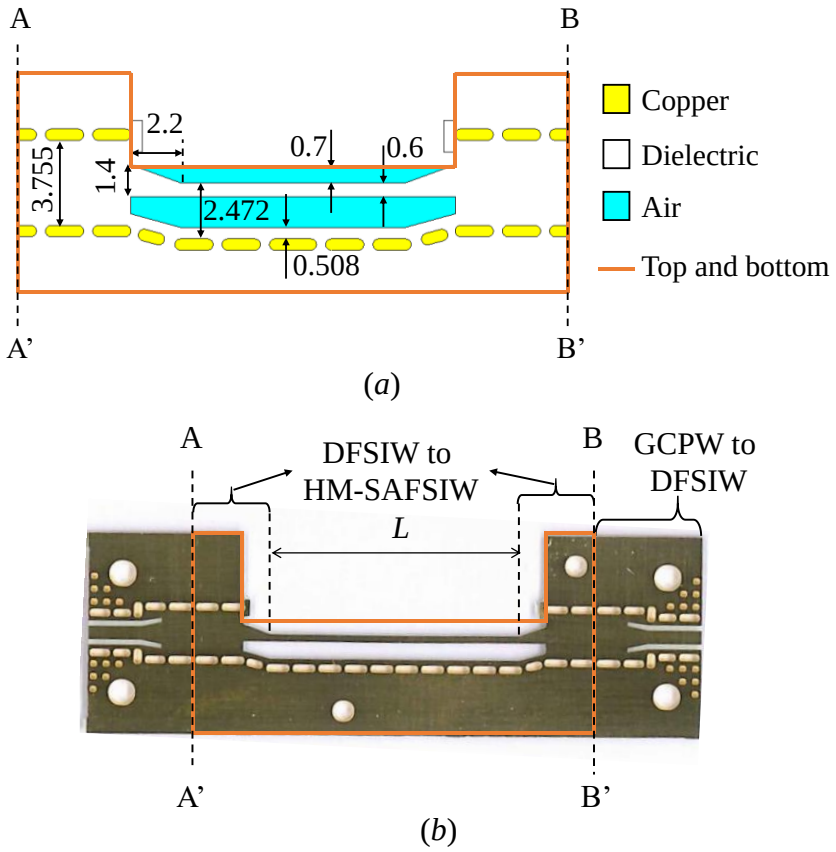

Figure 2.23 The offset slab HM-SAFSIW: (*a*) topology and (*b*) fabricated prototype.

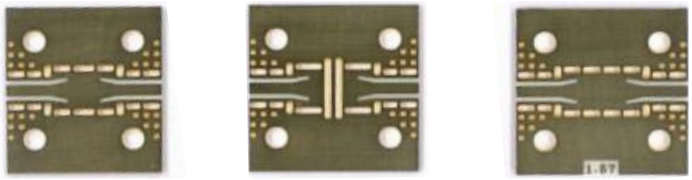

(*a*) (*b*) (*c*)

Figure 2.24 The TRL calibration kit: (*a*) thru, (*b*) reflect, and (*c*) line.

The simulated and measured *S*-parameters of the 10 mm length transmission line together with the simulated magnitude electrical field at 33 GHz are shown in Figure 2.25.

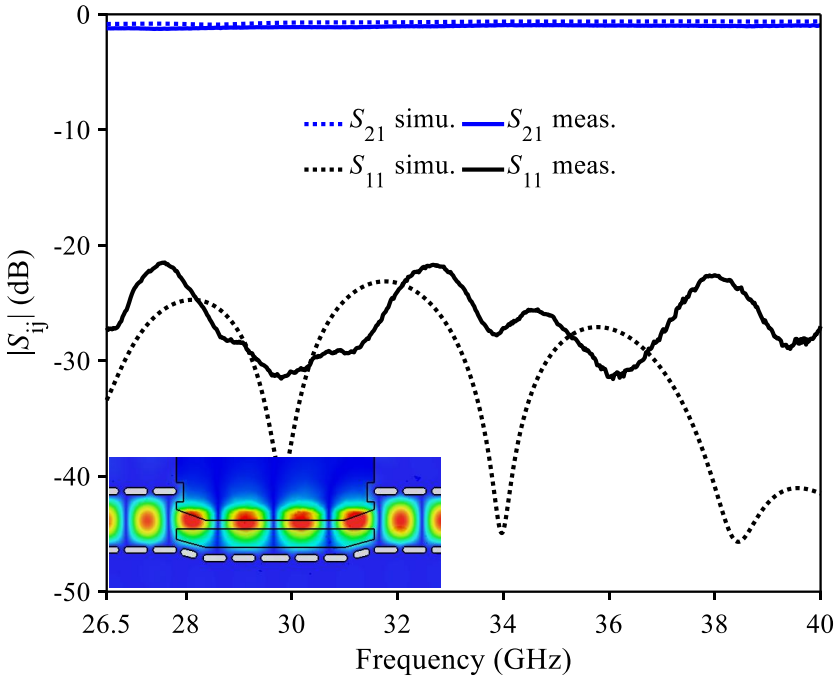

Figure 2.25 Simulated and measured *S*-parameters of the 10 mm offset slab HM-SAFSIW with simulated E-field magnitude at 33 GHz.

It can be observed from Figure 2.25 that the simulated and measured results are in a good agreement. The measurement shows a reflection coefficient $|S_{11}|$ less than -21.5 dB over the entire band. The obtained transmission coefficient $|S_{21}|$ is -1.1 ± 0.17 dB. The measurement presents about 0.4 dB loss higher than the simulation due to the surface roughness that is not considered in the simulation and the assembling process errors.

It can also be observed from the E-field distribution in Figure 2.25 that more electrical field concentrates in the air region, which confirms the above theory.

Concerning the 20 mm back-to-back transition, a reflection coefficient of $|S_{11}| < -20.5$ dB together with a transmission coefficient of $|S_{21}| = -1.3 \pm 0.18$ dB was also obtained.

Using the different length method, the attenuation constant can be extracted and compared with the simulated result in Figure 2.26, from where a good agreement can be observed.

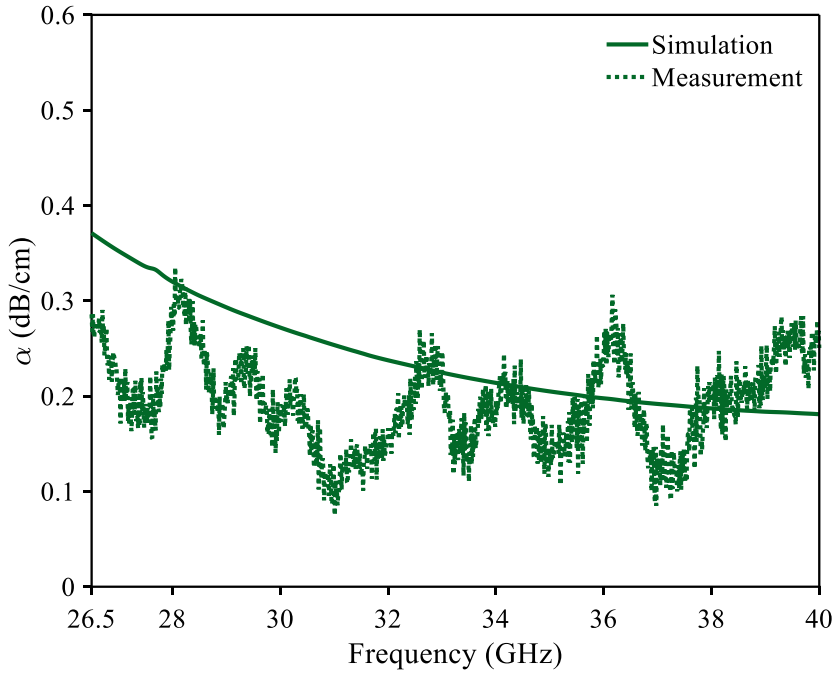

Figure 2.26 Simulated and measured attenuation constant of offset slab HM-SAFSIW.

2.3.5 Conclusion on HM-SAFSIW

A conventional HM-DFSIW and an HM-AFSIW were designed using the same substrate as the offset slab HM-SAFSIW and the same cutoff frequency $f_c = 17.83$ GHz for comparison. The total widths of HM-DFSIW and HM-AFSIW are $a_d = 2.233$ mm and $a_a = 4.206$ mm, respectively.

The performance comparisons are summarized in Table 2.3, from where a good compromise between HM-DFSIW and HM-AFSIW can be observed for HM-SAFSIW structure.

In conclusion, the HM-SAFSIW brings more freedom to designers for the development of high-performance circuits and components in millimeter-wave ranges. The offset slab HM-SAFSIW can be implemented in a non-uniform distribution for proper applications.

Table 2.3 Comparisons of simulated properties of HM-DFSIW, HM-SAFSIW, and HM-AFSIW at 33 GHz

Characteristics	HM-DFSIW	**HM-SAFSIW**	HM-AFSIW
Radiation loss (dB/cm)	0.030	**0.109**	0.401
Dielectric loss (dB/cm)	0.160	**0.077**	0
Ohmic loss (dB/cm)	0.055	**0.038**	0.031
Total loss (dB/cm)	0.245	**0.224**	0.432
Total width (mm)	2.233	**3.172**	4.206

CHAPTER 3 AFSIW/SAFSIW COMPONENTS FOR FEEDING NETWORK

Phase shifter and coupler are key components in feeding networks, especially for antenna array applications. This chapter aims to develop the compensating phase shifter and introduce the coupler based on AFSIW and SAFSIW technologies.

3.1 Compensating phase shifters

To generate a desired radiation pattern, it is possible to control the outputs phase, amplitude, or both. A phase shifter can be used to modulate or adjust the phase of output signals. A good phase shifter should have a flat phase shift response and a small variation in output amplitude over the operating frequency band. Phase shifters can be found in many communication systems such as antenna arrays, beamforming networks, and mono-pulse antennas.

In this chapter, compensating phase shifters will be presented and demonstrated. Firstly, the methodology to generate a compensating effect is introduced. Then, 90° phase shifters will be introduced using the SAFSIW for a shorter length. The 90° phase shifter will be used for the feeding network in a mono-pulse antenna array in section 4.3. Finally, a 45° phase shifter based on the conventional AFSIW is demonstrated. This 45° phase shifter will be then integrated into a Butler's matrix in Chapter 6.

3.1.1 Overview

In [38], an SIW broadband phase shifter was demonstrated for the first time as shown in Figure 3.1(a). The broadband compensating phase shifter was realized by combining two phase shifters: one with a positive slope differential phase and the other with a negative slope differential phase. The general idea of compensating phase shifter can be explained qualitatively in Figure 3.2. In that work, the positive slope differential phase is obtained with a delay line while the negative slope differential phase is realized with a broadened waveguide width. The delay line, however, gives an unequal-length topology, which is not preferred in complex feeding structures.

The idea of opposite dispersion slopes was investigated in the AFSIW platform for an unequal-width equal-length phase shifter [8] as shown in Figure 3.1(b). Two phase shifters were cascaded to generate the compensating effect. In the upstream phase shifter, the dielectric slab width is extended to generate a higher effective permittivity. Therefore, a positive slope

differential phase is observed. Meanwhile, the downstream phase shifter enlarges the waveguide width to generate a negative slope differential phase. As a combination, a compensating phase shifter is realized. However, by cascading two phase shifters, the obtained phase shifter becomes very long.

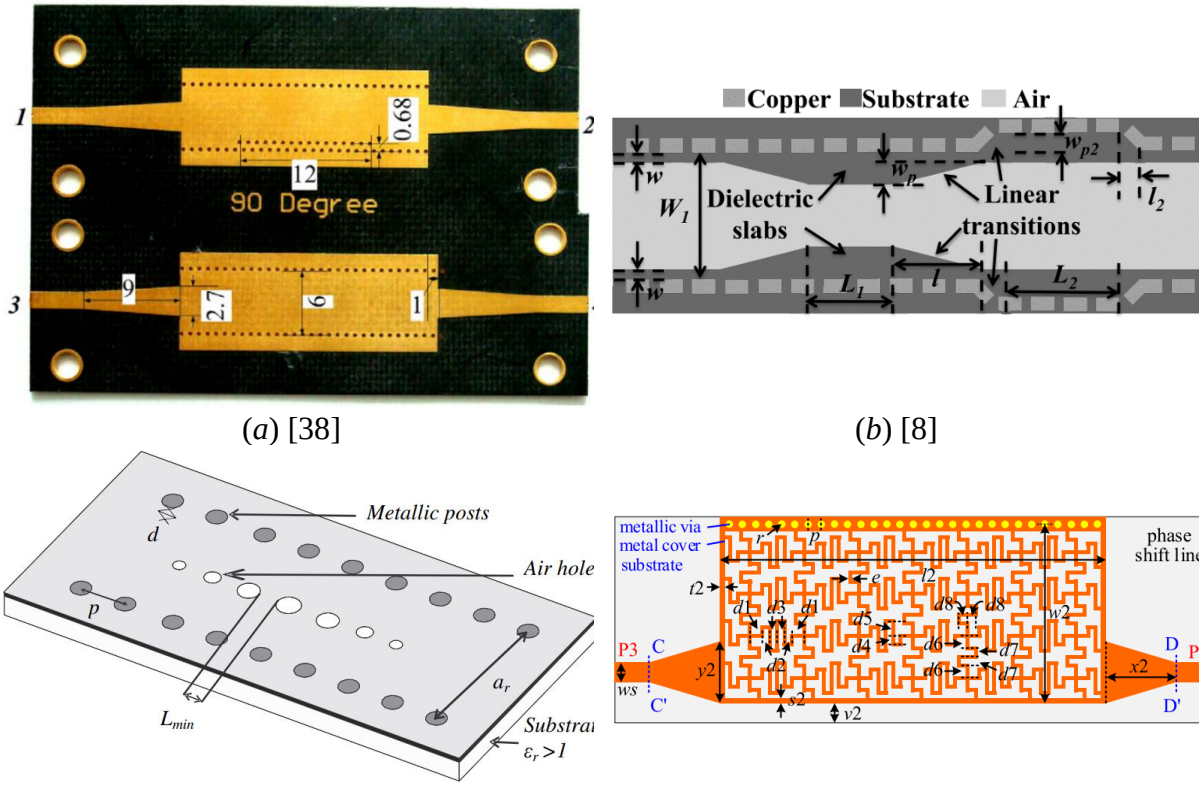

(*a*) [38] (*b*) [8]

(*c*) [39] (*d*) [40]

Figure 3.1 Compensating phase shifters in different technologies: (*a*) unequal-width unequal-length SIW [38], (*b*) unequal-width equal-length AFSIW [8], (*c*) equal-width equal-length SIW using air-holes [39], and (*d*) equal-width equal-length slow wave half-mode SIW [40].

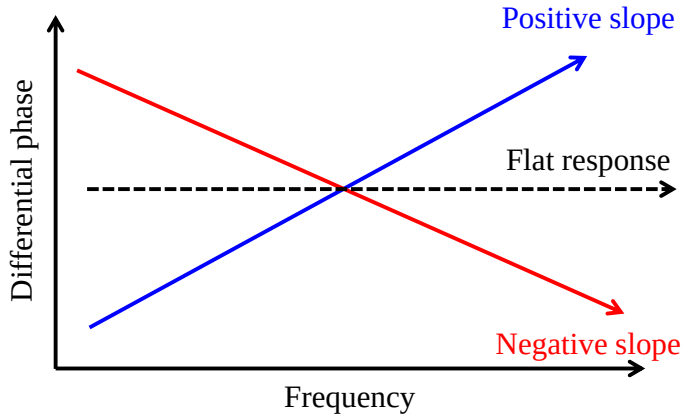

Figure 3.2 General idea of compensating phase shifter.

Instead of extending the dielectric to increase the effective permittivity, low permittivity could also be used to reduce the effective permittivity. The compensating phase shifter using air-holes to lower the relative permittivity was demonstrated in [39] as shown in Figure 3.1(c). Air-holes are cascaded to realize the desired phase shift. The operation mechanism can be explained qualitatively as follows: first, the air-holes reduce the effective permittivity, which gives a negative slope for the differential phase. Since the effective permittivity is reduced, the waveguide width needs to be enlarged to maintain the cutoff frequency. However, the waveguide width is maintained in [39], which can be considered as a "virtual reduction" of waveguide width. Therefore, a positive slop is generated for the differential phase. As a result, the obtained phase shift is flat over the operating frequency band. Since the low permittivity is used, a long footprint needs to be used for a large phase shift. Large air-holes could be used for higher phase shift. However, large air-holes will give other radiating problems.

To reduce the footprint of the phase shifter, the slow-wave half-mode concept was applied in SIW for a 90.5 ± 3° phase shifter in [40] as illustrated in Figure 3.1(d).

In this Ph.D. thesis, the low loss AFSIW solution together with dielectric slab are investigated for high-performance phase shifters, including 90° and 45° phase shifters. The dielectric slab helps increase the relative permittivity for a positive slope differential phase.

3.1.2 90° SAFSIW phase shifter

The 90° phase shifters can be widely found in circular polarized antennas [41], [42], Nolen's matrix [43], [44], Butler's matrix [45], [46], and mono-pulse antennas [47]-[50]. In this section, two different 90° phase shifters based on the SAFSIW will be introduced.

3.1.2.1 Equal-width unequal-length phase shifter

The topology of the equal-width unequal-length (EW-UEL) phase shifter is shown in Figure 3.3(*a*) together with the simulated magnitude E field at 33 GHz in Figure 3.3(*b*). The dimensions are given in mm. A dielectric slab is loaded at the center of the phase shifter, which can be represented by a SAFSIW section.

The total phase shift can be decomposed into three main parts: center dielectric slab of length L_{c1} = 1.78 mm, two transitions of length L_{t1} = 6.72 mm for each, and different length ΔL which can be puzzled out by Figure 3.4.

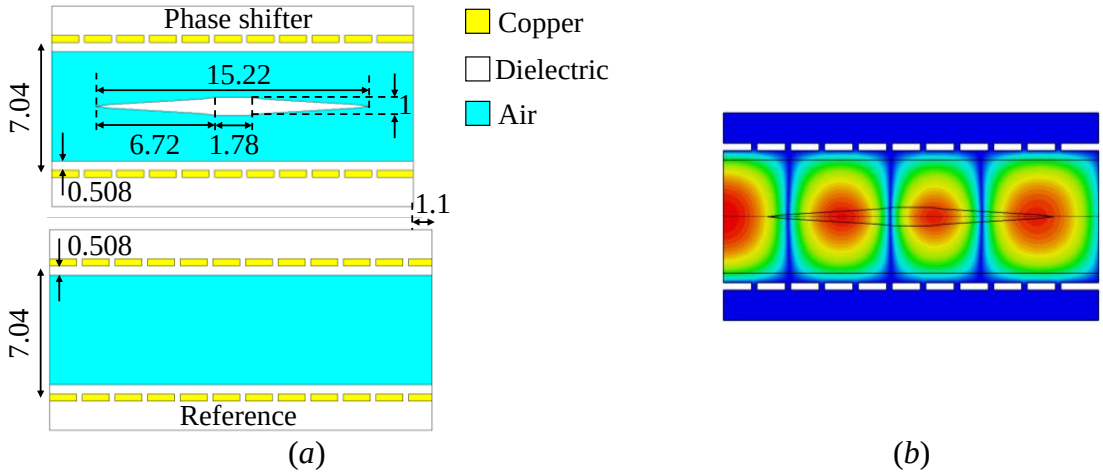

Figure 3.3 The EW-UEL phase shifter: (*a*) topology and (*b*) simulated magnitude E field at 33 GHz.

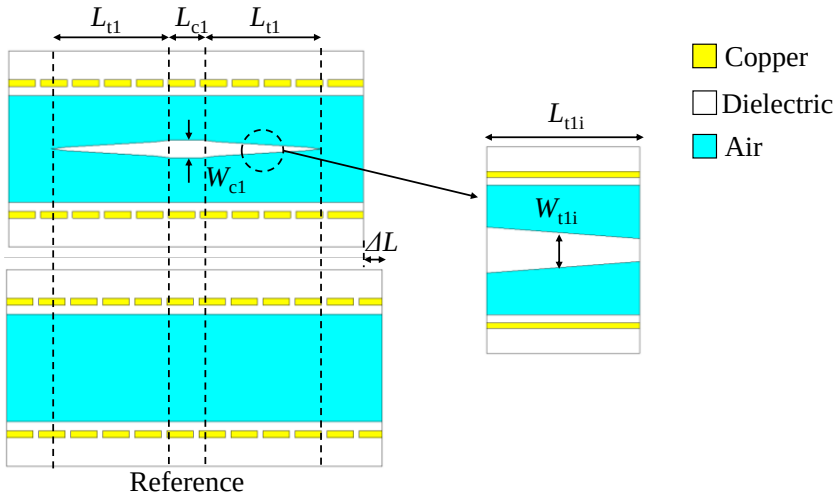

Figure 3.4 Different parts contributing to EW-UEL phase shifter.

As the phase shifter is designed symmetrically, only even modes (TE_{10}, TE_{30}, TE_{50}, …) can propagate. To prevent high order modes from occurring in the phase shifter, the cutoff frequency of the first (TE_{10}) and third (TE_{30}) modes should be under and above the operating band, respectively. Regarding the phase shifter, the AFSIW part was designed with a cutoff frequency of 21.2 GHz for the dominant mode. As it was explained in Chapter 2, the presence of the dielectric slab will lower the cutoff frequency of the dominant mode. Therefore, the cutoff frequencies of the first mode in the SAFSIW section are always lower than 21.2 GHz, which allows the operation in Ka-band (26.5 GHz to 40 GHz). Concerning the third mode, the center part width W_{c1} will give the lowest cutoff frequency. Therefore, this center part must be properly chosen to satisfy the mode supporting condition. For W_{c1} = 1 mm, the phase constants of the

first three propagation modes are shown in Figure 3.5, where it can be observed that the mode supporting condition is fulfilled.

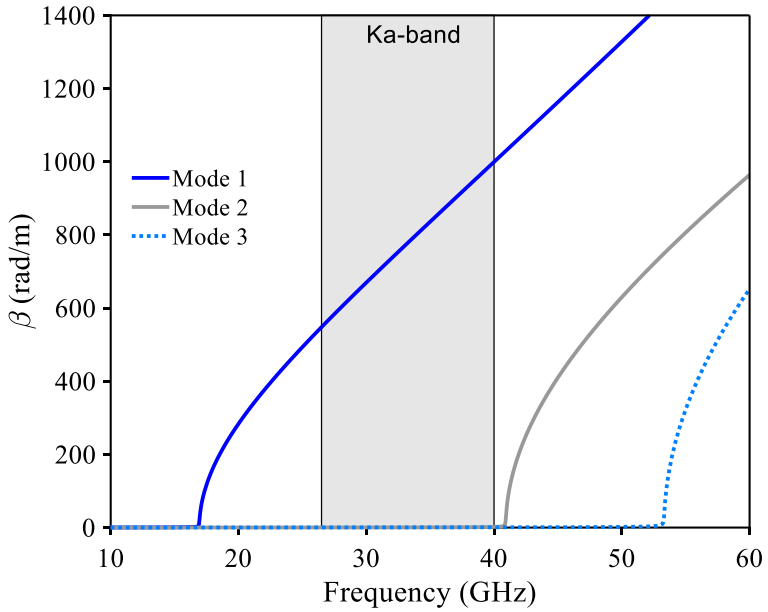

Figure 3.5 Phase constants of the first three modes in the center part of the EW-UEL phase shifter.

Once the mode supporting condition is satisfied, the contribution of the center part defined by L_{c1} and W_{c1} can be easily analyzed theoretically by using (6) to (9) in Chapter 2 to calculate the phase constant β_{c1}. Then, the phase shift φ_{c1} due to the center part is calculated by:

$$\varphi_{c1} = \beta_{c1} \times L_{c1} \tag{34}$$

Meanwhile, the transition parts are discretized into M sections defined by ΔL_{t1i} and ΔW_{t1i} as shown in Figure 3.4. For that, the average slab width ΔW_{av1i} for each section is defined by:

$$\Delta W_{av1i} = \frac{(\Delta W_{i-1} + \Delta W_i)}{2} \tag{35}$$

Then, the phase constant β_{t1i} in each segment can be analyzed by applying the average slab width ΔW_{av1i} and discretized length ΔL_{t1i} into (6) to (9). As a result, the phase shift φ_{t1} caused by each transition is:

$$\varphi_{t1} = \sum_{i=1}^{M} \beta_{t1i} \times \Delta L_{t1i} \tag{36}$$

Concerning the different length part, by applying (6) to (9) with a zero-slab width, the phase constant β_{AF} of the different length (AFSIW section) can be obtained. Then, the phase shift caused by different length φ_{Δ} is:

$$\varphi_{\Delta} = \beta_{AF} \times \Delta_{L} \tag{37}$$

Finally, the total phase shift obtained by differential phase constant φ_{tot1} is:

$$\varphi_{tot1} = \varphi_{c1} + 2\varphi_{t1} - \varphi_{\Delta} \tag{38}$$

For demonstration, the taper transition is discretized into 8 segments. The contribution of the total phase shift generated by differential phase constant is shown in Figure 3.6, where a very good agreement between discretization and simulated results can be observed.

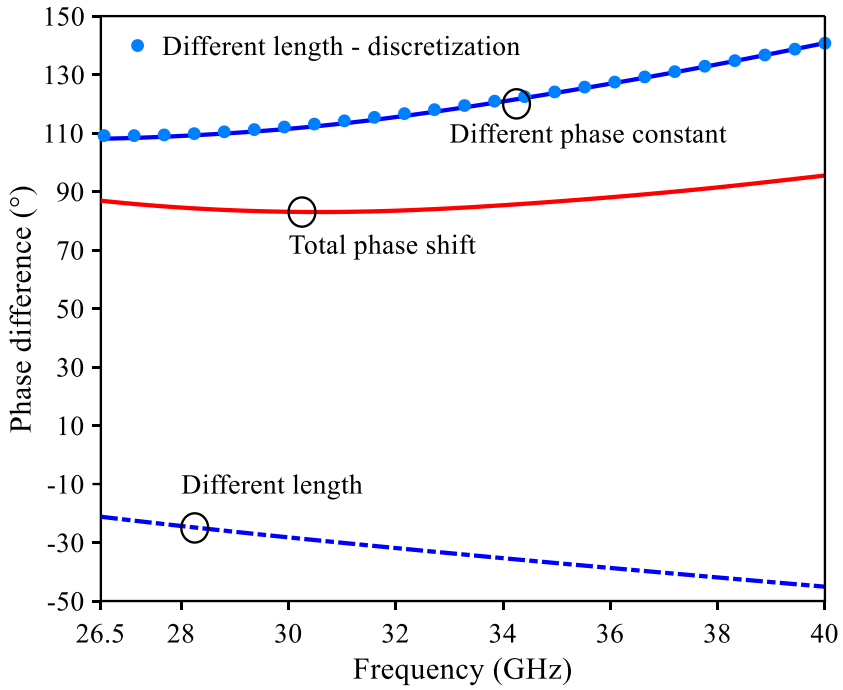

Figure 3.6 Compensating effect in the EW-UEL phase shifter.

By loading with dielectric, the equivalent permittivity is increased. Therefore, a positive slope is observed for the differential phase. To generate a negative slope, an extension of 1.1 mm is added to the reference. The compensating effect can be observed in Figure 3.6.

The fabricated prototype of the EW-UEL phase shifter is shown in Figure 3.7. A transition from GCPW to DFSIW to AFSIW is used for measurement purposes. In measurement, a TRL calibration kit is used to remove the effect of this transition. The measured reference planes are shown in Figure 3.7.

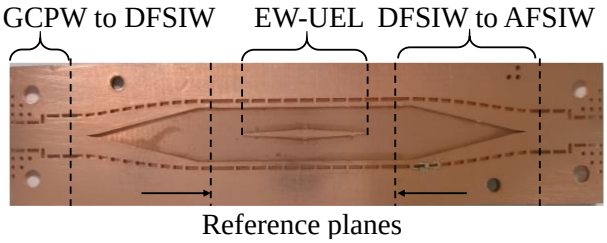

Figure 3.7 Fabricated prototype of the EW-UEL phase shifter.

The simulated and measured *S*-parameters of the EW-UEL phase shifter are compared in Figure 3.8, where a good agreement can be observed. The measured reflection coefficient $|S_{11}|$ is less than -12.3 dB over the Ka-band. The obtained measured transmission coefficient is $|S_{21}|$ = -0.38 ± 0.31 dB. More losses are observed in measurement due to the assembling process and the surface roughness that was not considered in the simulation.

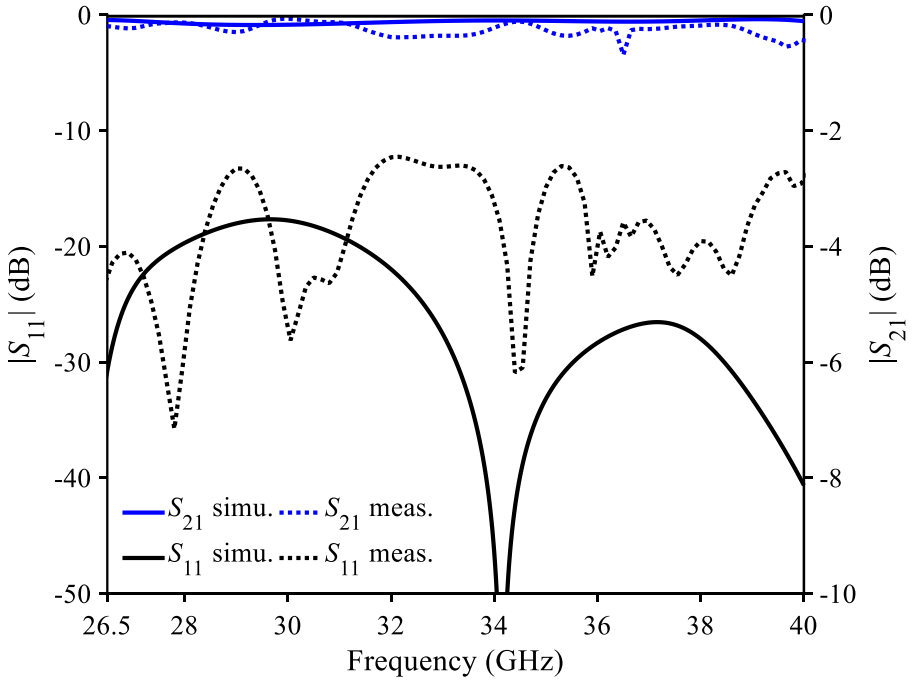

Figure 3.8 Simulated and measured *S*-parameters of the EW-UEL phase shifter.

The simulated and measured phase difference and amplitude imbalance are shown in Figure 3.9, where a good agreement can be observed. The measured phase difference is 85.3 ± 4.8° together with an amplitude imbalance of AI = 0.05 ± 0.15 dB. Again, the difference between simulation and measurement is mainly due to the manual assembling process.

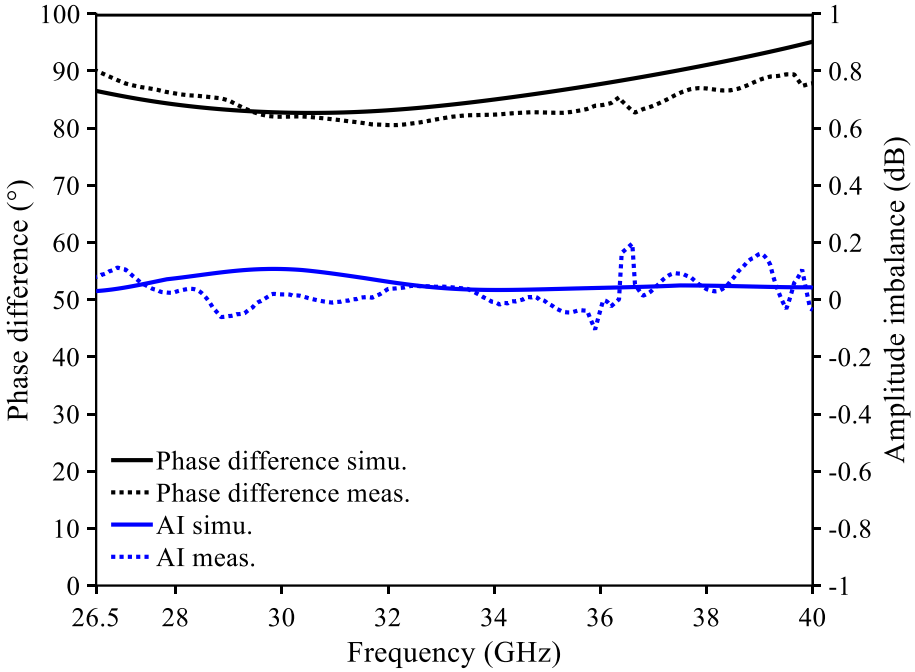

Figure 3.9 Simulated and measured phase difference and amplitude imbalance of the EW-UEL phase shifter.

3.1.2.2 Unequal-width equal-length phase shifter

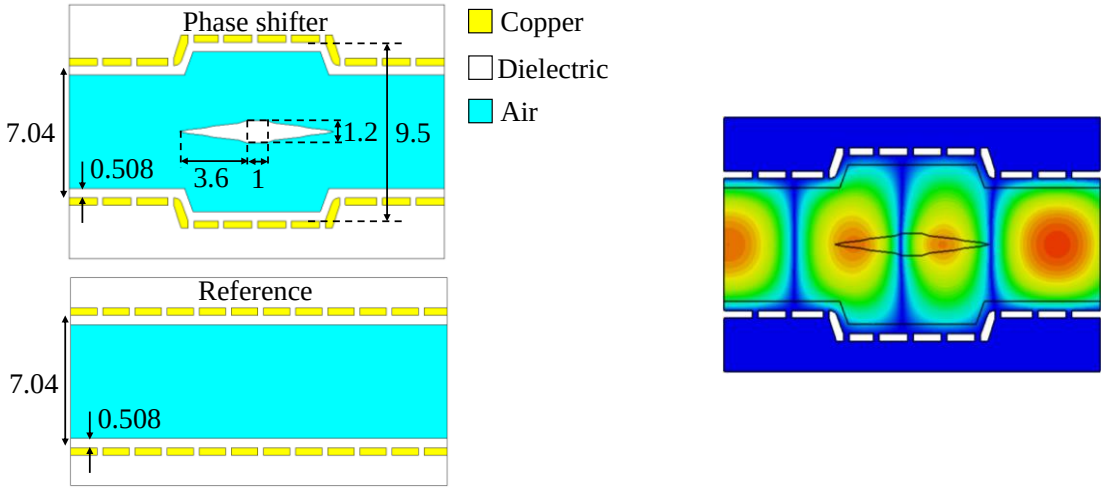

(*a*) (*b*)

Figure 3.10 The UEW-EL phase shifter: (*a*) topology and (*b*) simulated magnitude E field at 33 GHz.

In the EW-UEL phase shifter presented in section 3.1.2.1, an additional length of 1.1 mm was included to the reference to generate a negative slope effect for the differential phase, which results in an unequal length topology. To overcome this issue, the total width of the phase shifter could be enlarged to generate the negative slope effect.

The topology of the unequal-width equal-length (UEW-EL) phase shifter and the simulated magnitude E field at 33 GHz are shown in Figure 3.10. All the dimensions are given in mm.

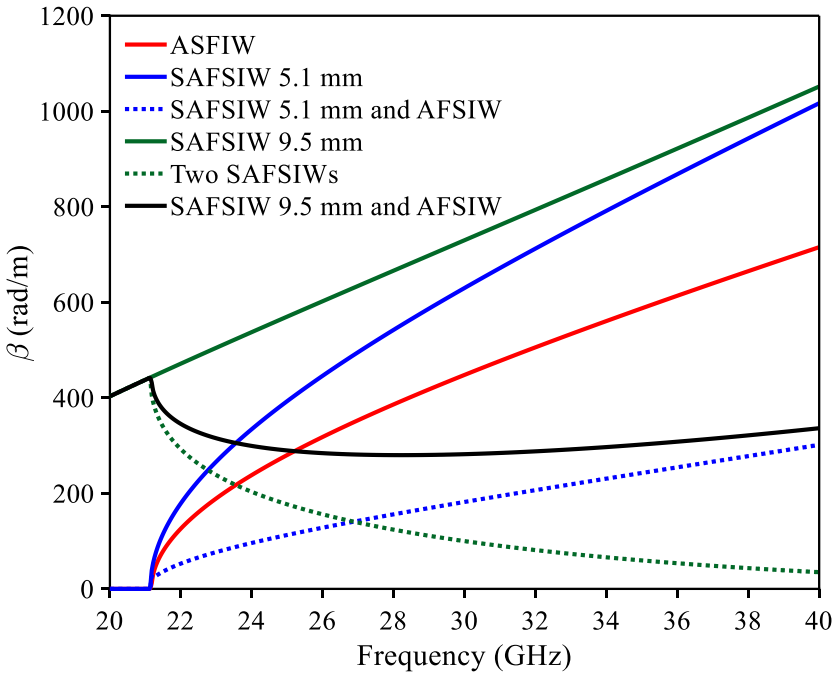

Figure 3.11 Simulated and measured phase difference and amplitude imbalance of the EW-UEL phase shifter.

To understand the compensating effect, different waveguide structures were analyzed to retrieve the differential phase constants:

- An AFSIW of width a = 7.04 mm and an SAFSIW of width a = 5.1 mm together with a dielectric slab of width w_s = 1.2 mm having the same cutoff frequency for dominant mode f_{c01} = 21.2 GHz. Since the presence of dielectric slab in SAFSIW tends to increase the effective permittivity, a positive slope differential phase constant is observed between the AFSIW and SAFSIW 5.1 mm, which can be observed in Figure 3.11.
- An enlarged-width SAFSIW with a = 9.5 mm, w_s = 1.2 mm and the previous SAFSIW with a = 5.1 mm, w_s = 1.2 mm. Since the broadened width tends to lower down the effective permittivity, a negative slope differential phase constant is observed between two SAFSIW structures as presented in Figure 3.11.
- At this stage, it can be observed that the combination of an SAFSIW with a = 9.5 mm, w_s = 1.2 mm and an AFSIW with a = 7.04 mm can generate a compensating effect for differential phase constant, as can be observed in Figure 3.11.

Here, the compensating effect is demonstrated for the center part only. However, this operation mechanism is valid also for the transition parts, since the center dielectric slab and enlarged-width sections are still there.

Similar to the EW-UEL phase shifter presented in 3.1.2.1, the center part of width 1.2 mm has to satisfy the mode supporting condition in Ka-band. The phase constants of the first three propagation modes in this section are shown in Figure 3.12, from where the mode supporting condition is fulfilled.

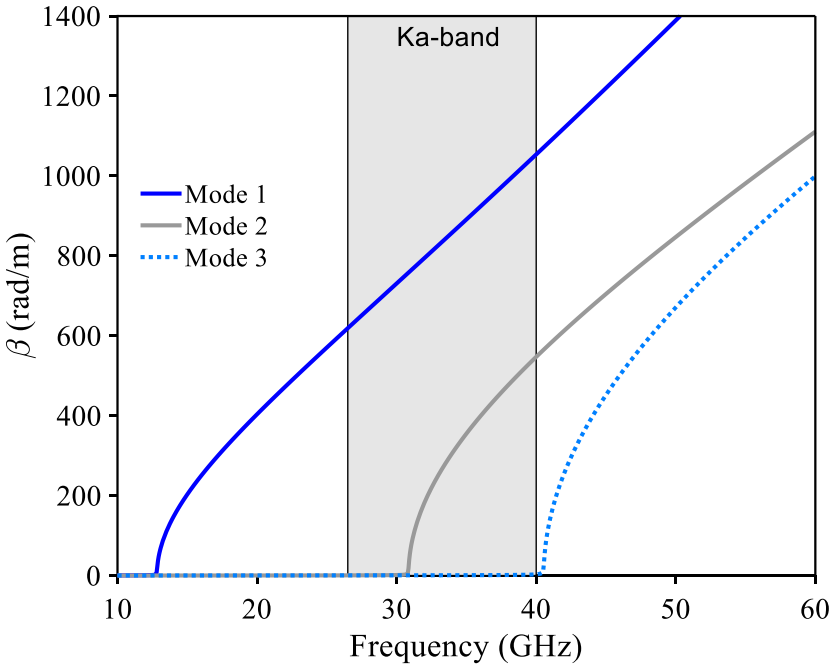

Figure 3.12 Phase constants of the first three modes in the center part of the UEW-EL phase shifter.

Again, the contribution on total phase shift can be analyzed by discretizing the phase shifter into two parts: the center part of width 1.2 mm, length 1 mm, and two transitions of length 3.6 mm for each. With 8 segments of discretization, the contributions on total phase shift are shown in Figure 3.13.

It can be observed from Figure 3.13 that the discretized phase differences are in good agreement with the entire phase differences. The accuracy can be enhanced by increasing the number of segments. Of course, the calculation time is increasing. In this case, a maximum difference of 7.3% is observed at 26.5 GHz, which is a good agreement.

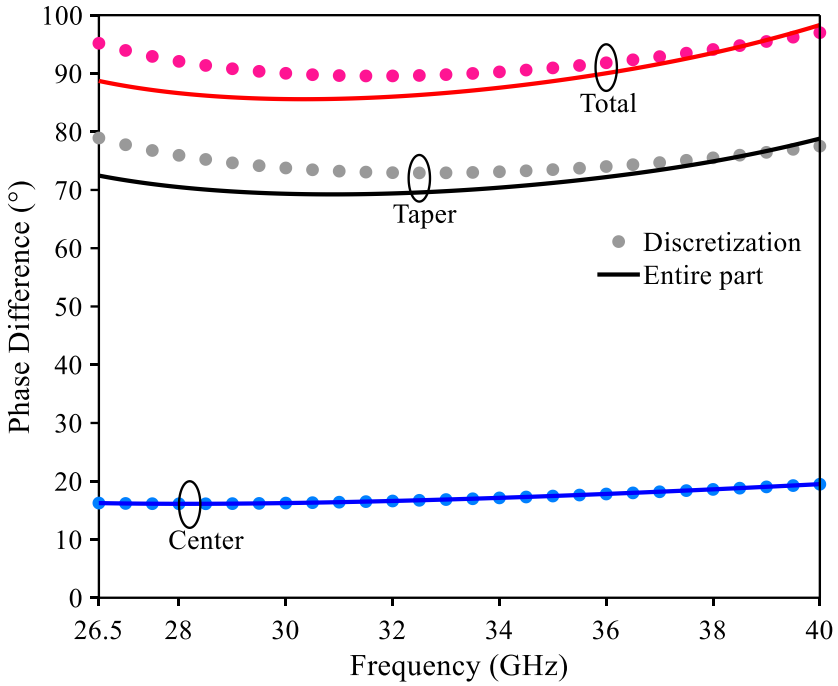

Figure 3.13 Contributions on total phase shift in the UEW-EL phase shifter.

For demonstration, the UEW-EL phase shifter was fabricated. The prototype is shown in Figure 3.14. Again, a TRL calibration kit was used to remove the effect of GCPW on AFSIW transitions. The measured reference planes are shown in Figure 3.14.

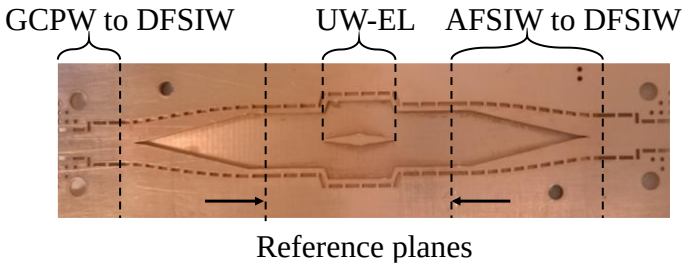

Figure 3.14 Fabricated prototype of the UEW-EL phase shifter.

The simulated and measured *S*-parameters of the UEW-EL phase shifter are compared in Figure 3.15, where a good agreement can be observed. The measured reflection coefficient $|S_{11}|$ is less than -10 dB for almost the entire Ka-band. Meanwhile, the simulated reflection coefficient $|S_{11}|$ is always less than -15 dB. More reflections occur in measurement due to the manual assembling process. The obtained measured transmission coefficient is $|S_{21}| = -0.33 \pm 0.24$ dB. More losses are observed in measurement due to the assembling process and the surface roughness that was not considered in the simulation.

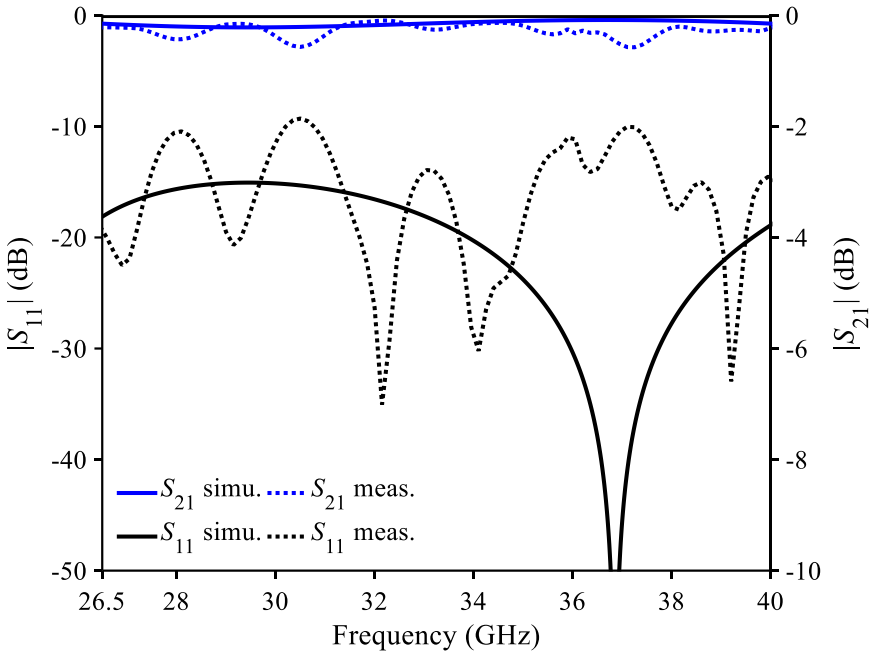

Figure 3.15 Simulated and measured *S*-parameters of the EW-UEL phase shifter.

The simulated and measured phase difference and amplitude imbalance are shown in Figure 3.16, where a good agreement can be observed. The measured phase difference is 86.9 ± 6.7° together with an amplitude imbalance of AI = 0.06 ± 0.15 dB. Again, the difference between simulation and measurement is mainly due to the manual assembling process.

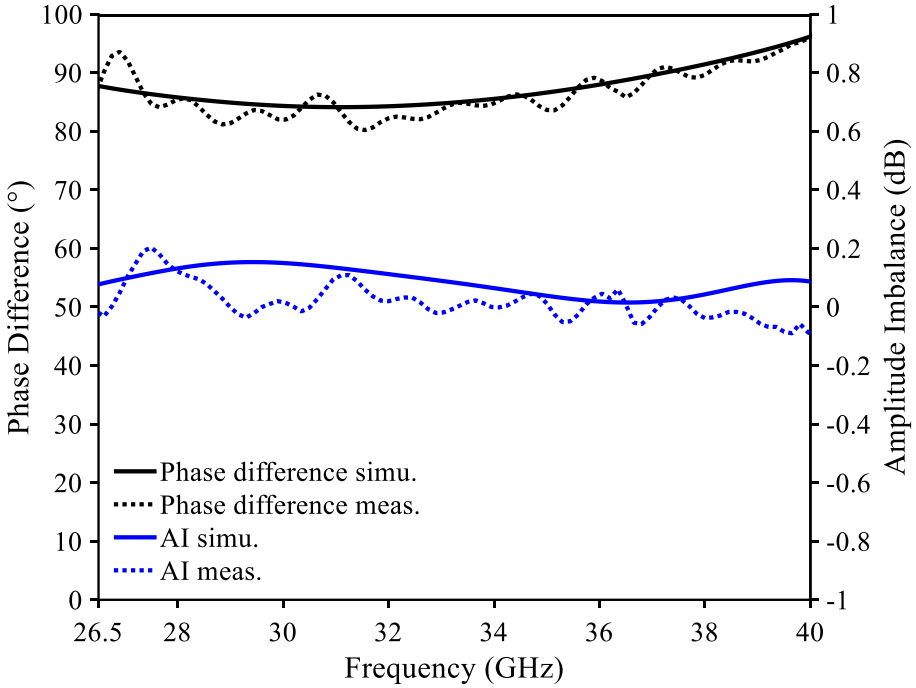

Figure 3.16 Simulated and measured phase difference and amplitude imbalance of the UEW-EL phase shifter.

3.1.3 45° AFSIW phase shifter

The 45° phase shifter is an important component that can be found in Butler's matrix. In this section, a UEW-EL 45° phase shifter will be developed for 5G applications operating from 27.5 GHz to 28.35 GHz. Regarding this kind of phase shifter, the AFSIW technology will be considered due to the low value of phase shift. The topology of the 45° AFSIW phase shifter together with the magnitude E field distribution at 28 GHz is presented in Figure 3.17. All dimensions are given in mm.

In this configuration, the sidewall dielectric slab is thickened to increase the effective permittivity to generate a positive slope differential phase constant. At the same time, the total width of this section is broadened to get a negative slope differential phase constant. As a result, a compensating phase shifter is obtained.

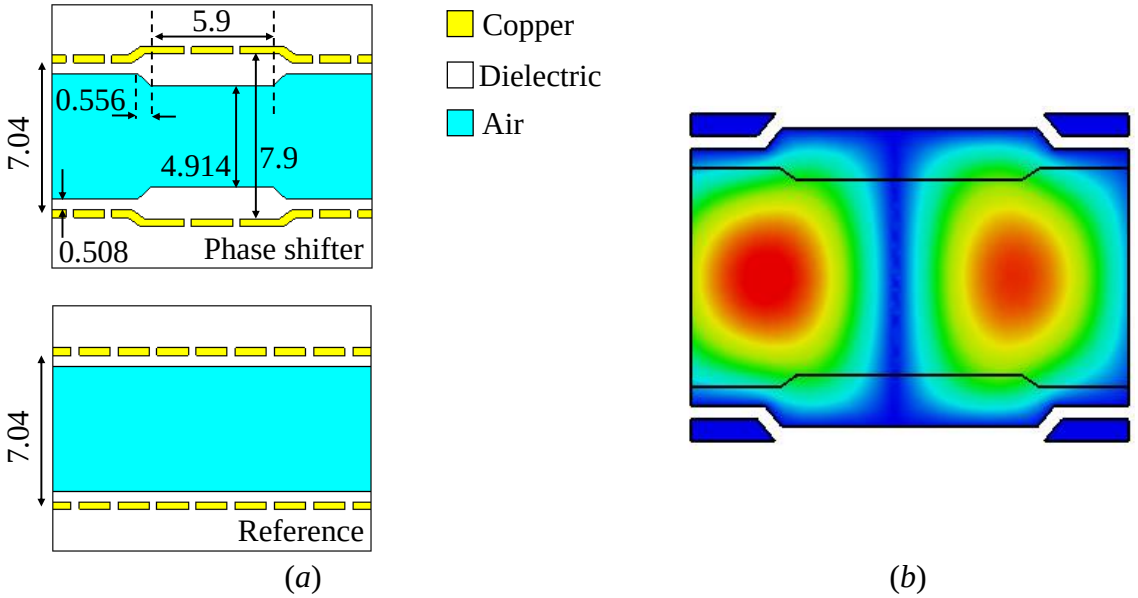

Figure 3.17 The UEW-EL 45° phase shifter: (*a*) topology and (*b*) simulated magnitude E field at 28 GHz.

Similar to the EW-UEL and UEW-EL phase shifters, the broadened sidewall dielectric slab with a length of 5.9 mm at the center needs to be designed carefully not to support high order modes in the operating frequency band. In the simulation, the cutoff frequencies of the TE_{10}, TE_{20}, TE_{30} modes are 17.45 GHz, 29.65 GHz, and 42.1 GHz, respectively. Due to the symmetry, only even modes can exist in this structure. As a result, the mode supporting condition is satisfied.

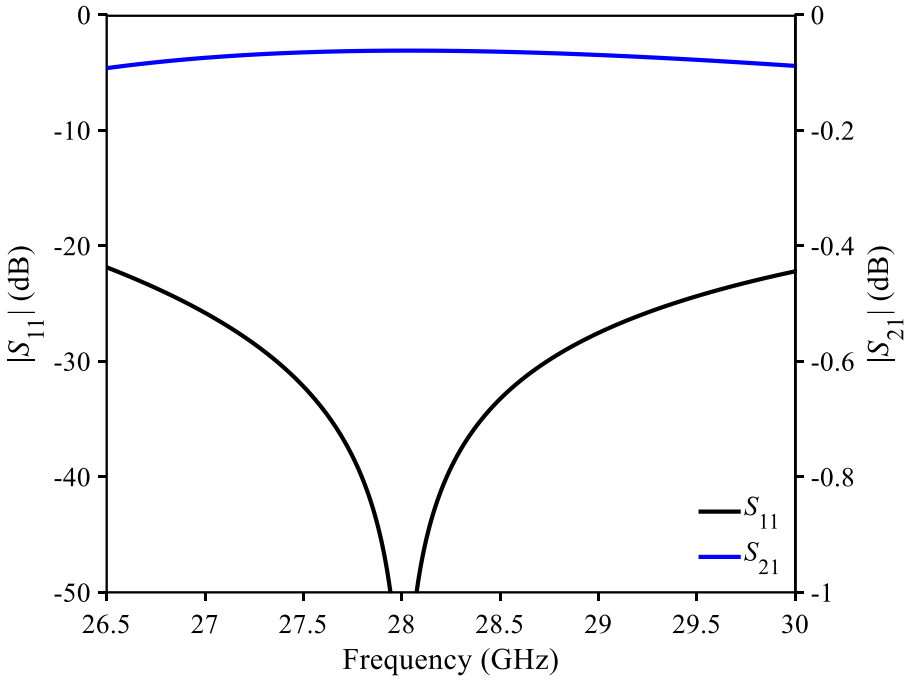

Figure 3.18 Simulated *S*-parameters of the 45° phase shifter.

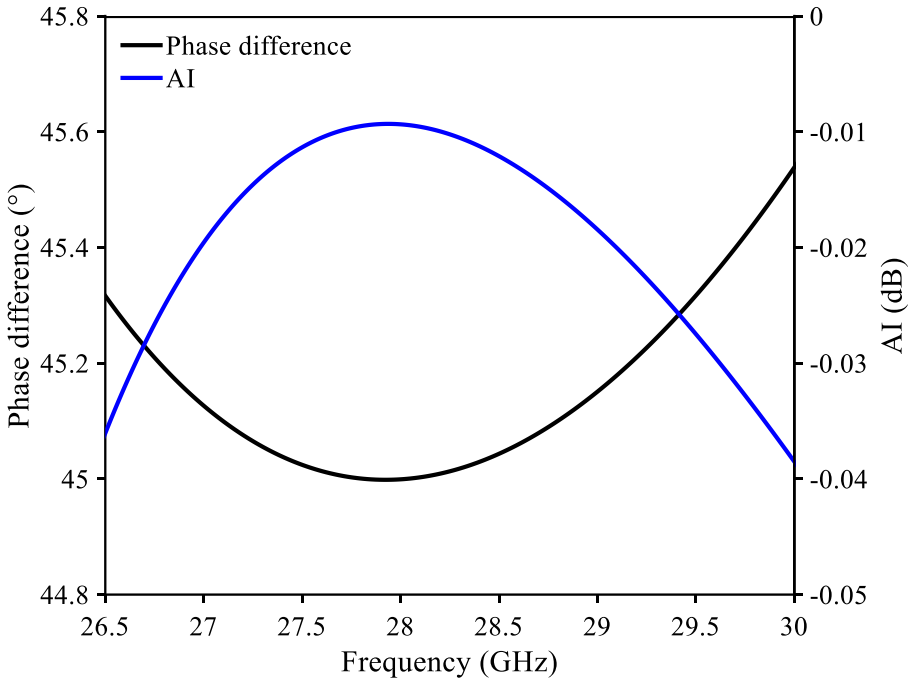

Figure 3.19 Simulated phase difference and amplitude imbalance of the 45° phase shifter.

The simulated *S*-parameters of the 45° phase shifter are shown in Figure 3.18. It can be observed from Figure 3.18 that the reflection coefficient $|S_{11}|$ is lower than -20 dB from 26.5 GHz to

30 GHz, especially in the 5G band from 27.5 GHz to 28.35 GHz, $|S_{11}|$ is lower than -30 dB. The simulated transmission coefficient is $|S_{21}|$ = -0.08 ± 0.02 dB from 26.5 GHz to 30 GHz.

The simulated phase difference and amplitude imbalance of the 45° phase shifter are presented in Figure 3.19. The obtained simulated phase difference is 45.3 ± 0.3° (phase error less than 1%) while the simulated AI is -0.02 ± 0.01 dB from 26.5 GHz to 30 GHz, which shows a very good balance at outputs.

3.1.4 Conclusion

For comparison, Table 3.1 summarizes different characteristics of various compensating phase shifters operating in Ka-band. It can be observed from Table 3.1 that the AFSIW-based solutions show their superiority to the DFSIW-based circuits in terms of losses. The obtained phase errors and amplitude imbalances are comparable with the DFSIW-based phase shifters. Furthermore, the self-compensating principle helps reduce the electrical size.

Table 3.1 Comparison of different compensating phase shifters operating in Ka-band.

Phase shifter	f_0 (GHz)	ΔL (mm)	$\Delta\varphi$ (°)	Phase error (%)	AI max (dB)	IL max (dB)	Electrical size (λ_g^2)
SIW [38]	30	1	90.5 ± 2.5	2.8	0.2	0.8	1.18
SIW [39]	35	0	40.8 ± 2.6	6.4	/	1.5	1.14
Slow wave HM-SIW [40]	4.5	0	90.5 ± 3	3.3	0.5	1.6	0.2
AFSIW [8]	33	0	43 ± 6	14	0.43	0.52	1.1
90° EW-UEL	33.25	1.1	85.3 ± 4.8	5.6	0.2	0.69	0.85
90° UEW-EL	33.25	0	86.9 ± 6.7	7.7	0.21	0.57	0.58
45° UEW-EL*	28.25	0	45.3 ± 0.3	0.7	0.04	0.1	0.23

*: simulated results

3.2 Cruciform coupler

3.2.1 Overview

Together with phase shifter, coupler is an important building block in the coupling matrices and beamforming networks. There are many types of couplers including Riblet [5], [51], cruciform [52], Bethe hole [53], and Moreno [6] couplers among many others.

The Riblet short slot coupler is one of the most popular forms used at millimeter-wave frequencies due to its simplicity for design and small size. The idea of the Riblet coupler was presented for the first time in RWG technology reported in [54]. Using the SIW technology, the

Riblet coupler can provide a coupling level up to 5 dB [52]. In [51], 3-dB and 0-dB Riblet short slot couplers operating at 60 GHz were introduced as fundamental components in a 4×4 Butler matrix. The design methodology was introduced as well. The topology and simulated E-field distributions of the 3-dB coupler are given in Figure 3.20(*a*) [51].

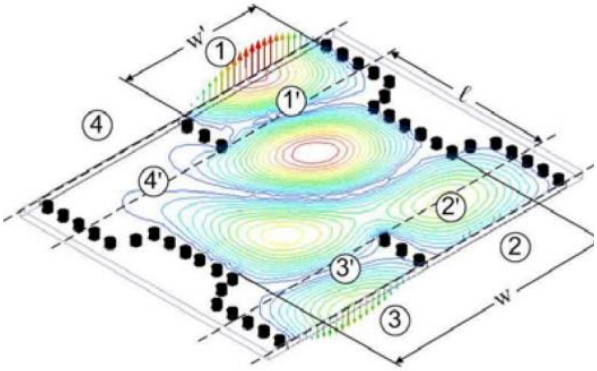

(*a*) [51]

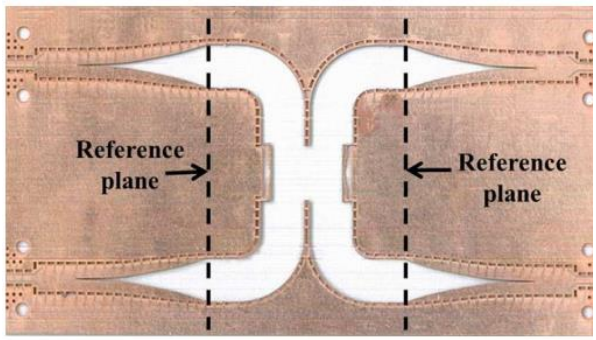

(*b*) [5]

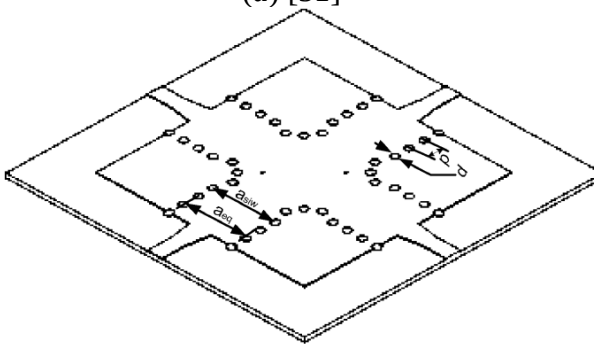

(*c*) [52]

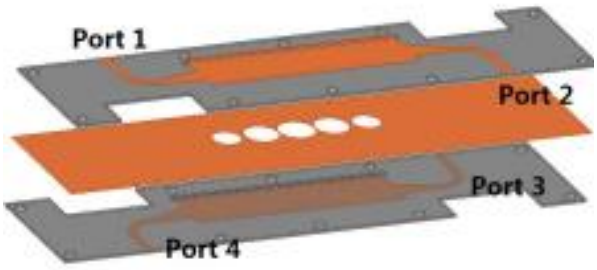

(*d*) [53]

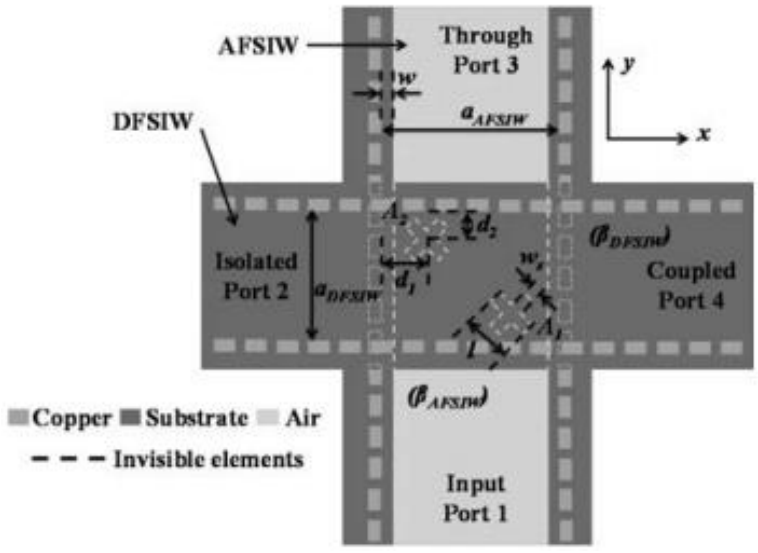

(*e*) [6]

Figure 3.20 Different type of couplers: (*a*) SIW Riblet coupler [51], (*b*) AFSIW Riblet coupler [5], (*c*) SIW cruciform coupler [52], (*d*) SIW Bethe hole coupler [53], and (*e*) AFSIW Moreno coupler [6].

In 2015, the Riblet coupler was realized in the AFSIW technological platform. A 3-dB coupler was demonstrated in Ka-band as topology shown in Figure 3.20(*b*) [5]. The obtained ±0.3 dB amplitude imbalance bandwidth is 11.8% centered at 34 GHz. The isolation is always better than -15 dB in this bandwidth. This AFSIW coupler presents 0.15 dB losses lower than the DFSIW counterpart having the same operating bandwidth.

Being an alternative to the Riblet coupler, the cruciform coupler was proposed for the first time in RWG technology [55]. The cruciform topology was implemented in SIW technology in [52] with a coupling capability of down to 7 dB. Its SIW-based topology is shown in Figure 3.20(*c*) [52]. A 3-dB coupler was demonstrated at the center frequency of 24 GHz. The measured ±0.5 dB amplitude imbalance bandwidth is 18% centered at 24 GHz. In this bandwidth, the measured isolation is better than -15 dB.

To further improve the operating bandwidth, the concept of half-mode SIW and Bethe hole coupler was investigated in a 3-dB coupler as topology shown in Figure 3.20(*d*) [53]. Thanks to this concept, an equal power splitting of 34.5% centered at 8.7 GHz was obtained with the variation of ±0.5 dB. In this equal amplitude bandwidth, the isolation level is better than 20 dB.

In order to obtain a weaker coupling level, especially for power monitoring applications, the Moreno coupler could be used. The first AFSIW-based Moreno coupler was introduced in 2016 as the topology shown in Figure 3.20(*e*) [6]. In this configuration, the top layer was benefited to implement the coupled port (port 4 in Figure 3.20(*e*)). The measurement results show a coupling level of 18.7 ± 1.3 dB together with an isolation level of 44.7 ± 13.7 dB over the entire Ka-band.

In the frame of this Ph.D. thesis, the cruciform coupler is chosen for development thanks to its compactness and wide coupling range. The cruciform coupler could be used in beamforming networks, especially in the Nolen matrix or Blass matrix thanks to its natural form that fits well with these coupling matrices [56].

3.2.2 SAFSIW cruciform coupler

The topology of the SAFSIW cruciform coupler is shown in Figure 3.21, where all dimensions are given in millimeters.

The center dielectric slab of 1.2 mm and the total width of 5.1 mm were chosen for implementation since they can give the optimum mono-mode bandwidth, as mentioned in 2.2.7. The coupling is mainly controlled by two metallic vias at the distance of d_r. Two dielectric arms

of 0.508 mm were implemented to maintain the stability of the center dielectric slab. At the input ports, inductive vias were added to improve the matching [57].

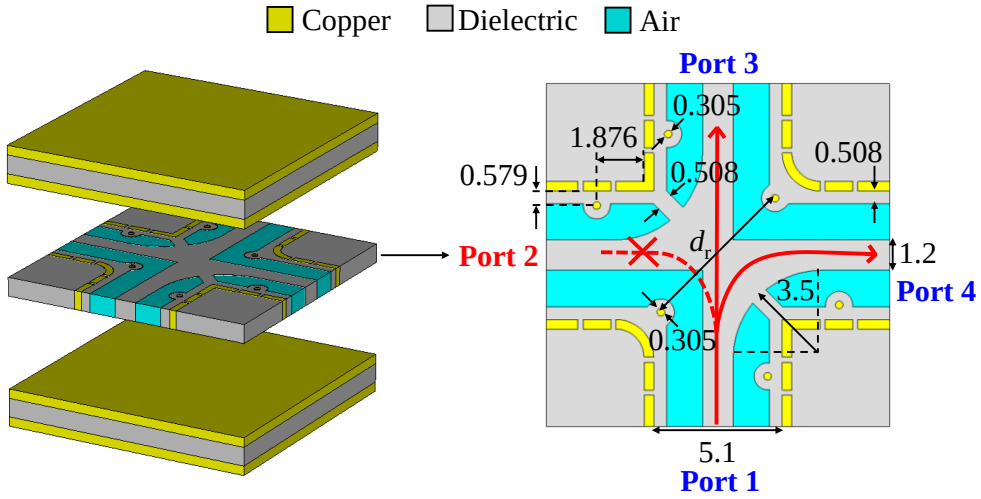

(*a*) (*b*)

Figure 3.21 The SAFSIW cruciform coupler: (*a*) 3D view and (*b*) top view of layer S2.

With reference to Figure 3.21, when port 1 is excited, the power is redirected to port 3 and coupled to port 4. Meanwhile, port 1 and port 2 are isolated. The circuit behaviors when exciting other ports are similar due to the symmetry.

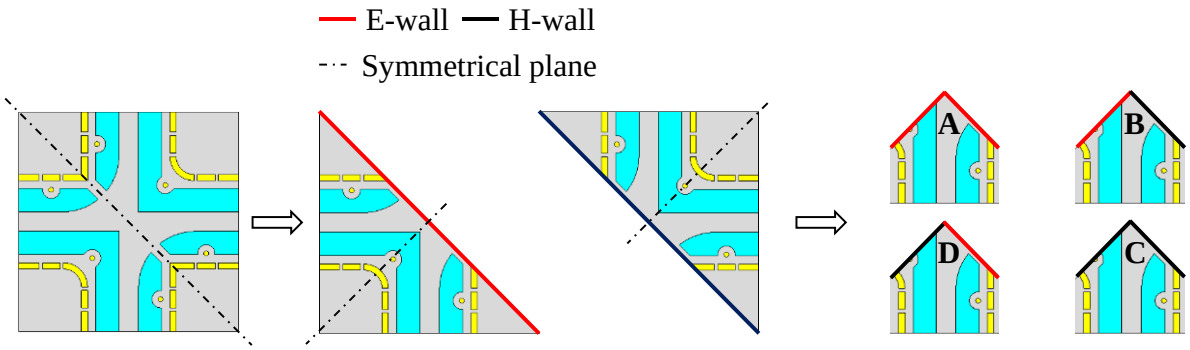

(*a*) (*b*) (*c*)

Figure 3.22 Decomposition procedure of cruciform coupler: (*a*) full structure, (*b*) two subcircuits, and (*c*) 4 subcircuits.

Also, thanks to the symmetry, the cruciform coupler can be designed by the odd-even mode decoupling approach as introduced in [58]. Based on that, the coupler can be decomposed into

4 subcircuits (A to D) as the procedure shown in Figure 3.22, where the symmetrical planes are decomposed into E-wall and H-wall.

According to the subcircuits in Figure 3.22(*c*), the scattering parameters of the full structure can be obtained by (39) to (42), where Γ_A, Γ_B, Γ_C, and Γ_D are the reflection coefficients of the subcircuits A, B, C, and D, respectively.

$$S_{11} = (\Gamma_A + \Gamma_B + \Gamma_C + \Gamma_D)/4 \tag{39}$$

$$S_{12} = (-\Gamma_A - \Gamma_B + \Gamma_C + \Gamma_D)/4 \tag{40}$$

$$S_{13} = (\Gamma_A - \Gamma_B + \Gamma_C - \Gamma_D)/4 \tag{41}$$

$$S_{14} = (-\Gamma_A + \Gamma_B + \Gamma_C - \Gamma_D)/4 \tag{42}$$

In comparison with the ideal scattering parameters of a 3-dB coupler given in (43), the conditions in (44) could be obtained, showing that the subcircuits A and B will generate the reflection coefficients with the same amplitude but out-of-phase. A similar phenomenon is observed for the subcircuits C and D.

$$[S] = -\frac{1}{\sqrt{2}}\begin{bmatrix} 0 & 0 & 1 & j \\ 0 & 0 & j & 1 \\ 1 & j & 0 & 0 \\ j & 1 & 0 & 0 \end{bmatrix} \tag{43}$$

$$\begin{cases} \Gamma_A = -\Gamma_B \\ \Gamma_c = -\Gamma_D \end{cases} \tag{44}$$

Using four subcircuits, all parameters are optimized to achieve the conditions in (44). For example, the effects of the distance d_r between the coupling vias are shown in Figure 3.23, where $d_r \approx 0.57\lambda_g$ is found to be satisfied the conditions in (44). The other parameters are optimized with a similar procedure. The final dimensions are given in Figure 3.21.

To verify the results obtained by the odd-even mode analysis, the scattering parameters calculated by (39) to (42) are compared to the simulated *S*-parameters of the full structure (Figure 3.22(*a*)) in Figure 3.24(*a*). It can be observed from Figure 3.24(*a*) that the odd-even mode analysis matches well with the full structure simulation. The simulated magnitude E-field distribution of the obtained coupler at 28 GHz is shown in Figure 3.24(*b*).

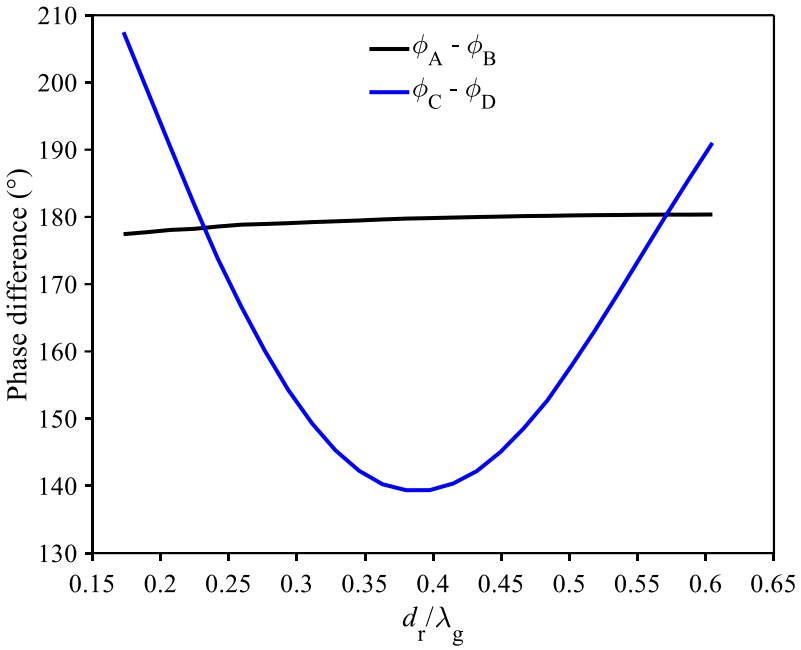

Figure 3.23 Effect of d_r on the phase difference between subcircuits A-B and C-D.

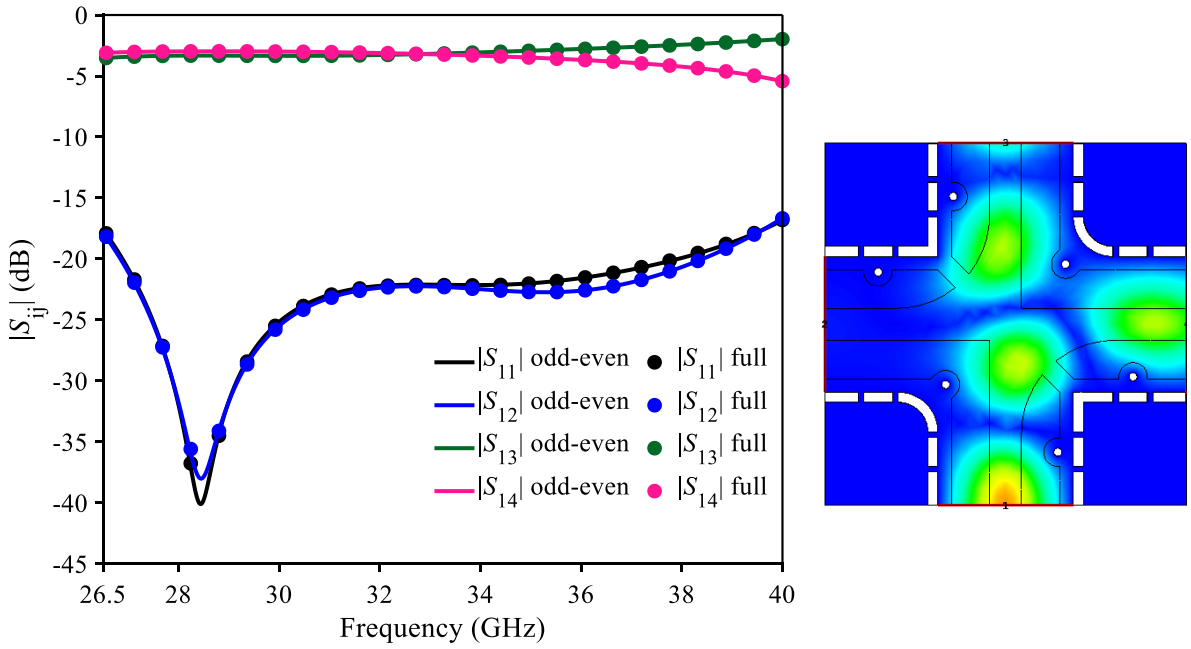

Figure 3.24 (*a*) Simulated *S*-parameters and (*b*) simulated magnitude E-field distribution at 28 GHz.

The SAFSIW cruciform coupler was fabricated as topology shown in Figure 3.25. In order to measure a four-port network using a two-port VNA, two terminations of 50Ω were used to terminate the unused ports. A SOLT calibration kit was used to de-embed the measured planes

with reference to the input of connectors (C-C’ and D-D’ in Figure 3.25). In the simulation, the effects of connectors were taken into account as well.

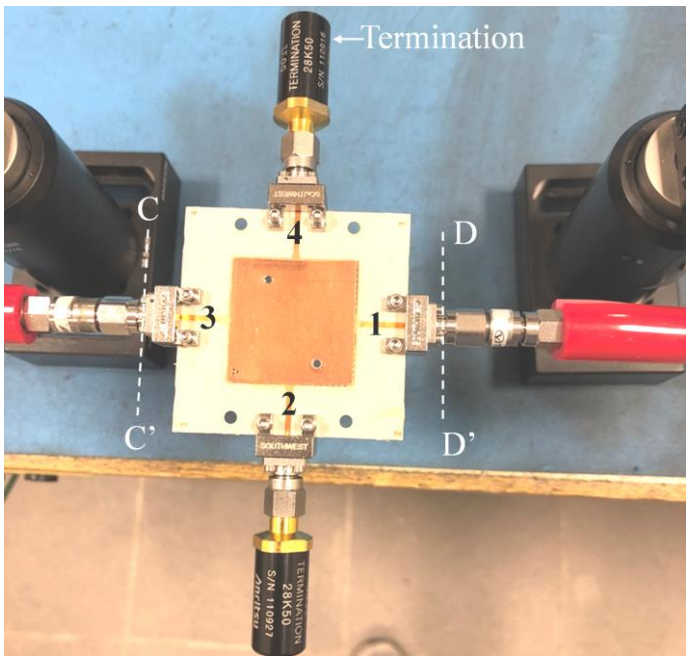

Figure 3.25 Fabricated prototype of SAFSIW cruciform coupler in measurement setup.

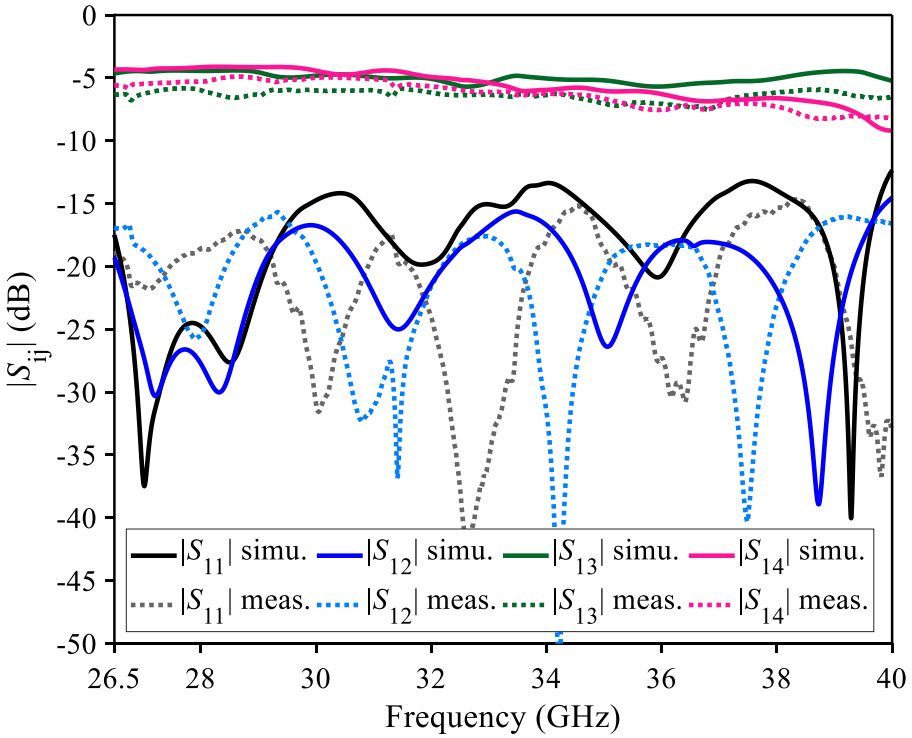

Figure 3.26 Simulated and measured *S*-parameters of the SAFSIW cruciform coupler.

The simulated and measured *S*-parameters are compared in Figure 3.26, exhibiting a good agreement. The differences that occurred between them are mainly attributed to manual assembling process errors as well as surface roughness that were not considered in the simulation. The measurement results show a reflection coefficient $|S_{11}|$ lower than -14.7 dB together with an isolation coefficient $|S_{12}|$ lower than -15.7 dB in the whole Ka-band. The ±0.5 dB amplitude imbalance of 9.9% centered at 34 GHz was obtained in measurement.

3.2.3 Conclusion

The SAFSIW cruciform coupler is proposed, designed with the aid of the odd-even mode decoupling technique, and demonstrated through measurement. The SAFSIW coupler is compared to some couplers found in the literature in Table 3.2.

It can be observed in this table that the proposed coupler presents a comparable equal splitting bandwidth compared to the couplers at millimeter-wave frequencies. Furthermore, the SAFSIW coupler presents the isolation level better than -15.7 dB over the entire Ka-band. This SAFSIW coupler can be used to develop a SAFSIW-based Nolen matrix in a beamforming network.

Table 3.2 Comparison of different SIW-based couplers.

Coupler	f_0 (GHz)	Equal splitting bandwidth (%)	Input reflection (dB) over frequency band (GHz)	Isolation (dB) over frequency band (GHz)
3-D DFSIW Riblet [59]	33.85	16.8	< -15 (31-36.7)	< -15 (31-36.7)
AFSIW Riblet [5]	34	11.8	< -15 (32-36)	< -15 (32-36)
SIW cruciform [52]	24	18	< -13 (22-26)	< -15 (22-26)
HM-DFSIW Bethe hole [53]	8.7	34.5	< -15 (6-10)	< -20 (7-10)
SAFSIW cruciform	34	9.9	< -14.7 (26.5-40)	< -15.7 (26.5-40)

CHAPTER 4 ANTENNA AND ANTENNA ARRAY

4.1 Overview on monopulse antenna

In tracking applications, monopulse antennas have shown their great potential due to single pulse application and accurate detection capability [60]. The general idea of monopulse antenna is shown in Figure 4.1. The monopulse antenna consists of two main parts: comparator (or monopulse feeding) and antenna (or radiator). The radiator is usually configured in an array form for high gain operation. When the sum port is excited, the sub-arrays will receive in-phase signals, which results in a sum beam radiation pattern (blue curve in Figure 4.1). When the delta port is excited, the sub-arrays will receive out-of-phase signals. The output radiation pattern has a null as indicated by the red curve in Figure 4.1 which is also called the difference beam.

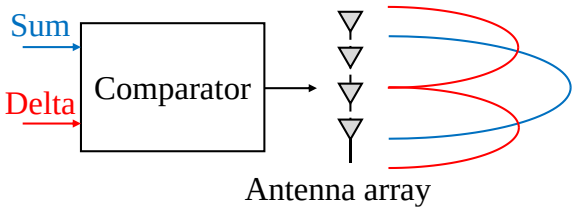

Figure 4.1 General idea of monopulse antenna.

Regarding the comparator, several techniques have been investigated to generate sum and delta signals including magic-tee [61]-[63], 180° hybrid coupler [47], [48], and coupling matrix [49], [50].

The magic-tee is one of the most common feeding techniques used in millimeter-wave monopulse antennas due to its compactness and good isolation between sum and delta ports. Nevertheless, because of the non-planar structure of the magic-tee, this type of feeding technique is usually implemented in metallic waveguides [62], [63].

In [61], the SIW technology was used to implement a monopulse antenna with the magic-tee feeding at 60 GHz. Direct transitions from metallic waveguide to the SIW power divider were used to serve as the delta port (port 2 in Figure 4.2(*a*)). Therefore, a single layer SIW could be used. However, the vertical transition using a metallic waveguide makes this solution bulky. With reference to this figure, port 1 is the sum port and port 2 serves as the delta port. This magic-tee was implemented into two types of monopulse using a 4 × 4 slot antenna array. The antenna configurations are shown in Figure 4.2(*b*). The configuration used in type A provide a

null depth (ND) in E-plane, meanwhile, the H-plane is possible in type B. In measurement reported in [61], type A exhibited a -10 dB bandwidth of 13.5% centered at 60.9 GHz and type B presented a -10 dB bandwidth of 14.2% centered at 61.15 GHz. The isolation between sum and delta ports is lower than -10 dB in the whole frequency band from 57 GHz to 65 GHz. At 60 GHz, both configurations offered ND levels less than -28 dB.

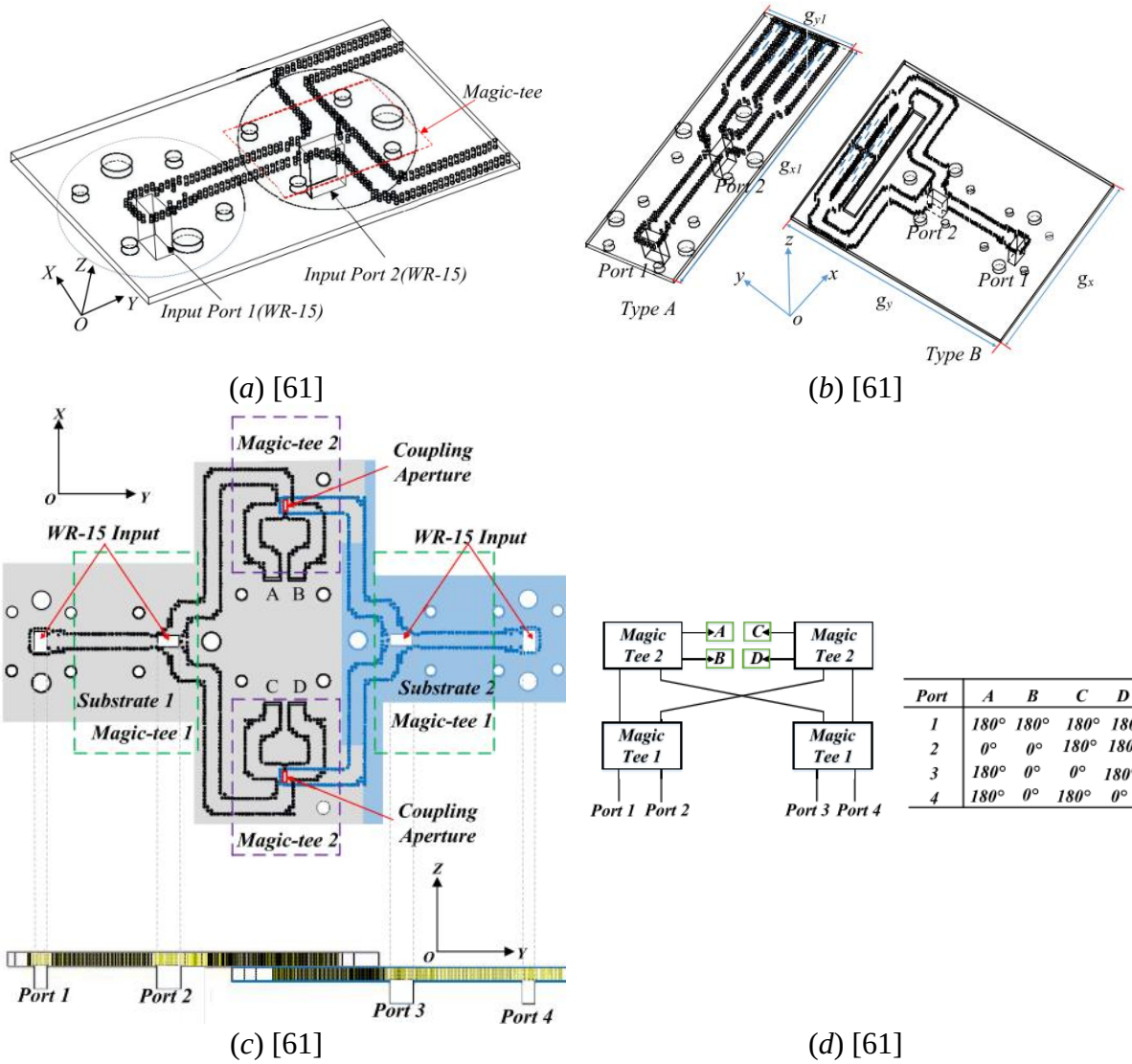

(*a*) [61] (*b*) [61]

(*c*) [61] (*d*) [61]

Figure 4.2 Monopulse antenna using magic-tee feeding: (*a*) single magic-tee [61], (*b*) 1D-scanning monopulse antenna using magic-tee [61], (*c*) 2D-scanning magic-tee feeding [61], and (*d*) circuit diagram and phase distributions of the 2D-scanning monopulse feeding using magic-tee [61].

In addition, four magic-tees were used to implement a comparator as shown in Figure 4.2(*c*) [61] to enable the 2D-scanning capability. This configuration is suitable for broadside scanning angles. Therefore, four 4 × 1 slot antenna arrays were connected to four outputs A-D in antenna

configuration. The circuit diagram and the phase distributions at outputs are presented in Figure 4.2(*d*) [61]. In measurement, a -10 dB bandwidth of 13.11% at the center frequency of 60.74 GHz was obtained. Moreover, the isolations between all ports were lower than -25 dB. A maximum ND of -31 dB was obtained in measurement when port 1 was excited.

Another possibility to implement the sum and delta ports using the SIW platform is to use a 90° coupler and a fixed 90° phase shifter to realize a 180° hybrid coupler as implemented in the topology shown in Figure 4.3(*a*) [47].

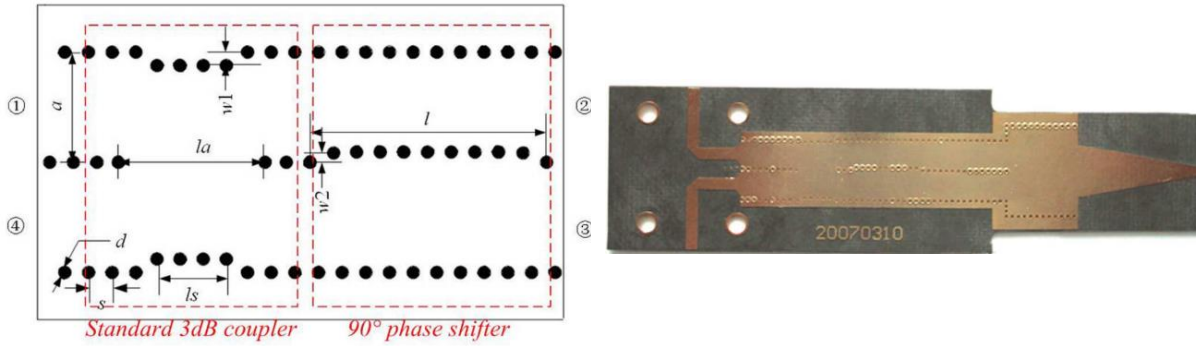

(*a*) [47] (*b*) [47]

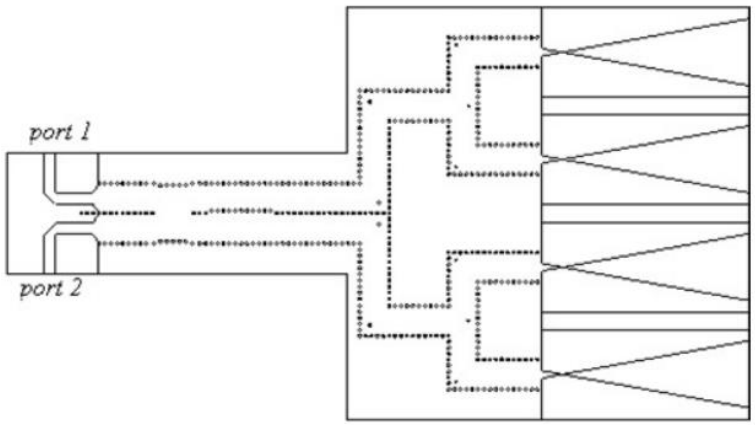

(*c*) [48]

Figure 4.3 Monopulse antenna using coupler and phase shifter: (*a*) the realization of the 180° coupler based on a 90° coupler and a 90° phase shifter, (*b*) single antenna implementation, and (*c*) antenna array implementation.

With reference to Figure 4.3(*a*), port 2 and port 3 are out-of-phase when port 1 is excited and is in-phase when port 4 is excited. This solution is simple and implementable using a single layer. Nevertheless, the operating bandwidth is limited by the coupler type and the fixed phase shifter.

In [47], a compensating phase shifter was implemented to improve the balance at outputs. The phase difference between outputs is maintained at ± 5° for both in-phase and out-of-phase excitation from 34.6 GHz to 37.3 GHz (7.5% centered at 35.95 GHz). A dual V-type tapered slot antenna (TSA) was used for the radiation part as implemented in the prototype shown in Figure 4.3(*b*). In measurement, a maximum gain of 10.6 dBi together with a half-power beamwidth (HPBW) of 22.5° was obtained at 36 GHz for the sum port. When the delta port was excited, a ND better than -35 dB was observed. Furthermore, the isolation between the sum and the delta port was maintained lower than -17.5 dB from 33 GHz to 40 GHz.

Instead of using a single antenna in [47], a linearly tapered slot antenna (LTSA) array could also be implemented to increase the gain as well as to reduce the antenna beamwidth as implemented in the topology shown in Figure 4.3(*c*) [48]. A phase imbalance of ± 5° was also obtained in [48] thanks to the compensating phase shifter. At 36.5 GHz, the measurement shows a maximum sum gain of 16.13 dBi, a HPBW of 7.2°, and a ND of -38.1 dB. The isolation between the sum and the delta ports is also maintained to be lower than -17.5 dB from 33 GHz to 40 GHz.

The 90° couplers and 90° phase shifters could also be implemented in a coupling matrix configuration as shown in Figure 4.4(*a*) [49], where ports 1-4 are inputs and port 5-6 are connected to antenna arrays. With reference to Figure 4.4(*a*), the normalized phase distributions at outputs are summarized in Figure 4.4(*b*). It can be observed in this figure that this configuration enables the difference pattern at the E-plane, H-plane, and diagonal planes at the expense of a larger and more complex feeding structure. The sum beam is obtained when port 2 is excited. Similar to the 2D-scanning using magic-tee in [61], this configuration is suitable for broadside scanning angle. Therefore, a slot antenna array was used in [49] for demonstration. In measurement, a maximum gain of 18.74 dBi was obtained at 31.5 GHz. A maximum ND of -46.3 dB was obtained in the H-plane at 31.25 GHz. In this work, phase shift was obtained by delay line which limits the output phase balance in a narrow band.

To improve the phase balance at outputs, compensating phase shifters were implemented into a coupling matrix for a monopulse antenna array operating at 94 GHz [50], whose topology is shown in Figure 4.4(*c*). In [50], the measurement results show a maximum sum gain of 25.21 dBi at 94 GHz. The corresponding ND of -27.97 dB was obtained in the H-plane when port 2 is excited.

Regarding the radiator, different types of antennas were used in the literature including the slot antenna array [49], [50], [61], the TSA [47], [48], and the horn antenna [64]. In fact, any type

of antenna could be used for the radiator as long as the radiated direction is consistent with and enabled by the feeding configuration.

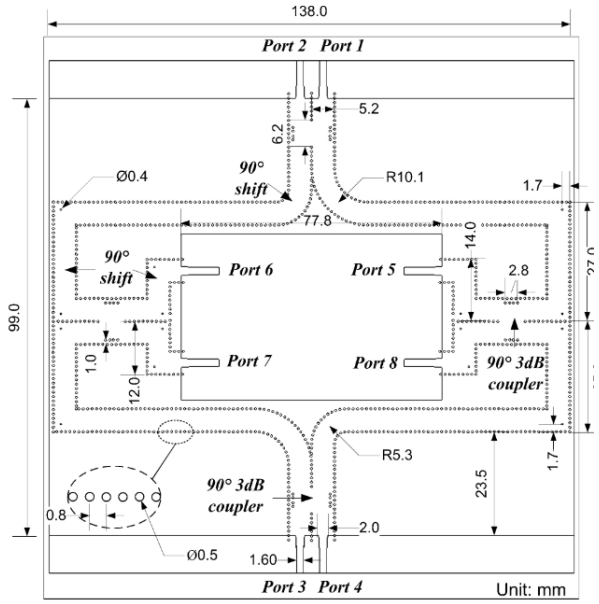

(*a*) [49]

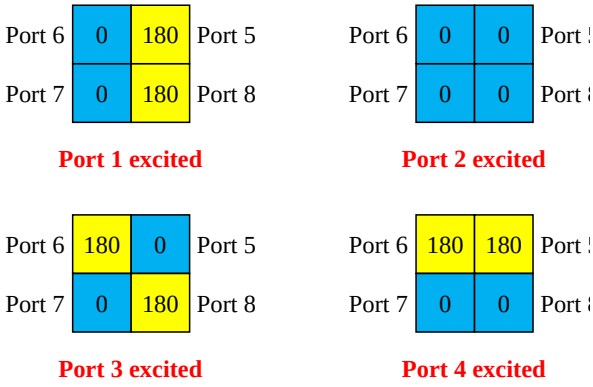

(*b*)

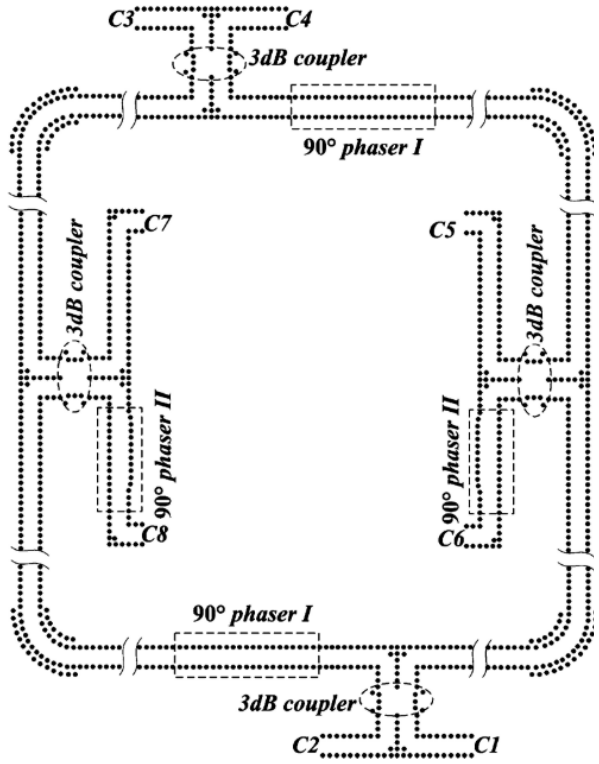

(*c*) [50]

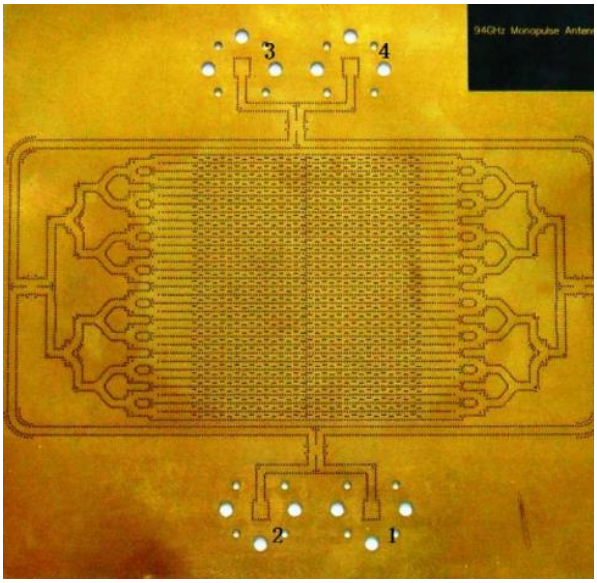

(*d*) [50]

Figure 4.4 Monopulse antennas based on coupling matrix: (*a*) coupling matrix with delay line, (*b*) phase distributions at outputs, (*c*) coupling matrix with compensating phase shifter, and (*d*) the fabricated prototype of monopulse antenna based on coupling matrix with compensating phase shifters.

In the frame of this Ph.D. thesis, the TSA is chosen for the radiator in the designed monopulse antenna due to its relatively flat and high gain. Furthermore, the TSA operating bandwidth can reach up to 10:1 or even more [65] thanks to the traveling wave operation mechanism.

Concerning the monopulse feeding, two configurations are introduced, namely the 180° hybrid coupler using compensating phase shifter and the magic-tee taking advantages of the AFSIW multilayer aspect.

4.2 Antipodal linearly tapered slot antenna

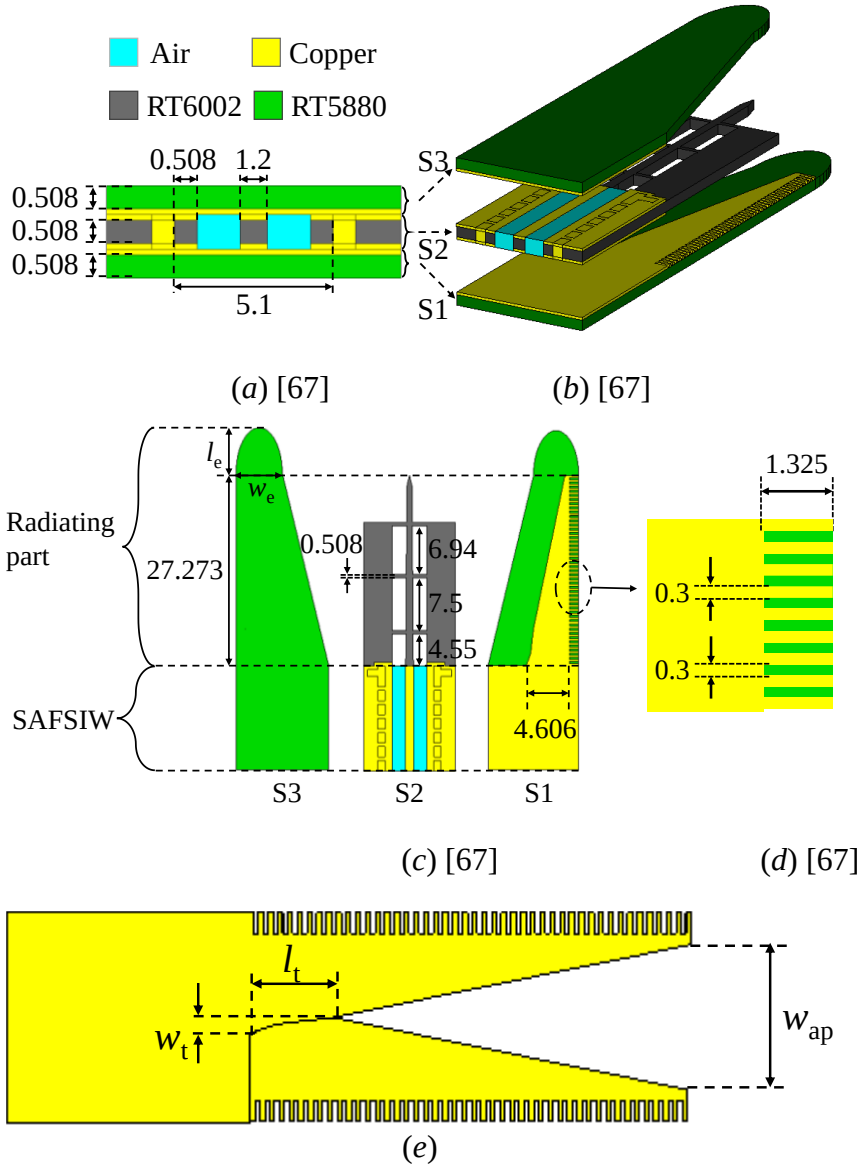

Figure 4.5 Structure of SAFSIW ALTSA: (*a*) cross-sectional view [67], (*b*) expanded 3D view [67], (*c*) expanded top view [67], (*d*) zoom-in view for the corrugation [67], and (*e*) illustration of the copper plates on top and bottom layers.

This section aims to develop a multilayer ALTSA. Since the ALTSA will be integrated with other multilayer circuits using the AFSIW or SAFSIW technology, the fabrication complexity is maintained. Although in [66], a multilayer AFSIW ALTSA was developed for applications in Ka-band with high efficiency, this antenna presents a high level of cross-polarisation (x-pol), which is not preferred for tracking applications. A low level of x-pol is desired to assume the purity of polarisation. Therefore, a new multilayer ALTSA was developed in the frame of this Ph.D. thesis. The proposed ALTSA is implemented based on the SAFSIW as shown in Figure 4.5 [67], where all parameters are given in millimeters.

The middle layer is made with RT6002 substrate of 0.508 mm thickness, meanwhile, the top and bottom layers are made of RT5880 substrate ($\varepsilon_r = 2.2$, $\tan\delta = 0.0009$) of 0.508 mm thickness. The RT5880 is chosen for the top and bottom layers as they will be used to implement the delta-port in magic-tee feeding which will be shown in section 4.4. The RT5880 helps reduce dielectric loss. Moreover, the copper plates on top of layer S3 and bottom of layer S1 are removed to prevent parallel plate modes. The center dielectric slab is extended in the radiating part (Figure 4.5(*c*) [67]) to rotate the radiated electrical field to reduce the x-pol level.

In the radiating part, the electrical field distribution without and with the center dielectric slab is shown in Figure 4.6.

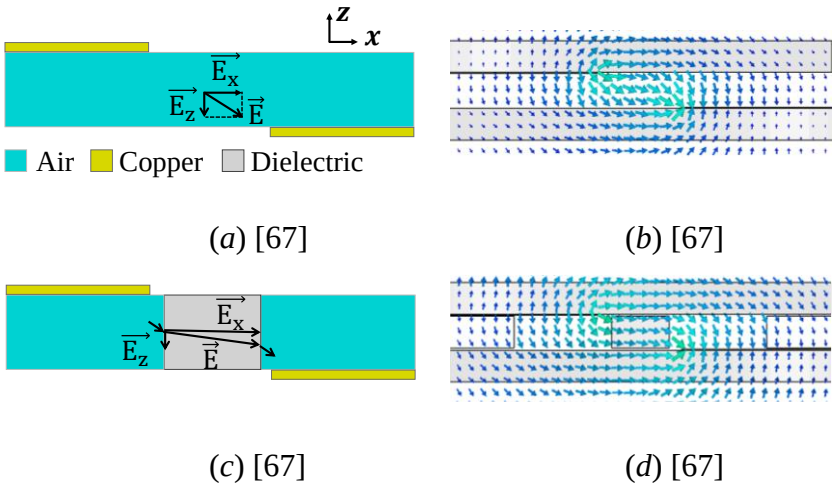

Figure 4.6 Distribution in the radiating part of (*a*) electrical field line in the air, (*b*) simulated electrical field at 33 GHz without center dielectric slab, (*c*) electrical field line at the presence of center dielectric slab, and (*d*) simulated electrical field at 33 GHz with center dielectric slab [67].

An electrical field line propagating between two copper plates in ***xz***-plane can be decomposed into ***x***- and ***z***-elements (Figure 4.6(*a*) and (*c*)). The elementary vector in ***x***-direction contributes

to the co-polarisation (co-pol) meanwhile the elementary vector in ***z***-direction contributes to the x-pol. At the presence of the center dielectric slab, the electrical field is rotated as can be observed in Figure 4.6(*c*) and (*d*). With a relative permittivity higher than 1, the center dielectric slab helps reduce the ***z***-elements, hence, decrease the x-pol level.

The SAFSIW ALTSA can be designed by the following steps:

- Step 1: SAFSIW feeding part. Based on the analytical equation (6) to (9) in Chapter 2, the dimensions of the SAFSIW can be calculated. In this work, an SAFSIW structure with a total width of 5.1 mm and a center dielectric slab width of 1.2 mm was chosen to operate at the optimum mono-mode bandwidth (as it was mentioned in 2.2.7). The obtained cutoff frequency for the dominant mode is 21.2 GHz.
- Step 2: Length of radiating part. It is recommended in [68] that its length should be at least $3\lambda_0$, where λ_0 is the free-space wavelength at the center frequency. In this work, the copper plate is tapered to the length of 27.273 mm ($3\lambda_0$ at 33 GHz).
- Step 3: Open aperture. In [65], it is recommended that the open aperture w_{ap} (Figure 4.5(*e*)) should be greater than $\lambda_L/2$, where λ_L is the free-space wavelength corresponding to the lowest operating frequency. The Ka-band is chosen for this work with the lowest operating frequency of f_L = 26.5 GHz. Therefore, the condition for the open aperture is $w_{ap} > 150/26.5 \approx 5.66$ (mm).
- Step 4: Corrugation. The copper plates are etched to create a corrugation structure as can be seen in Figure 4.5(*d*). It is suggested in [69] that the length of the corrugation should be about $\lambda_d/4$, where λ_d is the dielectric wavelength at the center frequency f_0. The corrugation technique helps increase the effective antenna aperture [69].
- Step 5: The center dielectric slab is extended with a length equal to the tapered copper plates ($3\lambda_0$ in this case). To prevent the extended dielectric slab from variability, dielectric arms of width 0.508 mm are used to fix the position of the slab.
- Step 6: Optimize the transition (l_t and w_t in Figure 4.5(*e*)). This transition aims to rotate the vertical electric field in the SAFSIW feeding part into the radiative horizontal electrical field in the radiating part.
- Step 7: Optimize compensating part (l_e and w_e in Figure 4.5(*c*)). This part is used to compensate for the output electromagnetic phase.

After optimization, the final parameters are w_{ap} = 5.862 mm, l_e = 4.931 mm, w_e = 4.931 mm, l_t = 5.19 mm, and w_t = 1 mm.

A simulation study was carried out to highlight the interest of the proposed antenna on the reduction of x-pol. Two SAFSIW ALTSAs are simulated: with and without the extended center dielectric slab. The SAFSIW ALTSA without the extended center dielectric slab is shown in Figure 4.7. It is obtained from the proposed SAFSIW ALTSA by removing the extended center dielectric slab and dielectric arms.

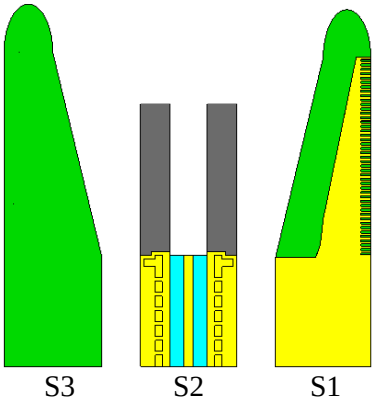

Figure 4.7 SAFSIW LTSA without extended center dielectric slab.

The normalized radiation patterns of these two SAFSIW ALTSAs are compared in Figure 4.8, where a reduction of 13.4 dB for x-pol can be observed in both E- and H-planes by using the extended center dielectric slab. The obtained maximum gain of the proposed antenna is slightly reduced (0.58 dB) due to losses in the extended center dielectric slab. However, this reduction is very small compared to the improvement of the isolation between co-pol and x-pol.

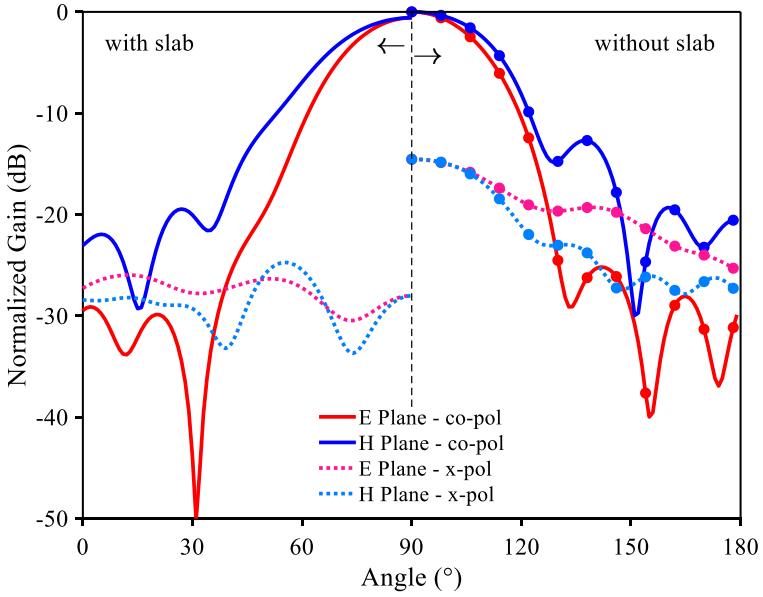

Figure 4.8 Comparison between two SAFSIW ALTSAs [67].

For demonstration, transitions from SAFSIW to DFSIW then to GCPW were implemented for measurement purposes. The fabricated prototype is shown in Figure 4.9 [67].

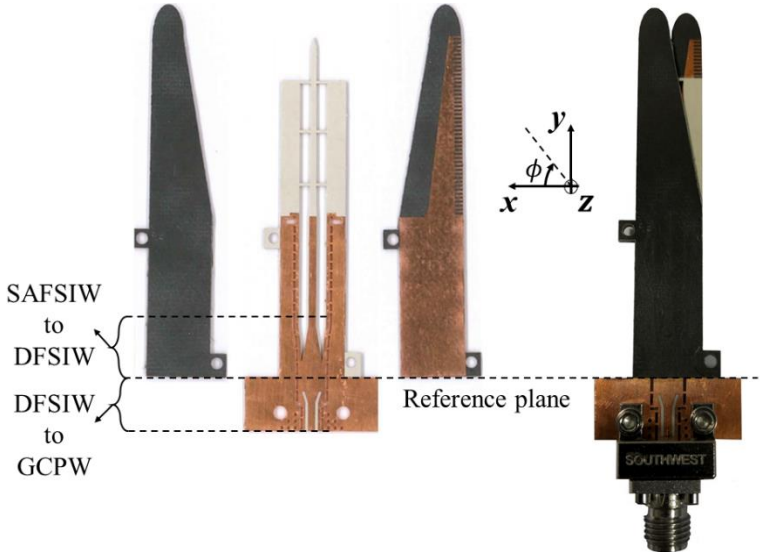

Figure 4.9 Fabricated prototype of the SAFSIW ALTSA: (*a*) top view of layer S3, (*b*) top view of layer S2, (*c*) top view of layer S1, and (*d*) the assembled antenna [67].

In measurement, a TRL calibration kit was used to remove the effect of the GCPW to DFSIW transition. The reference plane is shown in Figure 4.9. The simulated and measured reflection coefficients $|S_{11}|$ at this reference plane are compared in Figure 4.10 [67]. A good agreement is obtained. In measurement, a maximum reflection coefficient of $|S_{11}|$ = -17 dB was observed over the entire Ka-band.

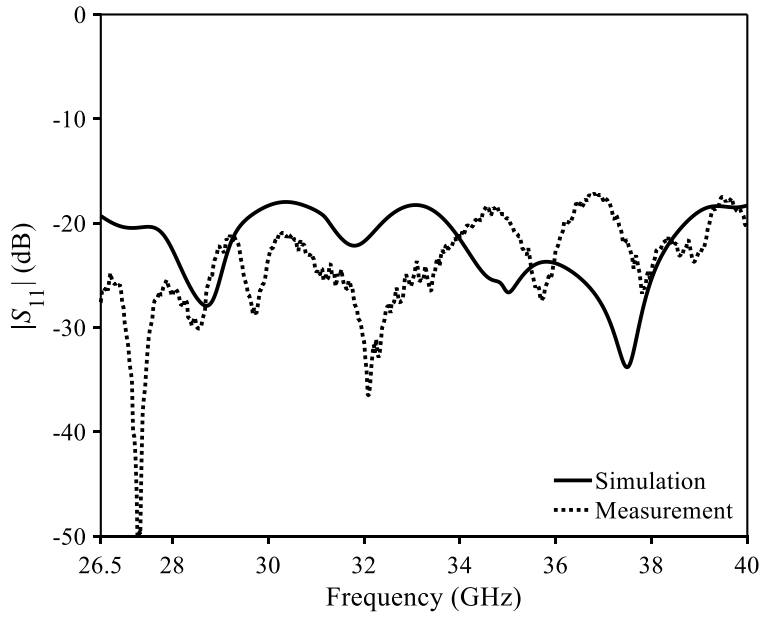

Figure 4.10 Simulated and measured $|S_{11}|$ of the SAFSIW LTSA [67].

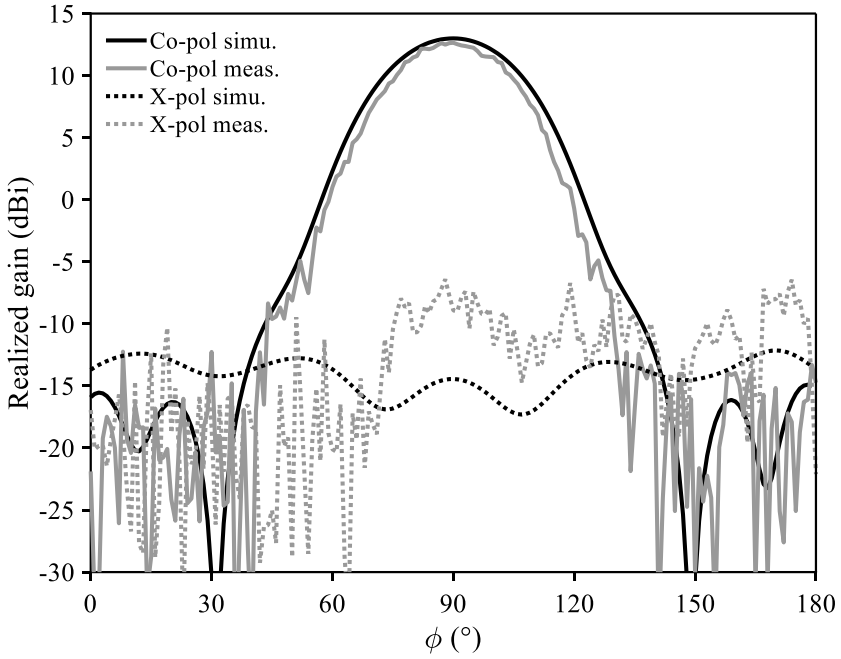

Figure 4.11 Simulated and measured radiation pattern in E-plane at 33 GHz [67].

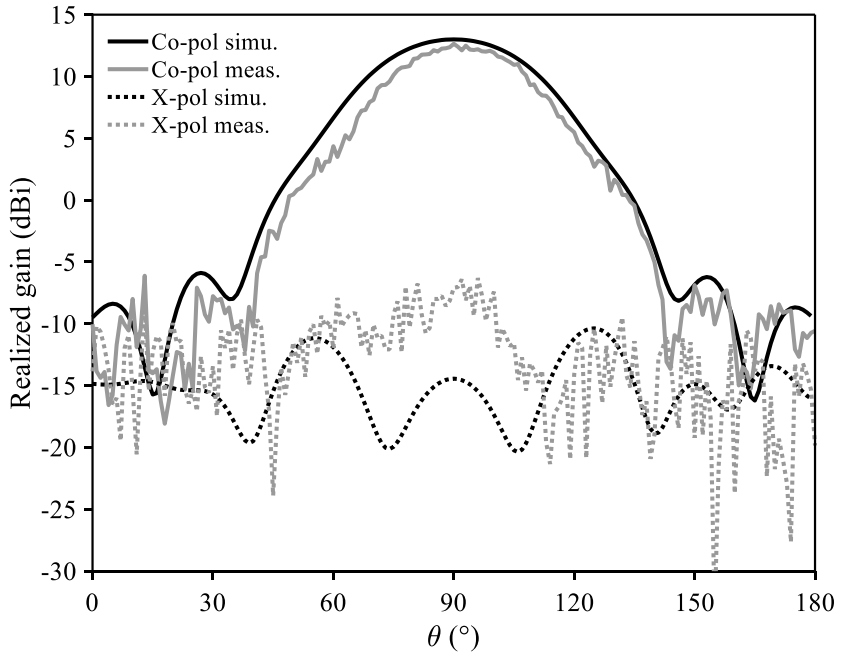

Figure 4.12 Simulated and measured radiation pattern in H-plane at 33 GHz [67].

Regarding the radiation pattern in the E-plane (***xy***-plane), Figure 4.11 [67] compares the simulated and measured results at 33 GHz. Again, a good agreement is obtained. The fluctuations observed in measurement are attributed to the low dynamic range in the measurement setup. Power amplifiers and low noise amplifiers were not available to

compensate for the losses over such high frequency ranges. A maximum measured gain of 12.65 dBi is obtained at the end-fire direction compared to 13 dBi in simulation. The degradation of 0.35 dB observed in measurement is mainly caused by a female-to-female adapter and a 90° connector used in measurement. Both were not considered in the simulation. In the HPBW angle, the measured isolation between co-pol and x-pol is greater than 19 dB.

Similar effects can be observed in the H-plane (***yz***-plane) at 33 GHz as presented in Figure 4.12 [67]. In the HPBW region, the measured isolation level between co-pol and x-pol is greater than 18.96 dB.

A broadband measurement was carried out to determine the maximum gain at end-fire direction over the entire Ka-band. The simulated and measured realized gains are compared in Figure 4.13 [67] with the simulated radiation efficiency. It can be seen in Figure 4.13 that the simulated and measured results are in good agreement. A maximum gain of 13 ± 1.35 dBi was obtained in measurement. Again, the differences between simulation and measurement are due to a low dynamic range. Over the entire Ka-band, the simulated radiation efficiency is better than 90%. High efficiency was obtained thanks to the AFSIW-based structure.

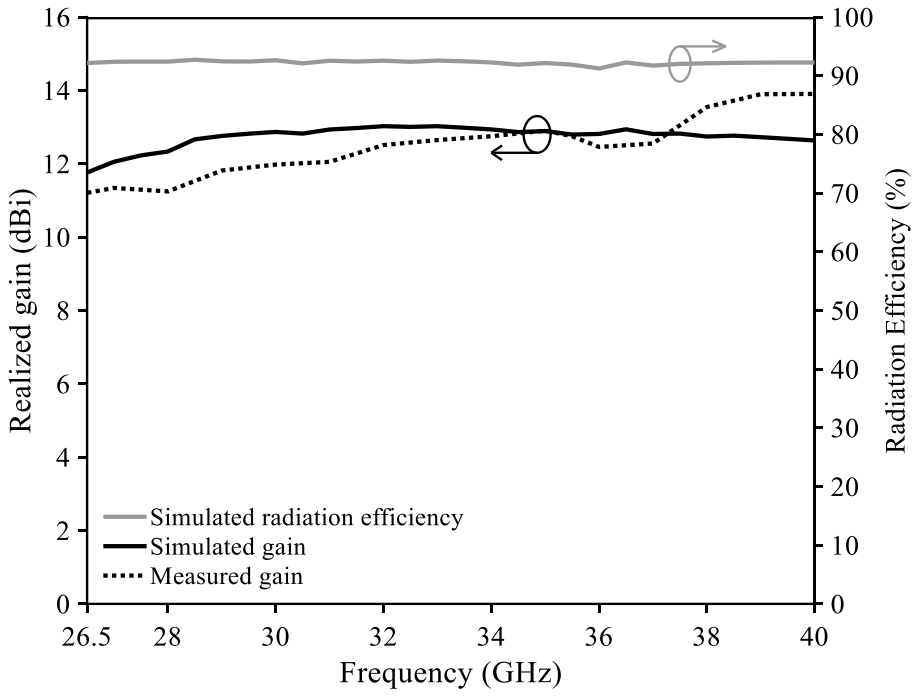

Figure 4.13 Simulated and measured maximum gain and simulated radiation efficiency [67].

Concerning the isolation level between co-pol and x-pol, Figure 4.14 compares the simulated and measured results obtained at the end-fire direction [67]. Over the whole Ka-band, the

measured isolation level is better than 16.07 dB. The variation observed in measurement is due to the limitation in dynamic range.

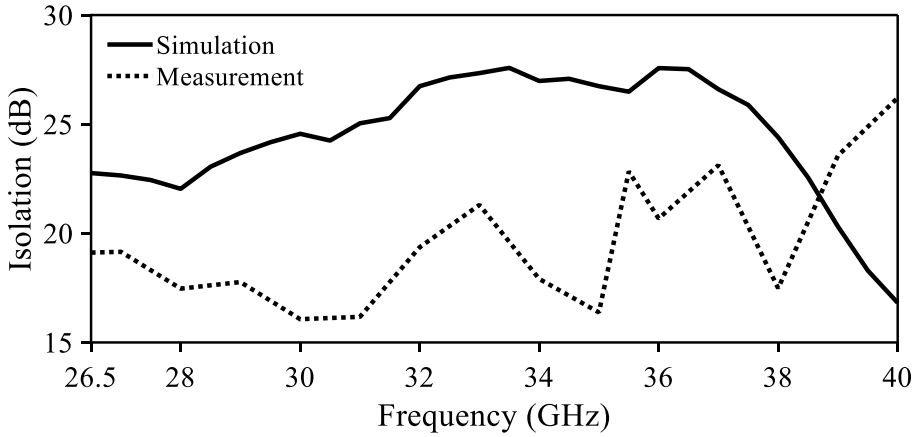

Figure 4.14 Simulated and measured isolation level between co-pol and x-pol at the end-fire direction [67].

To summarize, the superiority of the proposed SAFSIW ALTSA compared to the AFSIW ALTSA reported in [66] is emphasized. Table 4.1 compares the different performance characteristics between these two AFSIW-based ALTSAs, where the x-pol is considered in the HPBW region [67].

Table 4.1 Comparison of different AFSIW-based ALTSAs [67]

	AFSIW ALTSA in [66]	Proposed SAFSIW ALTSA
Number of layers	3	3
Metallization of the taper	YES	NO
Radiating length (mm)	34.3	32.2
HPBW in E-plane (°)*	39	30
HPBW in H-plane (°)*	56	35
Maximum gain (dBi)*	11.7	12.75
X-pol (dB)*	-8.5	< -15.53
Simulated radiation efficiency (%)*	99.4	91.9

*: data given at 35.5 GHz

It can be observed from Table 4.1 that the proposed SAFSIW ALTSA helps reduce the x-pol level (more than 7 dB at 35.5 GHz) without increasing the fabrication complexity. The radiation

efficiency of the proposed antenna is less than the AFSIW counterpart due to losses in the center dielectric slab. Still, it is always higher than 90%. Moreover, the SAFSIW ALTSA gives a higher gain with a shorter radiating length compared to the AFSIW antenna thanks to the narrower HPBW obtained by the corrugation technique [69]. Therefore, this proposed antenna is used to implement the mono-pulse antenna presented in the following sections.

4.3 Monopulse antenna using 180° hybrid coupler

In the first investigation, the idea of the 180° hybrid coupler based on a 90° coupler and a compensating phase shifter is chosen. The self-compensating UEW-EL phase shifter presented in 3.1.2.2 is chosen for the implementation.

The topology of the monopulse antenna using the 180° hybrid coupler (monopulse 1) is shown in Figure 4.15.

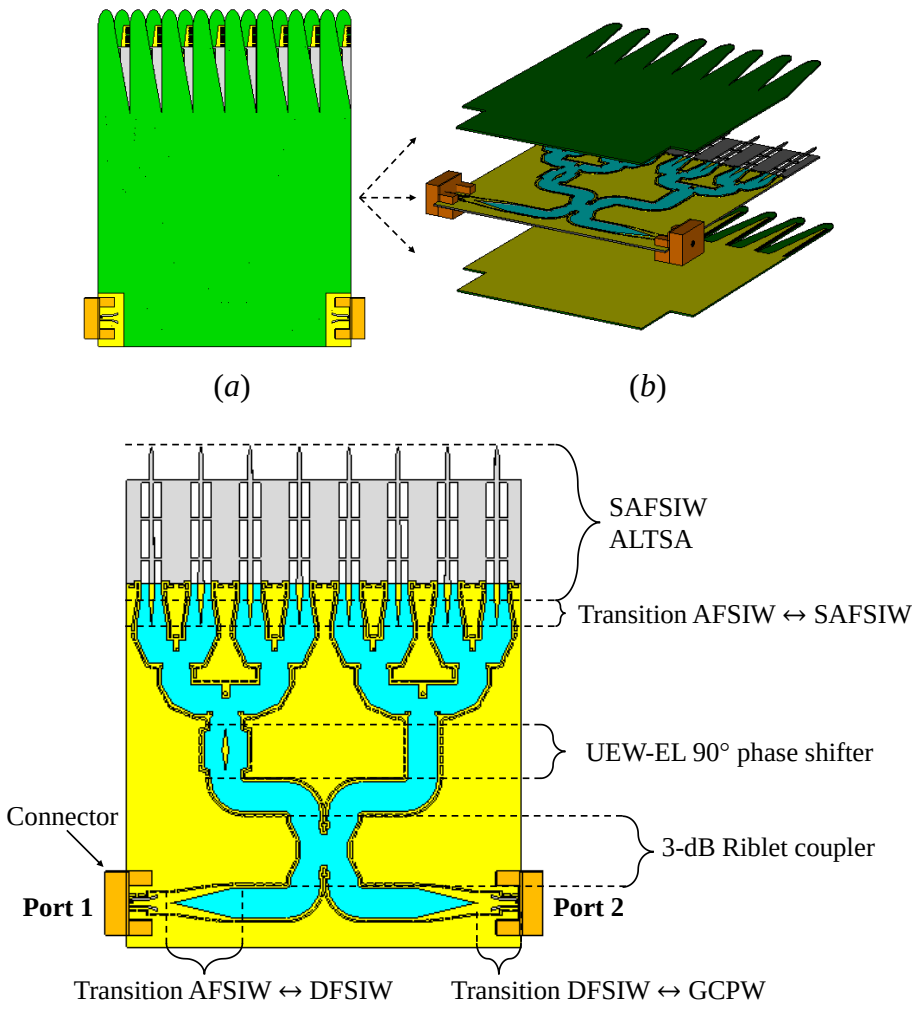

Figure 4.15 Topology of monopulse 1: (*a*) top view of the completed circuit, (*b*) expanded 3D view, and (*c*) top view of layer S2.

The top and bottom layers are symmetrical about the middle layer. With reference to Figure 4.15(*c*), port 1 will generate the in-phase signals and port 2 will generate the out-of-phase signal.

The elementary SAFSIW ALTSA is connected to the AFSIW feeding network by a transition from SAFSIW to AFSIW. This transition is designed based on the procedure presented in 2.2.6.1 to maintain the cutoff frequency at 21.2 GHz. For measurement purposes, transitions from AFSIW to DFSIW, then to GCPW, are implemented.

This work aims to develop a monopulse antenna array operating around 36 GHz. A broadband monopulse is not targeted. Therefore, the 3-dB Riblet coupler is chosen for the implementation due to its simplicity of analysis. Other types of couplers could be used to increase the operating bandwidth such as the multi-hole coupler, but at the expense of a longer footprint. This Riblet coupler is detailed in Figure 4.16 together with the simulated E-field distribution at 36 GHz, where all parameters are given in millimeters.

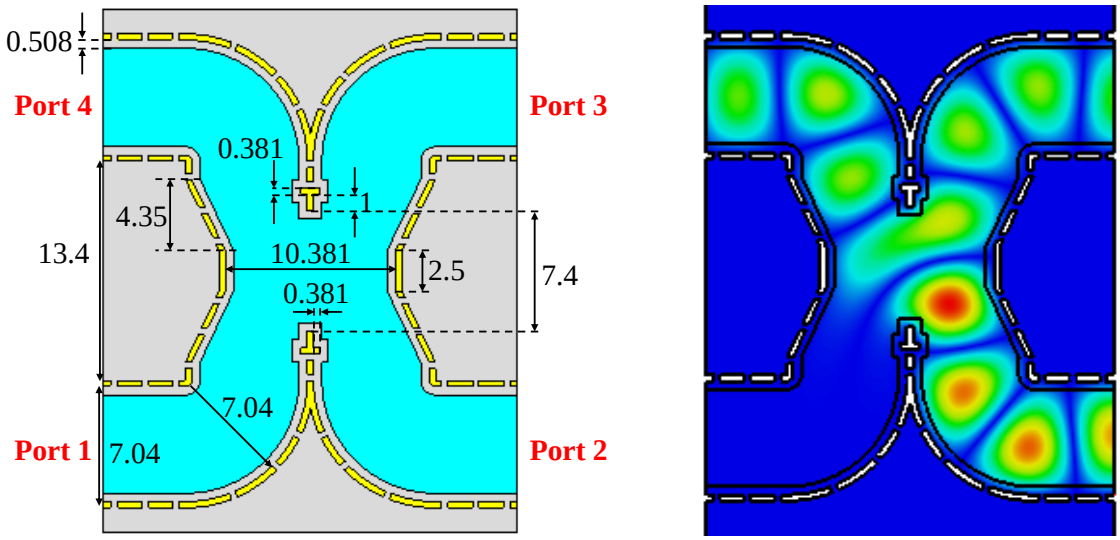

(*a*) (*b*)

Figure 4.16 3-dB Riblet coupler used in the monopulse 1: (*a*) top view of layer S2 and (*b*) simulated magnitude E-field at 36 GHz.

This type of coupler is well developed and analyzed in literature such as in [54] for metallic waveguide and in [51] for SIW. Therefore, the design of this Riblet coupler will not be mentioned. The simulated *S*-parameters and the E-field magnitude at 36 GHz when port 2 is excited are shown in Figure 4.17.

Due to the symmetry, the scattering parameters when other ports are excited will not be mentioned. An equal power splitting of 3.17 ± 0.5 dB is observed from 32.51 GHz to

39.45 GHz (19.3% centered at 35.98 GHz). Furthermore, both reflection coefficient $|S_{22}|$ and isolation coefficient $|S_{12}|$ are lower than -20 dB from 33.7 GHz to 38.67 GHz.

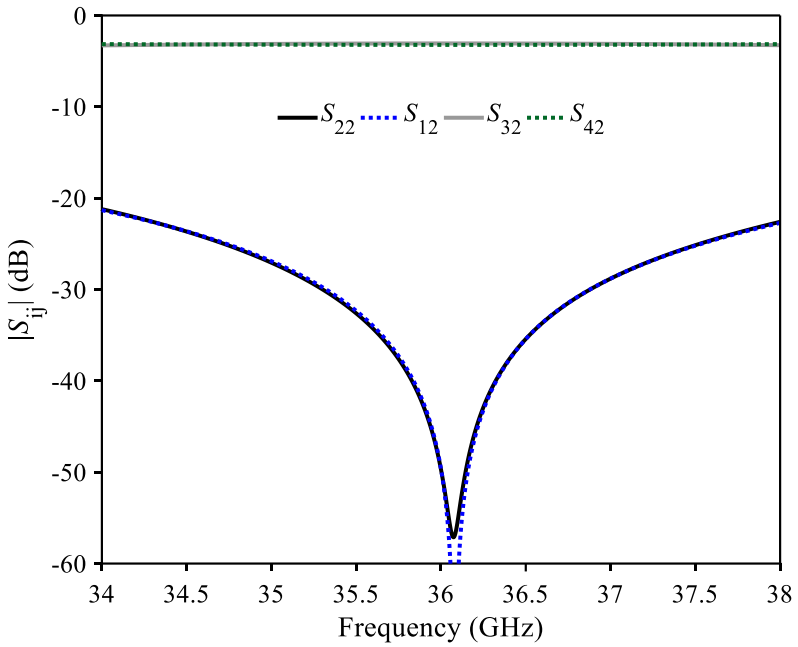

Figure 4.17 Simulated *S*-parameters of the 36 GHz AFSIW Riblet Coupler.

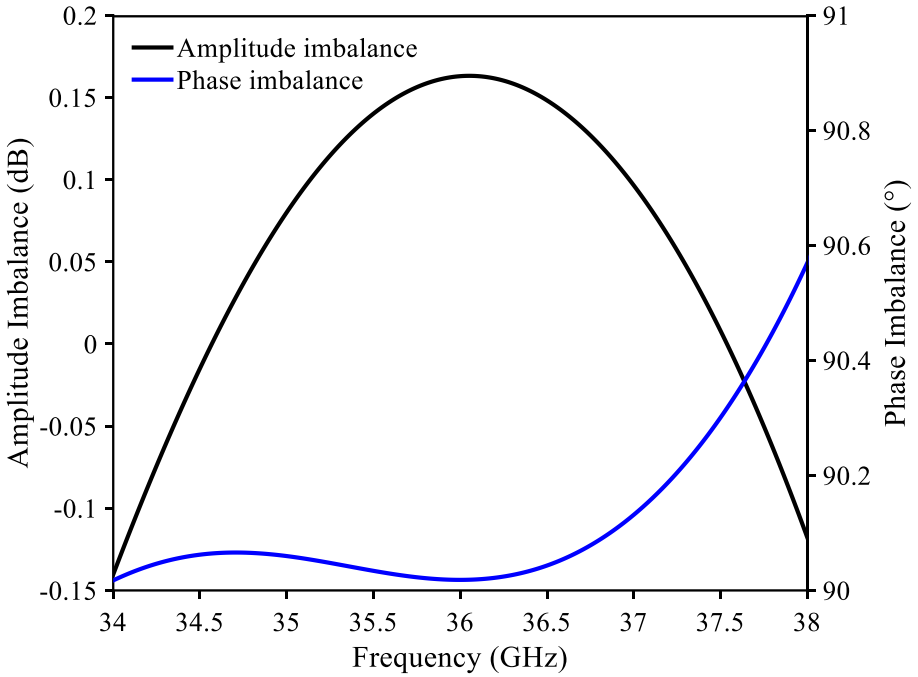

Figure 4.18 Simulated amplitude imbalance and phase imbalance between port 3 and port 4 of the AFSIW Riblet coupler when port 2 is excited.

The simulated amplitude imbalance (AI = $|S_{32}| - |S_{42}|$) and phase imbalance (PI = $\varphi(S_{32}) - \varphi(S_{42})$) when port 2 is excited are shown in Figure 4.18. An amplitude imbalance

of AI = 0.01 ± 0.15 dB and a phase imbalance of PI = 90.3° ± 0.3° are obtained in simulation from 34 GHz to 38 GHz.

The implementation of the 90° UEW-EL phase shifter with the 36 GHz Riblet coupler is shown in Figure 4.19 together with the simulated E-field at 36 GHz when port 1 or port 2 is excited. It can be observed in Figure 4.19(*b*) that two in-phase signals are obtained when port 1 is excited. On the contrary, two out-of-phase signals are obtained when port 2 is excited.

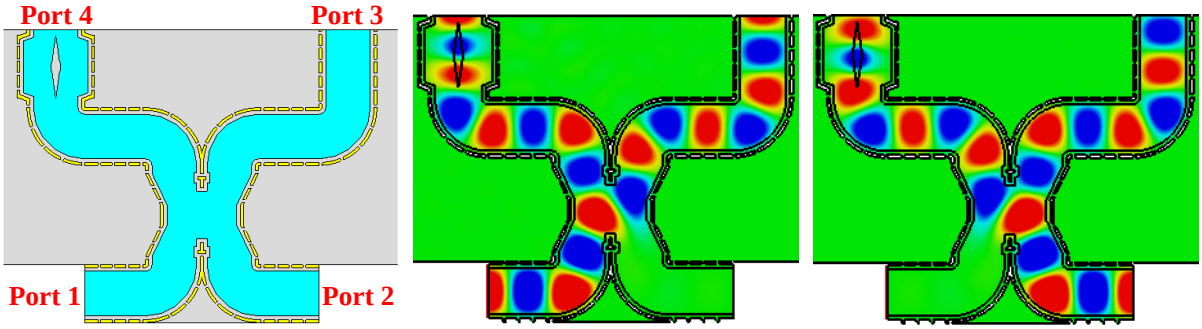

Figure 4.19 180° hybrid coupler using the 36 GHz Riblet coupler and the 90° UEW-EL phase shifter: (*a*) top view of layer S2 and simulated magnitude E-filed at 36 GHz when (*b*) port 1 is excited and (*c*) port 2 is excited.

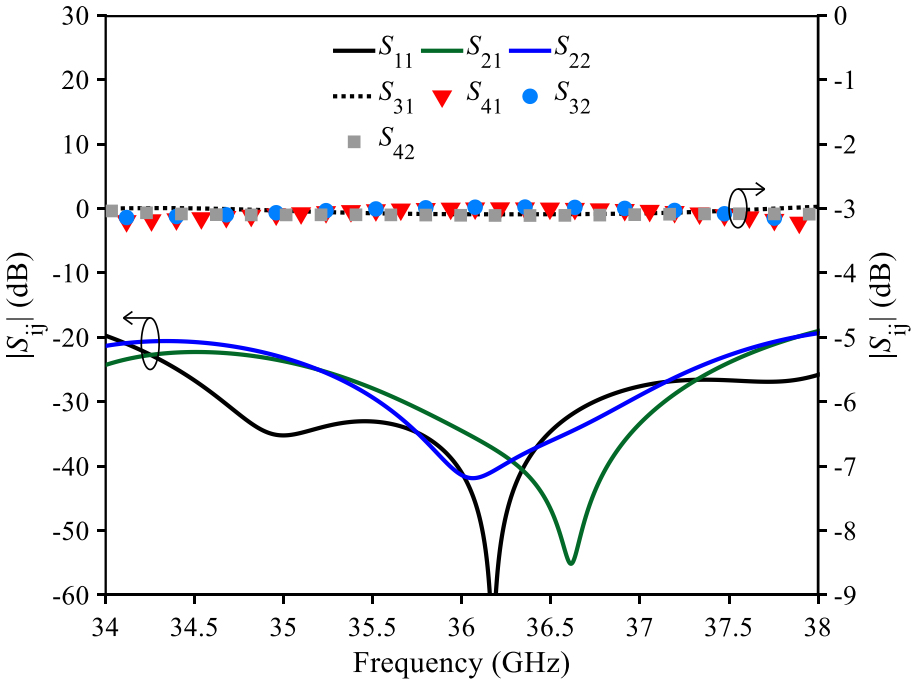

Figure 4.20 Simulated *S*-parameters of the 180° hybrid coupler.

The simulated *S*-parameters of the 180° hybrid coupler are shown in Figure 4.20. It can be observed in Figure 4.20 that the coupling and the directivity is around 3 dB. From 34 GHz to

38 GHz, the simulated reflection coefficients at port 1 and port 2 as well as the isolation between port 1 and port 2 are lower than -19 dB.

The simulated amplitude imbalance (AI = $|S_{3i}|$ - $|S_{4i}|$) and phase imbalance (PI = $\varphi(S_{3i})$ - $\varphi(S_{4i})$) when port i^{th} is excited are shown in Figure 4.21. When port 1 is excited, the simulated AI is lower than 0.28 dB and the simulated PI is within ± 3.1° from 34 GHz to 38 GHz. At 36 GHz, PI = -0.4° was obtained in the simulation. When port 2 is excited, the simulated AI is within ± 0.13 dB while a PI = 180.4° ± 3.7° was obtained. The simulated PI is 179.6° at 36 GHz. From the results shown above, port 1 will generate the in-phase signals and the port 2 will generate the out-of-phase signals.

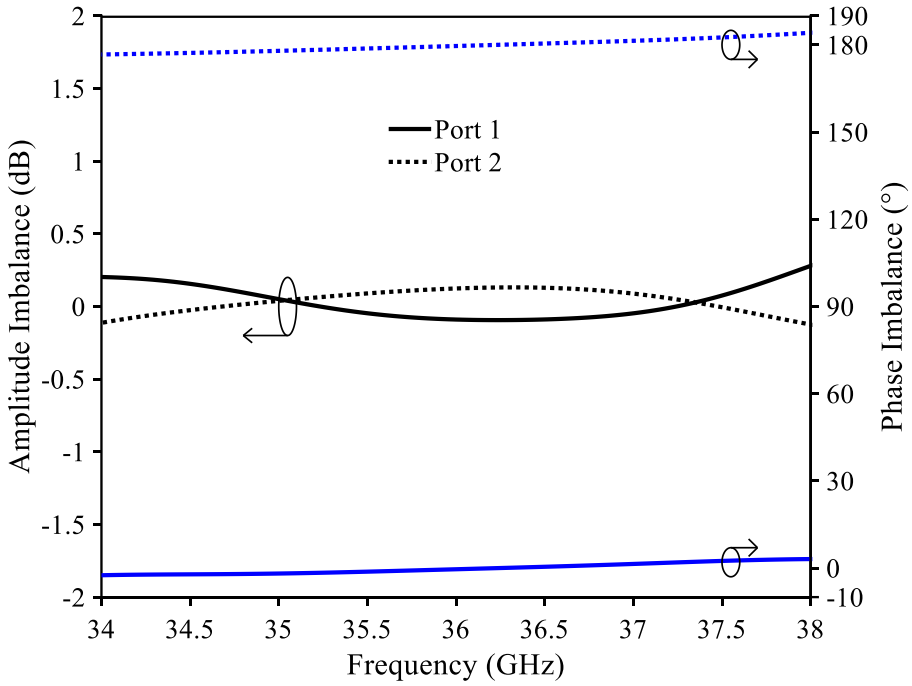

Figure 4.21 Simulated AI and PI of the 180° hybrid coupler.

All the elements are integrated into the monopulse antenna as illustrated in Figure 4.15. The simulated *S*-parameters of this monopulse antenna are shown in Figure 4.22. The simulation was carried out with connectors.

It can be observed in Figure 4.22 that the reflection coefficients at the two input ports are lower than -13.8 dB while the isolation between two input ports is lower than -18.7 dB over the whole frequency band from 34 GHz to 38 GHz. At 36 GHz, both $|S_{11}|$ and $|S_{22}|$ are lower than -22 dB and the isolation $|S_{21}|$ is lower than -38.9 dB.

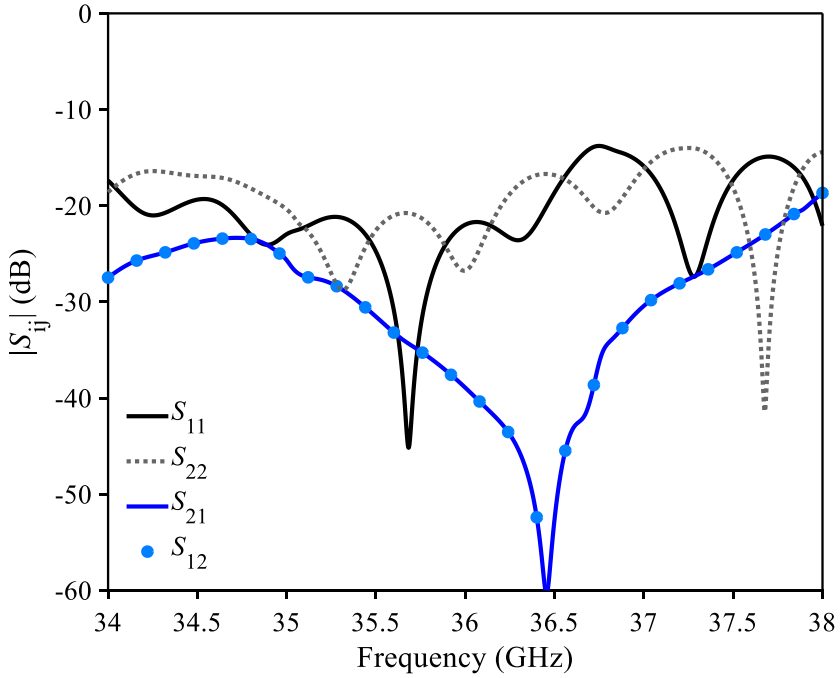

Figure 4.22 Simulated *S*-parameters of the monopulse 1.

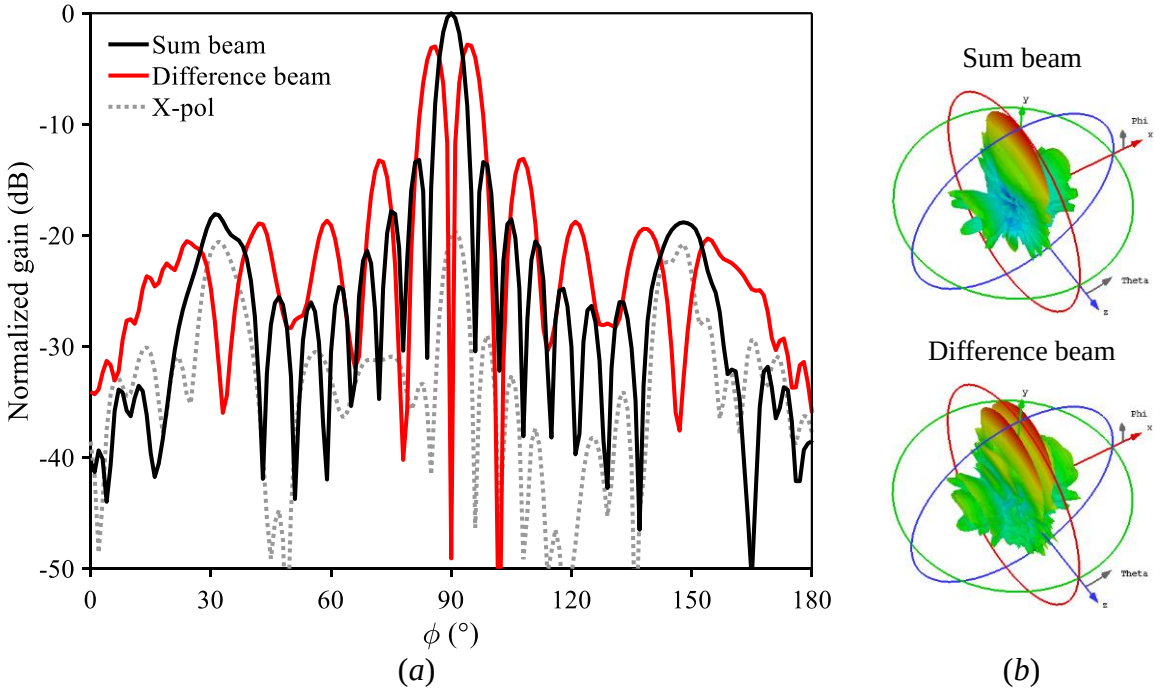

Figure 4.23 (*a*) Simulated normalized radiation pattern of monopulse 1 in E-plane and (*b*) the 3D radiation pattern of monopulse 1 at 36 GHz.

The simulated normalized gain in the E-plane at 36 GHz of the monopulse 1 is shown in Figure 4.23. A maximum sum gain of 20.5 dBi together with a maximum difference gain of 17.7 dBi and a null-depth level of ND = -49 dB are obtained in simulation. The imbalance

between the two peaks of the difference gain is 0.16 dB. The sum gain offers a HPBW = 5° and a side lobe level of SLL = -13.2 dB. In the HPBW angle, a minimum isolation level between the co-pol and x-pol of 19.63 dB is obtained.

The simulated normalized radiation pattern in the H-plane at 36 GHz is shown in Figure 4.24. In the simulation, a maximum gain of 20.5 dBi and an HPBW of 42° are obtained in the H-plane. In the HPBW angle, the polarization isolation is better than -19.83 dB.

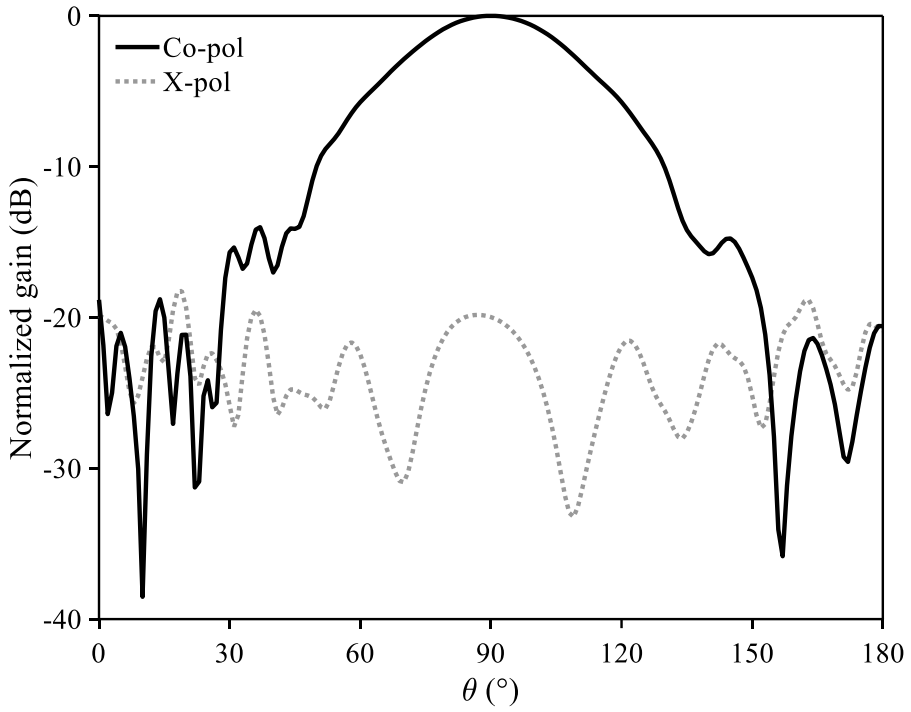

Figure 4.24 Simulated normalized radiation pattern of monopulse 1 in H-plane at 36 GHz.

The simulated maximum gain versus frequency, the isolation level between co-pol and x-pol, and the corresponding total efficiency are shown in Figure 4.25. Over the frequency band from 34 GHz to 38 GHz, the monopulse 1 offers a maximum gain of 20.3 ± 0.24 dB. The isolation level is better than 18.7 dB thanks to the extended center dielectric slab. Also, by using the low loss AFSIW-based components, the total efficiency of the monopulse 1 is higher than 82%.

Nevertheless, the monopulse 1 requires a coupler and a phase shifter for the feeding, which makes the antenna footprint larger. Also, the monopulse feeding is implemented using only the middle layer, the top and bottom layers are used to enclose the structure. In order to benefit from the multilayer aspect in AFSIW structure to realize a more compact monopulse antenna, the multilayer magic-tee feeding is investigated and presented in 4.4.

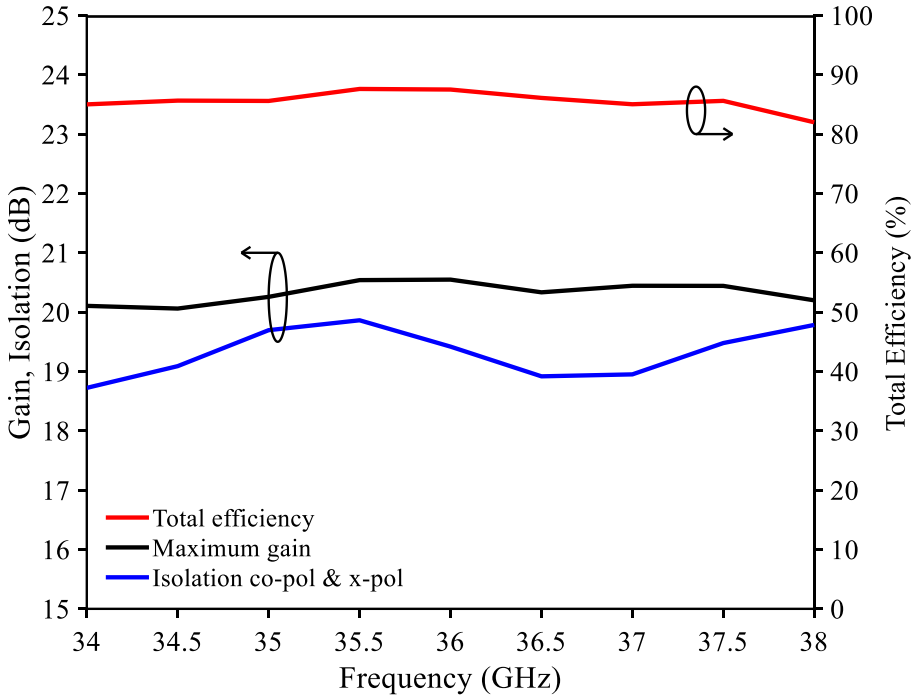

Figure 4.25 Simulated maximum gain, isolation between co-pol and x-pol, and total efficiency of the monopulse 1.

4.4 Multilayer monopulse antenna using magic-Tee

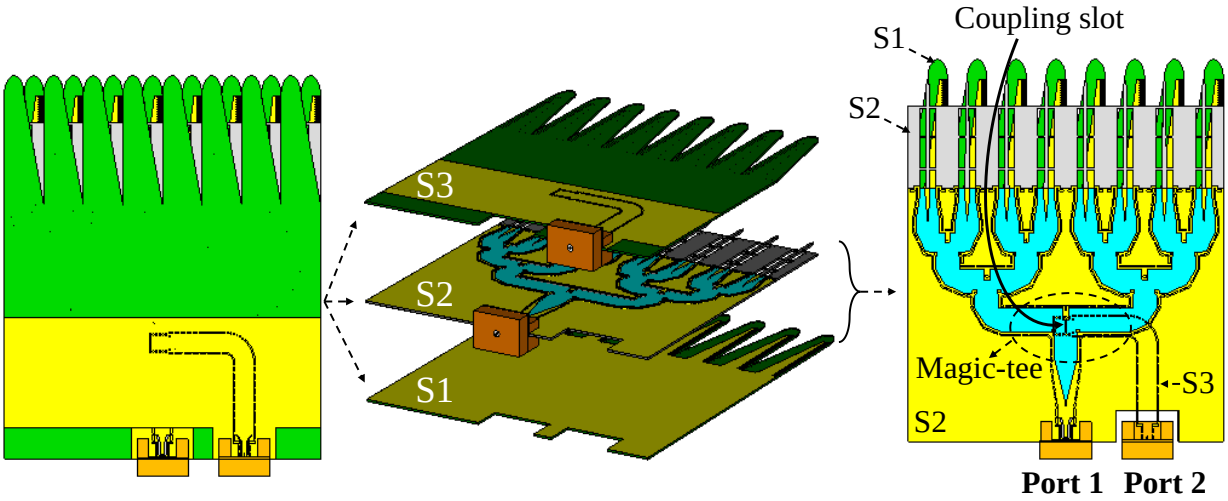

(*a*) (*b*) (*c*)

Figure 4.26 Topology of monopulse 2: (*a*) top view of the completed circuit, (*b*) expanded 3D view, (*c*) top view of layer S1, (*d*) top view of layer S3, (*e*) bottom view of layer S3, and (*f*) superposition of layer S3 on layer S1 and S2.

In the second investigation, the multilayer aspect of the AFSIW structure is benefited to implement a magic-tee feeding. The topology of the monopulse antenna using magic-tee (monopulse 2) is shown in Figure 4.26.

The delta port is implemented on layer S3 (RT5880). A slot is etched at the bottom of layer S3 to couple the energy from the delta port to the tee-junction. The magic-tee is detailed in Figure 4.27. Layer S2 is a conventional tee-junction. The width of the DFSIW in layer S3 is 4.77 mm to have the same cutoff frequency f_c = 21.2 GHz for the dominant mode as in the AFSIW structure. Since an E-plane junction will generate a capacitive effect [24], two inductive vias are added on layer S3 for matching purposes.

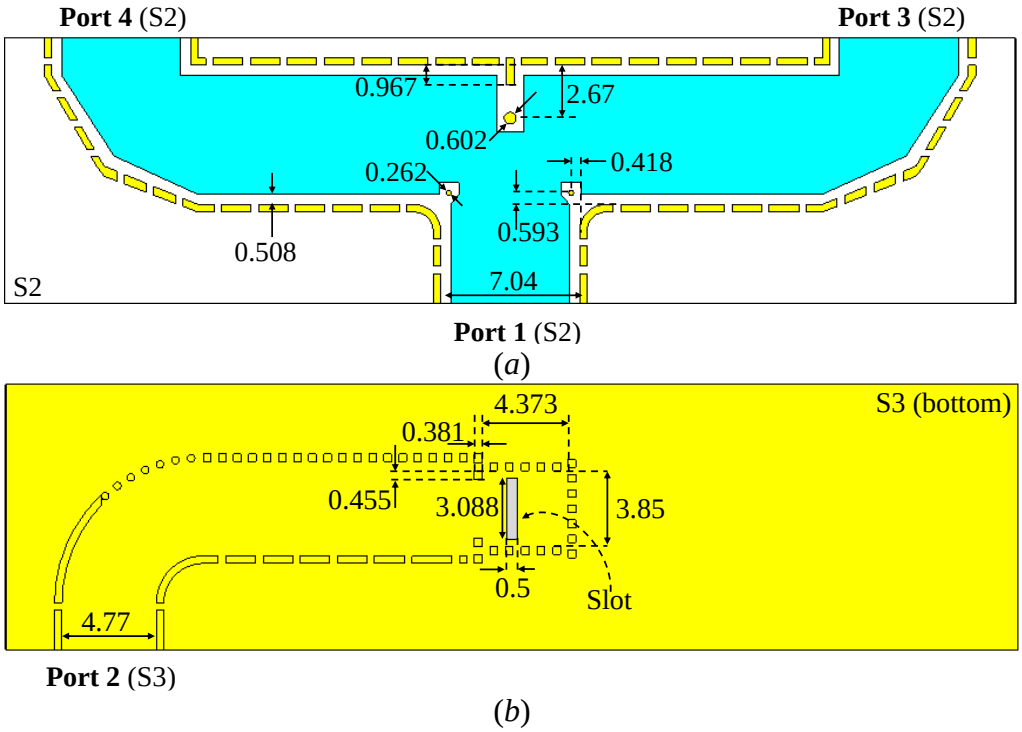

Figure 4.27 AFSIW magic-tee: (*a*) top view of layer S2 and (*b*) bottom view of layer S3.

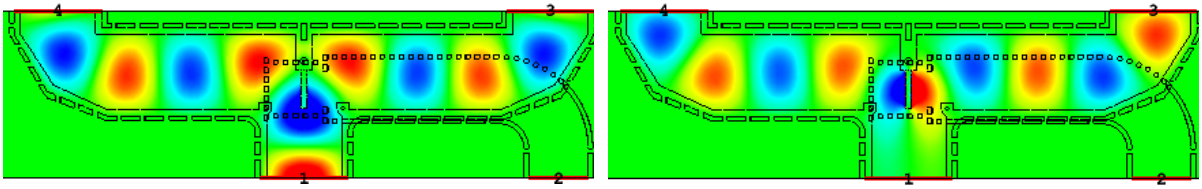

(*a*) (*b*)

Figure 4.28 Simulated magnitude E-field at 36 GHz when (*a*) port 1 is excited and (*b*) port 2 is excited.

The distributions of the E-field in layer S2 when port 1 or port 2 is excited are shown in Figure 4.28(*a*) and Figure 4.28(*b*), respectively. It can be observed in Figure 4.28(*a*) and

Figure 4.28(*b*) that port 1 will generate two in-phase signals and port 2 will generate two out-of-phase signals at outputs, as desired.

The simulated *S*-parameters of the AFSIW magic-tee are shown in Figure 4.29. When port 1 is excited, the power transferred to port 3 and port 4 is within 3.13 ± 14 dB from 34 GHz to 38 GHz. Meanwhile, an equal power splitting of 3.44 ± 0.5 dB is obtained from 34.95 GHz to 37.59 GHz when port 2 is excited. It can also be observed in Figure 4.29 that, from 34 GHz to 38 GHz, the reflection coefficient $|S_{11}|$ at port 1 is always lower than -25.5 dB and the isolation $|S_{21}|$ between port 1 and port 2 is lower than -30 dB. Nevertheless, port 2 exhibits a narrower bandwidth due to the narrowband matching of the planar magic-tee. The reflection $|S_{22}|$ is lower than -10 dB from 34.54 GHz to 37.77 GHz (8.9% centered at 36.16 GHz). At 36 GHz, all the coefficients $|S_{11}|$, $|S_{21}|$, and $|S_{22}|$ are lower than -25.8 dB.

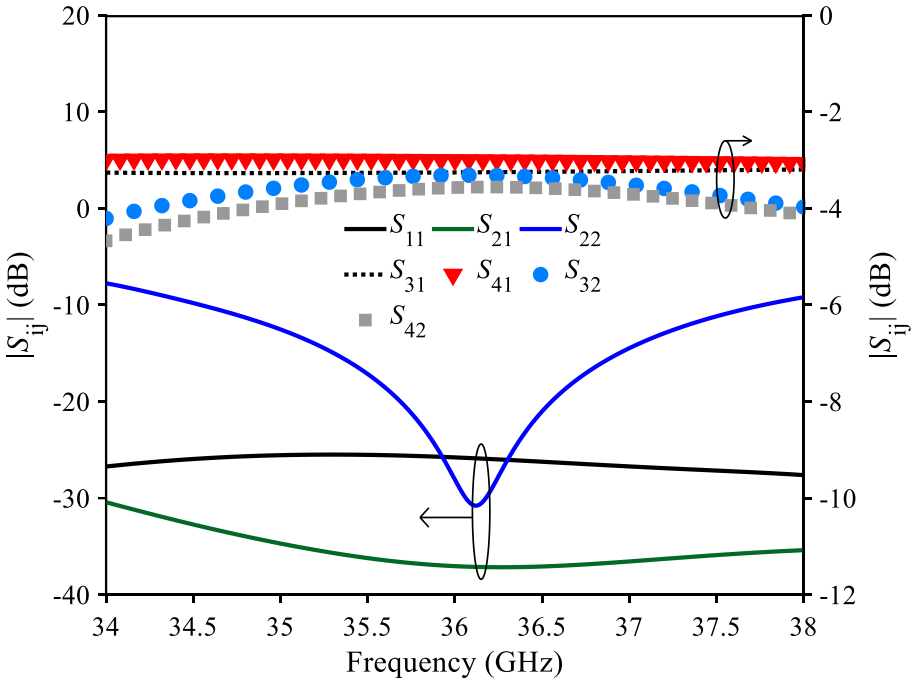

Figure 4.29 Simulated *S*-parameters of the AFSIW magic-tee.

The simulated amplitude imbalance (AI = $|S_{3i}|$ - $|S_{4i}|$) and phase imbalance (PI = $\varphi(S_{3i})$ - $\varphi(S_{4i})$) when port i^{th} is excited are shown in Figure 4.30. In the first case when port 1 is excited, an AI = 0.21 ± 0.08 dB and a PI = 0.2 ± 1.2° are obtained from 34 GHz to 38 GHz. The achieved AI and PI at 36 GHz are 0.26 dB and -0.3°, respectively. In the second case, when port 2 is excited, AI = -0.31 ± 0.15 dB and PI = 180.6 ± 2.4°. The obtained AI in the latter case is higher than in the first case due to the limited bandwidth of the magic-tee. However, the simulated AI

is within ±0.5 dB. In the second case, an AI = -0.25 dB and a PI = 179.6° are obtained at 36 GHz.

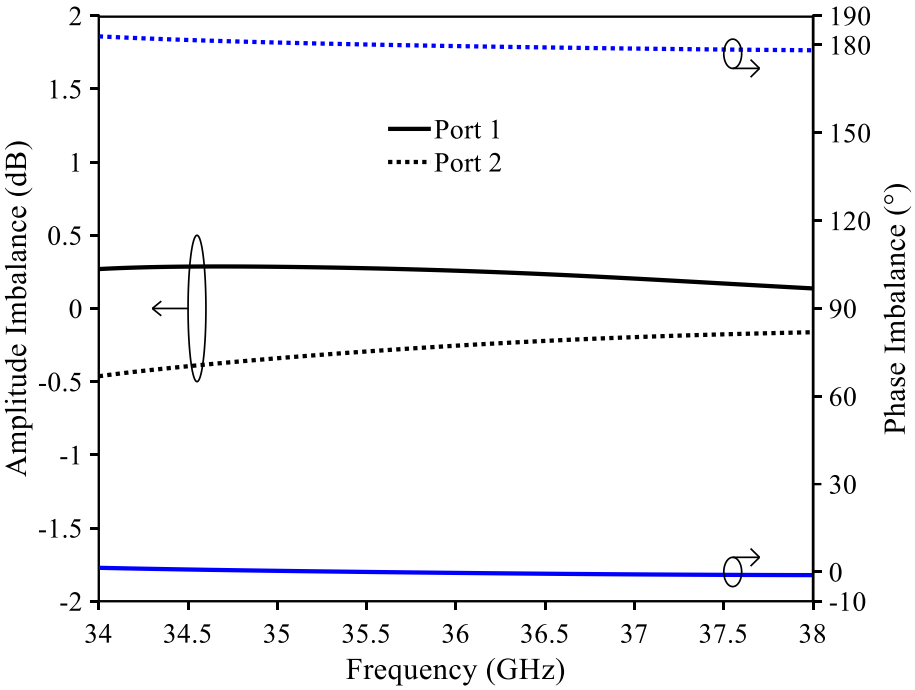

Figure 4.30 Simulated AI and PI of the AFSIW magic-tee.

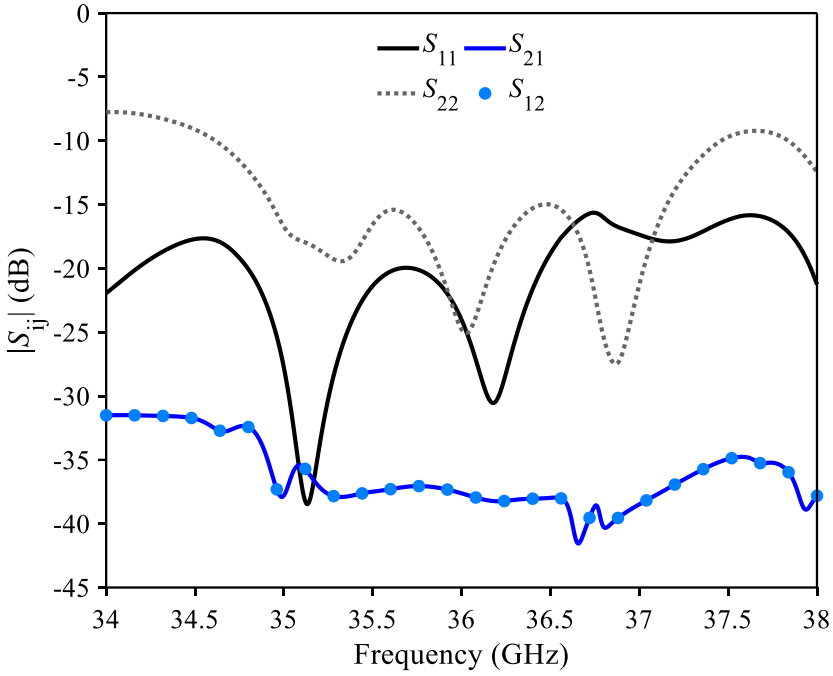

Figure 4.31 Simulated *S*-parameters of the monopulse 2.

With the above results, the AFSIW magic-tee satisfies the condition for in-phase and out-of-phase excitations. It is integrated into the monopulse 2 as shown in Figure 4.26.

The simulated *S*-parameters (with connectors) of the monopulse 2 are shown in Figure 4.31. All the *S*-parameters are lower than -10 dB from 34.61 GHz to 37.46 GHz (7.9% centered at 36.04 GHz). In this -10 dB bandwidth, the isolation between port 1 and port 2 is better than 32.55 dB. At the center frequency of 36 GHz, all parameters are lower than -24 dB.

The normalized radiation patterns of the monopulse 2 at 36 GHz in E-plane and H-plane are presented in Figure 4.32 and Figure 4.33, respectively. The obtained radiated results are given in Table 4.2.

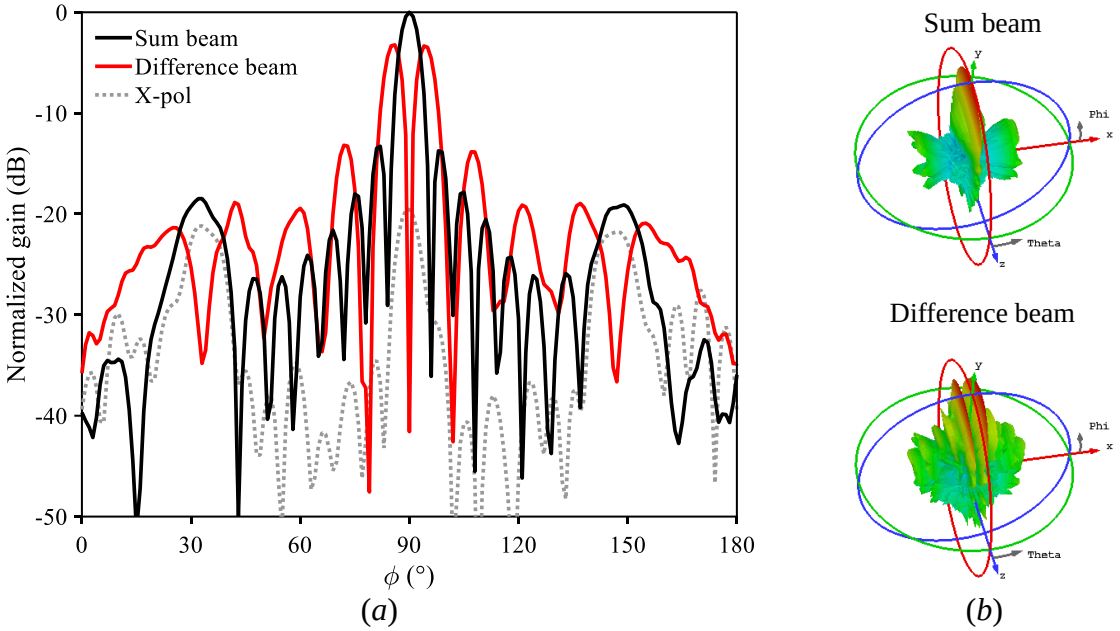

Figure 4.32 (*a*) Simulated normalized radiation pattern of the monopulse 2 in E-plane and (*b*) 3D radiation pattern of the monopulse 2 at 36 GHz.

The simulated maximum gain, isolation between two polarizations, and the total efficiency when port 1 is excited are presented in Figure 4.34. A maximum gain of 20.49 ± 0.18 is obtained from 34 GHz to 38 GHz. The corresponding total radiation efficiency is higher than 85.3%. Furthermore, the isolation between co-pol and x-pol is maintained to be higher than 19.59 dB.

To summarize, Table 4.2 compares the different characteristics of the two proposed monopulse antennas. It can be observed in Table 4.2 that these two antennas present similar performances. However, the monopulse 2 is more compact thanks to the multilayer magic-tee. Therefore, monopulse 2 is chosen for the experimental validation.

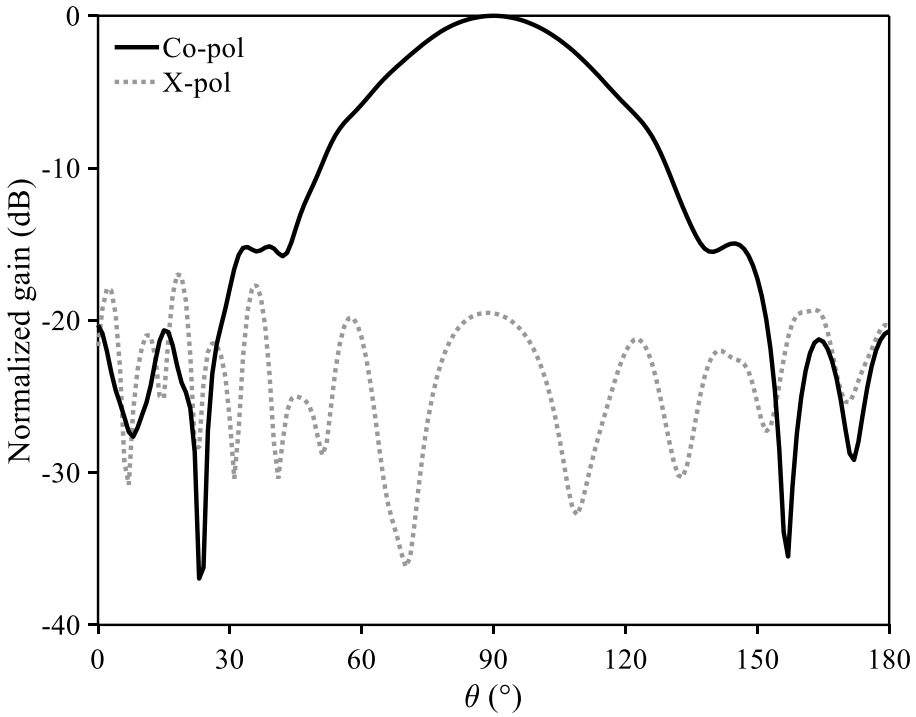

Figure 4.33 Simulated normalized radiation pattern of the monopulse 2 in H-plane at 36 GHz.

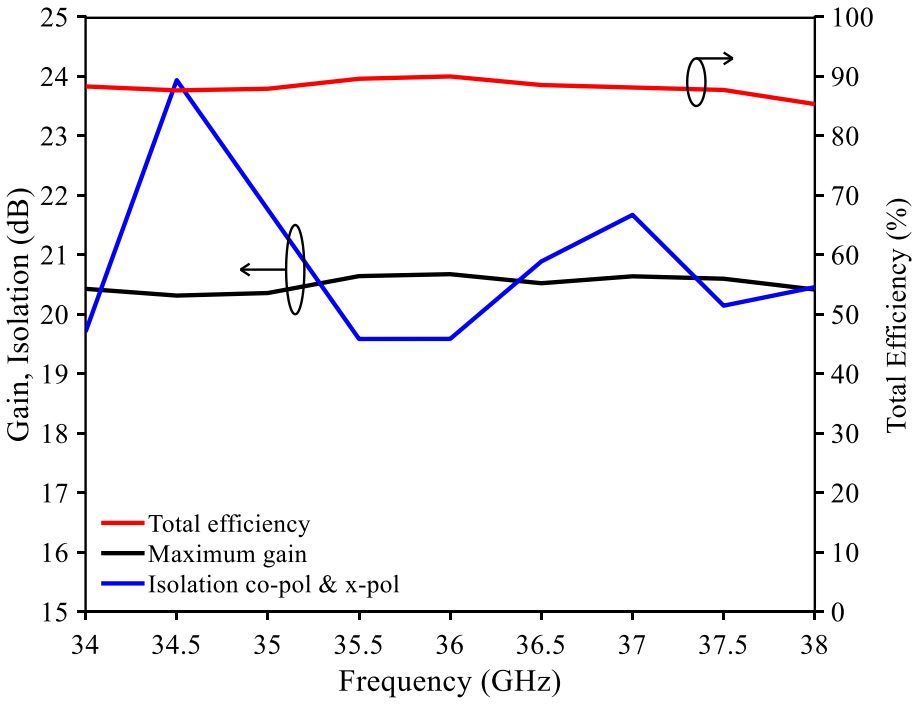

Figure 4.34 Simulated maximum gain, isolation between co-pol and x-pol, and the total efficiency of the monopulse 2.

Table 4.2 Comparison between the two proposed monopulse antennas.

	Monopulse 1 (180° hybrid coupler)	Monopulse 2 (magic-tee)
f_0 (GHz)	36	36
Realized sum gain (dB)	20.5	20.67
Realized difference gain (dB)	17.7	17.47
Amplitude imbalance of the difference beam (dB)	0.16	0.15
ND (dB)	-49	-41.6
HPBW of sum beam in E-plane/H-plane (°)	5/40.8	5.1/41.4
SLL of sum beam in E-plane/H-plane (dB)	-13.2/-14	-13.3/-14.9
-10 dB bandwidth (%)	11.11	7.9
Total efficiency (%)	87.5	89.9
Total efficiency variation	84.8 ± 2.8	87.6 ± 2.3
Isolation co-pol & x-pol (dB)	19.63	19.54
Dimension (mm × mm)	78.90 × 105.05	78.90 × 95.72

4.5 Experimental demonstration

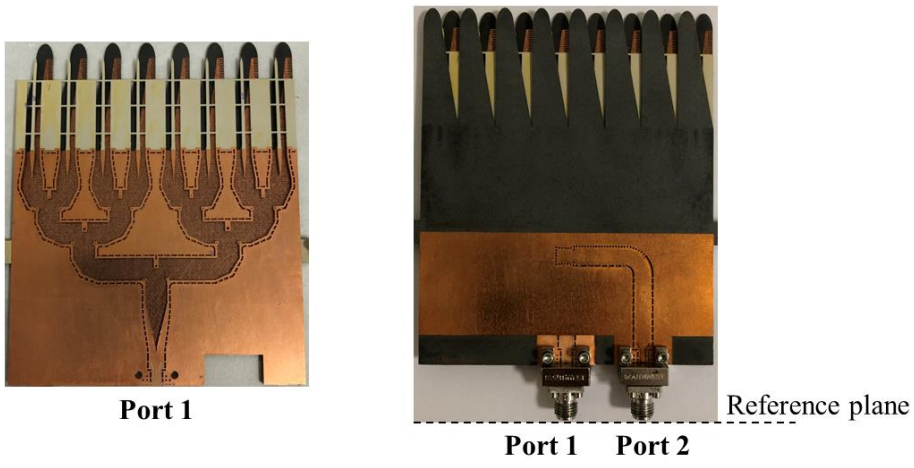

(*a*) (*b*)

Figure 4.35 Fabricated prototype of monopulse 2 (*a*) before and (*b*) after assembling.

The fabricated prototype of the monopulse 2 before and after assembling is shown in Figure 4.35.

In measurement, a standard SOLT calibration kit was used to de-embed the measured plane to the input of connectors as the reference plane shown in Figure 4.35(*b*). The simulated and measured *S*-parameters of the monopulse 2 are compared in Figure 4.36. A good agreement is obtained. Differences between simulation and measurement results are mainly caused by errors occurred in manual assembling.

In measurement, all the *S*-parameters are lower than -10.9 dB from 34 GHz to 38 GHz (11.11% centered at 36 GHz). Especially, the isolation between sum and delta ports is maintained lower than -24.57 dB. Good isolation is obtained thanks to the magic-tee topology. At the center frequency of 36 GHz, the measured reflection and isolation coefficients are $|S_{11}|$ = -22.17 dB, $|S_{22}|$ = -18.01 dB, and $|S_{21}|$ = -33.17 dB.

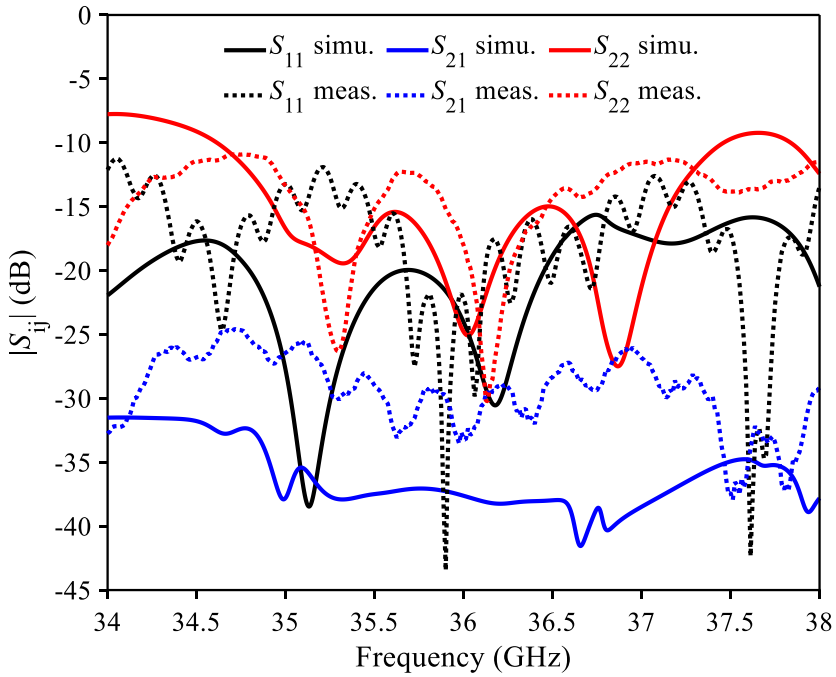

Figure 4.36 Simulated and measured *S*-parameters of the monopulse 2.

The radiation pattern generated by port 1 (or 2) is measured by terminating port 2 (or 1) with a 50Ω termination as shown in Figure 4.37. The termination is connected to the unused port by a male-to-male 90° junction. A plastic base is used to handle the antenna during measurement.

The simulated and measured normalized radiation patterns in the E-plane at 36 GHz when the sum port is excited are compared in Figure 4.38, where a good agreement can be observed.

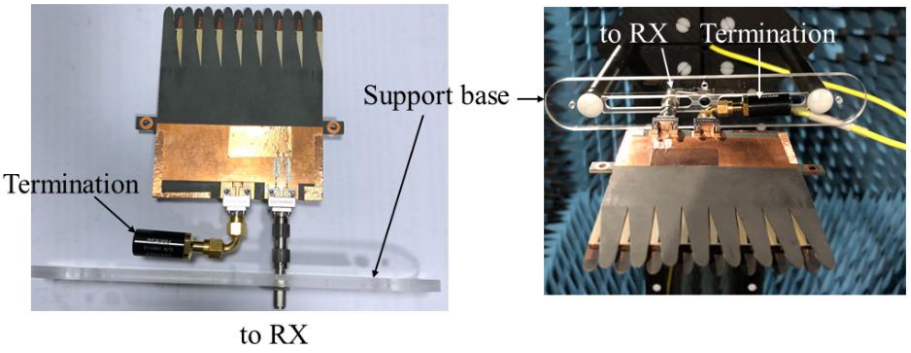

Figure 4.37 Measurement setup for radiation pattern.

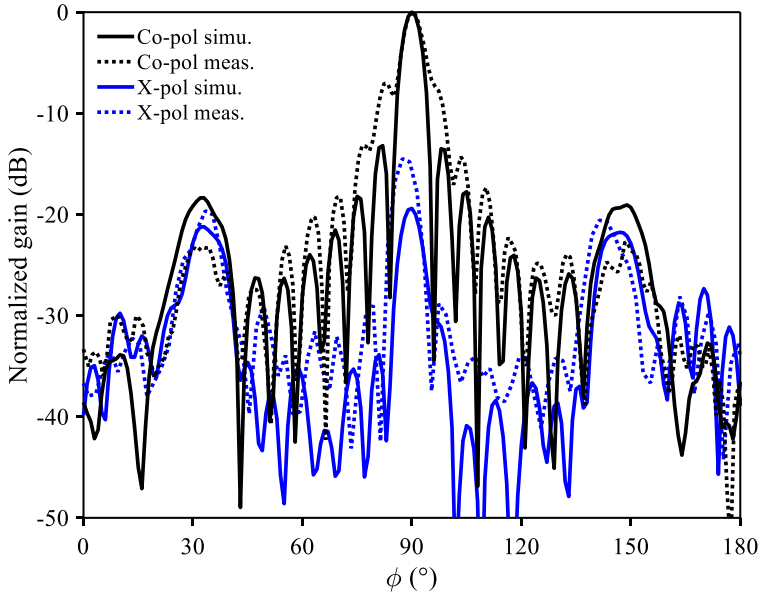

Figure 4.38 Simulated and measured normalized sum beam in E-plane at 36 GHz.

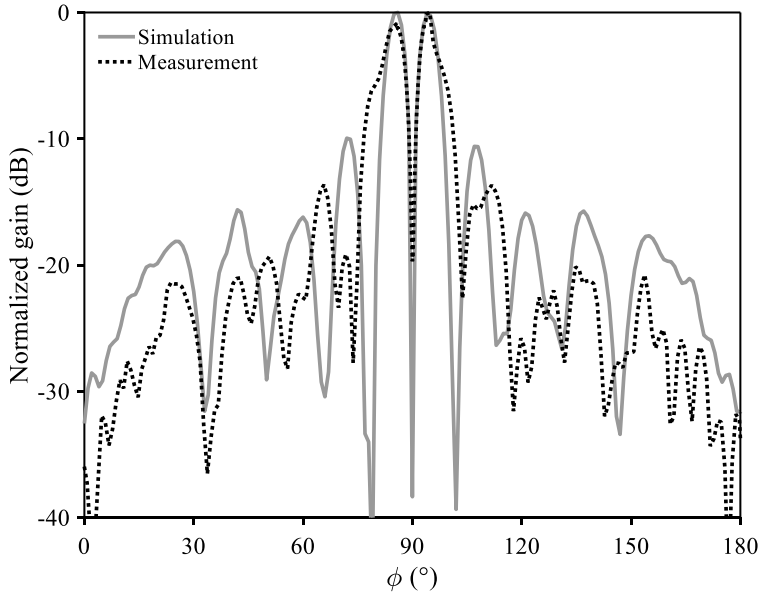

Figure 4.39 Simulated and measured normalized difference beam in E-plane at 36 GHz.

In measurement, a maximum gain of 17.82 dB is observed at ϕ = 90°. The reduction of gain is due to errors in manual assembling and fabrication, the surface roughness that was not considered in the simulation, the variation of loss tangent at high frequency, and a male-to-male adapter used for antenna mounting as well. In the HPBW angle, the obtained measured isolation between co-pol and x-pol is 14.49 dB.

The simulated and measured normalized E-plane radiation patterns at 36 GHz when port 2 is excited are presented in Figure 4.39. Again, errors in assembling and fabrication cause the degradation of maximum gain. The measured results show a maximum difference gain of 14.8 dB. The second maximum has a gain of 13.93 dB (0.87 dB imbalance between two peaks). The obtained measured ND is -22.72 dB. The ND occurs at ϕ = 90°.

Regarding the H-plane, Figure 4.40 compares the simulated and measured normalized radiation pattern at 36 GHz. Again, a good agreement is achieved. The measured maximum gain and the polarisation isolation are 17.24 dB and 13.31 dB, respectively.

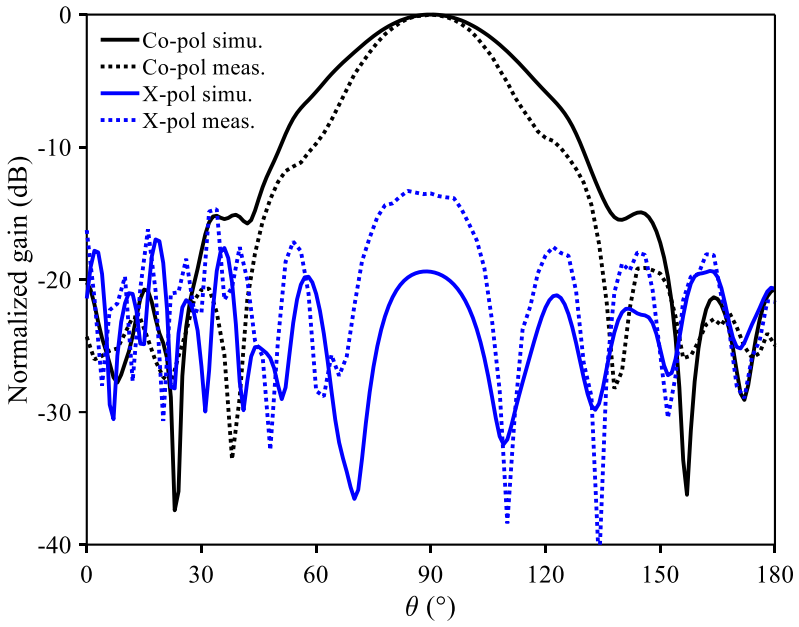

Figure 4.40 Simulated and measured normalized sum beam in H-plane at 36 GHz.

4.6 Conclusion

For comparison, Table 4.3 summarizes different important characteristics of various SIW-based monopulse antennas used at millimeter-wave frequencies. It can be observed in Table 4.3 that the proposed AFSIW monopulse antenna presents a comparable bandwidth, gain, and isolation compared to other works reported in literature. The difference between the sum and delta beams is around 3 dB as expected. Furthermore, by using the AFSIW technology, the

proposed monopulse antenna can offer high radiation efficiency. Although the measurement results present some degradations, the AFSIW monopulse works well in terms of sum and difference beams as well as the scattering parameters. A more careful assembling process is expected to provide better performances.

To our best knowledge, this is the first monopulse antenna implemented using the AFSIW platform. Also, for the first time, a quasi-planar magic-tee is used for SIW-based monopulse antenna at millimeter-wave frequencies. The SIW-based magic-tees reported in [61] and [70] use RWG as the delta ports, hence, eliminate the planar structure.

The proposed AFSIW monopulse antenna can be considered as the first passive AFSIW-based system on substrate (SoS).

Table 4.3 Comparison of different mmW SIW-based monopulse antennas.

Reference	**This work (Monopulse 2)**	[61] (2D scan)	[47]	[48]	[49]	[50]
Feeding configuration	**Magic-tee**	Magic-tee with RWG	180° hybrid coupler	180° hybrid coupler	Coupling matrix	Coupling matrix
f_0 (GHz)	**36**	60	36	36.5	31.25	94
Realized sum gain (dB)	**17.82**	13.8 to 15.8	10.6	16.13	18.74	25.21
E-plane HPBW (°)	**5.7**	--	22.5	7.2	--	2.77
Sum gain - difference gain (dB)	**3.02**	--	3	2.95	--	--
Amplitude imbalance of the difference beam (dB)	**0.87**	--	--	--	--	0.92 to 3.48
ND (dB)	**-22.72**	-31	-35	-38.1	-46.3	-27.97
-10 dB bandwidth (%)	**11.11**	13.11	19.2	19.2	7.39	--
Isolation sum/delta ports	**< -24.57**	< -25	< -17.5	< -17.5	--	--
Radiation efficiency (%)	**90***	--	57.5	--	--	15.2

*: simulated result

--: Not given

CHAPTER 5 ISOLATED POWER DIVIDER/COMBINER

As it was mentioned in Chapter 2, the AFSIW-based solutions can handle more power than the DFSIW for a continuous wave (CW) signal. In [71], it was valid via measurement that the AFSIW structure can handle a CW signal up to few hundred watts at 20 GHz. Therefore, the development of high power components is hugely desirable based on this technology to fulfill the AFSIW components library.

5.1 Overview

Power dividers/combiners are key components which help split or combine a desired portion of power. The mismatch or damage of outputs/inputs will cause high reflection and destroy the operation of power dividers/combiners. Therefore, the isolation between outputs/inputs is desirable and critical to prevent the system from overloading.

The Tee-junction power divider/combiner is the most common topology in splitting/combining applications due to the simplicity of design. However, this three-port network cannot generate a good matching and isolation at all ports in a lossless condition [24]. Lossy elements are implemented to dissipate the power flowing between outputs/inputs caused by circuit unbalance, hence, realize the isolation [24].

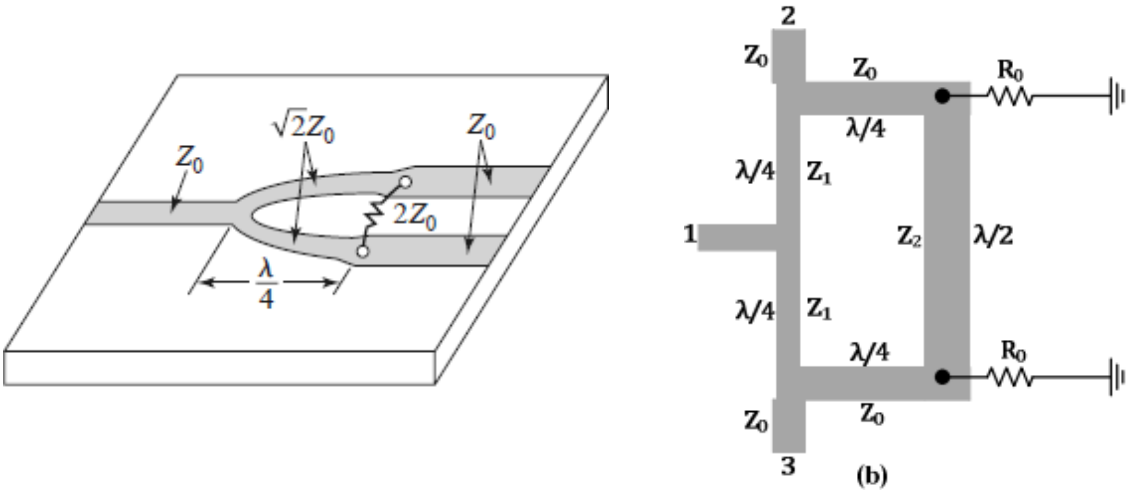

(*a*) [24] (*b*) [73]

Figure 5.1 Two-way configuration of (*a*) Wilkinson and (*b*) Gysel power divider/combiner.

In microstrip technology, Wilkinson and Gysel power dividers/combiners are two common topologies that use resistors to create the all-matching condition [72]. Their two-way topologies implemented in microstrip are shown in Figure 5.1. In the Wilkinson configuration, resistors

are accommodated between two branches [24] which are set to limit the thermal dissipation and then, the power handling capability. On the contrary, the Gysel topology terminates resistors to the ground [73], which provides a good thermal dissipation and high power handling capability.

The idea of the Wilkinson power dividers/combiners was demonstrated in the SIW platform for the first time in [74] (see Figure 5.2(*a*)). In that paper, the HM-SIW concept was used to broaden the operation bandwidth and to reduce the total footprint as well. The obtained -10 dB bandwidth is 64% at the center frequency of 26.5 GHz. Nevertheless, transitions from HM-SIW to 50Ω microstrip lines were used to accommodate the 100Ω resistor, which vanishes the self-shielded characteristic.

The full integration of resistors in the SIW platform was demonstrated in [75] which results in a -10 dB bandwidth of 25% centered at 10 GHz. In that paper, multilayer SIW was used in a ring-shaped configuration to satisfy the impedance ratio close to $\sqrt{2}$ between branches in the Wilkinson topology as illustrated in Figure 5.2(*b*). Furthermore, three resistors were implemented in a distributed network to increase the operation bandwidth as well as the power handling capability.

The impedance condition can also be fulfilled in a single layer DFSIW by using a modified Wilkinson topology as shown in Figure 5.2(*c*) [76]. In this modified structure, all branches have the same characteristic impedance. The additional arms represented by φ_2 were used to accommodate resistors. The resistor value was chosen to match the equivalent impedance seen at the slot. By using a distributed network of resistors, the obtained -10 dB bandwidth is 23% at the center frequency of 10 GHz.

In both [75] and [76], a slot was etched on the top copper plate to mount the resistors. Due to the limited bandwidth of the slot, these solutions are not suitable for broadband applications.

Using distributed resistors and slow wave HM-SIW structure, [77] introduced a compact power divider with 91.7% fractional bandwidth at 10.9 GHz (Figure 5.2(*d*)). Resistors are connected directly to two branches that allow larger bandwidth operation. Nevertheless, the copper plate was etched to generate slow wave effect, which could lead to high leakage at higher frequencies.

Another broadband resistive material-based power divider can be found in [78] (Figure 5.2(*e*)). In this paper, broadband isolation was obtained in X-band (8 GHz to 12 GHz) by using a carbon resistive layer and a vertical coupling scheme. The resistive card was buried into the E-plane junction which helps absorb the energy transmitting between two vertical branches and hence,

generates the isolation. Since the resistive layer was embedded between two layers, a strict fabrication process is needed to control the thickness of the carbon paste.

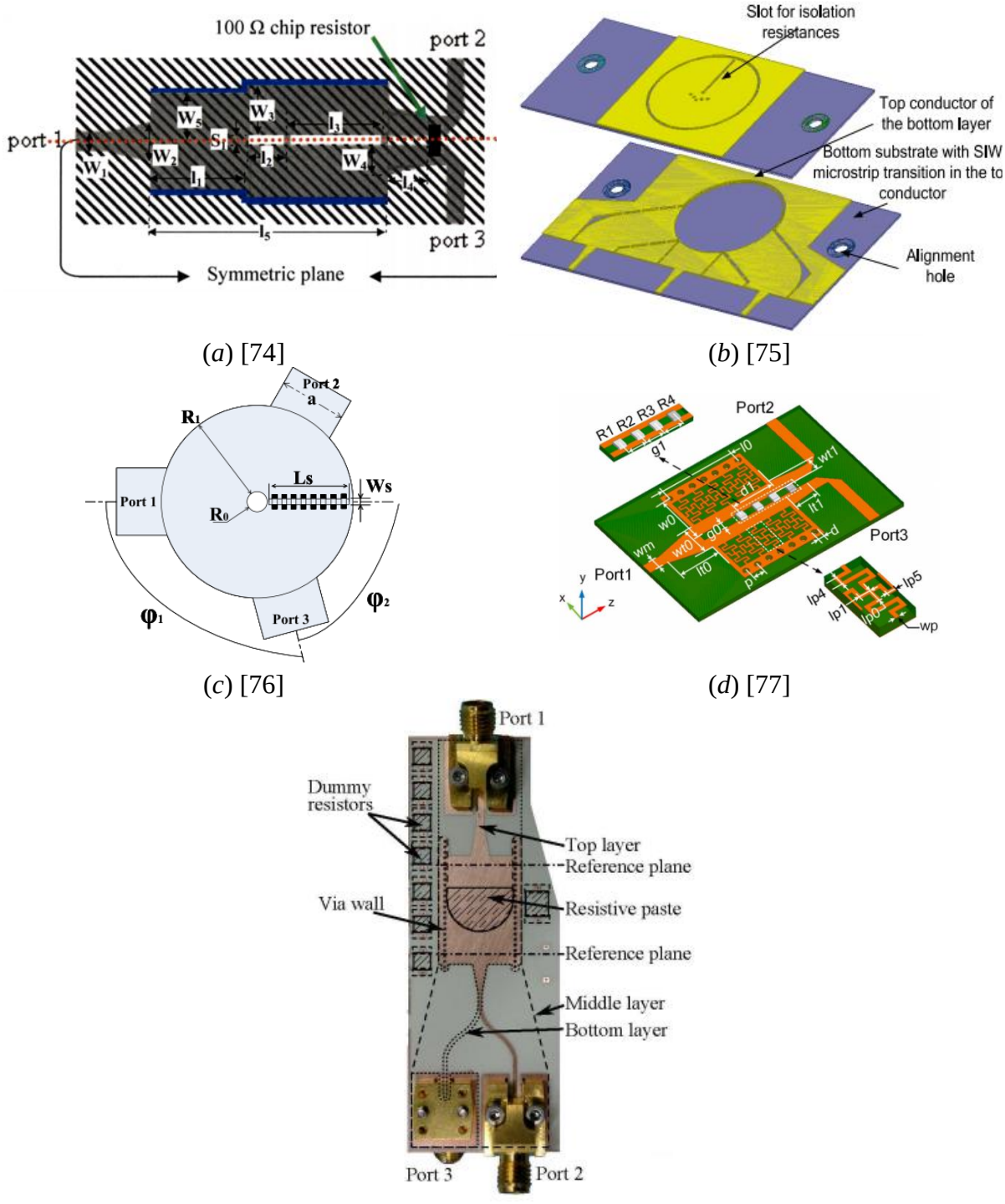

(*a*) [74] (*b*) [75]

(*c*) [76] (*d*) [77]

(*e*) [78]

Figure 5.2 Resistive-based power dividers/combiners using (*a*) HM-SIW and microstrip [74], (*b*) multi-layer ring-shaped DFSIW [75], (*c*) single-layer fixed-width DFSIW [76], (*d*) slow wave HM-SIW, and (*e*) multi-layer DFSIW with carbon paste [78].

Instead of using resistors to dissipate the energy between branches, the absorbing materials could be used as well. At high frequency, resistive materials-based solutions are usually limited by the rated power of resistors. The absorptive-based solutions show their superiority in terms of high power handling.

Inspired by the five-port RWG power divider reported in [79], the very first planar isolated power divider/combiner using absorbing material and DFSIW technology was reported in [80]. It is shown in Figure 5.3(*a*). The operation of this structure is similar to a Riblet coupler. Using two additional ports terminated with absorbing material, this solution gives an operating bandwidth of 36% centered at 16.5 GHz.

Alternatively, multilayer DFSIW was also used to implement an isolated power divider/combiner in [81] as represented in Figure 5.3(*b*). In this work, the magic-Tee concept was used to achieve a good isolation level between branches. The absorbing material was placed at the output of E-plane junction to terminate the Δ-port. The obtained -10 dB fractional bandwidth is 50% at the center frequency of 12.8 GHz.

In both [80] and [81], the absorbing materials were buried inside the DFSIW guided-wave structure. As a result, the responses of those solutions are sensitive to the geometry as well as the position of the absorbing materials.

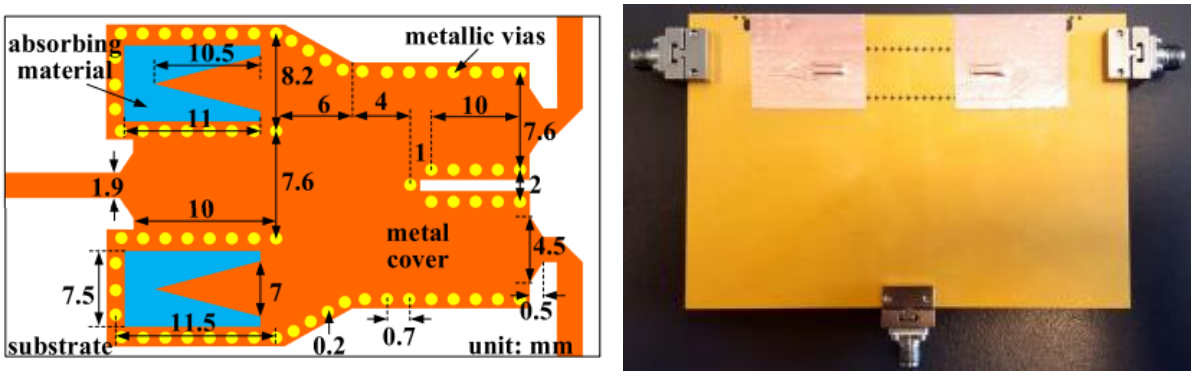

(*a*) [80] (*b*) [81]

Figure 5.3 Absorptive-based power dividers/combiners using (*a*) five-port DFSIW coupler [80] and (*b*) multilayer DFSIW magic-Tee [81].

In this section, we aim to introduce the isolated power dividers/combiners taking advantage of the multilayer aspect in the AFSIW structure. First, the innovative multilayer balanced-delta-port magic-Tee will be introduced as an upgraded version of the conventional magic-Tee. Then, two isolated power dividers/combiners approaches will be introduced and demonstrated: resistive- and absorptive-based solutions. The absorptive-based solutions are not

sensitive to the absorber dimensional errors as well as misalignment, which is an advantage for mass-production.

5.2 Balanced-delta-port magic-Tee

The balanced-delta-port magic-Tee is an evolution of the conventional magic-Tee. Its topology is shown in Figure 5.4. The balanced-delta-port magic-Tee benefits from the multilayer aspect of the AFSIW platform to introduce an additional delta-port (port 5 in Figure 5.4(*b*)). Thanks to an additional delta-port, the balanced-delta-port magic-Tee offers the possibility for broadband isolation with small coupling slots.

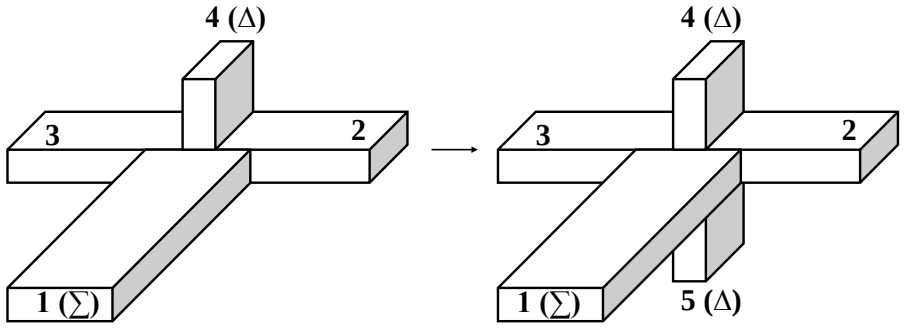

(*a*) (*b*)

Figure 5.4 Evolution from (*a*) conventional magic-Tee to (*b*) balanced-delta-port magic-Tee [82].

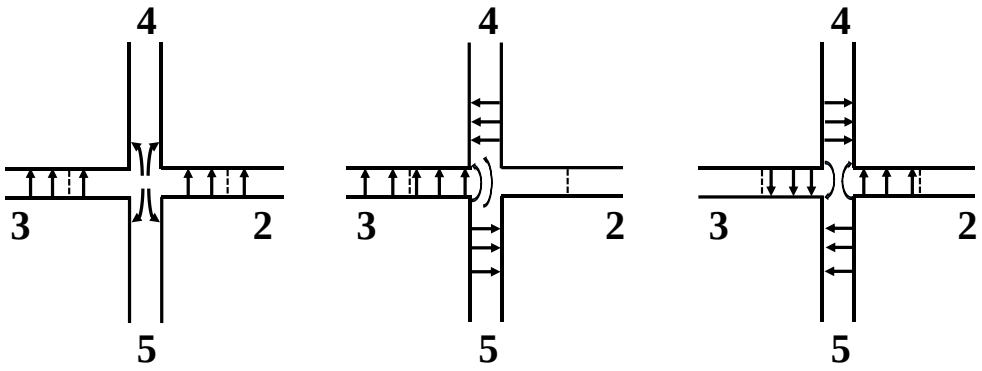

(*a*) (*b*) (*c*)

Figure 5.5 E-field distribution in balanced-delta-port magic-Tee when the signal is coming from (*a*) port 1, (*b*) port 3, and (*c*) port 4 [82].

To understand the benefit of an additional delta port, the distribution of the electrical field at the vertical junction plane was sketched as shown in Figure 5.5. In this analysis, the feeding port was excited by a TE_{10} mode signal to operate in the mono-mode bandwidth. In addition,

the lengths of the horizontal arms are assumed to be equal as well as the lengths of the vertical arms for an equal splitting/combining scenario.

Thanks to the similarity with the conventional magic-Tee, the operation mechanism of the balanced-delta-port magic-Tee can be analyzed as follows:

- When port 1 is excited (Figure 5.5(*a*)), power will be equally transferred to port 2 and port 3. The output signals at port 2 and port 3 are in phase. Due to the E-plane junction, the E-field line is odd-symmetric at the vertical ports. However, the symmetrical structure forces port 4 and port 5 to support only the even-mode. As a result, port 4 and port 5 do not allow the propagation of odd-mode from the vertical junction. In this case, port 4 and port 5 are isolated from port 1. A similar phenomenon is observed in the conventional magic-Tee [24].
- When port 3 is excited (Figure 5.5(*b*)), half of the power is redirected to port 1 as reciprocity to the first case in Figure 5.5(*a*). Port 3 is isolated from port 2 as an inherited characteristic from the conventional magic-Tee. Therefore, the rest of the power is transferred equally to port 4 and port 5 due to the symmetry. Again, the E-plane junction forces the signal at port 4 and port 5 to be out of phase. Since the power is redirected to both port 4 and port 5, the balanced-delta-port magic-Tee will be able to handle a power level 3 dB higher than the conventional magic-Tee.
- When port 4 is excited (Figure 5.5(*c*)), a quarter of the power is redirected to port 3 as reciprocity to the excitation case in Figure 5.5(*b*). The same amount of the power is transmitted to port 2 but with an out-of-phase direction due to the E-plane junction. A quarter of the power is transmitted to port 5 and the rest is reflected back to port 4.

With the above analysis, the scattering matrix of the balanced-delta-port magic-Tee could be given at center frequency as follows [82]:

$$S = \frac{1}{2}\begin{bmatrix} 0 & \sqrt{2} & \sqrt{2} & 0 & 0 \\ \sqrt{2} & 0 & 0 & -1 & 1 \\ \sqrt{2} & 0 & 0 & 1 & -1 \\ 0 & 1 & -1 & 1 & -1 \\ 0 & 1 & -1 & -1 & 1 \end{bmatrix} \tag{45}$$

In the perspective of realizing an isolated three-port junction, port 4 and port 5 are matched terminated. In this case, the scattering matrix is simplified as follows [82]:

$$S = \frac{1}{2}\begin{bmatrix} 0 & \sqrt{2} & \sqrt{2} \\ \sqrt{2} & 0 & 0 \\ \sqrt{2} & 0 & 0 \end{bmatrix} \quad (46)$$

The *S*-matrix in (46) implies that the power is divided to the output without losses. Similar effects are observed with the Wilkinson power divider/combiner [24]. Again, those equations are valid only at the center frequency.

The implementation of balanced-delta-port magic-Tee on the AFSIW technological platform is shown in Figure 5.6. The H-plane junction is implemented in the middle layer (layer S2 – air-filled layer). The H-plane junction can be designed as a conventional T-junction, Y-junction, or other forms [83]. Meanwhile, the two delta-ports are implemented on top (port 4) and bottom (port 5) layers (dielectric-filled layers). This implementation implies that port 4 and port 5 can be treated as DFSIW structures. Two slots are etched at the bottom of layer S3 and top of layer S1 to couple energy from layer S2.

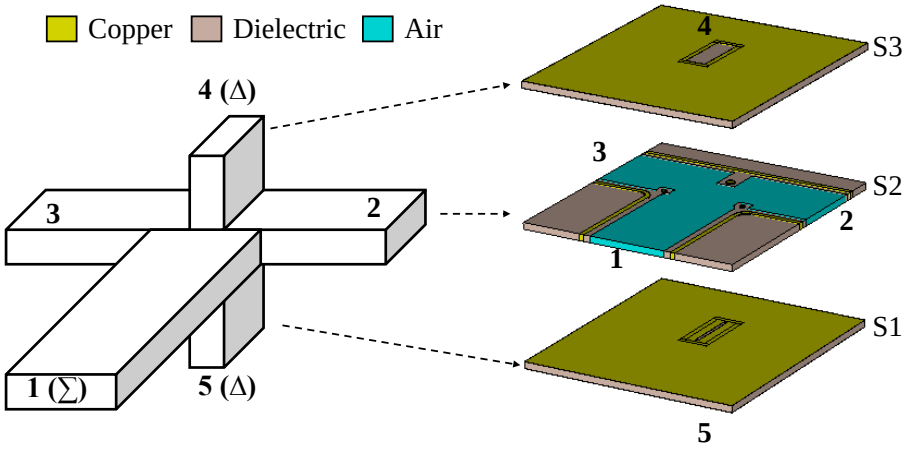

Figure 5.6 Implementation of AFSIW balanced-delta-port magic-Tee.

The dimension of the dielectric-filled port (port 4 and port 5) needs to be carefully designed to allow the propagation mode of the coming signal from layer S2. Since the structure is symmetrical, port 4 and port 5 support only the even-modes. Similar to the mode supporting condition mentioned in Chapter 2, the cutoff frequencies of the first (TE_{10}) and third (TE_{30}) modes in the delta-ports (port 4 and port 5) need to cover the dominant mode coming from other ports. An example of a satisfying mode supporting structure is shown in Figure 5.7 [82].

Once the mode supporting condition is fulfilled, the balanced-delta-port magic-Tee presents its superiority compared to the conventional Tee-junction as can be observed in Figure 5.8. The

isolation between port 2 and port 3 as well as their reflection coefficient are enhanced. Furthermore, the reflection coefficient at port 1 is almost unaffected if and only if the width of the coupling slot is kept small compared to the guided wavelength, to not perturb the electromagnetic propagation in the Tee-junction at the middle layer. Also, the isolation between the sum and delta port is high thanks to the inherited characteristic from the magic-Tee topology.

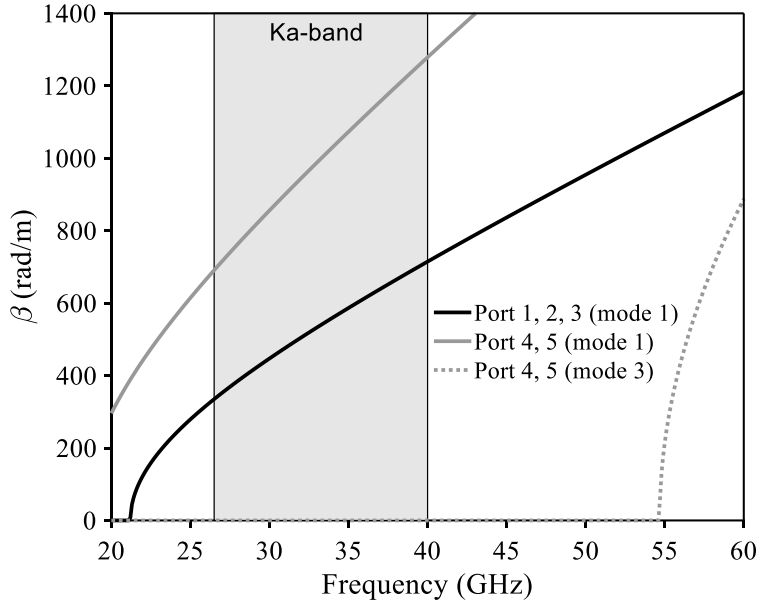

Figure 5.7 Propagation modes in AFSIW balanced-delta-port magic-Tee [82].

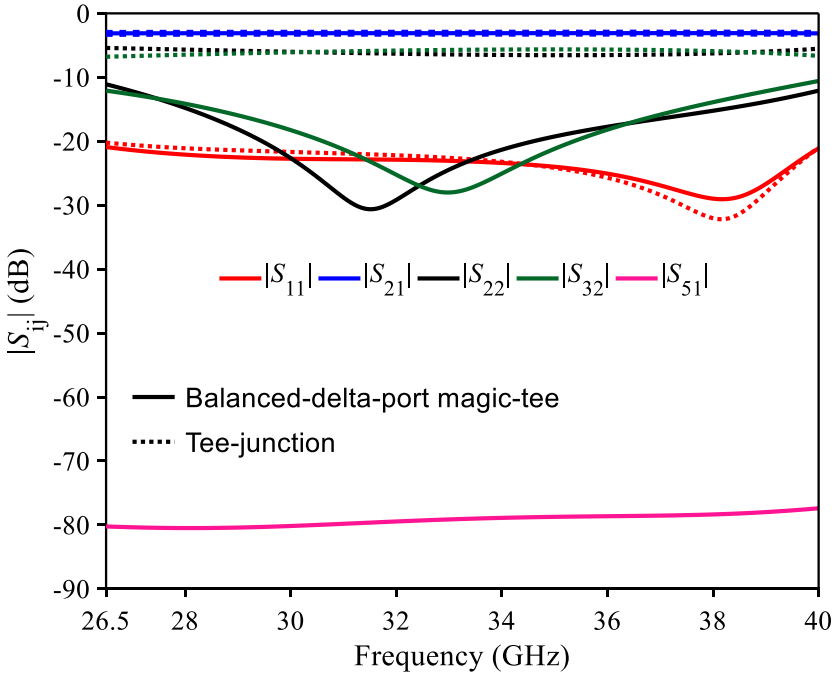

Figure 5.8 Simulated *S*-parameters of conventional Tee-junction and balanced-delta-port magic-Tee.

In an ideal case, the delta-port should be made of a continuous metallic wall to assume the continuity of current. However, in a real case, the metallic wall must be synthesized by the metallic via rows to integrate into the substrate as shown in Figure 5.9. Since the positions of the metallic vias lie on the air-filled region, their dimensions are kept as small as possible to prevent potential leakage. Due to the available fabrication process, the diameter of these vias is 0.254 mm with an edge-to-edge distance of 0.254 mm as well. It can be observed in Figure 5.9 that the effects of the synthesized via rows are negligible.

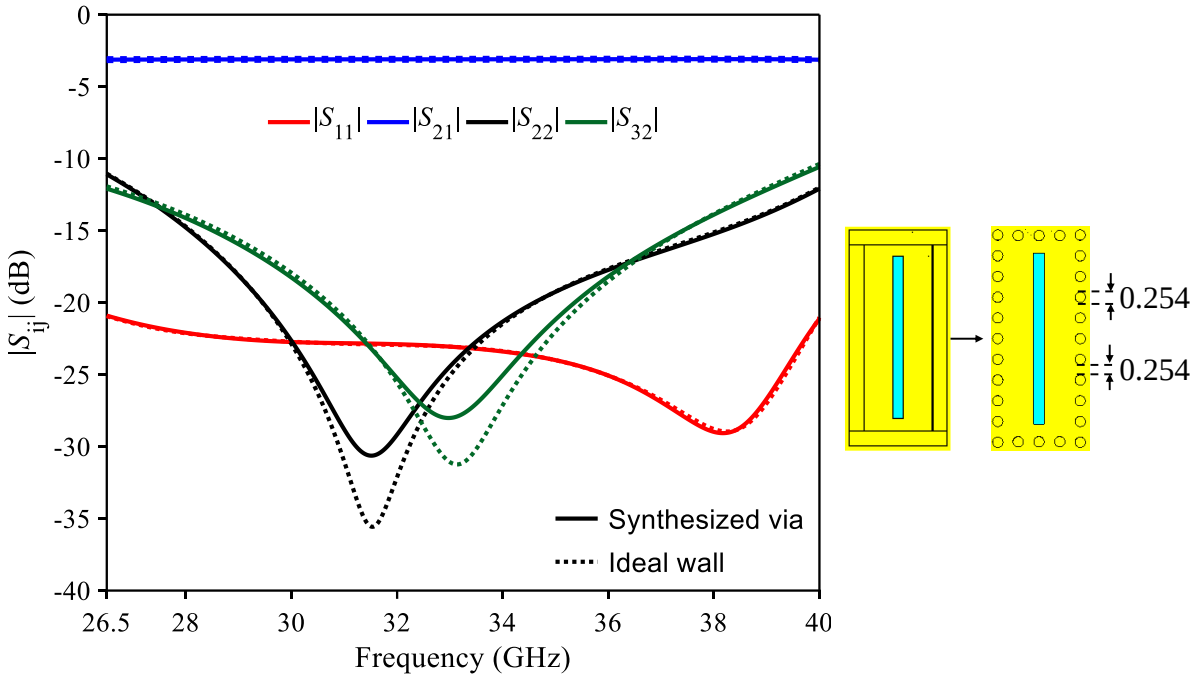

Figure 5.9 Synthesize of delta-port by metallic via rows.

Two approaches will be presented to realize the isolated power divider/combiner: resistive and absorptive solutions.

5.3 Resistive solution

The topology of the AFSIW power divider/combiner based on resistors is shown in Figure 5.10, where all parameters are given in millimeters. Layer S1 and S3 are symmetric about layer S2. In this approach, port 4 and port 5 will be terminated by resistors.

The value of resistors is chosen to match the characteristic impedance of the delta-ports. For a non-TEM propagating mode in such DFSIW structures, the definitions of characteristic impedances of these waveguides are not unique and depending on the calculation method

power-current (P-I), voltage-current (V-I), or power-voltage (P-V). To overcome this issue, a closed-form equation was developed using the *S*-parameter de-embedding algorithm in [84] to calculate the characteristic impedance in a DFSIW structure. According to [84], the characteristic impedance Z_0 of a DFSIW (port 4 and port 5) at frequency f can be calculated as follows:

$$Z_0 = \sqrt{2}\frac{h_d}{a_d}\frac{\eta}{\sqrt{\varepsilon_r}}\frac{1}{\sqrt{1-\left(\frac{f_c}{f}\right)^2}}, \tag{47}$$

where a_d and h_d are the total width and the height of the DFSIW, respectively, ε_r is the relative permittivity of the dielectric, $\eta = 120\pi$ is the free-space impedance, and f_c is the cut-off frequency of the DFSIW.

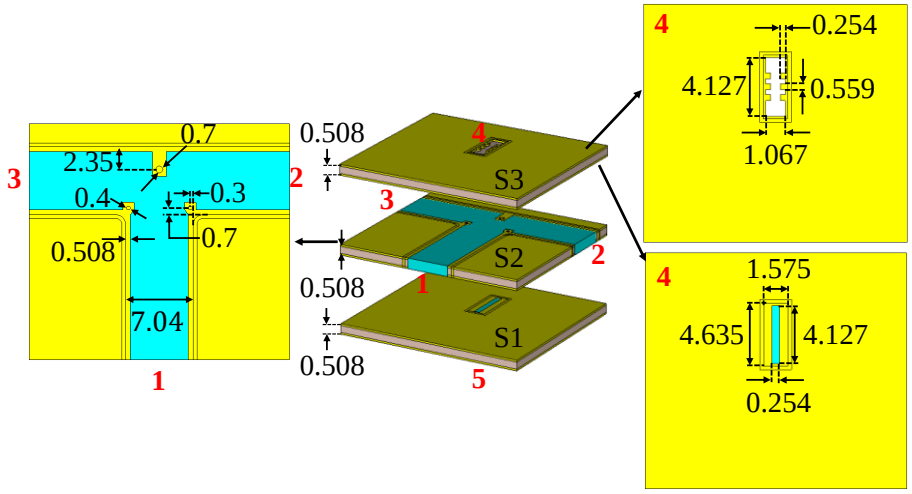

(*a*) (*b*) (*c*)

Figure 5.10 AFSIW power divider/combiner based on resistors : (*a*) top view of layer S2, (*b*) 3D view, and (*c*) top and bottom views of layer S3.

Regarding the dimensions of port 4 and port 5 given in Figure 5.10, the obtained calculated characteristic impedance is $Z_0 = 129\ \Omega$ at 33 GHz. For demonstration, one resistor with resistance $R_0 = 100\ \Omega$ (CH0402-100RGFTA from Vishay Sfernice [85]) is chosen to terminate each port.

The fabricated prototype of the AFSIW power divider/combiner using resistors is shown in Figure 5.11 [86]. Transitions from AFSIW to DFSIW and then to GCPW are used for measurement purposes. Direct connection from AFSIW to other circuits could be made in a

complete system. The delta-ports (port 4 and port 5) on top and bottom layers are synthesized by metallic via rows. The diameter of via is 0.254 mm with an edge-to-edge distance of 0.254 mm to neglect the discontinuity effect.

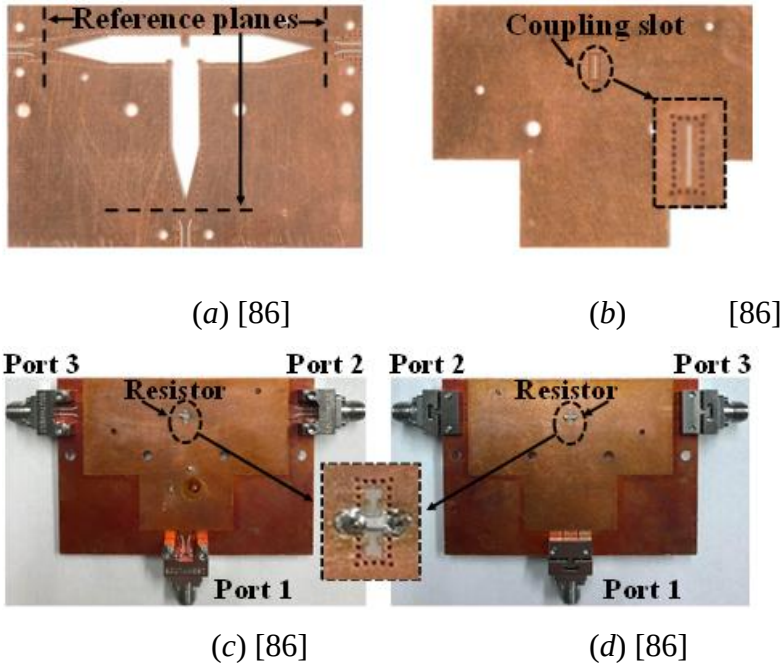

(*a*) [86] (*b*) [86]

(*c*) [86] (*d*) [86]

Figure 5.11 Fabricated prototype of AFSIW power divider/combiner using resistors : (*a*) top view of layer S2, (*b*) top view of layer S1 (bottom view of layer S3), (*c*) top view of the final circuit, and (*d*) bottom view of the final circuit [86].

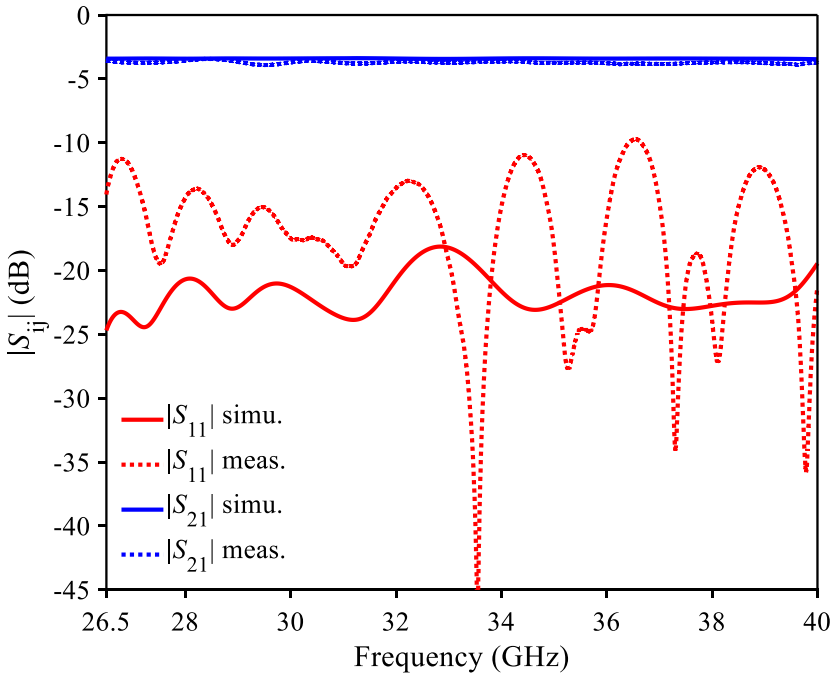

Figure 5.12 Simulated and measured return loss $|S_{11}|$ and insertion loss $|S_{21}|$ of the balanced-delta-port magic-Tee [86].

In measurement, a TRL calibration was used to remove the effect of the GCPW to DFSIW transitions. The measured and simulated reference planes are shown in Figure 5.11(*a*). The simulated and measured return loss $|S_{11}|$ and insertion loss $|S_{21}|$ are compared in Figure 5.12 [86], where a good agreement can be observed. The measured return loss $|S_{11}|$ is better than 10 dB in almost the whole frequency range. More reflections occur in measurement due to the assembling process. The measured insertion loss is $|S_{21}| = -3.68 \pm 0.25$ dB compared to $|S_{21}| = -3.42 \pm 0.04$ dB in simulation. More losses are observed in measurement due to the assembling process and the surface roughness that is not considered in the simulation.

The simulated and measured return loss $|S_{22}|$ and isolation $|S_{32}|$ are compared in Figure 5.13 [86], where a good agreement can be observed. At high frequency, the parasitic elements in resistors become important and cause the differences between simulation and measurement. The measured -10 dB bandwidth for both return loss $|S_{22}|$ and isolation $|S_{32}|$ is from 30.1 GHz to 40 GHz, which is about 28% centered at 35 GHz.

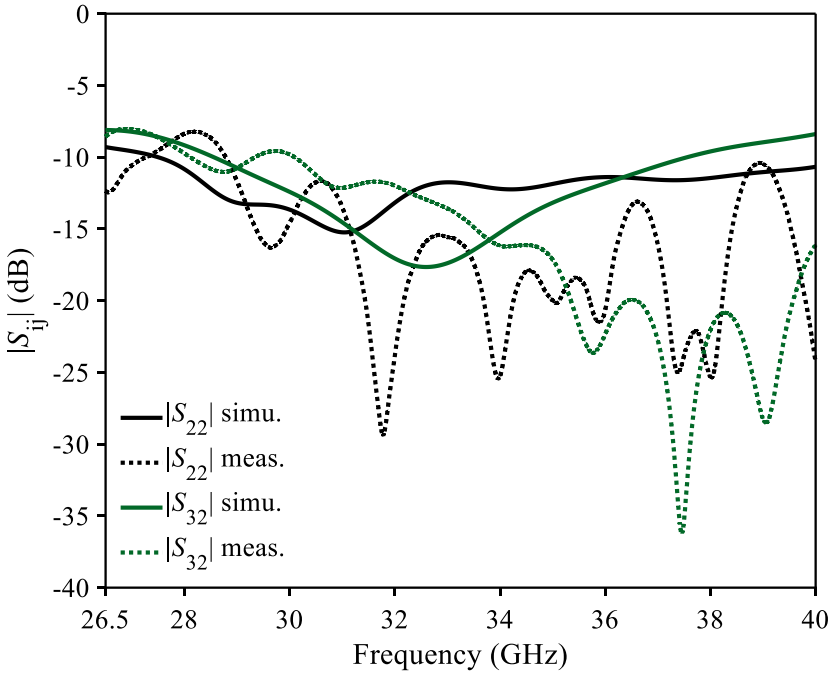

Figure 5.13 Simulated and measured return loss $|S_{22}|$ and isolation $|S_{32}|$ of the balanced-delta-port magic-Tee [86].

The measured imbalances between port 2 and port 3 are shown in Figure 5.14 [86]. Over the entire Ka-band, the AFSIW isolated power divider/combiner presents a maximum amplitude imbalance of 0.44 dB and a maximum phase imbalance of 4.2°. A good balance between port 2

and port 3 can be observed thanks to the proposed structure. The resistors are implemented at the delta-ports not to perturb the signal flows in the middle layer.

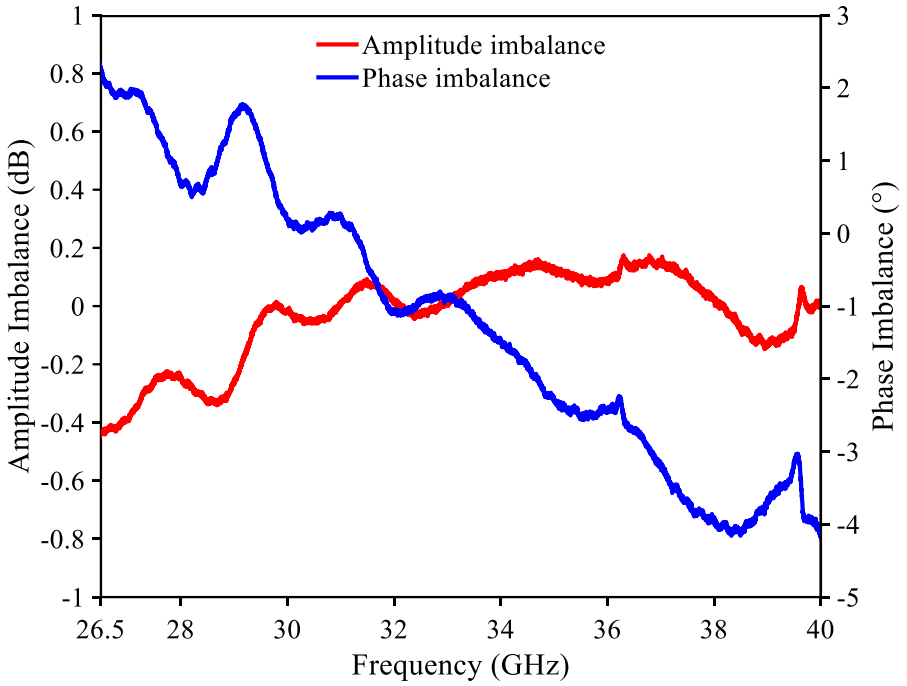

Figure 5.14 Measured phase imbalance and amplitude imbalance between port 2 and port 3 [86].

At high frequency, the power handling capability of this proposed structure is limited by the rated power of the resistors. To overcome this issue, carbon paste can be used as a resistive layer at the delta-ports to dissipate energy or absorbing materials could be placed at the output of the delta-ports as will be introduced in the following section.

5.4 Absorptive solution

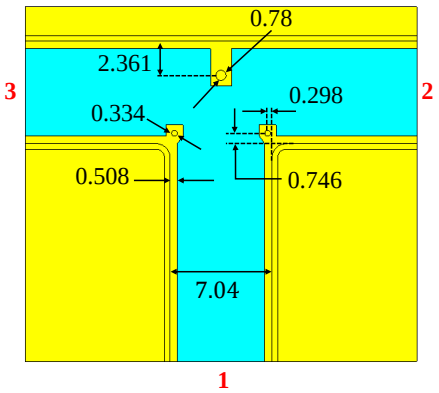

Figure 5.15 The middle layer used for the three versions of AFSIW power divider/combiner based on absorbing material.

In this section, three versions based on different coupling schemes will be presented and demonstrated. To simplify the analysis, the middle layer of the three versions is kept identical, as shown in Figure 5.15, where all dimensions are given in millimeters.

5.4.1 Version 1 – Waveguide coupling

The topology of the AFSIW absorptive power divider/combiner based on the waveguide coupling scheme and the simulated power loss density in the absorber is shown in Figure 5.16 with all parameters given in millimeters. Layer S1 and S3 are symmetric about layer S2.

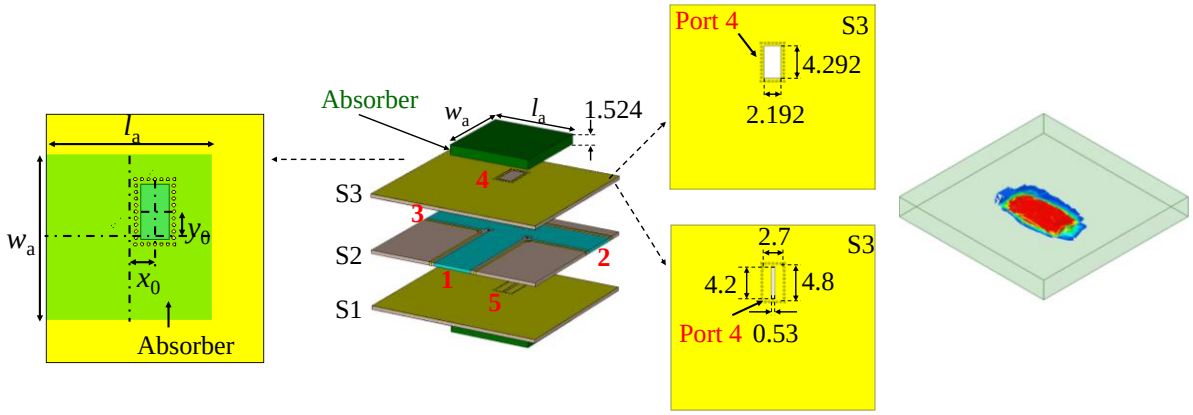

(*a*) [82] (*b*) (*c*) (*d*) [82]

Figure 5.16 Version 1: (*a*) absorber misalignment [82], (*b*) 3D view, (*c*) layer S3, and (*d*) simulated power loss density in absorber at 33 GHz when port 3 is excited [82].

The delta-ports are designed to satisfy the mode supporting condition as well as to neglect the effect of discontinuity as mentioned in 5.2. Instead of terminating the delta-ports by resistors, absorbing materials are implemented at the output of delta-ports. The absorbing material Eccosorb GDS silicone rubber ($\varepsilon_r = 13$, $\tan\delta_d = 0.2$, $\mu_r = 1.7$, $\tan\delta_m = 0.78$) was provided with adhesive. Two absorber layers of 0.762 mm were cascaded to realize a total thickness of 1.524 mm.

The effect of the adhesive layer on the return loss $|S_{33}|$ and isolation $|S_{32}|$ was carried out in simulation and shown in Figure 5.17 by assuming that the adhesive layer has a thickness of 10 μm with a relative permittivity $\varepsilon_r = 3.5$ and $\tan\delta = 0.03$ [82]. It can be observed in Figure 5.17 that the adhesive layers present a negligible effect on the return loss $|S_{33}|$ and isolation $|S_{32}|$ in version 1. The influences of the adhesive layers on return loss $|S_{11}|$ and insertion loss $|S_{21}|$ were not investigated since the delta-ports are isolated from port 1. In the simulation,

the effect of adhesive layers on the three versions can be neglected, only the simulated results in version 1 are presented.

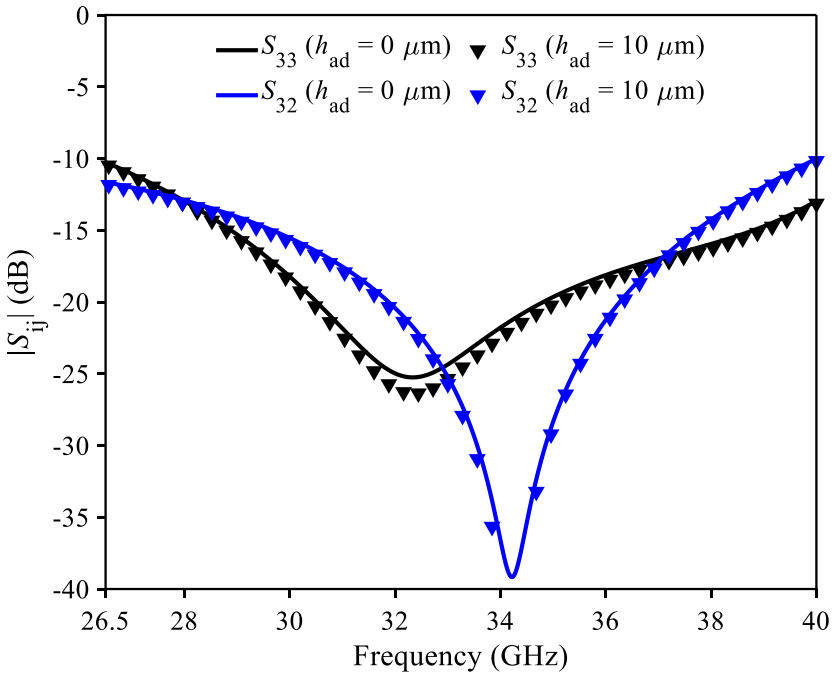

Figure 5.17 Effect of the adhesive layer on the response of version 1 (w_a = l_a = 12.9 mm and x_0 = y_0 = 0 mm) [82].

After cascading the two layers of absorbing material, the absorber was mounted at the output of the delta-ports using the adhesive layer. During the manual assembling process, misalignment and cutting errors could occur as illustrated in Figure 5.16(*a*) which cause in a different dimension ($l_a \times w_a$) of absorber as well as an offset position ($x_0 \times y_0$) from the center of the delta-ports.

Again, the effect of absorber misalignment and dimensions will not be investigated for return loss $|S_{11}|$ and insertion loss $|S_{21}|$.

Regarding return loss $|S_{33}|$ and isolation $|S_{32}|$, the effect of absorber dimensional error is studied in simulation and presented in Figure 5.18 [82]. It could be noticed from Figure 5.18 that the influence of absorber dimensional errors on the return loss $|S_{33}|$ and isolation $|S_{32}|$ is negligible once the absorber can cover the area of the delta-ports to absorb power. This hypothesis is confirmed by the power loss density shown in Figure 5.16(*d*).

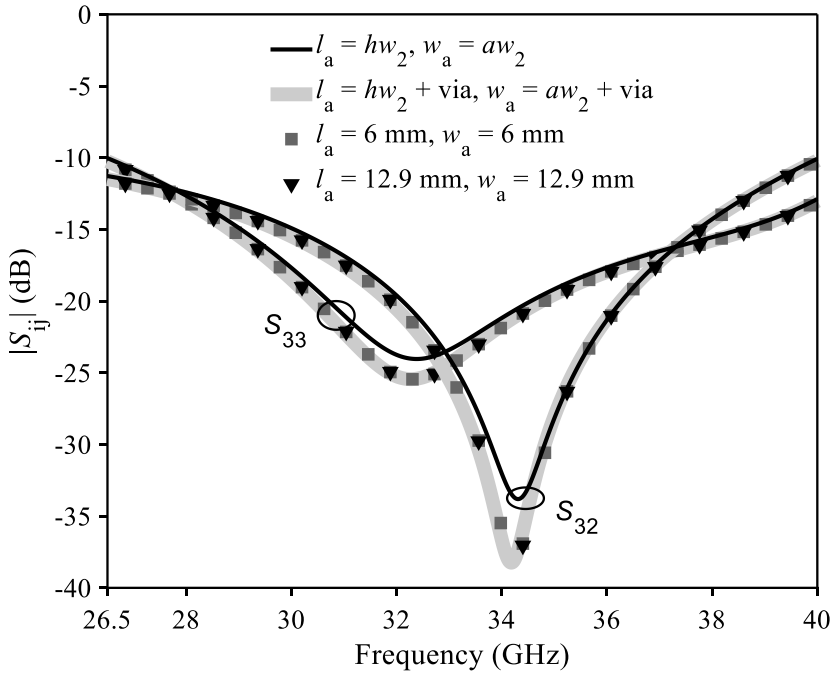

Figure 5.18 Effect of absorber dimensional errors on the responses of version 1 ($x_0 = y_0 = 0$ mm). $hw_2 \times aw_2$ represents the area covered by delta-port and (hw_2 + via) × (aw_2 + via) represents the area covered by the waveguide and two metallic via walls [82].

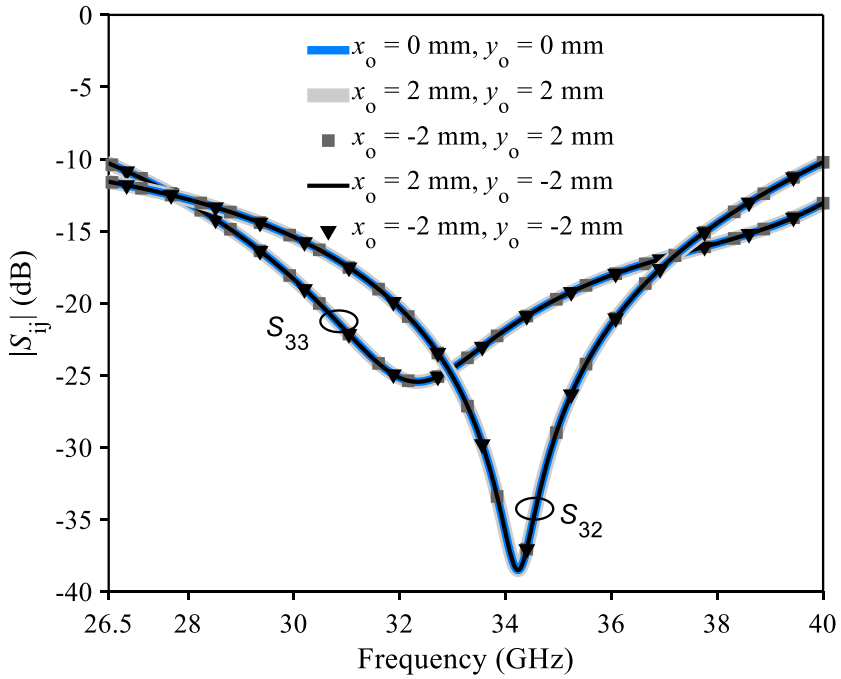

Figure 5.19 Effect of absorber misalignment on the responses of version 1 ($l_a = w_a$ = 12.9 mm) [82].

The effect of absorber misalignment on the return loss $|S_{33}|$ and isolation $|S_{32}|$ is simulated and presented in Figure 5.19 [82]. In the simulation, a maximum offset of 2 mm was studied. In fact, the manual assembling process precision is better than 2 mm. It can be observed in Figure 5.19 that the absorber misalignment introduces a negligible effect on the responses of version 1. In this investigation, the absorber always covers the area of delta-ports with a maximum offset of 2 mm. Therefore, the responses of version 1 are insensitive to this change.

These interesting results confirm that by placing absorbing material at the output of delta-ports, the version 1 of AFSIW power divider/combiner is error-tolerant to the absorber misalignment and dimensions as well.

After mounting to the PCB, the absorbing materials are covered by RFI shields MS135-20C from Masach Tech to prevent potential leakage, especially at high power applications. The implementation of the RFI shield is shown in Figure 5.20.

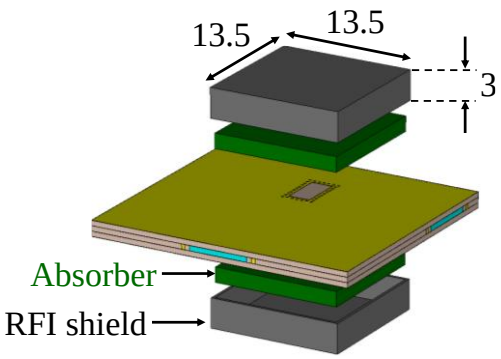

Figure 5.20 Implementation of RFI shield in version 1.

For demonstration, the absorber size is chosen as $l_a = w_a = 12.9$ mm to have the RFI shield filled. The fabricated prototype of version 1 is shown in Figure 5.21 [82].

In measurement, a TRL calibration kit was used to remove the effect of the GCPW to AFSIW transitions. The simulated and measured reference planes are shown in Figure 5.21(*b*).

The proposed circuit was simulated with and without RFI shields to evaluate its effect on the responses of the power divider/combiner. Meanwhile, the measurement was carried out with RFI shields.

The simulated and measured return loss $|S_{11}|$ and insertion loss $|S_{21}|$ are compared in Figure 5.22 [82], where a good agreement can be observed. It can be noticed from Figure 5.22 that the RFI shield has no effect on the circuit responses since the energy at delta-ports is well absorbed by

the absorber. However, the presence of the RFI shields enhances the electromagnetic compatibility (EMC) of the whole structure. The measurement shows a maximum return loss $|S_{11}|$ of -12 dB over the entire Ka-band. The measured insertion loss is $|S_{21}| = -3.59 \pm 0.51$ dB. More losses are observed in measurement due to errors in the manual assembling process that could lead to a potential gap between layers.

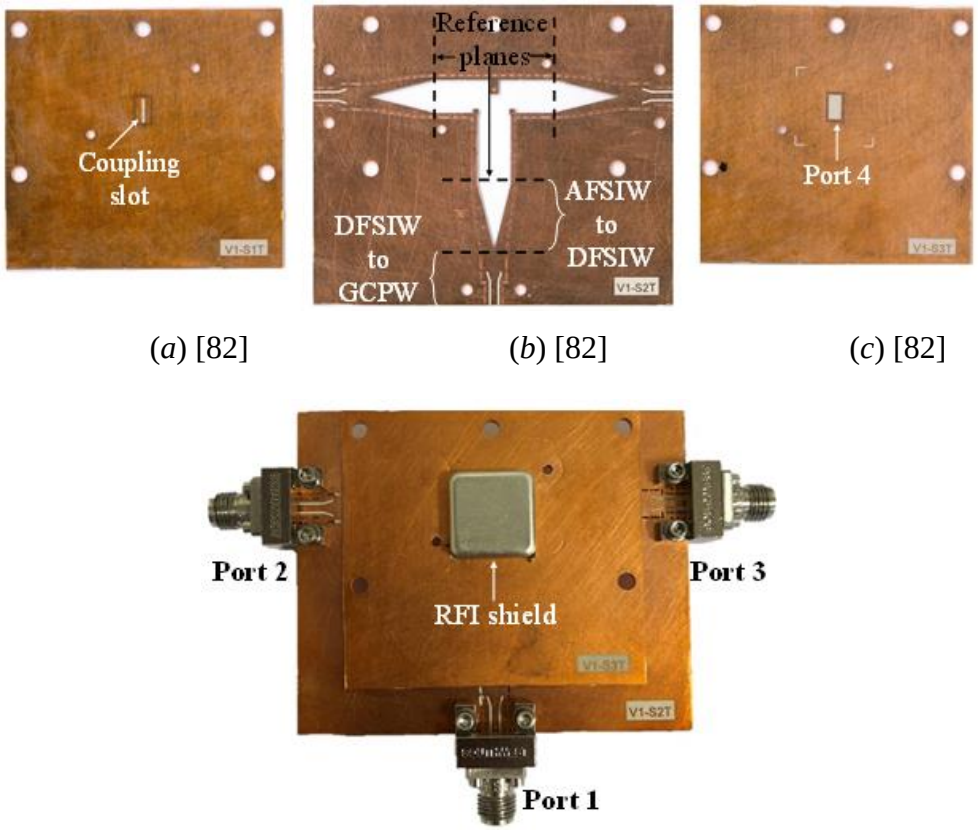

(*a*) [82] (*b*) [82] (*c*) [82]

(*d*) [82]

Figure 5.21 Fabricated prototype of version 1: (*a*) top view of layer S1 [82], (*b*) top view of layer S2 [82], (*c*) bottom view of layer S3 [82], and (*d*) the assembled circuit [82].

The simulated and measured return loss $|S_{33}|$ and isolation $|S_{32}|$ are compared in Figure 5.23 [82]. Again, the effect of the RFI shields is negligible. The measurement results show good agreement with the simulation. In measurement, the return loss $|S_{33}|$ is better than -10 dB over the entire Ka-band while the 10 dB isolation level of $|S_{32}|$ covers 38.8% bandwidth at the center frequency of 33.5 GHz. In the simulation, both the return loss $|S_{33}|$ and isolation $|S_{32}|$ are better than -10 dB over the Ka-band.

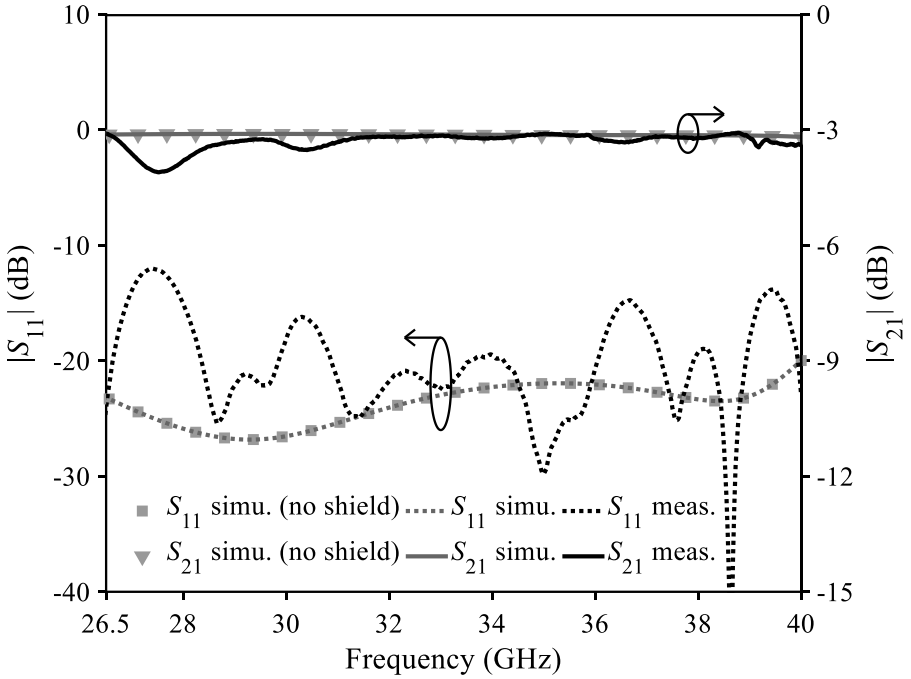

Figure 5.22 Simulated and measured return loss $|S_{11}|$ and insertion loss $|S_{21}|$ of version 1 [82].

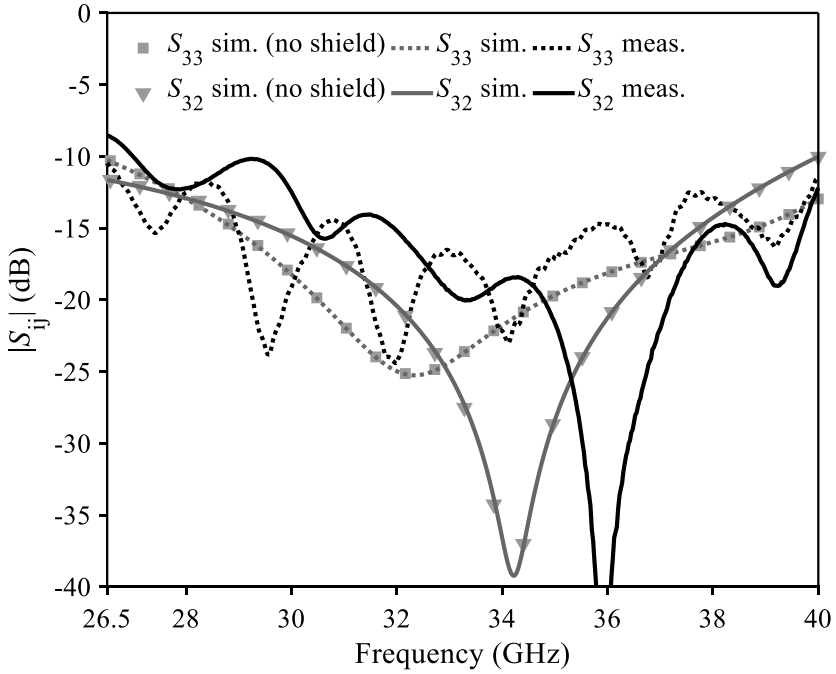

Figure 5.23 Simulated and measured return loss $|S_{33}|$ and isolation $|S_{32}|$ of version 1 [82].

The measured imbalances between port 2 and port 3 are shown in Figure 5.24 [82]. The measurement results show an amplitude imbalance of AI = 0.11 ± 0.4 dB and a phase imbalance of PI = -0.2 ± 3.71° over the Ka-band.

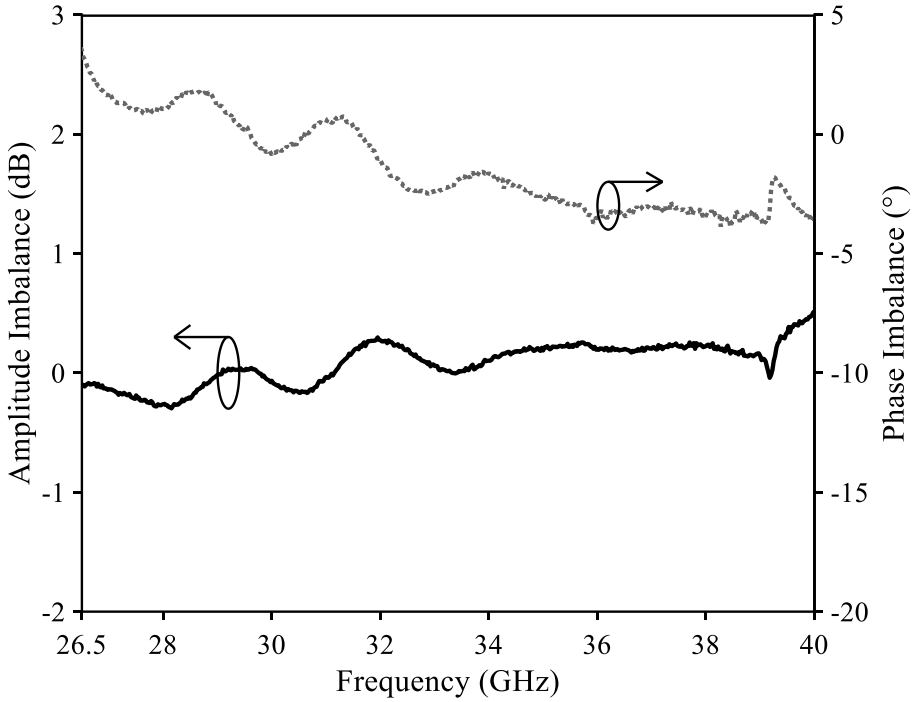

Figure 5.24 Measured amplitude imbalance and phase imbalance between port 2 and port 3 of version 1 [82].

5.4.2 Version 2 – Slot coupling

It can be observed in Figure 5.16(*d*) that the power concentrates at the output of the delta-ports. This phenomenon could lead to limitations in power handling capability in high power applications. Therefore, version 2 was investigated to spread out the power as well as to increase the design flexibility. The topology of version 2 based on slot coupling is shown in Figure 5.25 together with the simulated power loss density at 33 GHz where all dimensions are given in millimeters. The coupling slot at the bottom of layer S3 can be represented by an admittance Y_s (see Figure 5.25(*a*)). When port 2 or port 3 is excited, the energy from the middle layer (S2) is coupled through the slot to layer S1 and S3. This power will then be absorbed by the absorbing material placed at the output. This way, power is better spreading out in the absorber compared to version 1 (see Figure 5.25(*d*)). RFI shield are used to cover the absorbers for EMC improvement. In layers S1 and S3, metallic via walls having the same area with RFI shields (13.5×13.5 mm^2) were implemented to prevent potential parallel plate mode.

Similar to version 1, the dimensions of the absorber can be modified due to fabrication errors. The effects of absorber dimensional errors on the return loss $|S_{33}|$ and isolation $|S_{32}|$ were investigated in simulation and are shown in Figure 5.26 where λ is the wavelength in the dielectric.

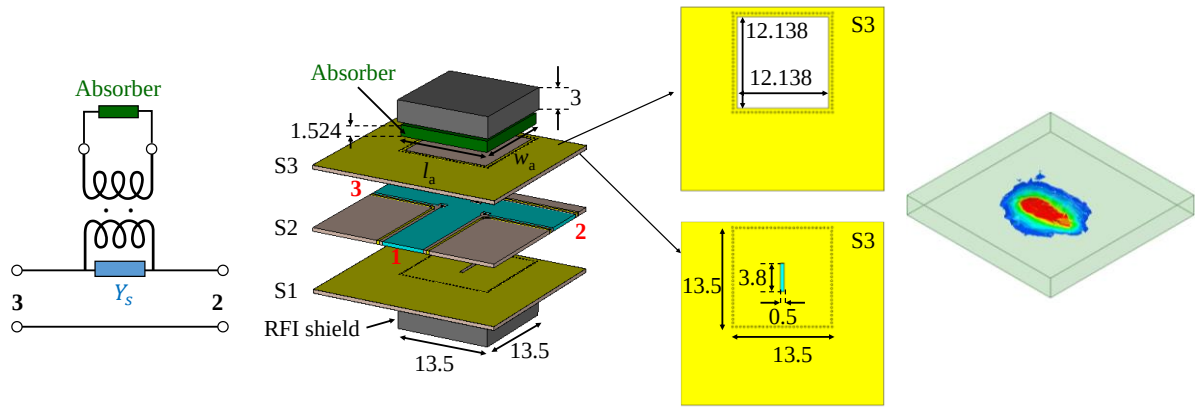

(*a*) [82] (*b*) (*c*) (*d*) [82]

Figure 5.25 Version 2: (*a*) coupling scheme [82], (*b*) 3D view, (*c*) layer S3, and (*d*) simulated power loss density in absorber at 33 GHz when port 3 is excited [82].

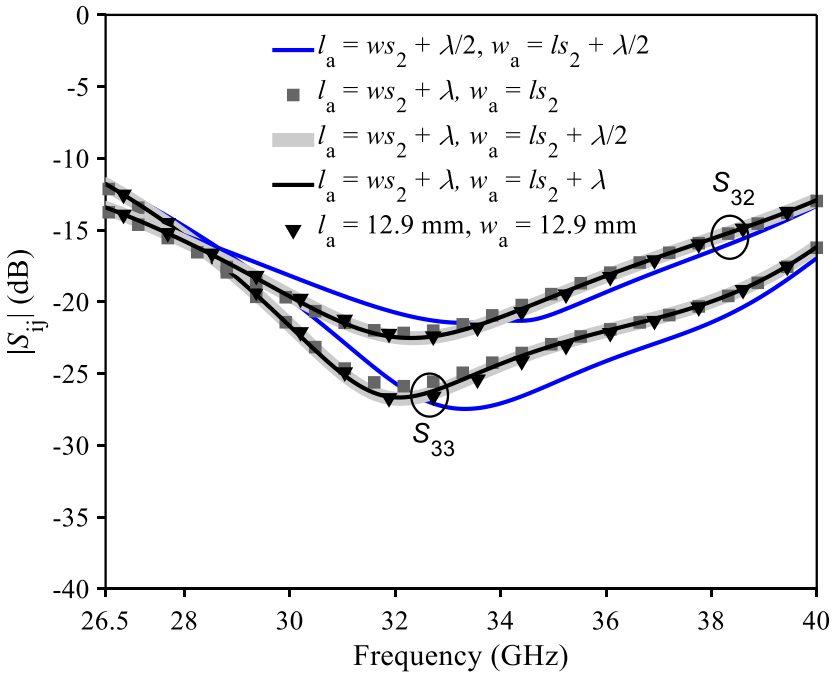

Figure 5.26 Effect of absorber dimensional errors on the responses of version 2 ($x_0 = y_0 = 0$ mm). $ws_2 \times ls_2$ represents the dimension of the coupling slot [82].

The simulation results show stable responses once the absorbing material can cover an area of about one λ around the slot. For an error-tolerant response, the dimension of absorbing material should be $l_a \geq ws_2 + \lambda$ and $w_a \geq ls_2$, where ws_2 and ls_2 are the width and the length of the coupling slot, respectively. In this case, $ws_2 = 0.5$ mm and $ls_2 = 3.8$ mm.

Also, the absorber could be offset regarding the center as in version 1. The effect of absorber misalignment on the return loss $|S_{33}|$ and isolation $|S_{32}|$ was studied in simulation and is

presented in Figure 5.27. Again, the responses of version 2 are seen to be insensitive to the absorber misalignment once the covered area is sufficient as mentioned above.

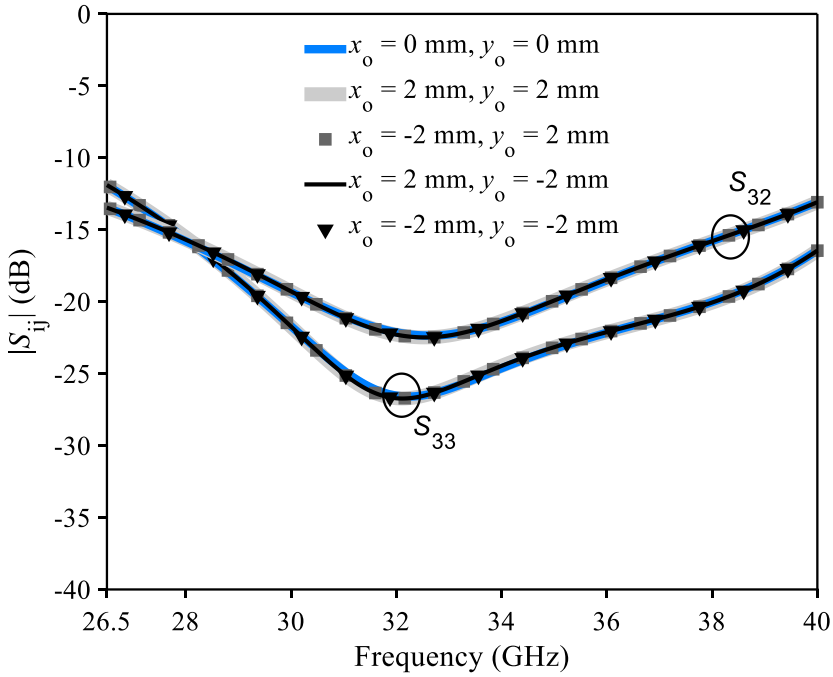

Figure 5.27 Effect of absorber misalignment on the responses of version 2 (l_a = w_a = 12.9 mm) [82].

The fabricated prototype of version 2 is shown in Figure 5.28 [82]. Again, a TRL calibration kit was used in measurement to remove the effect of GCPW to AFSIW transitions.

The simulated and measured return loss $|S_{11}|$ and insertion loss $|S_{21}|$ are compared in Figure 5.29 [82], where a good agreement can be observed. The measured insertion loss is $|S_{21}|$ = -3.64 ± 0.49 dB. More losses are observed in measurement due to the manual assembling process and the surface roughness that is not considered in the simulation. However, the return loss $|S_{11}|$ is lower than -14 dB over the whole Ka-band.

The simulated and measured return loss $|S_{33}|$ and isolation $|S_{32}|$ are presented in Figure 5.30 [82] with a good agreement. Both simulation and measurement show broadband responses over the Ka-band with a return loss $|S_{33}|$ and isolation $|S_{32}|$ both better than -10 dB. From 28.6 GHz to 37.3 GHz, the measured return loss $|S_{33}|$ and isolation $|S_{32}|$ are lower than -15 dB (about 26.4% at the center frequency of 32.95 GHz).

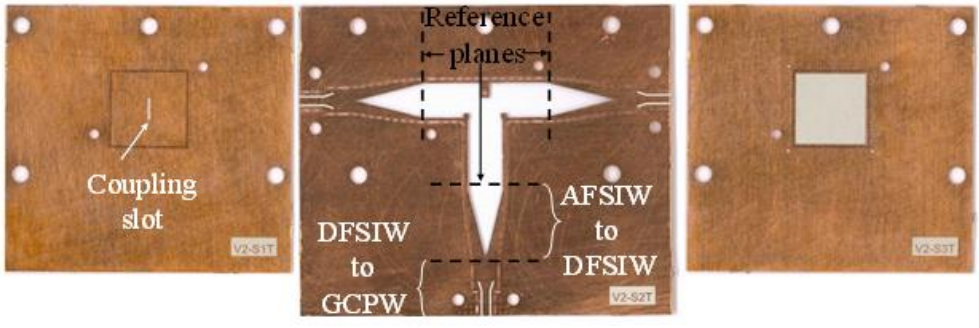

(*a*) [82] (*b*) [82] (*c*) [82]

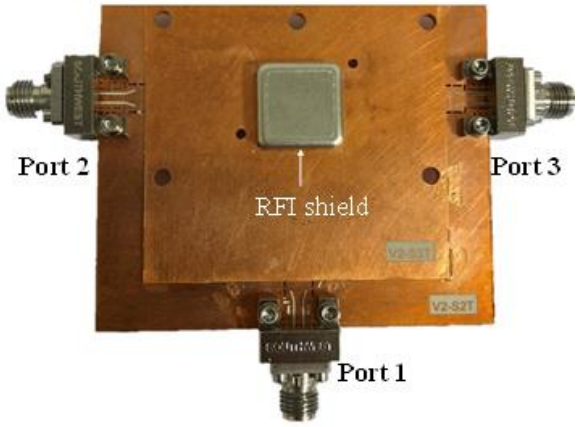

(*d*) [82]

Figure 5.28 Fabricated prototype of version 2: (*a*) top view of layer S1 [82], (*b*) top view of layer S2 [82], (*c*) bottom view of layer S3 [82], and (*d*) the assembled circuit [82].

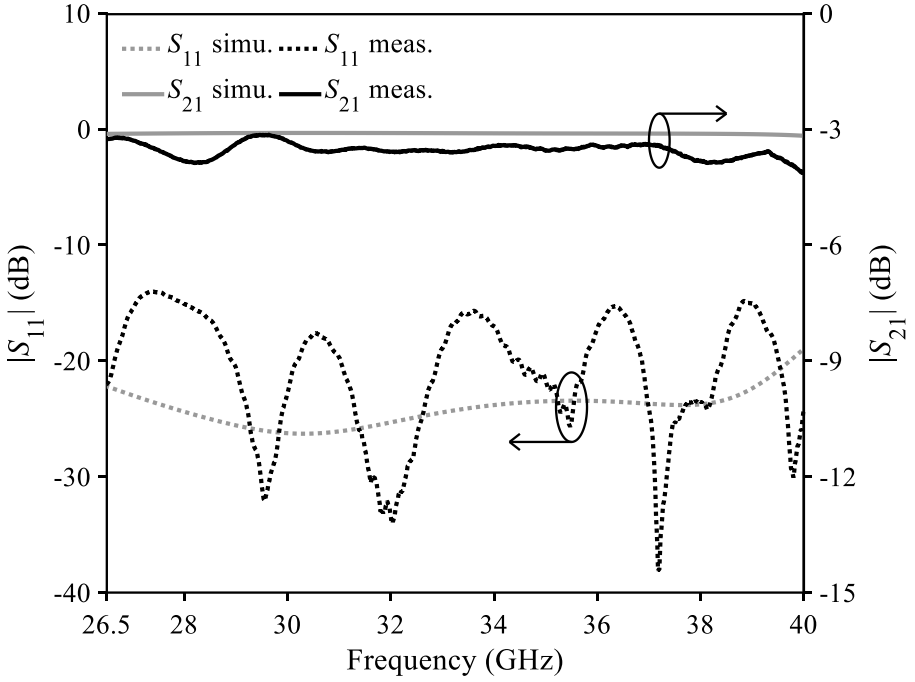

Figure 5.29 Simulated and measured return loss $|S_{11}|$ and insertion loss $|S_{21}|$ of version 2 [82].

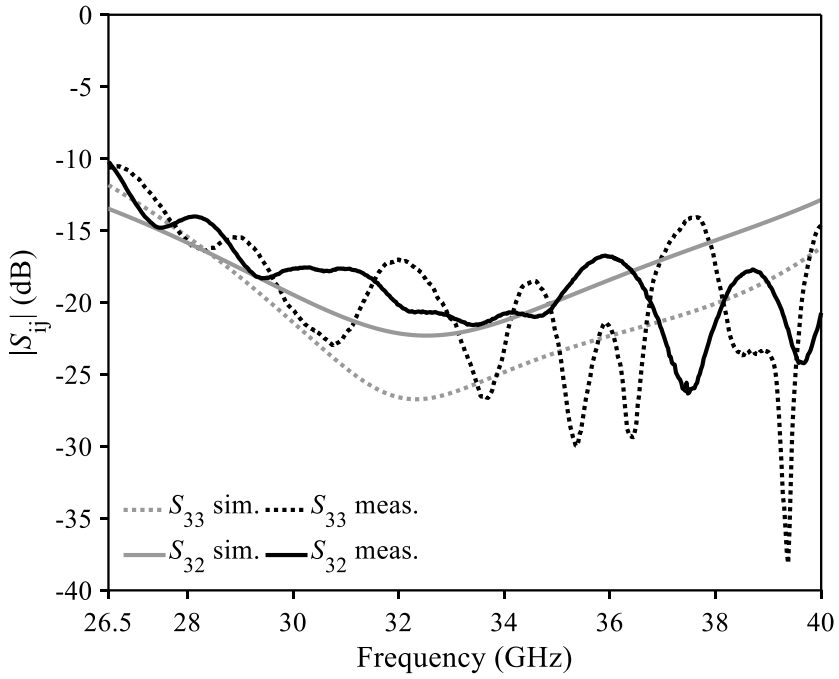

Figure 5.30 Simulated and measured return loss $|S_{33}|$ and isolation $|S_{32}|$ of version 2 [82].

The imbalances between port 2 and port 3 are presented in Figure 5.31 [82]. The measurement shows an amplitude imbalance of AI = -0.03 ± 0.43 dB and a phase imbalance of PI = -0.89 ± 2.25° over the entire Ka-band.

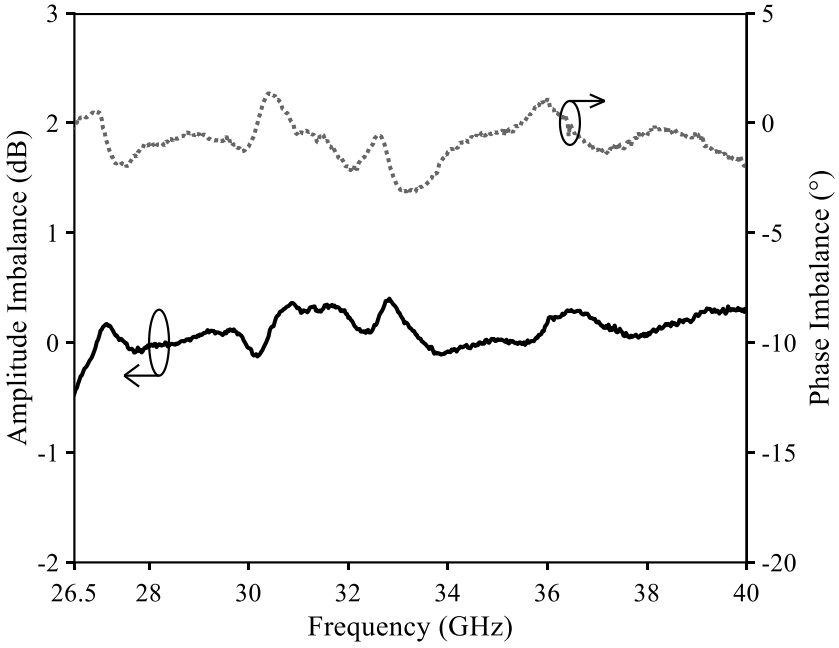

Figure 5.31 Measured amplitude imbalance and phase imbalance between port 2 and port 3 of version 2 [82].

5.4.3 Version 3 – Patch coupling

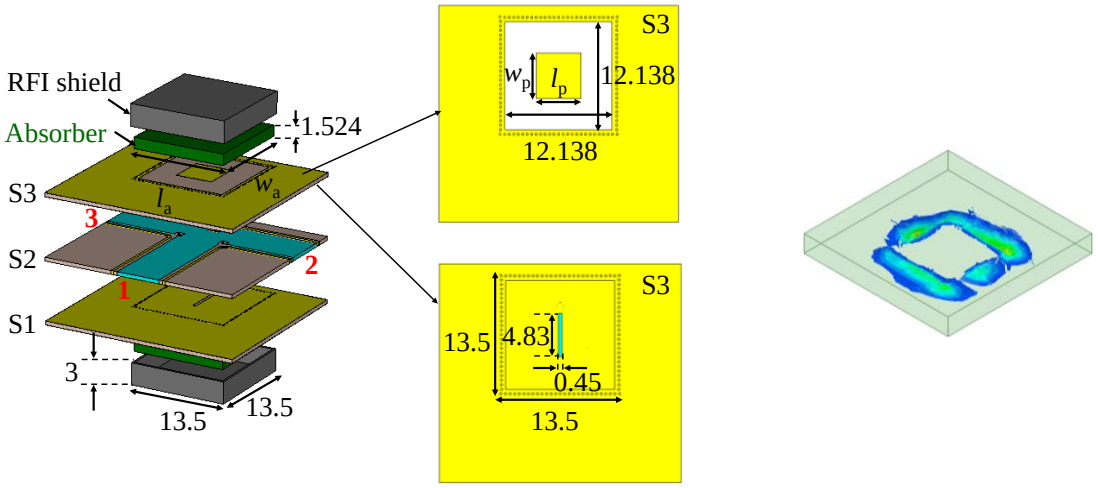

(*a*) (*b*) (*c*) [82]

Figure 5.32 Version 3: (*a*) 3D view, (*b*) layer S3, and (*c*) simulated power loss density in absorber at 33 GHz when port 3 is excited [82].

In order to spread out the power in a better way as well as to introduce the capability in controlling the isolation level, a third version was investigated. Its topology is shown in Figure 5.32. All dimensions are given in millimeters.

Similar to version 2, metallic via walls (13.5 × 13.5 mm^2) are used to prevent potential parallel plate modes in layers S1 and S3. Two slots are etched at the top of layer S1 and bottom of layer S2 with the width ws_2 = 0.45 mm and length ls_2 = 4.83 mm to couple energy to the patch ($l_p \times w_p$) at the bottom of layer S1 and top of layer S3. Absorbing materials are then placed on top of the patch to absorb the output energy. The simulated power loss density in the absorber at 33 GHz is shown in Figure 5.32(*c*). Figure 5.32(*c*) shows that power is spread out to all edges of the patch. In this way, better thermal dissipation is achieved.

For demonstration, a square patch will be used ($l_p = w_p$). The effects of the patch dimension on the return loss $|S_{33}|$ and isolation $|S_{32}|$ are simulated and presented in Figure 5.33 [82].

It can be observed in Figure 5.33 that by controlling the dimension of the microstrip patch, the return loss $|S_{33}|$ as well as the isolation $|S_{32}|$ can be tuned to the desired level. In fact, by changing the dimension of the patch, the coupling coefficient between the slot and the microstrip patch will change which leads to the change of the return loss $|S_{33}|$ and the isolation $|S_{32}|$. For demonstration, the dimension of the square microstrip patch was chosen as $l_p = w_p$ = 5.1 mm for a 10 dB broadband isolation $|S_{32}|$ and return loss $|S_{33}|$.

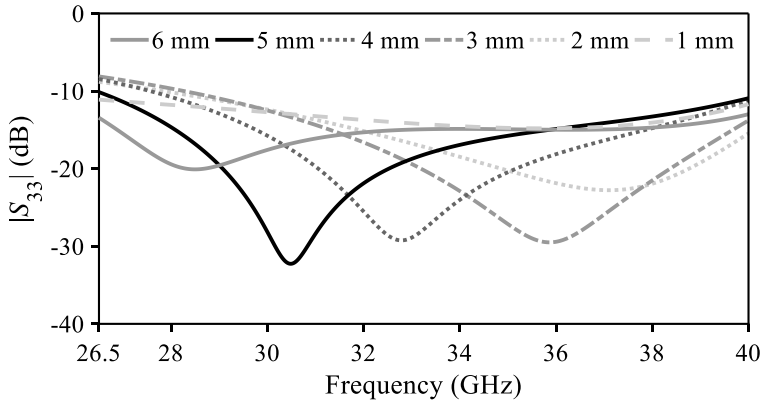

(*a*) [82]

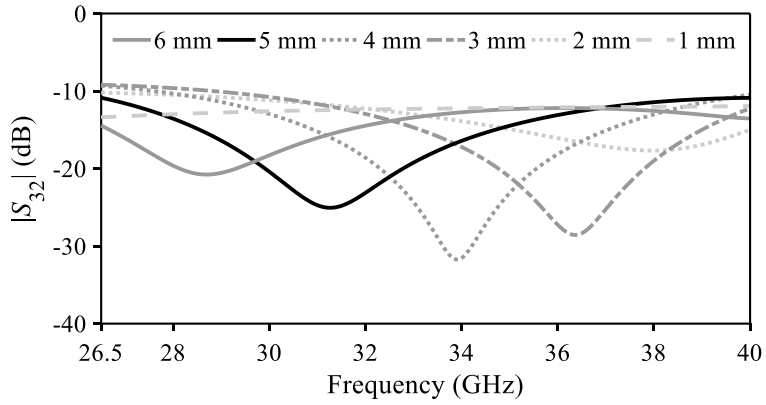

(*b*) [82]

Figure 5.33 Effect of square patch dimension on the (*a*) return loss and (*b*) isolation of version 3 [82].

Similar to the two previous versions, the effects of the absorber dimensional errors and misalignment are investigated in simulation to highlight the error-tolerant characteristic of the proposed structure.

The influences of absorber dimensional errors on the return loss $|S_{33}|$ and the isolation $|S_{32}|$ are shown in Figure 5.34 [82]. In the simulation, the responses are seen to be stable once the absorber dimension satisfies the condition: $l_a \geq l_p + \lambda$ and $w_a \geq w_p + \lambda/2$, where λ is the dielectric wavelength. This condition assumes the absorption of the fringing field at the edges of the microstrip patch [87].

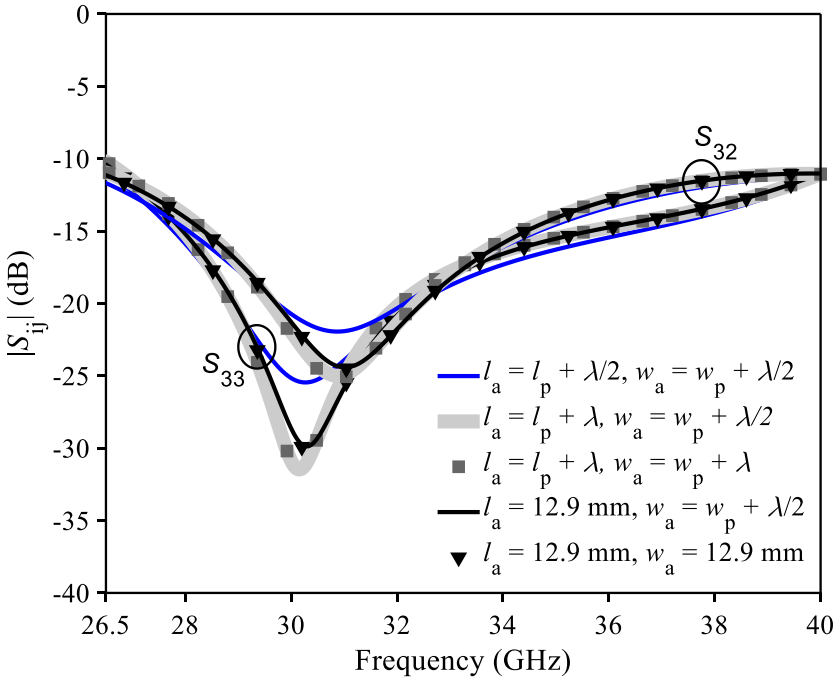

Figure 5.34 Effect of absorber dimensional errors on the responses of version 3 ($x_0 = y_0 = 0$ mm). $ws_2 \times ls_2$ represents the dimension of the coupling slot [82].

The effect of absorber misalignment on the return loss $|S_{33}|$ and the isolation $|S_{32}|$ are presented in Figure 5.35 [82]. Once the covered area of the absorber satisfies the required dimension, the responses are stable.

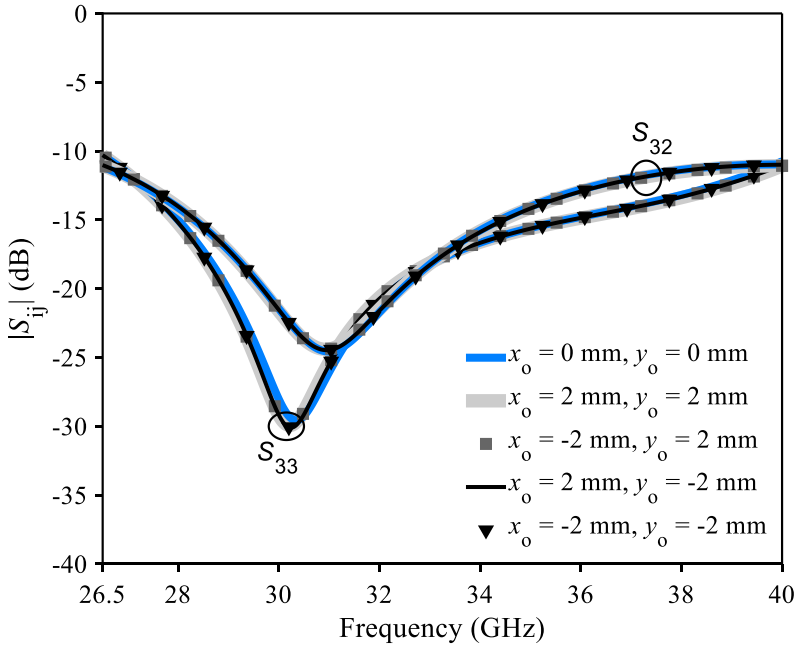

Figure 5.35 The effect of absorber misalignment on the responses of version 3 ($l_a = w_a = 12.9$ mm) [82].

The fabricated prototype of version 3 is shown in Figure 5.36 [82]. In measurement, a TRL calibration kit was used to de-embed the measurement plane to the reference plans as shown in Figure 5.36(*b*).

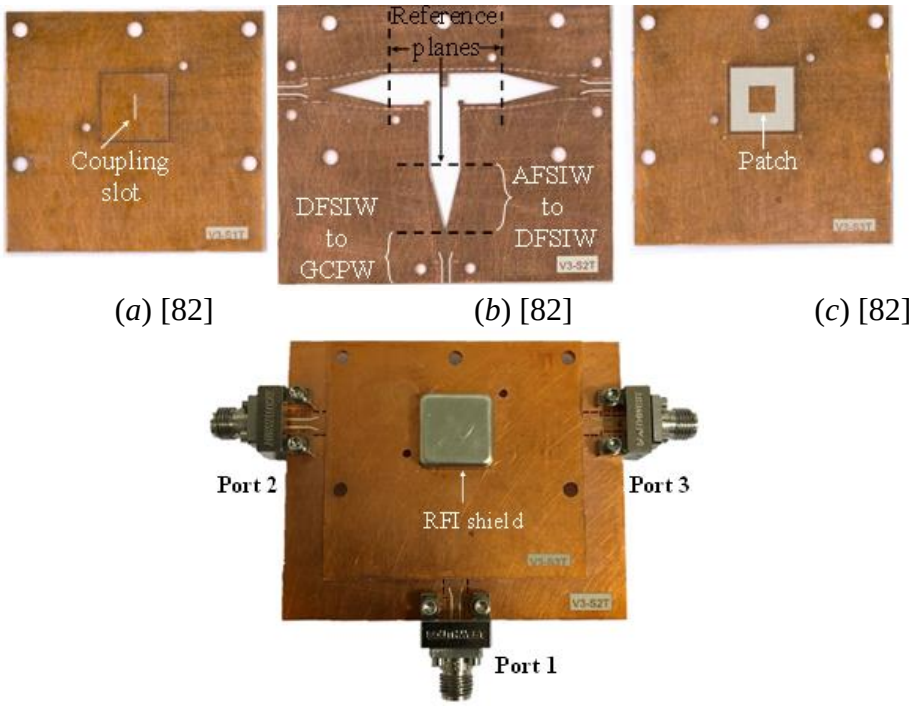

(*a*) [82] (*b*) [82] (*c*) [82]

(*d*) [82]

Figure 5.36 Fabricated prototype of version 3: (*a*) top view of layer S1 [82], (*b*) top view of layer S2 [82], (*c*) bottom view of layer S3 [82], and (*d*) the assembled circuit [82].

The simulated and measured return loss $|S_{11}|$ and insertion loss $|S_{21}|$ are compared in Figure 5.37 [82] with a good agreement. The measured insertion loss is $|S_{21}| = 3.08 \pm 0.3$ dB. Again, errors in the manual assembling process, as well as the surface roughness, contribute to the difference between simulation and measurement. Over the entire Ka-band, the return loss $|S_{11}|$ is lower than -11.6 dB.

The simulated and measured return loss $|S_{33}|$ and isolation $|S_{32}|$ are shown in Figure 5.38 [82], where the simulation and measurement results are seen to be in good agreement. Regarding the return loss $|S_{33}|$, a broadband -10 dB response is observed in both simulation and measurement. Meanwhile, the measured isolation -10 dB bandwidth is about 39.7% at the center frequency of 33.37 GHz.

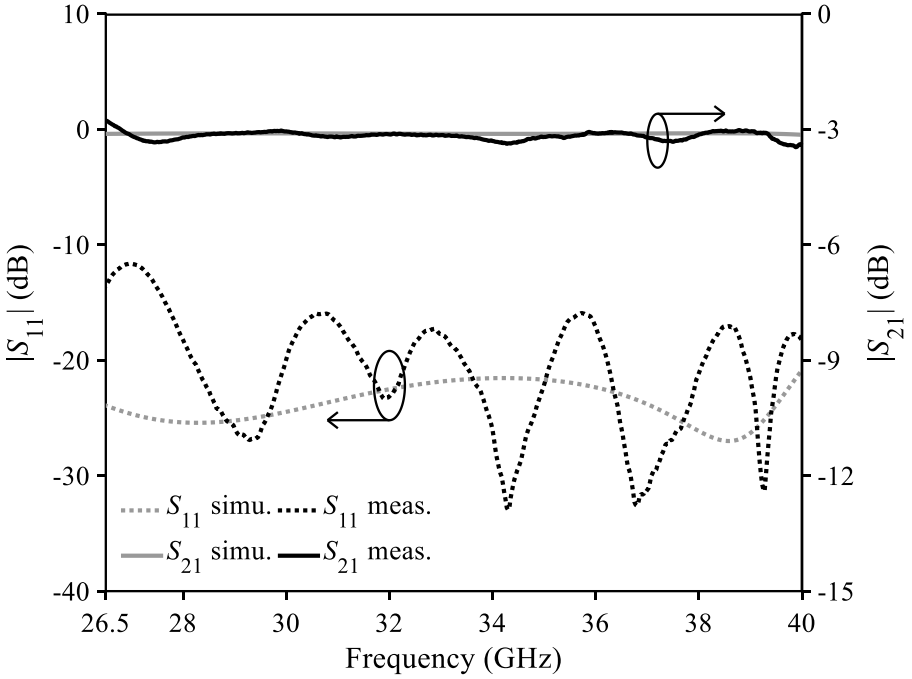

Figure 5.37 Simulated and measured return loss $|S_{11}|$ and insertion loss $|S_{21}|$ of version 3 [82].

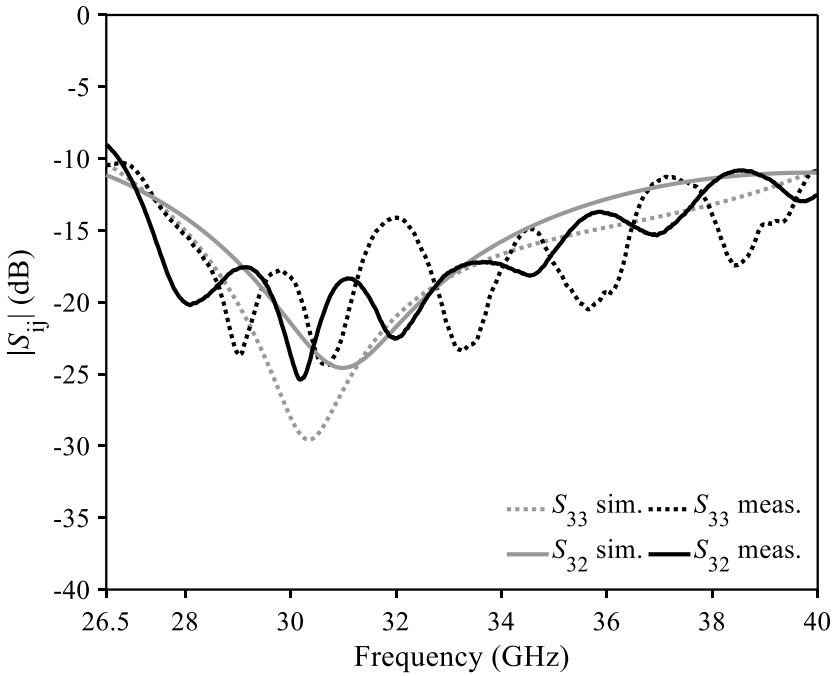

Figure 5.38 Simulated and measured return loss $|S_{33}|$ and isolation $|S_{32}|$ of version 3 [82].

The measured imbalances between port 2 and port 3 are presented in Figure 5.39 [82]. The measurement results show an amplitude imbalance of AI = 0.34 ± 0.37 dB and a phase imbalance of PI = -8.1 ± 4.86° in the whole Ka-band.

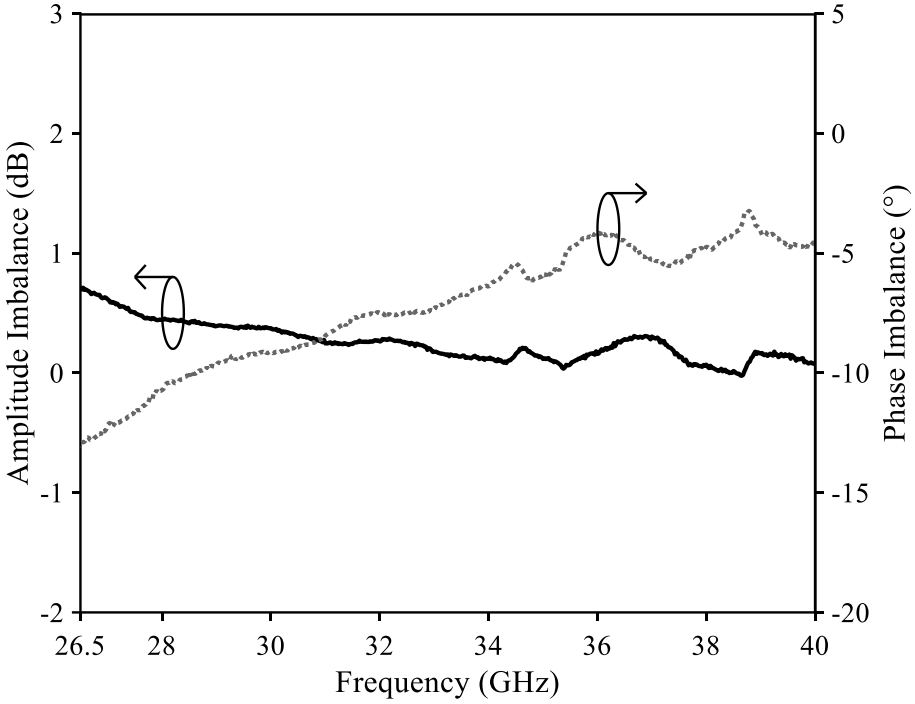

Figure 5.39 Measured amplitude imbalance and phase imbalance between port 2 and port 3 of version 3 [82].

5.4.4 Discussion on the absorptive-based solution

All of the proposed absorptive-based AFSIW power dividers/combiners possess error-tolerant characteristics (both in absorber dimensions and misalignment) thanks to the use of absorbing materials and the balanced-delta-port magic-Tee topology. The error-tolerant characteristic is an important factor considering the mass-production process.

Three different versions with different coupling schemes were proposed with their pros and cons. A qualitative comparison between the three versions could be summarized in Table 5.1.

By concentrating the electromagnetic power at the waveguide area, version 1 requires the smallest absorber size for a stable response at the expense of the lowest power handling capability, compared to the other two versions.

Version 3 gives the best power spreading in the absorber thanks to the presence of the microstrip patch. In this way, the power handling capability of version 3 is the highest. Nevertheless, the absorber dimension becomes the largest.

Version 2 is a compromise between version 1 and version 3.

The three proposed error-tolerant absorptive-based AFSIW power dividers/combiners give flexibility for an AFSIW system design.

Table 5.1 Qualitative comparison between the three absorptive-based solutions.

Version	**Version 1**	**Version 2**	**Version 3**
Absorber dimension	Smallest	Medium	Largest
Power handling capability	Smallest	Medium	Highest

5.5 Conclusion

For comparison, Table 5.2 summarizes different important characteristics of various isolated power dividers/combiners based on the SIW technology [82]. The relative bandwidth is defined with reference to the -10 dB reference for both reflection coefficients ($|S_{11}|$ and $|S_{33}|$) and isolation ($|S_{32}|$).

Table 5.2 Comparison of different isolated power dividers/combiners [82].

Reference	Technology	Lossy element	f_0 (GHz)	BW (%)
[74]	Single layer HMSIW	Resistor	26.5	64
This work (resistive solution)	**Multilayer AFSIW**	**Resistor**	**35**	**28**
[75]	Multilayer SIW	Distributed resistors	10	24
[76]	Single layer SIW	Distributed resistors	9.95	23
[78]	Multilayer SIW	Carbon paste resistive layer	10	40 (Broadband)
[80]	Single layer SIW	Absorber	16.5	42
[81]	Multilayer SIW	Absorber	12.8	50
This work (V1)	**Multilayer AFSIW**	**Absorber**	**33.5**	**38.8**
This work (V2)	**Multilayer AFSIW**	**Absorber**	**33.25**	**40.6 (Broadband)**
This work (V3)	**Multilayer AFSIW**	**Absorber**	**33.37**	**39.7**

Regarding the resistive-based solutions, the proposed AFSIW power divider/combiner presents a large relative bandwidth while maintaining the self-packaging characteristic. To the author's best knowledge, this is the first isolated power divider/combiner based on the AFSIW technological platform which uses the commercially available of-the-shelf components in

Ka-band. Instead of using resistors, distributed network of resistors or carbon-paste resistive layer could be used to terminate the delta-ports.

All the resistive-based solutions have a limitation in power handling capability due to the low rated power of resistors at high frequency. For high power applications, absorptive-based solutions are preferable. All the absorptive-based solutions found in the literature embed the absorbing materials in the guided-wave structure, which results in sensitive responses to the errors of absorber dimension and misalignment. Based on the balanced-delta-port magic-Tee, three error-tolerant AFSIW power dividers/combiners are presented and demonstrated with their advantages and disadvantages.

CHAPTER 6 CONCLUSION AND PERSPECTIVES

During this Ph.D. thesis research, several scientific and technical contributions have been made including:

- Alternative guided-wave structures named slab air-filled substrate integrated waveguide (SAFSIW) and half-mode SAFSIW were proposed with theoretical analysis and experimental demonstration. These flexibles solutions offer a larger mono-mode bandwidth together with the possibility to control the attenuation and phase constants for proper applications.
- Using the SAFSIW structures, broadband compensating phase shifters and cruciform coupler were developed and demonstrated. Thanks to the self-compensating principle, the proposed phase shifter offers a low-loss solution with a compact electrical size.
- A simple technique to reduce cross-polarization levels in multilayer antipodal linearly tapered slot antenna (ALTSA) was proposed taking the advantages of the SAFSIW structure. This ALTSA was validated with broadband, relatively flat gain, and low cross-polarization characteristics.
- Two monopulse antennas using the proposed ALTSA and self-compensating phase shifters were proposed. The monopulse antenna using magic-tee feeding was fabricated and demonstrated as the first AFSIW-based system on substrate.
- New five-port network named balanced-delta-port magic-tee was proposed and analysed, which is superior to the conventional magic-tee in term of power handling capability and is implementable using the multilayer AFSISW structure. Based on that, multilayer isolated power dividers/combiners were developed with two approaches: resistive-based and absorptive-based to highlight flexibility in design. In particular, a new method to implement the absorbing material was proposed, which allows the components to be insensitive to misalignment and dimensional errors of the absorber.

To further exploit the multilayer aspects of the AFSIW structure, multilayer beamforming network could also be developed. Among these passive solutions for beamforming network, the Butler matrix seemed to be the most attractive candidate thanks to its high performance and its simplicity in terms of design and number of components, compared to other solutions such as Blass matrix or Nolen matrix having the same number of ports. In [88], the idea of a Butler matrix without any cross-over was presented, which enhances the deployment of Butler matrix.

Based on this idea, a Butler matrix was demonstrated successfully at 77 GHz using the SIW technology [89]. Since the AFSIW offers low loss transmission, it is extremely interesting to develop a multilayer high performance AFSIW Butler matrix. An example of 4 × 4 multilayer Butler matrix is illustrated in Figure 6.1. With reference to this figure, the main part of coupling matrix (coupler, phase shifter) is implemented in the middle layer using the AFSIW structure. Meanwhile, the outputs are implemented on the top layer (S3).

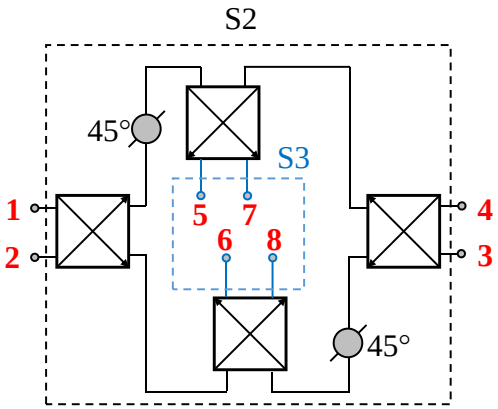

Figure 6.1 Multilayer Butler matrix without cross-over.

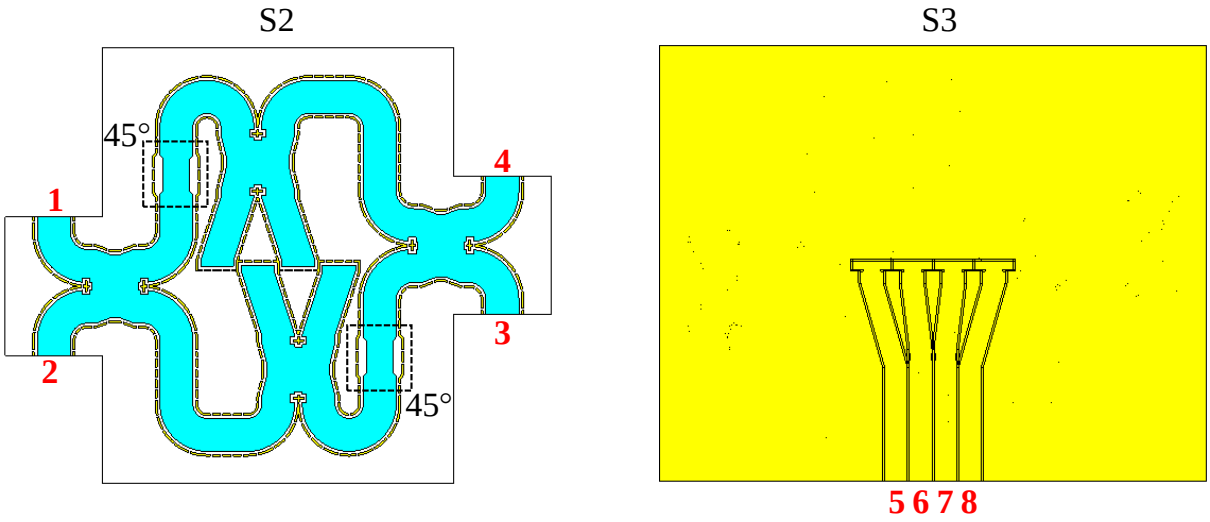

(*a*) (*b*)

Figure 6.2 Multilayer AFSIW Butler matrix without cross-over: (*a*) top view of layer S2 and (*b*) top view of layer S3.

Taking this idea to develop a Butler matrix for 5G applications around 28 GHz, an AFSIW Butler matrix is designed as shown in Figure 6.2. It implements the UEW-EL 45° AFSIW phase shifter presented in 3.1.3.

To couple energy from layer S2 to layer S3, four coupling slots were implemented as presented in Figure 6.3. Since the total width of the AFSIW is relatively large compared to the free-space waveguide (7.04 mm ≈ 0.66λ_0 at 28 GHz), tapered guided-wave structures were used to reduce the distance between the adjacent ports, hence, to reduce the grating lobe

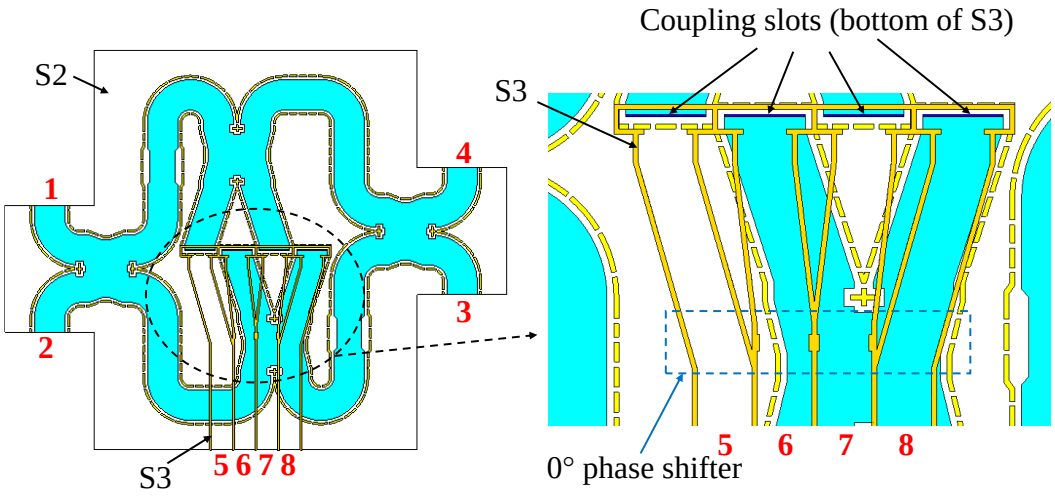

Figure 6.3 Illustration of the coupling between two layers in AFSIW Butler matrix.

The simulated reflection coefficient and isolation between input ports when port 1 is excited are given in Figure 6.4. In the 5G band from 27.5 GHz to 28.35 GHz, all the reflection and isolation coefficients are lower than -19.7 dB.

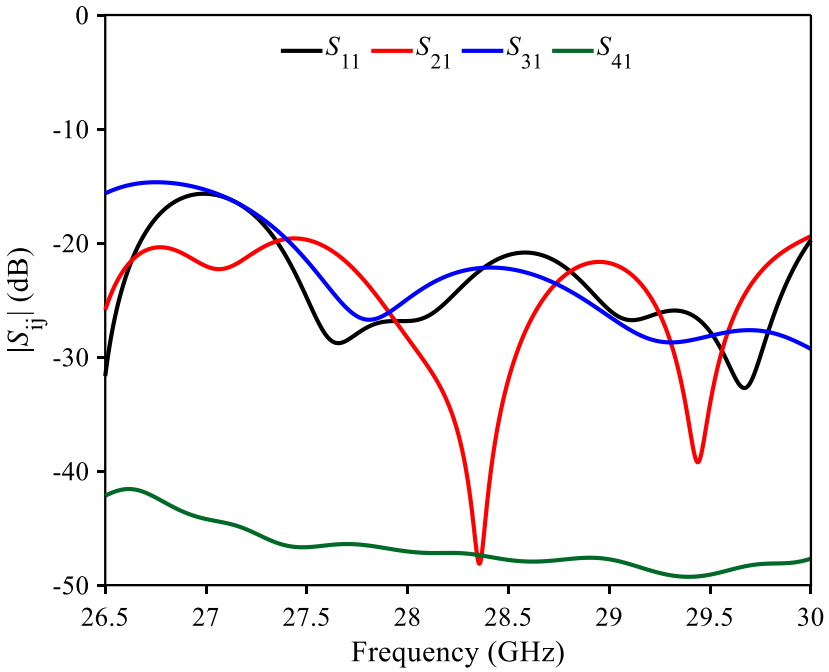

Figure 6.4 Simulated amplitude imbalances at outputs of the AFSIW Butler matrix.

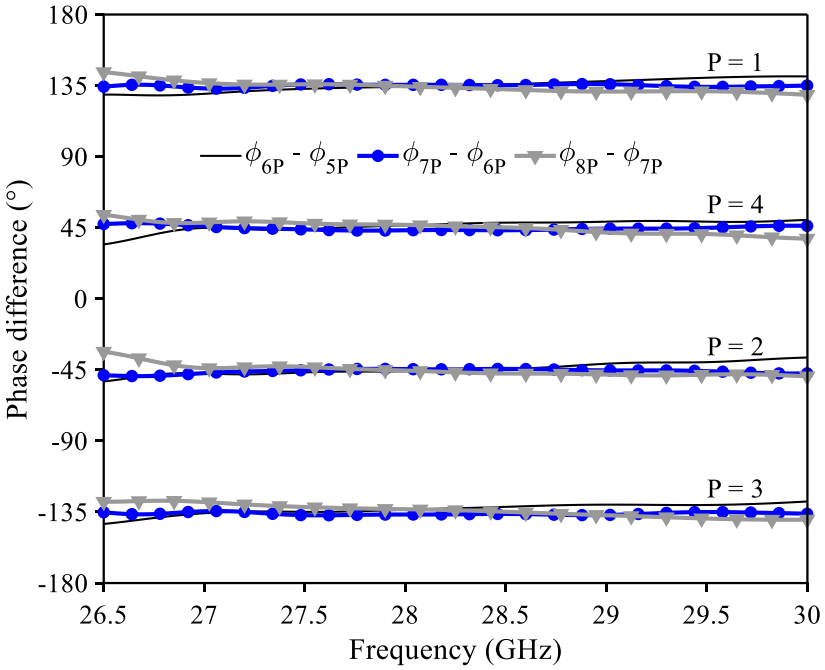

Figure 6.5 Simulated differential phases at outputs in AFSIW Butler matrix.

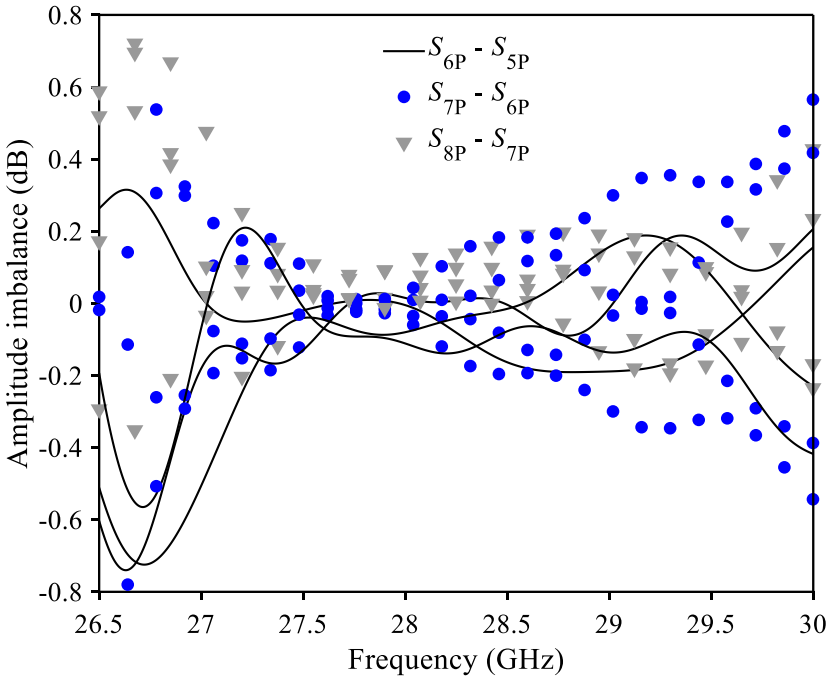

Figure 6.6 Simulated amplitude imbalances at outputs of the AFSIW Butler matrix.

The simulated differential phases between outputs are presented in Figure 6.5. It can be observed in Figure 6.5 that the differential phases at outputs variate around -135°, -45°, +45°,

and +135° when port 3, port 2, port 4, or port 1 is excited, respectively. In the 5G band from 27.5 GHz to 28.35 GHz, the phases errors are less than 5.17°.

The simulated amplitude imbalances between outputs are presented in Figure 6.6. In the 5G band (27.5 GHz to 28.35 GHz), the maximum amplitude imbalance between two adjacent ports is 0.18 dB.

It can be noticed from the simulated results that the AFSIW multilayer Butler matrix works well. After that, antennas could be integrated at outputs to show the beamforming capability.

To summarize, this Ph.D. thesis research contributes to exploit the degrees of freedom provided by the AFSIW structure and to enrich the AFSIW component library. Still, there are many works to be done to improve and to exploit further the AFSIW technological platform.

Due to the available fabrication process in our establishments, sidewall dielectric slabs must be kept for via integrity. This fact could limit the operation over higher frequency ranges as the waveguide width is reduced, and more electrical fields will concentrate in the sidewall dielectric slab. Hence, the AFSIW behaviour tends to be the DFSIW. In [23], it was demonstrated that in an SAFSIW structure, the 2^{nd} mode presents lower attenuation than the 1^{st} mode at higher frequency. This interesting characteristic could be used to develop the circuits and components at higher frequency ranges using high order mode operations.

Regarding the HM-SAFSIW, non-uniform leaky wave antenna could be developed thanks to the open-ended structure and the capability to control the attenuation and phase constants. Other components could also be developed using HM-SAFSIW such as multilayer coupler and so on.

In demonstration, the monopulse antenna was designed with normal power divider for in-lab measurement and for simplification. For high power measurements and radar applications, the absorptive-based isolated power dividers/combiners could be implemented to prevent the systems from damage.

Regarding the resistive-based isolated power divider/combiner, distribution network of resistors or resistive carbon paste could be used to improve the operation bandwidth as well as to increase the power handling capability.

SYNTHÈSE EN FRANÇAIS

Les systèmes de communication à faible coût et à haut débit sont cruciaux pour répondre aux besoins des utilisateurs en raison de l'augmentation des besoins de communication, ainsi que des services en ligne. Une des stratégies possibles pour augmenter le débit de transmission est d'élargir la bande passante du canal. Cependant, les basses fréquences deviennent saturées à cause du nombre important d'applications comme le GSM, le Wi-Fi, … Afin d'avoir plus de canaux libres, ainsi que des bandes passantes plus larges, des fréquences millimétriques doivent être exploitées.

Dans les bandes millimétriques, les pertes deviennent le problème le plus important à résoudre. Pour réduire les pertes, le guide d'ondes métallique rectangulaire (rectangular waveguide en anglais (RWG)) est préféré grâce à sa haute performance. Cependant, le RWG est volumineux, couteux, et difficile à intégrer avec les structures planaires. Le haut niveau d'intégration va réduire le coût de fabrication et permettre la production en série. Ce sont les avantages de la technologie planaire comme la ligne de micro-ruban. Malgré son avantage au niveau d'intégration et de coût, la technologie planaire, comme la ligne de micro-ruban, donne plus de pertes et fuites d'énergies à haute fréquence.

En héritant des avantages du RWG, ainsi que la technologie planaire, l'idée du guide d'ondes intégré au substrat (substrate integrated waveguide en anglais (SIW)) a été présentée en 2001 [1]. Ce nouveau type de guide permet de réaliser des systèmes hautes performances à faible coût dans les bandes millimétriques. Le SIW est obtenu en intégrant un RWG dans le substrat PCB comme illustré dans la Figure 1. En remplaçant les murs métalliques par des trous métallisés, le SIW peut conserver une structure auto-blindée et permet un haut niveau d'intégration grâce aux avantages de la technologie planaire. Depuis l'introduction du SIW, cette topologie a été exploitée largement pour développer des circuits et composants y compris des fonctions passives et actives [2], [3].

En 2014, une évolution du SIW qui s'appelle guide d'ondes intégré au substrat creux (air-filled SIW en anglais (AFSIW)) [4] a été introduite dans la perspective de réduire la perte diélectrique, qui est une contribution importante dans la bande millimétrique. L'AFSIW est une structure multicouche basée sur la technologie PCB comme illustrée dans la Figure 2. Puisque le guide d'onde AFSIW est rempli par l'air au lieu de diélectrique comme dans le SIW conventionnel (dielectric-filled SIW en anglais (DFSIW)), l'AFSIW a une empreinte d'un facteur $\sqrt{\varepsilon_r}$ fois plus large que le DFSIW ayant la même fréquence de coupure, où ε_r est la permittivité relative

du diélectrique. Par conséquent, il est nécessaire de développer une solution alternative donnant un compromis entre l'AFSIW et le DFSIW en termes de la taille et de la perte.

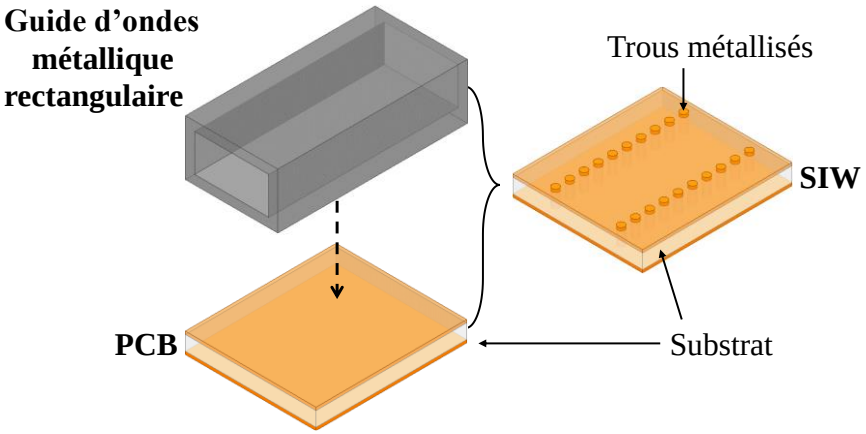

Figure 1 La réalisation du SIW

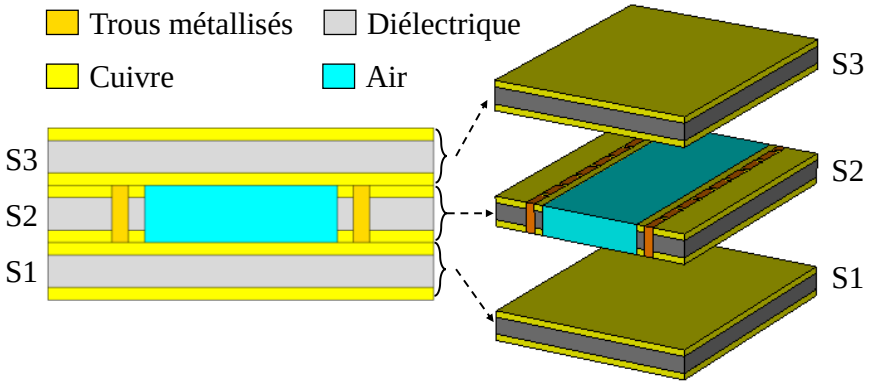

Figure 2 La structure de l'AFSIW

Depuis son introduction, de nombreux composants basés sur l'AFSIW ont été reportés comme des diviseurs de puissance [5], coupleurs [5], [6], déphaseurs [7], [8], filtres [9]-[13], antennes [14], [15], et terminaisons [16]. Cependant, la plupart de ces composants n'utilisent que la couche au milieu (S2) pour développer leurs fonctionnalités (Figure 3). L'exploitation de l'aspect multicouche est encore limitée [6], [10], [13], [15] (Figure 4). Donc, l'investigation sur la caractéristique multicouche est nécessaire pour mettre en profit le procédé de fabrication ainsi que pour augmenter la densité d'intégration.

En outre, comme l'idée de l'AFSIW a été présentée récemment, la bibliothèque de composants basés sur l'AFSIW est limitée. En plus, un système au substrat (system on substrate en anglais

(SoS)) basé sur l'AFSIW n'a pas encore été reporté pour mettre en profit les avantages de cette technologie.

Dans ce contexte, cette thèse en cotutelle est réalisée dans le cadre d'une collaboration internationale entre l'IMEP-LaHC en France, l'IMS en France, et le centre de recherche Poly-Grames au Canada. Le parcours de cette thèse est présenté dans la Figure 5.

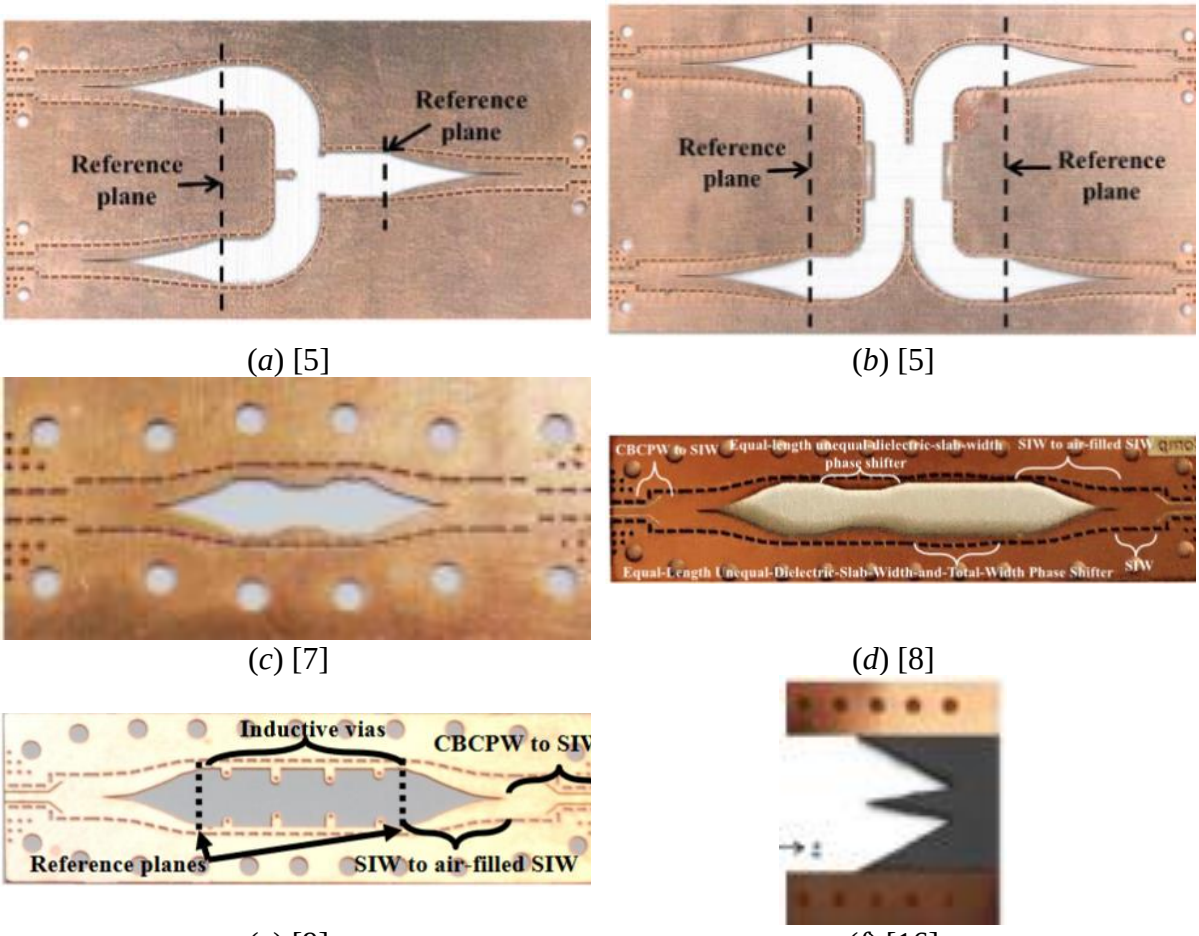

(*a*) [5] (*b*) [5]

(*c*) [7] (*d*) [8]

(*e*) [9] (*f*) [16]

Figure 3 Composants utilisant la couche au milieu de l'AFSIW: (*a*) diviseur de puissance [5], (*b*) coupleur de Riblet [5], (*c*) déphaseur dans la bande U [7], (*d*) déphaseur dans la bande Ka [8], (*e*) filtre IRIS [9], et (*f*) terminaison [16]

L'objectif principal de cette thèse est d'exploiter les degrés de liberté de la technologie AFSIW, y compris l'espace creux au milieu (la couche S2) ainsi que l'aspect multicouche, pour développer des circuits et composants dans la bande millimétrique afin d'enrichir la bibliothèque de composants de l'AFSIW. Pour la première fois, un système antennaire intégré au substrat à base de guides d'ondes AFSIW a été étudié et démontré en bande Ka.

Afin de pouvoir réaliser cet objectif, le Chapter 2 propose une nouvelle structure alternative qui s'appelle guide d'onde intégré au substrat creux à barreau diélectrique (slab AFSIW en anglais (SAFSIW)). Cette nouvelle structure offre un bon compromis entre l'AFSIW et le DFSIW en termes de pertes, d'empreinte, de capabilité de tenue en puissance, et de facteur de qualité *Q*. De plus, le SAFSIW donne une bande passante monomode plus large en comparaison avec l'AFSIW et le DFSIW ainsi que la possibilité de contrôler les constantes de phase et d'atténuation pour des applications spécifiques. Des analyses théoriques, ainsi que des validations expérimentales ont été réalisées pour démontrer la flexibilité de la structure SAFSIW. Afin de réduire la taille des composants ainsi que d'augmenter la flexibilité du design, l'idée de SAFSIW à demi-mode a été présentée et démontrée.

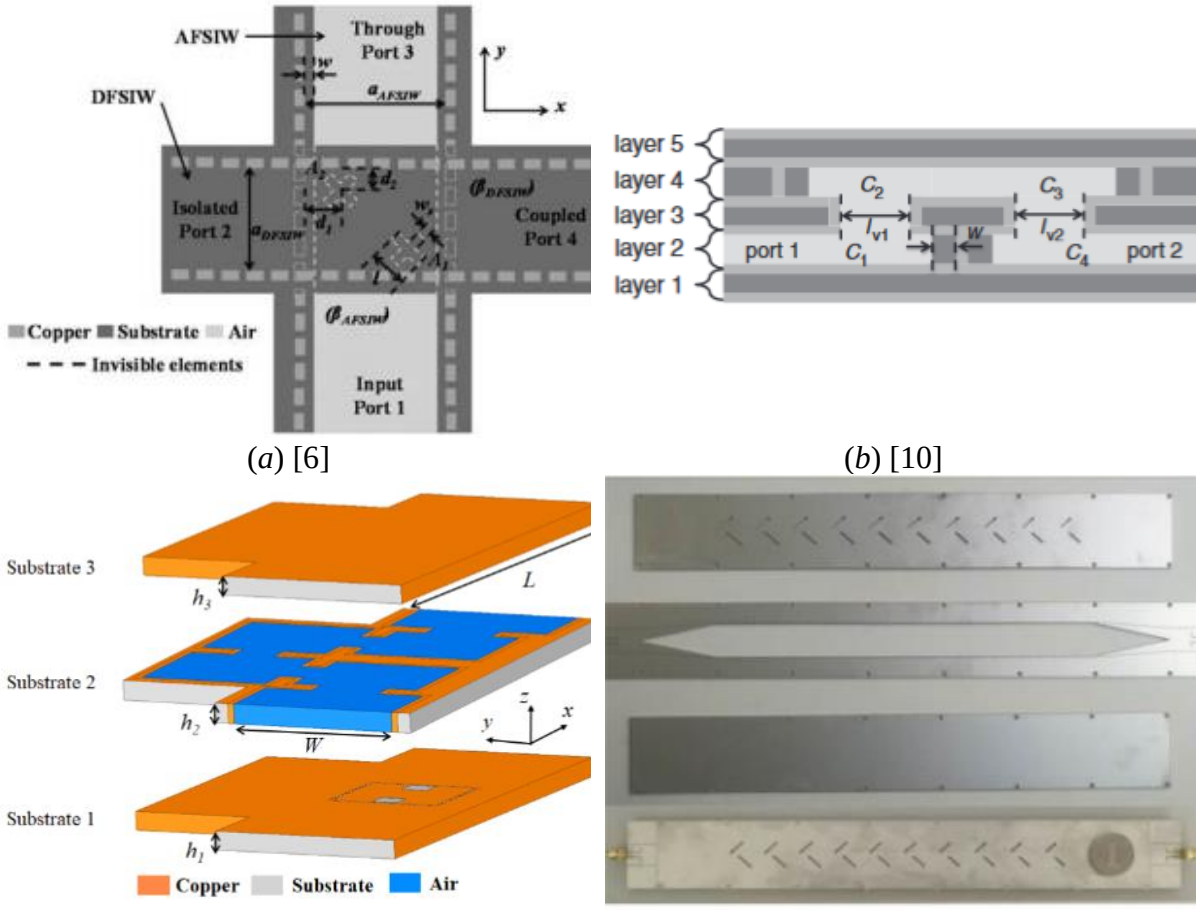

(*a*) [6] (*b*) [10]

(*c*) [13] (*d*) [15]

Figure 4 Composants exploitant l'aspect multicouche de l'AFSIW: (*a*) coupleur de Moreno [6], (*b*) filtre dans la bande Ka [10], (*c*) filtre dans la bande K [13], et (*d*) antenne à ondes de fuite [15]

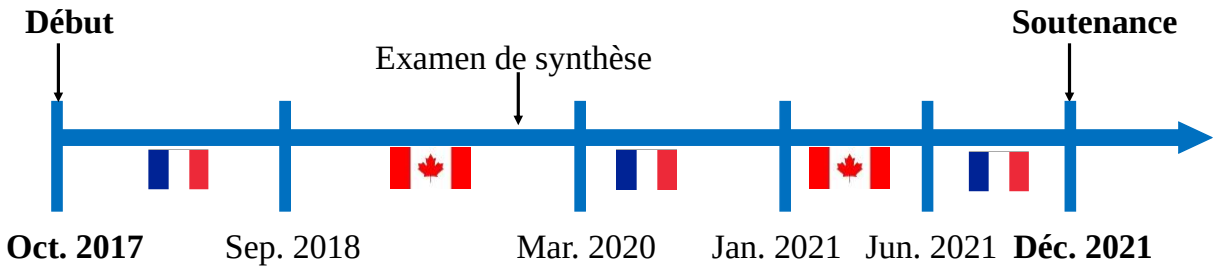

Figure 5 Le parcours de cette thèse en cotutelle

En utilisant le barreau diélectrique central du SAFSIW, des déphaseurs auto-compensés et un coupleur cruciforme sont développés et présentés dans le Chapter 3. Grâce à l'effet auto-compensé, le déphaseur peut conserver une topologie de longueur équilibrée avec une taille plus compacte. Ce déphaseur auto-compensé va être utilisé pour développer un système antennaire monopulse dans le Chapter 4.

En plus, le barreau diélectrique central du SAFSIW peut-être mis à profit pour réduire la polarisation croisée dans une antenne antipodale à fentes coniques linéaires (antipodal linearly tapered slot antenne en anglais (ALTSA)). Cette idée est validée dans le Chapter 4 avec une réduction de la polarisation croisée de 13.4 dB à 33 GHz. Cette antenne élémentaire est utilisée pour développer deux réseaux d'antennes monopulse, l'un basé sur le coupleur hybride de 180° et l'autre basé sur la jonction T magique pour la partie d'alimentation. Le réseau d'antennes utilisant la jonction T magique a été fabriqué et démontré. Ce réseau d'antennes peut-être considéré comme le premier système au substrat basé sur l'AFSIW.

Concernant l'aspect multicouche, il est exploité davantage dans le Chapter 5. Un nouveau concept de structure 5-port appelée la jonction T magique aux ports deltas équilibrés (balanced-delta-port magique-tee en anglais) a été introduit avec la possibilité de tenir plus de puissance que la jonction T magique traditionnelle. Cette nouvelle topologie a été mise à profit pour développer des diviseurs/combineurs de puissance avec les sorties/entrées isolées. Afin de renforcer le niveau d'isolation, deux solutions basées sur des résistances et un matériau absorbant ont été proposées. La solution absorbante donne une large bande d'isolation avec une meilleure tolérance aux erreurs de fabrication, ce qui est important pour une production en série.

Dans chaque chapitre, une revue de la littérature est faite pour fournir une vision générale et mettre en évidence les besoins. Une brève conclusion est donnée à la fin de chaque chapitre pour mettre en avant les avantages des solutions proposées ainsi que l'originalité des travaux présentés.

Finalement, le Chapter 6 conclut cette thèse en synthétisant les contributions scientifiques et techniques proposées. En perspective de cette thèse, le Chapter 6 présente des idées d’exploitation des résultats obtenus.

REFERENCES

[1] D. Deslandes and K. Wu, “Integrated microstrip and rectangular waveguide in planar form,” in *IEEE Microwave and Wireless Components Letters*, vol. 11, no. 2, pp. 68–70, Feb. 2001.

[2] K. Wu, D. Deslandes, and Y. Cassivi, “The substrate integrated circuits - a new concept for high-frequency electronics and optoelectronics, ” *6th International Conference on Telecommunications in Modern Satellite, Cable and Broadcasting Service, 2003. TELSIKS 2003.*, Nis, Yugoslavia, 2003, pp. P-III.

[3] M. Bozzi, A. Georgiadis, and K. Wu, “Review of substrate-integrated waveguide circuits and antennas,” in *IET Microwavve, Antennas & Propagation*, vol. 5, no. 8, pp. 909-920, 6 June 2011.

[4] F. Parment, A. Ghiotto, T.P. Vuong, J.M. Duchamp, and K. Wu, “Broadband transition from dielectric-filled to air-filled substrate integrated waveguide for low loss and high power handling millimeter-wave substrate integrated circuits,” *2014 IEEE MTT-S International Microwave Symposium (IMS2014)*, Tampa, FL, Jun. 2014, pp. 1-3.

[5] F. Parment, A. Ghiotto, T. Vuong, J. Duchamp, and K. Wu, “Air-Filled Substrate Integrated Waveguide for Low-Loss and High Power-Handling Millimeter-Wave Substrate Integrated Circuits,” in *IEEE Transactions on Microwave Theory and Techniques*, vol. 63, no. 4, pp. 1228-1238, April 2015.

[6] F. Parment, A. Ghiotto, T. Vuong, J. Duchamp, and K. Wu, “Broadband directional Moreno coupler for high-performance air-filled SIW-based Substrate Integrated Systems,” *2016 IEEE MTT-S International Microwave Symposium (IMS)*, San Francisco, CA, 2016, pp. 1-3.

[7] F. Parment, A. Ghiotto, T. Vuong, J. Duchamp, and K. Wu, “Air-filled SIW transmission line and phase shifter for high-performance and low-cost U-Band integrated circuits and systems,” *IEEE Global Symposium on Millimeter-Waves (GSMM)*, Montreal, QC, 2015, pp. 1-3.

[8] F. Parment, A. Ghiotto, T. P. Vuong, J. M. Duchamp and K. Wu, “Double dielectric slab-loaded air-filled SIW phase shifters for high-performance millimeter-wave integration,” in *IEEE Transactions on Microwave Theory and Techniques*, vol. 64, no. 9, pp. 2833-2842, Sept. 2016.

[9] F. Parment, A. Ghiotto, T. Vuong, J. Duchamp, and K. Wu, “Low-loss air-filled Substrate Integrated Waveguide (SIW) band-pass filter with inductive posts,” *2015 European Microwave Conference (EuMC)*, Paris, 2015, pp. 761-764.

[10] F. Parment, A. Ghiotto, T.P. Vuong, J.M. Duchamp, K. Wu, “Ka-band compact and high performance bandpass filter based on multilayer airfilled SIW,” *in IET Electronics Letters*, Feb. 2017.

[11] T. Martin, A. Ghiotto, T. Vuong, F. Lotz, and P. Monteil, “High performance air-filled substrate integrated waveguide filter post-process tuning using capacitive post,” *2017 IEEE MTT-S International Microwave Symposium (IMS)*, Honololu, HI, 2017, pp. 196-199.

[12] T. Martin, A. Ghiotto, T. Vuong, and F. Lotz, “Self-Temperature-Compensated Air-Filled Substrate-Integrated Waveguide Cavities and Filters,” in *IEEE Transactions on Microwave Theory and Techniques*, vol. 66, no. 8, pp. 3611-3621, Aug. 2018.

[13] T. Martin, A. Ghiotto, T. Vuong, K. Wu, and F. Lotz, “Compact Quasi-Elliptic and Highly Selective AFSIW Filter with Multilayer Cross-Coupling,” *2019 IEEE MTT-S International Microwave Symposium (IMS)*, Boston, MA, USA, 2019, pp. 718-721.

[14] A. Ghiotto, F. Parment, T. Vuong, and K. Wu, “Millimeter-Wave Air-Filled SIW Antipodal Linearly Tapered Slot Antenna,” in *IEEE Antennas and Wireless Propagation Letters*, vol. 16, pp. 768-771, 2017.

[15] R. Hong, J. Shi, D. Guan, W. Cao and Z. Qian, “Wideband and Low-Loss Beam-Scanning Circularly Polarized Antenna Based on Air-Filled SIW,” *in IEEE Antennas and Wireless Propagation Letters*, vol. 20, no. 7, pp. 1254-1258, July 2021.

[16] I. Marah, A. Ghiotto, J. Pham, T. Martin and A. Boisse, “AFSIW Termination with Full- and Partial-Height Absorbing Material Loading,” 2019 49th European Microwave Conference (EuMC), 2019, pp. 686-689.

[17] T. Martin, F. Parment, A. Ghiotto, T. Vuong, and K. Wu, “Air-Filled SIW interconnections for high performance millimeter-wave circuit and system prototyping and assembly,” *2017 IEEE MTT-S International Conference on Numerical Electromagnetic and Multiphysics Modeling and Optimization for RF, Microwave, and Terahertz Applications (NEMO)*, Seville, 2017, pp. 302-304.

[18] F. Parment, A. Ghiotto, T. Vuong, L. Carpentier, and K. Wu, “Substrate integrated suspended line to air-filled SIW transition for high-performance millimeter-wave multilayer

integration," *2017 IEEE MTT-S International Microwave Symposium (IMS)*, Honololu, HI, 2017, pp. 719-722.

[19] N. H. Nguyen, A. Ghiotto, T. P. Vuong, A. Vilcot, F. Parment and K. Wu, "Slab Air-Filled Substrate Integrated Waveguide," *2018 IEEE/MTT-S International Microwave Symposium - IMS*, Philadelphia, PA, 2018, pp. 312-315.

[20] W. P. Ayres, P. H. Vartanian and A. L. Helgesson, "Propagation in dielectric slab loaded rectangular waveguide," *IRE Transactions on Microwave Theory and Techniques*, vol. 6, no. 2, pp. 215-222, April 1958.

[21] M. Bozzi, D. Deslanddes, P. Arcioni, L. Perregrini, K. Wu and G. Conciauro, "Efficient analysis and experimental verification of substrate-integrated slab waveguides for wideband microwave applications," in *International Journal of RF and Microwave Computuer-Aided Engineering*, vol. 15, no. 3, pp. 296–306, May 2005.

[22] N. H. Nguyen, A. Ghiotto, T. Martin, A. Vilcot, K. Wu, and T. P. Vuong, "A 90° self-compensating slab air-filled substrate integrated waveguide phase shifter," *2019 IEEE MTT-S International Microwave Symposium (IMS)*, Boston, MA, USA, 2019, pp. 580-583.

[23] E. Massoni, M. Bozzi, and K. Wu, "Increasing efficiency of leaky-wave antenna by using substrate integrated slab waveguide," in *IEEE Antennas and Wireless Propagation Letters*, vol. 18, no. 8, pp. 1596-1600, Aug. 2019.

[24] D. M. Pozar, Microwave Engineering. 3rd edition. Hoboken, NJ : John Wiley & Son, Inc, 2005.

[25] M. Bozzi, S. A. Winkler and K. Wu, "Broadband and compact ridge substrate-integrated waveguides," *IET Microwaves, Antennas and Propagation*, vol. 4, no. 11, pp. 1965-1973, Nov. 2010.

[26] T. Liang, S. Hall, H. Heck and G. Brist, "A practical method for modeling PCB transmission lines with conductor surface roughness and wideband dielectric properties," *2006 IEEE MTT-S International Microwave Symposium Digest*, 2006, pp. 1780-1783.

[27] F. Parment, A. Ghiotto, T. P. Vuong, J. M. Duchamp and K. Wu, "Air-filled substrate integrated waveguide for low-loss and high power-handling millimeter-wave substrate integrated circuits," in *IEEE Transactions on Microwave Theory and Techniques*, vol. 63, no. 4, pp. 1228-1238, Apr. 2015.

[28] Y. J. Cheng, K. Wu and W. Hong, “Power handling capability of substrate integrated waveguide interconnects and related transmission line systems,” in *IEEE Transactions on Advanced Packaging*, vol. 31, no. 4, pp. 900-909, Nov. 2008.

[29] N. Grigoropoulos, B. Sanz-Izquierdo, and P. R. Young, “Substrate integrated folded waveguides (SIFW) and filters,” in *IEEE Microwave and Wireless Components Letters*, vol. 15, no. 12, pp. 829-831, Dec. 2005.

[30] M. Bozzi, L. Perregrini and C. Tomassoni, “A Review of Compact Substrate Integrated Waveguide (SIW) Interconnects and Components,” *IEEE 23rd Workshop on Signal and Power Integrity (SPI)*, pp. 1-4, 2019.

[31] W. Hong *et al*., “Half mode substrate integrated waveguide: A new guided wave structure for microwave and millimeter wave application,” *Joint 31st International Conference on Infrared Millimeter Waves and 14th International Conference on Teraherz Electronics*, Shanghai, pp. 219-219, 2006.

[32] W. Che, C. Li, P. Russer, and Y. L. Chow, “Propagation and band broadening effect of planar integrated ridged waveguide in multilayer dielectric substrates,” *2008 IEEE MTT-S International Microwave Symposium Digest*, Atlanta, GA, USA, pp. 217-220, 2008.

[33] A. Niembro-Martin *et al*., “Slow-wave substrate integrated waveguide,” in *IEEE Transactions on Microwave Theory and Techniques*, vol. 62, no. 8, pp. 1625–1633, Aug. 2014.

[34] I. S. S. Lima, F. Parment, A. Ghiotto, T. Vuong and K. Wu, “Broadband Dielectric-to-Half-Mode Air-Filled Substrate Integrated Waveguide Transition,” in *IEEE Microwave and Wireless Components Letters*, vol. 26, no. 6, pp. 383-385, June 2016.

[35] C. -W. Ting, S. Chen and T. -L. Wu, “A Cost-efficient Air-Filled Substrate Integrated Ridge Waveguide for mmWave Application,” *2020 IEEE/MTT-S International Microwave Symposium (IMS)*, 2020, pp. 165-168.

[36] N. H. Nguyen, A. Ghiotto, A. Vilcot, K. Wu, and T. P. Vuong, “Half-mode slab air-filled substrate integrated waveguide (SAFSIW),” *2021 IEEE MTT-S International Microwave Symposium (IMS)*, Atlanta, GA, USA, pp. 335-338, Jun. 2021.

[37] N. Nguyen-Trong and C. Fumeaux, “Half-Mode Substrate-Integrated Waveguides and Their Applications for Antenna Technology: A Review of the Possibilities for Antenna Design,” in *IEEE Antennas and Propagation Magazine*, vol. 60, no. 6, pp. 20-31, Dec. 2018.

[38] Y. J. Cheng, K. Wu and W. Hong, "Substrate integrated waveguide (SIW) broadband compensating phase shifter," *2009 IEEE MTT-S International Microwave Symposium Digest*, Boston, MA, 2009, pp. 845-848.

[39] I. Boudreau, K. Wu and D. Deslandes, "Broadband phase shifter using air holes in Substrate Integrated Waveguide," *2011 IEEE MTT-S International Microwave Symposium*, Baltimore, MD, 2011, pp. 1-4.

[40] Y. M. Huang, S. Ding, G. Wang and M. Bozzi, "Compact Equal-Width Equal-Length Phase Shifter With Slow-Wave Half-Mode Substrate Integrated Waveguide for 5G Applications," in *IEEE Access*, vol. 7, pp. 160595-160609, 2019.

[41] Y. Wang, B. Wu, N. Zhang, Y. Zhao and T. Su, "Wideband Circularly Polarized Magneto-Electric Dipole 1 × 2Antenna Array for Millimeter-Wave Applications," in *IEEE Access*, vol. 8, pp. 27516-27523, 2020.

[42] E. Y. Jung, T. Y. Seo, J. H. Kang, J. W. Lee, T. K. Lee and W. K. Lee, "A novel circular-polarized array antenna based on substrate integrated waveguide for satellite communication," *Proceedings of the Fourth European Conference on Antennas and Propagation*, 2010, pp. 1-4.

[43] T. Djerafi, N. J. G. Fonseca and K. Wu, "Planar Ku-Band 4×4 Nolen Matrix in SIW Technology," in *IEEE Transactions on Microwave Theory and Techniques*, vol. 58, no. 2, pp. 259-266, Feb. 2010.

[44] T. Djerafi, N. J. G. Fonseca and K. Wu, "Broadband Substrate Integrated Waveguide 4×4 Nolen Matrix Based on Coupler Delay Compensation," in *IEEE Transactions on Microwave Theory and Techniques*, vol. 59, no. 7, pp. 1740-1745, July 2011.

[45] S. Odrobina, K. Staszek, K. Wincza and S. Gruszczynski, "Broadband 3 x 3 butler matrix," *2017 Conference on Microwave Techniques (COMITE)*, 2017, pp. 1-5.

[46] C. Qin, F. -C. Chen and K. -R. Xiang, "A 5 x 8 Butler Matrix Based on Substrate Integrated Waveguide Technology for Millimeter-Wave Multibeam Application," in *IEEE Antennas and Wireless Propagation Letters*.

[47] Y. J. Cheng, W. Hong and K. Wu, "Design of a Monopulse Antenna Using a Dual V-Type Linearly Tapered Slot Antenna (DVLTSA)," in *IEEE Transactions on Antennas and Propagation*, vol. 56, no. 9, pp. 2903-2909, Sept. 2008.

[48] Y. J. Cheng, W. Hong, and K. Wu, “Millimetre-wave monopulse antenna incorporating substrate integrated waveguide phase shifter,” *IET Microwaves, Antennas & Propagation*, vol. 2, no. 1, pp. 48-52, Feb. 2008.

[49] B. Liu *et al.*, “Substrate Integrated Waveguide (SIW) Monopulse Slot Antenna Array,” in *IEEE Transactions on Antennas and Propagation*, vol. 57, no. 1, pp. 275-279, Jan. 2009.

[50] Y. J. Cheng, W. Hong and K. Wu, “94 GHz Substrate Integrated Monopulse Antenna Array,” in *IEEE Transactions on Antennas and Propagation*, vol. 60, no. 1, pp. 121-129, Jan. 2012.

[51] C. Chen and T. Chu, “Design of a 60-GHz Substrate Integrated Waveguide Butler Matrix—A Systematic Approach,” in *IEEE Transactions on Microwave Theory and Techniques*, vol. 58, no. 7, pp. 1724-1733, July 2010.

[52] T. Djerafi and K. Wu, “Super-Compact Substrate Integrated Waveguide Cruciform Directional Coupler,” *in IEEE Microwave and Wireless Components Letters*, vol. 17, no. 11, pp. 757-759, Nov. 2007.

[53] S. Liu and F. Xu, “Compact Multilayer Half Mode Substrate Integrated Waveguide 3-dB Coupler,” *in IEEE Microwave and Wireless Components Letters*, vol. 28, no. 7, pp. 564-566, July 2018.

[54] H. J. Riblet, “The Short-Slot Hybrid Junction,” in *Proceedings of the IRE*, vol. 40, no. 2, pp. 180-184, Feb. 1952.

[55] I. Ohta, Y. Yumita, K. Toda and M. Kishihara, “Cruciform directional couplers in H-plane rectangular waveguide,” *2005 Asia-Pacific Microwave Conference Proceedings*, pp. 4, 2005.

[56] T. Djerafi, N. J. G. Fonseca and K. Wu, “Planar Ku-Band 4×4 Nolen Matrix in SIW Technology,” *in IEEE Transactions on Microwave Theory and Techniques*, vol. 58, no. 2, pp. 259-266, Feb. 2010.

[57] M. Kishihara, M. Komatsubara, K. Okubo and I. Ohta, “Broad-band cruciform substrate integrated waveguide couplers,” *2009 Asia Pacific Microwave Conference*, pp. 2100-2103, 2009.

[58] T. Djerafi and K. Wu, “60 GHz substrate integrated waveguide crossover structure,” *2009 European* Microwave *Conference (EuMC)*, pp. 1014-1017, 2009.

[59] A. Doghri, T. Djerafi, A. Ghiotto and K. Wu, “Substrate Integrated Waveguide Directional Couplers for Compact Three-Dimensional Integrated Circuits,” *in IEEE Transactions on Microwave Theory and Techniques*, vol. 63, no. 1, pp. 209-221, Jan. 2015.

[60] S. M. Sherman and D. K. Barton, Monopulse Principles and Techniques. Norwood, MA, USA: Artech House, 2011.

[61] J. Zhu, S. Liao, S. Li and Q. Xue, “60 GHz Substrate-Integrated Waveguide-Based Monopulse Slot Antenna Arrays,” in *IEEE Transactions on Antennas and Propagation*, vol. 66, no. 9, pp. 4860-4865, Sept. 2018.

[62] G. Huang, S. Zhou and T. Chio, “Highly-Efficient Self-Compact Monopulse Antenna System With Integrated Comparator Network for RF Industrial Applications,” in *IEEE Transactions on Industrial Electronics*, vol. 64, no. 1, pp. 674-681, Jan. 2017.

[63] G. Huang, S. Zhou, T. Chio, C. Sim and T. Yeo, “Wideband Dual-Polarized and Dual-Monopulse Compact Array for SAR System Integration Applications,” in *IEEE Geoscience and Remote Sensing Letters*, vol. 13, no. 8, pp. 1203-1207, Aug. 2016.

[64] H. Wang, D. Fang, B. Zhang and W. Che, “Dielectric Loaded Substrate Integrated Waveguide (SIW) H-Plane Horn Antennas,” in *IEEE Transactions on Antennas and Propagation*, vol. 58, no. 3, pp. 640-647, March 2010.

[65] Warren L. Stutzman and Gary A. Thiele, Antenna Theory and Design. 3rd edition. Hoboken, NJ : John Wiley & Son, Inc, 2012.

[66] A. Ghiotto, F. Parment, T. Vuong, and K. Wu, “Millimeter-wave air-filled SIW antipodal linearly tapered slot antenna,” in *IEEE Antennas and Wireless Propagation Letter*, vol. 16, pp. 768-771, 2017.

[67] N. H. Nguyen, A. Ghiotto, A. Vilcot, T. P. Vuong and K. Wu, “Multilayer Slab AFSIW Antipodal Linearly Tapered Slot Antenna With Cross-Polarization Reduction,” in *IEEE Antennas and Wireless Propagation Letters*, vol. 20, no. 5, pp. 763-767, May 2021.

[68] D. Schaubert, E. Kollberg, T. Korzeniowski, T. Thungren, J. Johansson, and K. Yngvesson, “Endfire tapered slot antennas on dielectric substrates,” *IEEE Trans. Antennas Propag.*, vol. 33, no. 12, pp. 1392-1400, Dec. 1985.

[69] T. Djerafi and K. Wu, “Corrugated substrate integrated waveguide (SIW) antipodal linearly tapered slot antenna array fed by quasi-triangular power divider,” *Prog. Electromagn. Res. C*, vol. 26, pp. 139-151, 2012.

[70] C. Chu, J. Zhu, S. Liao, Q. Xue and A. Zhu, "Dual-Polarized Substrate-Integrated-Waveguide Cavity-Backed Monopulse Antenna Array for 5G Millimeter-Wave Applications," *2019 IEEE MTT-S International Microwave Conference on Hardware and Systems for 5G and Beyond (IMC-5G)*, pp. 1-3, 2019.

[71] T. Martin, A. Ghiotto, T. Vuong, and F. Lotz, "Configurable perforated air-filled substrate integrated waveguide (AFSIW) for generic high-performance systems on substrate," *IEEE Trans. Microw. Theory Techn.*, vol. 67, no. 11, pp. 4308-4321, Nov. 2019.

[72] A. Moulay and T. Djerafi, "Gysel Power Divider with Fixed Characteristic Impedance," *2020 IEEE/MTT-S International Microwave Symposium (IMS)*, 2020, pp. 896-899.

[73] S. E. Hosseini, M. Amrollahzadeh and F. Ahmadfard, "A Novel Two-Way Gysel Power Divider Based on Ridge-Gap Waveguide Technology," *2019 Sixth Iranian Conference on Radar and Surveillance Systems*, 2019, pp. 1-4.

[74] Z. Y. Zhang and K. Wu, "Broadband half-mode substrate integrated waveguide (HMSIW) Wilkinson power divider," *2008 IEEE MTT-S International Microwave Symposium Digest*, Atlanta, GA, USA, 2008, pp. 879-882.

[75] T. Djerafi, D. Hammou, K. Wu, S. O. Tatu, "Ring-shaped substrate integrated waveguide Wilkinson power dividers/combiners", in *IEEE Transactions on Components, Packaging and Manufacturing Technology*, vol. 4, no. 9, pp. 1461-1469, Sep. 2014.

[76] A. Moulay and T. Djerafi, "Wilkinson Power Divider With Fixed Width Substrate-Integrated Waveguide Line and a Distributed Isolation Resistance," in *IEEE Microwave and Wireless Components Letters*, vol. 28, no. 2, pp. 114-116, Feb. 2018.

[77] Y. Zhou *et al.*, "Slow-Wave Half-Mode Substrate Integrated Waveguide 3-dB Wilkinson Power Divider/Combiner Incorporating Nonperiodic Patterning," in *IEEE Microwave and Wireless Components Letters*, vol. 28, no. 9, pp. 765-767, Sept. 2018.

[78] M. Pasian *et al.*, "Substrate-integrated-waveguide E-plane 3-dB power-divider/combiner based on resistive layers," *IEEE Trans. Microw. Theory Techn.*, vol. 65, no. 5, pp. 1498-1510, May 2017.

[79] J. Ding, Q. Wang, Y. Zhang and C. Wang, "A Novel Five-Port Waveguide Power Divider," in *IEEE Microwave and Wireless Components Letters*, vol. 24, no. 4, pp. 224-226, April 2014.

[80] Y. M. Huang *et al*., "Substrate-integrated waveguide power combiner/divider incorporating absorbing material," *IEEE Microw. Wireless Compon. Lett.*, vol. 27, no. 10, pp. 885-887, Oct. 2017.

[81] R. Vincenti Gatti and R. Rossi, "Hermetic broadband 3-dB power divider/combiner in substrate-integrated waveguide (SIW) technology," *IEEE Trans. Microw. Theory Techn.*, vol. 66, no. 6, pp. 3048-3054, Jun. 2018.

[82] N. H. Nguyen, A. Ghiotto, T. Martin, A. Vilcot, K. Wu and T. P. Vuong, "Fabrication-Tolerant Broadband Air-Filled SIW Isolated Power Dividers/Combiners," in *IEEE Transactions on Microwave Theory and Techniques*, vol. 69, no. 1, pp. 603-615, Jan. 2021.

[83] S. Germain, D. Deslandes and K. Wu, "Development of substrate integrated waveguide power dividers," *CCECE 2003 - Canadian Conference on Electrical and Computer Engineering. Toward a Caring and Humane Technology (Cat. No.03CH37436)*, vol.3, pp. 1921-1924, 2003.

[84] F. Fesharaki, T. Djerafi, M. Chaker, and K. Wu, "S-parameter deembedding algorithm and its application to substrate integrated waveguide lumped circuit model extraction," in *IEEE Transactions on Microwave Theory and Techniques*, vol. 65, no. 4, pp. 1179-1190, April 2017.

[85] https://www.vishay.com/docs/53014/ch.pdf

[86] N. H. Nguyen, A. Ghiotto, T. Martin, A. Vilcot, T. P. Vuong and K. Wu, "AFSIW Power Divider with Isolated Outputs Based on Balanced-Delta-Port Magic-Tee Topology," 2020 *IEEE/MTT-S International Microwave Symposium (IMS)*, pp. 743-746, 2020.

[87] C. A. Balanis, Antenna Theory, Analysis and Design. 3rd edition. Hoboken, NJ: John Wiley, 2005.

[88] K. Uehara, T. Seki and K. Kagoshima, "A planar sector antenna for indoor high-speed wireless communication terminals," *IEEE Antennas and Propagation Society International Symposium 1997. Digest*, vol.2, pp. 1352-1355, 1997.

[89] T. Djerafi and K. Wu, "A Low-Cost Wideband 77-GHz Planar Butler Matrix in SIW Technology," *in IEEE Transactions on Antennas and Propagation*, vol. 60, no. 10, pp. 4949-4954, Oct. 2012.

LIST OF PUBLICATIONS

International journal

1. **N. H. Nguyen**, A. Ghiotto, T. P. Vuong, A. Vilcot, T. Martin, and K. Wu, "Dielectric slab air-filled substrate integrated waveguide (SAFSIW) bandpass filters," in *IEEE Microwave and Wireless Components Letters*, vol. 30, no. 4, pp. 363-366, Apr. 2020.
2. **N. H. Nguyen**, A. Ghiotto, T. Martin, A. Vilcot, K. Wu, and T. P. Vuong, "Fabrication-tolerant broadband air-filled SIW isolated power dividers/combiners," in *IEEE Transactions on Microwave Theory and Techniques*, vol. 69, no. 1, pp. 603-615, Jan. 2021.
3. **N. H. Nguyen**, A. Ghiotto, A. Vilcot, T. P. Vuong, and K. Wu, "Multilayer slab AFSIW antipodal linearly tapered slot antenna with cross-polarization reduction," in *IEEE Antennas and Wireless Propagation Letters*, , vol. 20, no. 5, pp. 763-767, May 2021.

International conference

1. **N. H. Nguyen**, A. Ghiotto, T. P. Vuong, A. Vilcot, F. Parment, and K. Wu, "Slab air-filled substrate integrated waveguide," *IEEE MTT-S International Microwave Symposium (IMS)*, Philadelphia, PA, USA, pp. 312-315, Jun. 2018.
2. **N. H. Nguyen**, A. Ghiotto, T. Martin, A. Vilcot, K. Wu, and T. P. Vuong, "A 90° self-compensating slab air-filled substrate integrated waveguide phase shifter," *IEEE MTT-S International Microwave Symposium (IMS)*, Boston, MA, USA, pp. 580-583, Jun. 2019.
3. **N. H. Nguyen**, A. Ghiotto, T. Martin, A. Vilcot, T. P. Vuong, and K. Wu, "AFSIW power divider with isolated outputs based on balanced-delta-port magic-tee topology," *IEEE MTT-S International Microwave Symposium (IMS)*, Los Angeles, CA, USA, pp. 743-746, Aug. 2020.
4. **N. H. Nguyen**, A. Ghiotto, A. Vilcot, K. Wu, and T. P. Vuong, "Half-mode slab air-filled substrate integrated waveguide (SAFSIW)," *IEEE MTT-S International Microwave Symposium (IMS)*, Atlanta, GA, USA, Jun. 2021. (Selected for the IMS2021 Student Paper Competition Finalist)
5. **N. H. Nguyen**, A. Ghiotto, A. Vilcot, T. P. Vuong, and K. Wu, "Slab air-filled substrate integrated waveguide (SAFSIW) cruciform coupler," *IEEE International Microwave*

Workshop Series On Advanced Materials and Processes for RF and THz Applications (IMWS-AMP 2021), Chongqing, China, pp. 196-198, Nov. 2021. (Selected for the IMWS-AMP 2021 Best Student Paper Contest)

6. **N. H. Nguyen**, A. Ghiotto, A. Vilcot, T. P. Vuong, and K. Wu, "Mass-producible broadband AFSIW termination," *IEEE International Microwave and RF Conference 2021 (IMaRC 2021)*, Kanpur, India, pp. 1-4, Dec. 2021.

National conference

1. **N. H. Nguyen**, A. Ghiotto, A. Vilcot, K. Wu, and T. P. Vuong, "Guide d'onde intégré au substrat creux a barreau diélectrique," *Journée Nationales Microondes*, France, Caen, Mai 2019.